Understanding the mechanisms leading to copper migration in supported oxygen carrier for chemical looping combustion

Sharmin Sharna

UNIVERSITÉ DE STRASBOURG

ÉCOLE DOCTORALE PHYSIQUE ET CHIMIE-PHYSIQUE

Institut de physique et de chimie des Matériaux de Strasbourg

THÈSE présentée par :

Sharmin SHARNA

Soutenue le : 26th Novembre 2021

Pour obtenir le grade de : **Docteur de l'université de Strasbourg**

Discipline/ Spécialité : Chimie Physique

Etude des mécanismes de migration du cuivre utilisé comme porteur d'oxygène dans le procédé de combustion en boucle chimique

THÈSE dirigée par :

M. ERSEN Ovidiu	Professeur, Université de Strasbourg

RAPPORTEURS :

M. RICOLLEAU Christian	Professeur, Université de Paris
M. ABAD Alberto	Chargé de recherche, Instituto de Carboquimica (Espagne)

AUTRES MEMBRES DU JURY :

Mme BRIOIS Valérie	Directrice de Recherche, Synchrotron Soleil
Mme SAVINOVA Elena	Professeur, Université de Strasbourg
M. YAZDANPANAH Mahdi	Ingénieur de recherche, TOTAL Energies
Mme GAY Anne-Sophie	Ingénieur de recherche, IFP Energies Nouvelles
M. CHICHE David	Ingénieur de recherche, IFP Energies Nouvelles

INVITEE :

M. LAMBERT Arnold	Ingénieur de recherche, IFP Energies Nouvelles
M. ROUCHON Virgile	Ingénieur de recherche, IFP Energies Nouvelles
Mme BOUILLET Corinne	Ingénieur de recherche, CNRS, Université de Strasbourg

Acknowledgements

This thesis was carried out in collaboration between IFP Energies Nouvelles and IPCMS Strasbourg. I am thankful to people of both organisations for welcoming and supporting me during these three years of work.

I am very grateful to my supervising teams: David Chiche, Anne-Sophie Gay, Ovidiu Ersen, Arnold Lambert, Virgile Rouchon and Corinne Bouillet for their guidance and constructive advices. Especially, during the writing process, I am truly thankful for their tremendous support and patience.

I would like to acknowledge the support of Anne-Lise Taleb and all the members of microscopy team for their help with the trainings. Chritèle Legens, for accompanying and guiding me through XAS experiments and data treatment.

I would like to thank Stefan Stanescu from HERMES beamline for his help with the STXM experiments. I am also thankful to Valerié Briois for her support and valuable advices during the XAS run.

Finally, I would like to thank the jury members for the evaluation of my manuscript.

TABLE OF CONTENTS

INTRODUCTION 1

CHAPTER 1 : LITERATURE REVIEW

1 Introduction 5

2 CO_2 Capture: Chemical Looping Combustion 5

2.1 Climate emergency 5

2.2 Carbon dioxide capture, storage, and sequestration 6

2.2.1 Transportation of CO_2 8

2.2.2 CO_2 Storage and Utilisation 8

2.3 Chemical Looping Combustion (CLC) – Principle 9

2.4 Scaling-up of CLC 10

2.5 Conclusion 11

3 Oxygen Carriers 11

3.1 Properties of oxygen carriers 12

3.2 Copper based oxygen carriers 14

3.2.1 CuO/SiO_2 and CuO/TiO_2 materials 15

3.2.2 CuO/Al_2O_3 materials 16

3.3 Conclusion 20

4 Behaviour of metallic nanoparticles at nanoscale 21

4.1 Oxidation of metal copper 21

4.2 Reduction of copper oxide 24

4.3 Mobility and growth of copper-based nanoparticles 25

4.4 Conclusions 28

5 Conclusions and Strategies 29

6 References 32

CHAPTER 2 : EXPERIMENTAL PART

1 Material preparation 42

1.1 Preparation of the oxygen carriers 42

1.2 Synthesis of the reference samples 43

2 Material ageing 44

3 Material characterisations 46

3.1 Hg porosimetry 47

3.2 Nitrogen physisorption 48

3.3 Powder X-ray diffraction 48

3.4 In situ XRD 49

3.5 Scanning Electron Microscopy 49

3.6 X-ray Absorption Spectroscopy (XAS) 50

3.6.1 Scanning Transmission X-ray Microscopy (STXM) 50

3.6.2 Quick X-ray Absorption Spectroscopy (XAS) 51

3.7 Transmission Electron Microscopy (TEM) 51

3.7.1 Principle of TEM 51

3.7.2 Conventional TEM and STEM setup 53

3.7.3 Imaging Modes 53

3.7.4 *Ex situ* and post-mortem STEM protocol 55

3.7.5 *In situ* STEM protocol 55

4 References 59

CHAPTER 3 : GRAIN-SCALE MIGRATION OF COPPER

1 Introduction 61

2 Experimental approach 62

2.1 Scanning Transmission X-ray Microscopy: principle and experimental set-up 62

2.1.1 Principle 62

2.1.2 Beamline presentation 64

2.1.3 Data acquisition and analysis 64

2.1.4 Sample preparation 67

2.1.5 Reference samples 68

3 Results and discussions 72

3.1 Fresh 13 wt% CuO/Al_2O_3 72

3.1.1 Identification of the phases 72

3.1.2 Morphology and the spatial distribution of the components 77

3.1.3 Morphology of the fresh samples at nanoscale 83

3.1.4 Conclusion 85

3.2 Effect of cycling temperatures 86

3.2.1 Redox cycles at 700 °C 86

3.2.2 Redox cycles at 800 °C 89

3.2.3 Redox cycles at 900 °C 94

3.2.4 Effect of cycling temperature on the fresh material calcined at 900°C 103

3.3 Discussion 105

4 Conclusions 111

5 References 112

CHAPTER 4 : PHASE EVOLUTION OF OXYGEN CARRIER DURING REDOX CYCLING

1 Introduction 115

2 Morphological evolution during TGA cyclings 116

3 XAS experimental and data analysis protocol 119

3.1 Experimental setup 119

3.2 Experimental Program 121

3.3 Data treatment 123

3.4 Reference samples 126

3.4.1 $CuAl_2O_4$ 128

3.4.2 $CuAlO_2$ 128

3.4.3 CuO 129

3.4.4 Cu_2O 129

3.4.5 Metallic copper, Cu^0 129

3.4.6 Conclusion 130

4.3.1 Oxidation reaction 151

4.3.2 Reduction reaction 153

4.3.3 Post-mortem SEM characterisation 154

4.4 Comparison with *ex situ* cycling 155

4.5 Discussion 156

5 Challenges and perspectives 159

6 Conclusion 160

7 References 161

CHAPTER 5 : REDOX BEHAVIOUR AND MOBILITY OF COPPER NANOPARTICLES

1. Introduction 164

1 Experimental and data treatment protocol 165

2 Beam effect consideration 166

3 Results and Discussion 167

3.1 Model System – Copper Nanoparticles on SiNx substrate 167

3.2 *In*-situ STEM study on the morphological evolution of copper-based nanoparticles during high-temperature redox reactions 168

3.2.1 Abstract 168

3.2.2 Introduction 169

3.2.3 Experimental 172

3.2.4 Results and Discussion 174

3.2.5 Conclusions 187

3.3 Model System – Cu/Al_2O_3 substrate 189

3.3.1 Experimental 189

3.3.2 Mobility under H_2 190

3.3.3 Reaction under O_2 194

4 Conclusion 199

5 References 200

CHAPTER 6 : NANOSCALE INTERACTION IN CU-AL_2O_3 SYSTEMS UNDER REDOX CONDITIONS

1 Introduction 209

2 Experimental section 211

2.1 Samples description and experimental steps 211

2.1.1 13wt% CuO /Al_2O_3 – 900 °C sample 211

2.1.2 28wt% CuO supported on alumina 211

2.1.3 Cu-Al nanospheres 213

3 Results and Discussion 218

3.1 Reactions at low temperature (< 500 °C) 218

3.1.1 CuO/Al_2O_3 – calcined at 900 °C 218

3.1.2 Cu-Al NP – 900 °C redox reaction 223

3.1.3 Conclusion 225

3.2 Reactions at high temperature (> 500 °C) 226

3.2.1 Heating under O_2 atmosphere 226

3.2.2 Heating under H_2 atmosphere 228

3.2.3 Conclusion 230

3.3 Calcination of Cu-Al-NP under O_2 230

3.3.1 Cu-Al NP – 800 °C sample 230

3.3.2 Cu-Al NP – 900 °C sample 233

3.3.3 Calcination in static O_2 235

3.3.4 “Quasi” *in situ* experiment 236

3.3.5 Conclusion 238

3.4 Alumina phase transition 239

3.4.1 Cu-Al 800 °C sample 239

3.4.2 Cu-Al 900 °C sample 240

3.5 Discussion 242

4 Conclusion 243

5 References 245

CONCLUSIONS 247

PERSPECTIVES 250

APPENDIXES

A. Standard Characterisation of 13wt%/CuO/Al_2O_3 253

B. Working principle of the Analysis techniques used 254

B.1 Appendix 1: X-ray absorption spectroscopy (XAS) 254

B.1.1 X-ray absorption Near Edge Spectroscopy (XANES) 256

B.1.2 Extended X-ray Absorption Fine Structure (EXAFS) 256

B.2 Operation of TEM 259

B.3 Aberration correctors 260

B.4 In situ electron microscopy 261

C. XRD 263

C.1 Diffractogram of $CuAl_2O_4$ 263

C.2 Diffractogram of 28wt% CuO/Al_2O_3 264

D. SEM 265

D.1 Post-mortem sem image of the samples after cycled in TGA 265

D.2 Post-Mortem SEM images of the 13wt%CuO/Al_2O_3 after the *in situ* XAS experiment 266

E. STEM image 268

F. *in situ* XAS 269

F.1 Evolution of the metallic copper species 269

F.2 Overall concentration profile during the *in situ* cycling 271

G. Supplementary information 274
G.1 Nanoparticle synthesis 274
G.1.1 Sputtered nanoparticles: 274
G.2 Chemically synthesized nanoparticles: 276
G.3 In-situ STEM analysis 277
G.3.1 Oxidation of metallic Copper 277
G.3.2 Kirkendall Void Formation 278
G.3.3 Nanoparticle Size Distribution: 280
G.3.4 Reduction of Copper Oxide Nanoparticles 281
G.3.5 Evaporation of the copper phase 285
Résumé long en français 299

INTRODUCTION

The rise in the global economy and the associated energy consumption entails the increase of greenhouse gases (GHG) in the atmosphere, which has a lasting impact on the overall change in Earth's climate [1]. Recent years have seen extreme weather conditions such as drought in some areas and flooding in others; and an overall rise in the temperature of the Earth. Leaders from around the world signed the Paris Agreement in 2015 to limit the increase in temperature to 2°C and ideally to 1.5°C above the pre-industrial era (1880's). This encourages many countries to limit their GHG emissions by transitioning and adapting to new technologies. This includes increasing the efficiency of the current energy production system, switching to less carbon-intensive fuel sources, transitioning to renewable energy and/or emphasising on carbon dioxide capture and sequestration strategies. However, only one technology is not enough to limit damages caused, a combination of the above technologies will be required [2].

According to an International Energy Agency (IEA) report, ~80 % of the global energy consumption is predicted to be coming from hydrocarbon sources until 2040 [3]. This leads to a strong emphasis on carbon capture and storage (CCS) technologies. The current CCS technologies are based on pre-or post-combustion separation of gases. The most popular and industrially used systems are amines-based scrubbers to absorb and desorb CO_2 coming out of the flue gas. However, amines based processes are very energy-intensive and require further developments in terms of the solvent material [4]. In this regard, a very promising technology is Chemical Looping Combustion (CLC) which would satisfy the demand for power production with inherent carbon dioxide capture facility [5,6]. CLC utilises an oxygen carrier material for indirect combustion of fuel which avoids dilution of the combustion product by N_2 coming from air as comburant in classical power plants, and eventually allows easy separation of the CO_2.

Synthesised supported metal oxides and natural ones have been used as oxygen carriers to carry out successive oxidation-reduction reactions at high temperature (above 800 °C) [7–9]. One material of interest is CuO supported on Al_2O_3. Owing to high temperature redox cycles in fluidised bed reactors, these oxygen carriers are subjected to severe chemical,

thermal and mechanical stresses, resulting in changes in their chemical and physical properties eventually degrading their reactivity. Moreover, the migration of the copper containing phases during the redox cycles results in phase segregation, cavity and macropore formation, and the sintering of the active phase [10]. However, comprehension of the ageing of the material, especially concerning the migration mechanisms of the supported active phases within the support grain remains a puzzle. Utilisation of advanced characterisation tools has been highlighted to analyse the effect of ageing on the evolution of oxygen carrier phases and texture. Understanding the physical properties influencing this behaviour of the copper phases is essential to designing better oxygen carriers with longer lifetime.

The goal of this PhD thesis is to understand the mechanisms by which the metal/metal oxide phase migrates within the support during alternative oxidation and reduction cycles. The behaviour of the copper phase is influenced by the active phase – support interaction, and the associated phase transitions. The strategy employed here is to study an oxygen carrier which is representative of an industrial material, based on 13wt% of CuO supported on commercial γ-Al_2O_3 support composed of 100-300 µm sized grains and to compare its structural evolution to the behaviour of some model systems, characterised by well-known structural characteristics. In this regard, comparative studies have been performed on model systems made of copper nanoparticles supported on flat SiN_x, amorphous Al_2O_3 film, as well as synthesised Al_2O_3 nanospheres (250-350 nm). The prepared oxygen carrier has been aged in CLC reaction conditions by varying the temperature and the number of cycles. A multi-scale characterisation approach has been used to analyse the materials at the macroscopic scale of the support grain and at the nanometeric scale.

Thermo-Gravimetric Analysis device was used for the ageing the materials at different temperatures and with various cycles numbers. XRD and SEM analysis were first performed to have an overview of the evolution of texture, morphology and phases content according to the ageing of the material. Then, more advanced techniques were employed to have a deeper understanding of the various phenomena taking place. Spectro-microscopic characterisation tool employing Scanning Transmission X-ray Microscope (STXM) coupled with X-ray Absorption Near Edge Spectroscopy (XANES) has been used to locate the

different copper and alumina phases within the support grain and to identify the possible phase transition mechanism encountered during the cycling. *Operando* quick XAS has been also employed to monitor the phase transitions of the Cu-species as a function of the gases, and the overall phase distribution over the course of 50 redox cycles, at 900 °C. Furthermore, aberration corrected Scanning Transmission Electron Microscope (STEM) in *operando* condition has been used to observe the dynamic evolution of the oxygen carrier during the redox reaction. Notably, the main focus of this work is to develop a strategy to perform high temperature reactions (up to 900 °C) on various copper-based systems using the *in situ* gas setup in STEM.

The first chapter presents an overview of the relevance of the present study in the context of climate change, development of the carbon capture technologies, and the need for a better material understanding for the development of oxygen carriers. Latest development and the current understanding of the copper-based oxygen carriers will also be detailed. In addition to that, the oxidation, reduction, and the migration mechanisms of nanoparticles will be presented, with special focus on the STEM studies.

In Chapter 2, description and the choice of the material used, the experimental devices used to carry out the oxidation-reduction cycles and the working principle of the different characterisation tools are presented.

Chapter 3 is dedicated to the characterisation of the 13wt% CuO/Al_2O_3 oxygen carriers, calcined, and cycled at different temperatures. The spatial distribution of the various chemical and polymorphic phases containing copper and alumina are identified using a combination of the mentioned techniques (principally STXM). From the transformation of the material, a global migration mechanism will be proposed as a function of the number of cycles and the reaction temperatures.

In Chapter 4, the progression of the redox cycling of the same oxygen carrier material is followed by probing the copper species using XAS. Complementary morphological information from scanning electron microscopy (SEM) observations allowed to correlate the evolution of the copper containing species to the alumina phase transition.

In Chapter 5 *in situ* STEM is employed to monitor the dynamic changes in the two model systems (copper nanoparticles supported upon flat SiN_x and Al_2O_3). The results based on the SiN_x support will be presented in the form of published article "*In situ* STEM study on the morphological evolution of copper-based nanoparticles during high-temperature redox reactions" [11]. This study focuses on the oxidation-reduction behaviour of the nanoparticles. The second part of this chapter deals with the mobility of the nanoparticles on the Al_2O_3 support. Mobility of copper containing phases in relation to metal-support and gas interactions will be studied.

Chapter 6 presents the real-time evolution of supported alumina nanospheres and of CuO/Al_2O_3 samples during redox reactions at variable temperatures, using *in situ* STEM. The morphological changes and the mobility of the copper containing phases will be investigated. Additionally, diffraction studies, will provide information on the alumina phase transition. This chapter also highlights the challenges associated to the gas phase reaction at high temperature.

Finally, the main conclusions and perspectives of the current work will be presented.

Chapter 1:
Literature review

1 INTRODUCTION

The literature review is divided into three sections. The first part provides an outlook of challenges faced by CO_2 capture and the development of Chemical Looping Combustion as a solution. The second part describes the materials used as oxygen carriers in the CLC process with emphasis given on Cu based oxygen carrier materials (OC), the limitation and gap at the nanoscale understanding of material is identified. Material behaviours at the nanoscale concerning oxidation, reduction and migration of transition metal nanoparticles (NPs) are identified with emphasis of studies that can help understand copper oxide supported systems.

Finally, a conclusion and the proposed strategy of the present work is provided.

2 CO_2 CAPTURE: CHEMICAL LOOPING COMBUSTION

2.1 CLIMATE EMERGENCY

The inevitable crisis induced by the changing climate we are facing in the 21st century is the result of the rise in industrialisation, increase in global consumption requiring the utilisation of a vast amount of fossil fuel thereby releasing a copious amount of greenhouse gases (GHG) in the atmosphere. Recent trends in extreme weather conditions and overall increase in Earth's temperature have been attributed to human activities, since the beginning of industrial revolution and the rise of greenhouse gases emission as a result [1,2,12–14]. The heat trapping properties of carbon dioxide and its contribution to the increase in surface temperature through greenhouse gas effect has been known since the mid-19th century [15]. Naturally occurring CO_2 and other greenhouse gases are essential to keep agreeable temperature on Earth by preventing the long wave radiation from leaving the atmosphere.

However, the problem arises when the amount of emitted CO_2 is far greater than the Earth's system can buffer to maintain the stability. The steady rise of temperature (1.1 °C since late 19th century) is positively correlated to the rise in CO_2 atmospheric concentration (411 ppm, a 37 % increase compared to the pre-industrial era of 280 ppm) [16]. The Earth's system is heading towards a disastrous outcome since it results in ice melting, rise of the sea level (3.3 mm/year), increased ocean acidification and extreme weather events like drought, wildfire and frequent cyclones [17].

The principal GHG affecting the climate change are H_2O, CH_4, CO_2, N_2O, CFCs and SF_6 resulting from human activities, each of these gaseous compounds exhibiting different global warming potential (GWP) [18]. Considering its GWP, high residence time, and volume of emission, CO_2 has the largest contribution to the greenhouse effect [19]. The increase in carbon dioxide concentration is attributed to the utilisation of fossil fuels for energy production which is likely to increase even further due to economic growth.

In order to meet the Paris Agreement aimed at limiting the global temperature rise to 1.5 °C, the increase in CO_2 concentration should be limited to 450 ppm. This goal is possible to achieve via the following proposed routes [20]:

- Increasing the efficiency of energy conversion and utilisation,
- Switching to less carbon intensive fuels,
- Transition to renewable energy sources (solar and wind),
- Development of carbon dioxide capture technologies.

A combination of these technologies is required to address the reduction of GHG and continued utilisation of fossil fuel, since the latter will still satisfy 80 % of the energy demand of the 21st century [3]. Until the proper maturation of the renewable energy sector, implementation of carbon dioxide capture solutions is inevitable to meet the above criteria according to the Intergovernmental Panel on Climate Change (IPCC) and the International Energy Agency (IEA) [3,20].

2.2 CARBON DIOXIDE CAPTURE, STORAGE, AND SEQUESTRATION

Carbon dioxide capture, use or storage involves separation of CO_2 from single point sources such as fossil fuel-based power plants and transporting it to a storage or utilisation location.

In the case of storage, further processing is required such as long term isolation from the atmosphere by means of geological, biological, or mineral storage. The IPCC special report outlines the different options for carbon dioxide capture [20]. As outlined in *Figure 1.1*, CO_2 emitted from large emission sources such as power plants and refineries can be separated via post-combustion, oxy-fuel, or pre-combustion separation techniques.

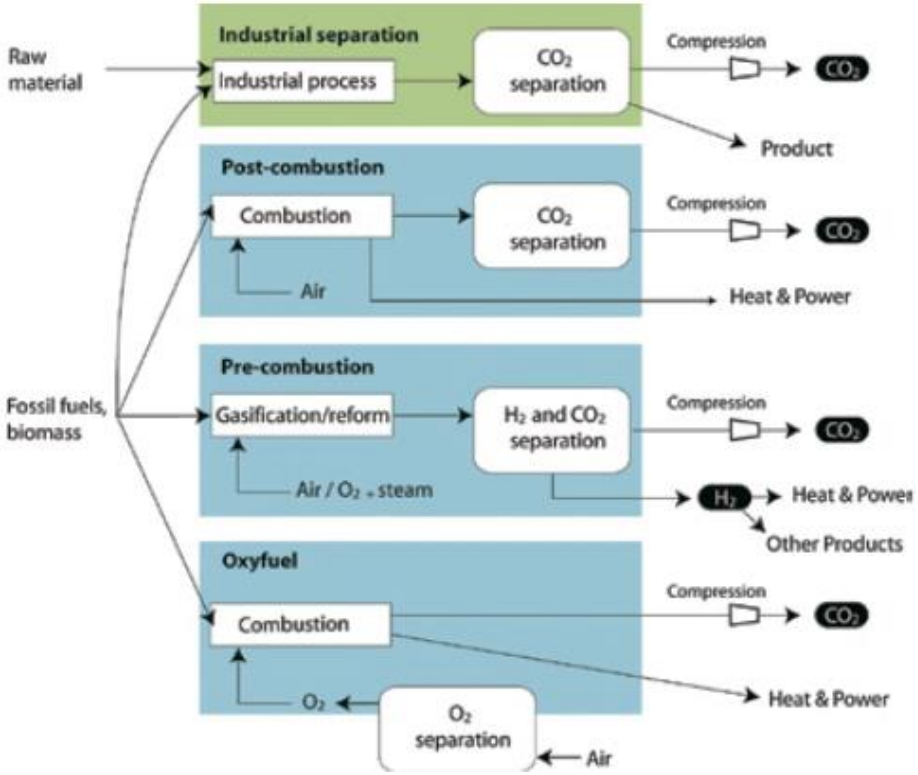

Figure 1.1: Schematic representation of carbon capture systems. Fuels and products are indicated for oxyfuel combustion, pre-combustion (including hydrogen and fertiliser production), post-combustion and industrial sources of CO_2 (including natural gas processing facilities and steel and cement production) [20].

In post combustion technologies, CO_2 is separated from the flue gas after the combustion of the primary fuel. Industrially, this is a mature and established technology since existing power plants can be retrofitted to include such separation units. Separation of CO_2 can be achieved via amines scrubbing processes, adsorption/desorption on solids, or membrane gas separation technologies. Carbon dioxide scrubbing with amines is the dominant technology as it is already used industrially for natural gas processing [4].

In pre-combustion capture, gasification of the feed (*e.g.* coal) at high temperature and pressure results in the production of a synthesis gas composed mainly of H_2, CO and CO_2. This synthesis gas can undergo water gas shift reaction to produce a carbon dioxide and

hydrogen rich gas mixture. CO_2 is then separated, transported, and sequestered, while H_2 can undergo combustion for energy production or can be used in other processes.

In oxy-fuel combustion, oxygen is used instead of air for combustion, which produces a flue gas containing streams of CO_2 and H_2O which can be easily separated via condensation. The sustainability of this technology depends on the supply of pure oxygen. This process uses oxygen produced via separation by cryogenic distillation of air, which is energy-intensive, hence the process is economic up to a certain volume of oxygen. Another example of oxy-fuel combustion relies on Chemical Looping Combustion (CLC) which utilizes an oxide-based material to carry out indirect combustion [21].

Based on several economic and environmental studies, CLC incurs less environmental impact, and the estimated cost of capture of CO_2 is lower when compared to pre-combustion technologies such as Integrated Gasification Combined Cycles (IGCC) power plants and other oxy-fuel processes. However, compared to a power plant without any carbon capture solution, CLC contributes in a 71 % increase in capital investment and 24 % increase in the cost of energy [6].

2.2.1 Transportation of CO_2

Concentrated streams of CO_2 can be transported through pipelines at high pressure. Such infrastructures already exist in the USA and in Norway, where they are used for enhanced oil recovery. In some cases, for longer distance or overseas, CO_2 can be transported by ship after liquefaction of the gas [22].

2.2.2 CO_2 Storage and Utilisation

A range of options has been considered for the storage and utilisation of CO_2 such as injecting CO_2 in geological formations, reacting with metal oxides to produce carbonates and CO_2 degradation by bacteria/algae [3]. Geological storage can be performed by injecting supercritical CO_2 in oil fields, gas fields or deep saline aquifers for example. However, the risk of leakage is a big environmental and health concern. The long-term storage feasibility of such sites must be well assessed with constant monitoring of potential CO_2 leakage. Regarding the option of mineral storage, CO_2 reacts exothermically with oxides of calcium or magnesium to form carbonates like calcite and magnesite respectively. Carbon dioxide

utilisation processes include injection of CO_2 for enhanced oil recovery, algal synthesis, production of hydrocarbon and methanol.

2.3 CHEMICAL LOOPING COMBUSTION (CLC) – PRINCIPLE

CLC is an oxy-fuel combustion technology with inherent CO_2 capture solution [23]. The principle of CLC is to separate the combustion process in two steps: reduction and oxidation [24]. The two-steps process is visualized in *Figure 1.2*. The process uses a metal-oxide based material termed as the oxygen carrier (OC). The OC is circulated in the "fuel reactor" where it provides oxygen to the fuel for indirect combustion. The OC material is either fully or partially reduced through reaction 1 provided below. The by-products of the indirect combustion, which are CO_2 and H_2O, are easily separated by condensation. A highly concentrated CO_2 stream is hence produced, ready for storage or utilisation in other processes. The reduced OC is then regenerated, *i.e*. re-oxidised, by circulating through the "air reactor". During the regeneration process, the (partially) reduced material reacts with air to re-form metal oxide via reaction 2. The flue gas of the air reactor contains N_2 and unreacted oxygen. Thus, a full cycle of the reaction involves a redox reaction. The CLC process is based on materials' multiple cycling between the fuel and air reactors whereby the material undergoes changes in overall oxidation states via reduction to provide oxygen and oxidation to regenerate its oxide form. During its life-time the material undergoes numerous successive redox cycles at very high temperature, typically above 800 °C [6].

Reduction: $(2n + m)\ Me_xO_y + C_nH_{2m} \rightarrow (2n + m)\ Me_xO_{y-1} + m\ H_2O + n\ CO_2$ Reaction 1.1

Oxidation: $Me_xO_{y-1} + ½\ O_2 \rightarrow Me_xO_y$ Reaction 1.2

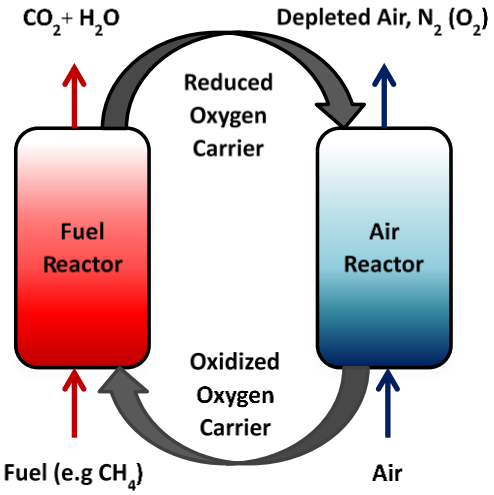

Figure 1.2: Schematic representation of chemical looping combustion (CLC) process.

The advantage of the process lies in the separation of the oxidation and reduction steps, thus separating the CO_2 from N_2 and residual O_2 which otherwise would require a post-combustion solution for separation. Therefore, CLC serves as a combustion process producing energy with the benefit of carbon dioxide separation, incurring low energy penalty.

2.4 SCALING-UP OF CLC

Various fluidised bed reactors configurations have been demonstrated at pilot scale [16,17]. For example, at IFP Energies Nouvelles, a 10 kW_{th} CLC pilot based on interconnected bubbling fluidised bed reactors has been operated for several hundred hours both with gas and solid fuels. The bubbling fluidised bed gives the advantage of optimum fuel and OC conversion by providing the required contact time between the solid and gas/air. The IFPEN pilot unit is composed of 3 reactors; one for combustion of fuel (referred as fuel reactor FR) and two others for the oxidation of oxygen carrier (air reactors AR1 and AR2) according to the 3D schematic representation reported in *Figure 1.3* [18]. In addition to that, a carbon

stripper has been added to the unit for combustion of solid fuels, to ensure separation of unburnt carbon compounds before going to the oxidation reactors.

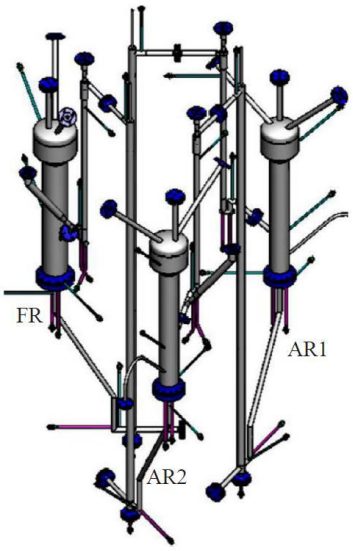

Figure 1.3: Schematic representation of the pilot plant at IFPEN.

2.5 CONCLUSION

The rise of CO_2 level in the atmosphere and the corresponding effect on the global climate demand for immediate actions in terms of reducing the emission of CO_2. A single solution is not enough to address this issue, therefore a range of solutions is proposed, including transition to lower carbon fuel, renewable energies, improving the efficiency of existing power plants and CO_2 capture solutions. The implementation of CO_2 capture technologies is indeed imperative due to the rising demand for fossil fuel because of global population and economic growth. While post-combustion carbon capture technologies through amines based processes are the most dominant technologies due to their advantage of possible retrofitting in existing power plants, new power plants could benefit from the development of the latest technologies such as Chemical Looping Combustion (CLC).

3 OXYGEN CARRIERS

Oxygen carriers are at the heart of the CLC process. Both synthesized materials and natural ores have been considered for use in the CLC process. Natural ores such as ilmenite ($FeTiO_3$), hematite (Fe_2O_3), malachite ($Cu_2CO_3(OH)_2$) are among the materials tested as oxygen

carrying materials for CLC [6]. Among synthetic materials, oxides of transition metals such as Ni, Cu, Co, Fe and Mn have been used. Typically, the synthesized oxygen carriers are composed of a metal oxide supported on a porous ceramic material which provides a high surface area, increased mechanical strength and resistance to attrition [24].

3.1 PROPERTIES OF OXYGEN CARRIERS

Oxygen carriers must fulfill the following key performance-based properties:

- High oxygen transport capacity
- Favorable thermodynamics concerning the conversion of fuel to CO_2 and H_2O
- High reduction and oxidation reactivity
- Attrition resistance
- Negligible carbon deposition that would lead to loss of carbon dioxide capture efficiency
- Good fluidization properties (no agglomeration)
- Low cost
- Environmentally friendly for end of life disposal

The total cost of the OC is dependent on the initial material price and the overall lifetime of the material in the process [25].

In general, Ni and Co metal oxide based materials exhibit health and safety concerns while Cu, Fe and Mn based OC are more acceptable as non-hazardous waste [26].

The lifetime of OC and their attrition properties concerning both chemical stress and physical crushing strength are an important consideration in order to assess the total cost of the process. The lifetime of OC is the ability of the material to undergo redox cycling without loss of reactivity and fragmentation. Attrition leads to fines formation (particles < 45 µm), which have a short residence time, thus lowering the process efficiency [27]. Typically, nickel based OC show a rather high lifetime while copper based OC experience lower lifetime in the process [27,28].

Carbon deposition on the OC reduces the CO_2 capture efficiency since the carbon deposited on the OC in the fuel reactor undergoes combustion in the air reactor. This effect is linked

to the amount of metal oxide, support material and H_2O/fuel ratio and is most likely to occur towards the end of the reduction period when most of the oxygen is consumed [29].

Agglomeration causes bed defluidization, degrading the gas circulation and contact with the solid inventory. Nickel based OC (NiO/Al_2O_3, NiO/ZrO_2) generally do not agglomerate at CLC operating temperature of 900-950 °C except when TiO_2 is used as support [30]. The problem of agglomeration has also observed when Mn based active phase was supported on ZrO_2 [21]. For copper-based OC, the problem associated with particles agglomeration is well known and attributed to copper's low melting temperature. However, this could be minimised using the right combination of metal oxide content and support material [28,31–33].

Figure 1.4 shows a comparison among available oxygen carriers based on the above requirements. Among them, nickel based OC have been studied and developed extensively due to their high reactivity and resistance to agglomeration and attrition. Copper and iron-based OC have received attention owing to their relative abundance and lower cost. However, both of the materials are comparatively less resistant to agglomeration than Ni-based materials.

Nevertheless, L.S. Fan's group from Ohio University studied Fe based oxygen carriers, and highlighted the ionic/atomic migration of Fe within the particles [34]. Homogeneously dispersed Fe_2O_3/Al_2O_3 particles end up forming an Al_2O_3 core surrounded by an Fe_2O_3 shell after 50 redox cycles at 900 °C. The change in morphology resulting in surface enrichment with iron oxide occurred due to outward diffusion of iron cations during the oxidation step. On the other hand, such a surface enrichment was not observed with a Fe_2O_3/TiO_2 sample, as the presence of titania increased the ionic diffusivity of the O^{2-} leading to oxidation through inward diffusion of the anions [35,36].

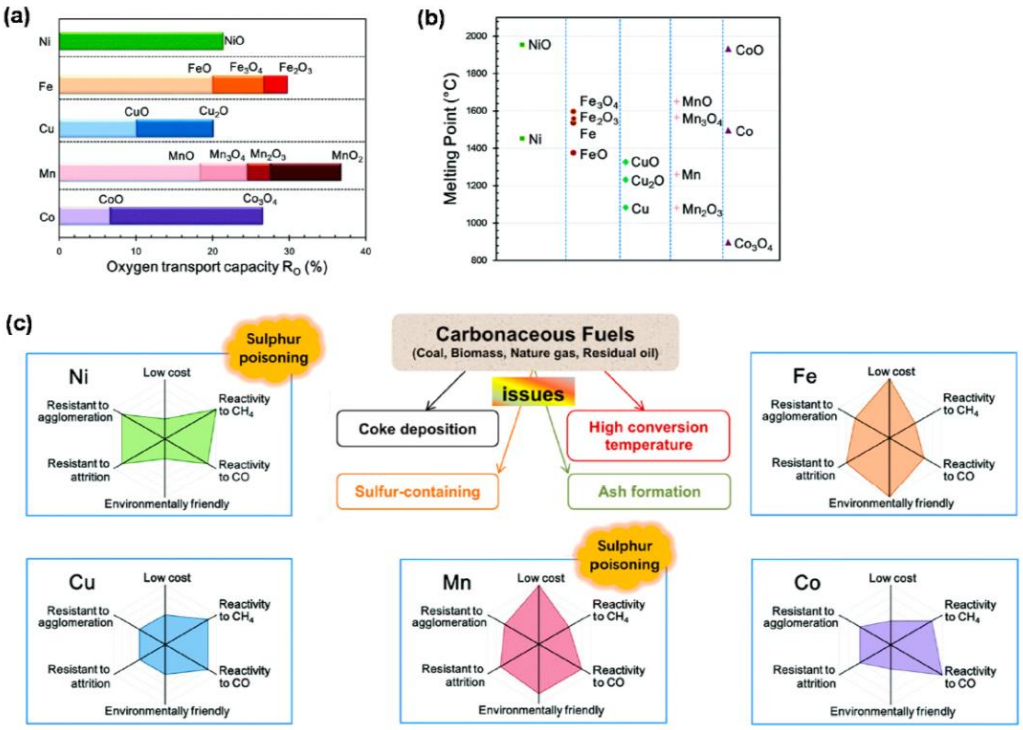

Figure 1.4: Comparison of different properties among the synthesized oxygen carriers taken from [37].

3.2 COPPER BASED OXYGEN CARRIERS

In the current study we are interested in supported copper-based oxygen carriers due to multiple advantages including high reaction rate [38], high oxygen transfer capacity (0.2 g O_2/g CuO), thus requiring lower amount of active phase/material flow [25], and no thermodynamic restrictions towards the complete conversion of methane to CO_2 and H_2O [39]. Thus, a growing interest on substituting Ni for relatively cheaper and environmentally friendlier Cu based materials led to the study of supported copper oxide OC.

However, disadvantages of the Cu-based OC reported in the early studies include sintering of the copper-phase due to the low melting point of metallic copper and related oxides, imposing a limitation to the operating temperature to 800 or 850 °C, thereby lowering the efficiency of the CLC process. Defluidisation due to agglomeration is another disadvantage of using copper-based OC. In some other studies, partial loss of the copper phase has been reported, thereby affecting the overall conversion. Due to disadvantages posed by copper-based oxygen carriers, the material was almost rejected as a potential OC for large scale operations.

Extensive tests were carried out by the ICB-CSIC group on copper-based oxygen carriers [25,32,40,41]. The authors could demonstrate the applicability of copper-based oxygen carriers based on their screening tests with variable copper concentration, a wide range of supports and preparation methods.

A variety of support materials such as Al_2O_3, SiO_2, bentonite, barium hexaaluminate, aluminate spinel, TiO_2 and ZrO_2 are reported in the literature. In addition, different preparation techniques have been employed to achieve OC with superior stability and longer lifetime. A summary of feasibility of different preparation techniques based on chemical/physical stability of Cu based OC shows that dry impregnation results in very high performance OC while wet impregnation gives satisfactory properties [34,40].

3.2.1 CuO/SiO_2 and CuO/TiO_2 materials

OC with 40 wt% copper supported on silica displayed good chemical stability, high reactivity as well as structural integrity when prepared via impregnation, compared to OC prepared by either mechanical mixing or co-precipitation, which showed cracks and holes formation after about 100 cycles [40]. Similarly, Zafar et al. reported high reactivity for CuO/SiO_2 OC at 850 °C but only 4 redox cycles were performed, and no information on the morphology of the used materials is provided [42]. Liu et al. studied 9 wt% CuO impregnated on silica compared to 14 wt% CuO on alumina, over 11 cycles at 850 °C [43]. SEM observation of used particles showed that the copper phase had sintered on silica, but not on alumina. The authors concluded that the presence of $CuAl_2O_4$ has an anchoring effect on copper. Previosuly, Van Garderen et al. have concluded that the presence of a combination of mesopores and macropores affects the performance of the Cu-silica OC [44].

According to an earlier study by Corbella et al., $CuO\text{-}TiO_2$ oxygen carriers with different CuO concentrations are suitable OC displaying high reactivity and no significant degradation up to 20 cycles at 900 °C [45]. The copper phases did not react with the support to form any mixed oxide and no carbonaceous deposits were found. However, after 20 cycles the materials displayed a decrease in surface area and an increased pore size due to possible sintering of the support and partial reduction of the support. A study of de Diego et al. also confirms the high reactivity of the CuO-titania OC where the material undergoes little to no change over 100 redox cycles [40].

Nevertheless, no conclusion can be drawn from either of these studies as long term effect of cycling on the silica or titania material is not mentioned in the literature.

3.2.2 CuO/Al_2O_3 materials

The study of copper based OC is mainly focused on the utilisation of the alumina support. The CuO/Al_2O_3 carriers are composed of either CuO homogeneously dispersed on alumina or a mixture of $CuAl_2O_4$ and alumina, depending on the temperature of calcination [10,28]. The aged oxygen carriers can undergo different phase transitions during their lifetime and may contain different transition aluminas (gamma, delta and theta), alpha alumina, Cu_2O, CuO, Cu, $CuAl_2O_4$ and $CuAlO_2$ as a function of the number of cycles and reaction conditions.

Following paragraphs present some different observations and issues related to Cu/Al_2O_3 oxygen carrier.

3.2.2.1 Optimum Cu concentration and agglomeration

The copper content very much affects the extent of agglomeration during the cycling of the oxygen carriers. For example, Cho et al. conducted redox cycling at 850 °C on 60 wt% CuO supported on $CuAl_2O_4$ produced via freeze granulation. The material showed high reactivity, but after 6 redox cycles, a loss of reactivity was observed due to the agglomeration of the oxygen carrier particles [46]. In contrast, Mattisson et al. successfully conducted TGA cycles of CuO (33 wt%) supported on alumina synthesized via dry impregnation without any loss of reactivity up to a temperature of 950 °C and over 6 cycles [47]. The difference in reactivity between the two samples is believed to be due to the preparation method as well as the proportion of CuO present in the oxygen carrier.

Indeed, the agglomeration of CuO increases with increasing copper content, as demonstrated by de Diego et al. [32]. Based on oxygen carriers with different CuO contents (10-26 wt%) supported on alumina, the authors concluded that OC with more than 20 wt% of CuO displayed agglomeration while OC with less than 20 wt% CuO could be used without any agglomeration problem [32].

Subsequently, 15 wt% CuO impregnated on gamma alumina was selected to carry out further testing in a 10 kW_{th} pilot plant [28,33]. Several process parameters such as oxygen carrier to fuel ratio, fuel gas velocity, OC particle size and fuel to reactor temperature have

been tested to understand the effect on fuel conversion. Generally, the OC displayed high reactivity with no carbon formation nor agglomeration [10,28,33].

3.2.2.2 Attrition

A high initial rate of attrition has been observed regardless of temperature in most of the reported studies, which may be linked to the presence of surface copper oxide in the fresh oxygen carrier [10,28,33,38]. Often, the recovered fine particles contain high copper concentration indicating a loss of copper which may eventually affect the reactivity of the material. Pishahang et al. suggested that the attrition and the consequent loss of copper can be reduced or avoided if all the active phase is fully impregnated within the support during the preparation step [48]. Izquierdo et al. also reported the generation of fines to be higher at 900 °C, compared to 800 °C. The authors suggest to carry out the reaction at 800 °C to minimise the copper loss [49].

In addition to attrition, fragmentation of the material is observed, mostly at the end of a long operation. Lambert et al. reported interruption in the cycling after 160 hours of operation at 900 °C due to loss of solid [10]. The loss of solid is attributed to the fragmentation of the aged particles that displayed lower mechanical resistance owing to macroporosity and cracks in the support grains. Similar observations have been reported by Forero et al. in a circulating fluidised bed at 900 °C or above, where an excessive generation of fines and cracking of the oxygen carrier interrupted the operation after 30 hours [50].

3.2.2.3 Phase transition and sintering

Owing to high chemical and thermal stress during the successive oxidation-reduction cycles, the oxygen carrier material may undergo phase transformations.

Regarding the structural properties of Cu based oxygen carrier, one important aspect to consider is the effect of interaction between CuO and alumina on the sintering of the copper phase. Notably, CuO and Al_2O_3 phases undergo solid state reaction at high temperature resulting in $CuAl_2O_4$ formation [32,40,47,50]. The presence of $CuAl_2O_4$ is generally observed for fresh OC only when calcined above 800 °C [40]. However when the OC is subjected to multiple redox cycles, $CuAl_2O_4$ forms at a temperature of 750 °C and above [47]. Furthermore, the percentage of $CuAl_2O_4$ increases with increasing temperature up to a certain number of cycles [10,40,47]. In a study by de Diego et al., the fresh OC was

composed of $CuAl_2O_4$, gamma alumina and traces of CuO, but after 10 h of redox cycling at 800 °C, the material mainly contained CuO along with gamma alumina and $CuAl_2O_4$, and after 100 h of cycling, alpha alumina appeared [28].

Another phase transition that occurs for fresh OC calcined at 900 °C or above, is the formation of α-Al_2O_3 phase. The γ to α-Al_2O_3 phase transformation has been observed at temperatures as low as 800 °C when multiple redox cycling is involved as noted by de Diego et al. [40]. In the absence of Cu, the transformation of transition aluminas to α-Al_2O_3 only occurs at higher temperatures (above 1000 °C) [51]. This implies that the presence of copper in OC promotes the alpha alumina formation. Indeed the alpha alumina phase transition can be triggered by several factors [52].

Recently, Izquierdo et al. reported the effect of chemical and thermal stress on the stability of a 14 wt%CuO/Al_2O_3 OC using a high OC to fuel ratio, which avoids the complete reduction of Cu^{II} to Cu^0 [49]. Instead Cu_2O or $CuAlO_2$ were formed in the fuel reactor at 800 °C and 900 °C, respectively. The authors proposed that at 800 °C, the copper remains inside the support due to the preferential migration of the Cu_2O phase towards the interior of the grain or due to the absence of metallic copper which is known to be very mobile, whereas at 900 °C, copper is mostly found in $CuAlO_2$, which helps anchoring Cu, thus preventing the loss of copper phase [49]. This study also reports the phase transition to α-Al_2O_3 at relatively low temperature. Izquierdo et al. suggest that the transformation could be led by the decomposition of $CuAl_2O_4$ to $CuAlO_2$ or Cu_2O and α-Al_2O_3, based on the mechanism proposed by Hu et al. [53]. Nevertheless, it should be noted that alpha alumina formation is reported in most of the CuO-Alumina systems studied for the CLC application, be it at low or at ambient O_2 partial pressure [10,31,40,47,50,54].

3.2.2.4 Sintering mechanism of copper

Lambert et al. tested 14.9 wt% CuO supported on γ-Al_2O_3 over 276 redox cycles at 900 °C at IFPEN's 10 KW_{th} circulating fluidised bed reactor and characterised the oxygen carrier with increasing number of cycles to understand the evolution in terms of morphology, textural properties and phase transformations [10]. Based on XRD analysis, the authors proposed a mechanism concerning the various transformations induced during successive oxidation and reduction reactions as depicted in Figure 1.5. The proposed mechanism illustrates that

the reduction of $CuAl_2O_4$ phase leads to the formation of metallic copper which may sinter with the neighboring particles, thus forming bigger copper nodules and minimizing surface energy. During re-oxidation, the Cu^{2+} ions diffuse through the porous support to react with δ-Al_2O_3 to form $CuAl_2O_4$ again. However, due to limitations induced by the large copper nodules, some of the copper cannot react back to $CuAl_2O_4$. As a result, at elast some of the remaining δ-Al_2O_3 phase transforms to α-Al_2O_3. Thus, more and more metallic copper forms after every reduction step. Eventually, after n cycles only α-Al_2O_3 phase and large crystallites of CuO would remain [10].

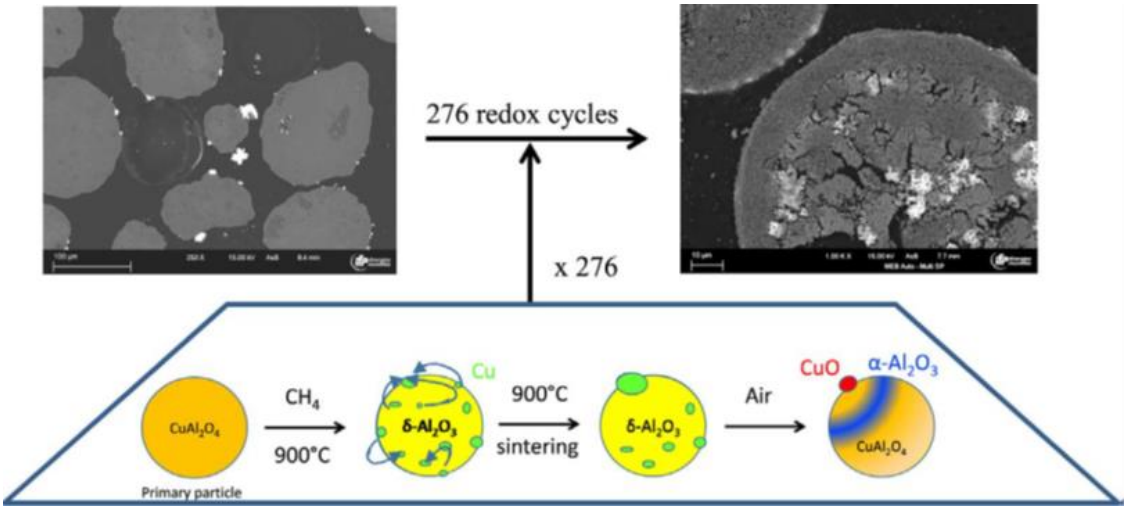

Figure 1.5: Tentative mechanism for the formation of copper nodules during redox cycling [10].

Globally, this mechanism paints a picture of the step-wise transformation occuring in the material. Also, this study paves the way to delve deeper into each step of the transformation. For example, what is the exact mechanism and parameters affecting the migration and sintering of Cu and/or CuO within the support? After reduction, the metallic copper on the support is likely to be found as nanoparticles. At this scale, the migration can occur via surface, grain boundary or bulk diffusion depending on the temperature, and other factors will impact the mobility of Cu species, such as particle size, metal-support interactions, nature of the gas phase and distance between particles.

3.3 CONCLUSION

A great variety of oxygen carriers has been studied and tested to be used in CLC. Among them copper based oxygen carriers have received considerable interest due to their favorable redox behaviour and environmentally friendly nature. Nevertheless, the disadvantage of copper based oxygen carrier is their susceptibility to degradation that results in loss of reactivity *via* various processes including, agglomeration, attrition, sintering and fragmentation.

For CuO/Al_2O_3 materials, the issue with agglomeration can be resolved by adjusting either the copper concentration, synthesis method or calcination temperature. However, the outward migration of copper results in the loss of the copper as fine particles because of attrition during bed circulation. Copper migration and sintering are also associated to the overall phase transitions in the oxygen carrier. It has been suggested that the sintering of metallic copper plays a crucial role in the support's phase transition. Consequently, after many cycles the support is composed of α-Al_2O_3 containing large sintered CuO particles. This has two consequences: sintering of the copper phase may pose kinetic limitations during the redox reaction causing an overall loss in reactivity, and, depending on the extent of macroposity and cracks caused by α-Al_2O_3 phase formation, the material may lose mechanical resistance. A global mechanism of the transformation of the CuO/Al_2O_3 oxygen carrier has been suggested by Lambert et al. that ties the above mentioned issues with the copper phase migration, sintering and phase transition, based on macroscopic, *ex situ* characterisation of aged OC particles.

In order to delve deeper into the mechanisms and physical parameters responsible for the migration of Cu and the alumina phase transitions, characterisation at the nanoscale may be well suited to track the evolution of such systems, especially under reactive conditions. Tranmission Electron Microscpy (TEM) can provide morphological, as well as phase information of the oxygen carriers. Some relevant examples concerning the phenomena observed in the CLC process (oxidation, reduction and particle growth) are outlined in the next section for readers to have an overview on what has been carried out in the literature.

4 BEHAVIOUR OF METALLIC NANOPARTICLES AT NANOSCALE

The synthesised supported oxygen carriers are often composed of nano-sized oxides of metal as the active phase. Thus, comprehending the evolution of the oxygen carriers at the nanoscale is crucial for the development of materials. While the high operating temperature can cause sintering of particles via Ostwald ripening or via particle migration and coalescence, the additional stress caused by redox reactions can lead to severe sintering and agglomeration due to ionic migration and phase transformations. Moreover, several recent reviews have identified the significance of *in situ* and *operando* characterisation tools for the comprehension of local structural changes as a result of oxidation and reduction reactions [9,34,55].

In this section, a literature review on the nanoscale behaviour of materials is presented, namely oxidation of metal, reduction of metal oxide and sintering behaviour of metal. A brief description of the oxidation/reduction properties and the corresponding dynamic changes in copper based systems are discussed. Following that, the nanoparticle mobility and growth mechanisms are presented.

4.1 OXIDATION OF METAL COPPER

Although an enormous amount of work has been dedicated to the comprehension of the oxidation of copper, much of it remains within the realm of thin films [56]. Notable works on nanoparticles (NP) oxidation have been carried out by Nakamura et al. using TEM [57–60], Yabuki and Tanaka [61], Mansoor et al. [62] on the kinetic study of the oxidation of copper nanoparticles using TGA, LaGrow et al. [63] using *in situ* TEM, Rice et al. [64] and Susman et al. [65] using real-time plasmon spectroscopy.

Oxidation mechanism of metallic nanoparticles is size and temperature sensitive. for instance 30 nm sized copper NP oxidise to form Cu@Cu_2O, whereas 5 nm size Cu NP undergo complete oxidation to form compact Cu_2O NP when exposed to air at ambient conditions [66]. In another study, very small (~2 nm) copper NP form hollow Cu_2O NP upon oxidation in air at room temperature [63].

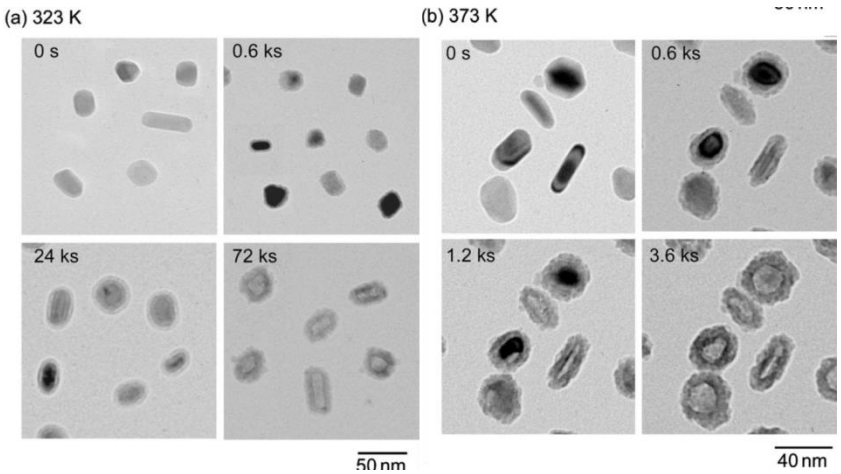

Figure 1.6: Bright-Field images of nanoparticle morphology before and during oxidation of Cu nanoparticles (a) at 323 K and (b) 373 K [60].

In any case, above 50 °C, most studies on copper nanoparticle oxidations have reported void formation via Nanoscale Kirkendall Effect. The nano-Kirkendall effect arises when the outwards diffusion of the cationic species is faster than the inward diffusion of the anionic ions (namely O^{2-} ions in the case of oxidation). As a consequence, the difference in the diffusion rate results in vacancies formation and coalescence leading to void or hollowing of the nanoparticles [67].

The TEM observation on 5-50 nm sized Cu NP at 50-150 °C suggests that the oxidation proceeds via formation of an initial oxide layer surrounding the copper core [60]. Following the Cu@Cu_2O formation, hollowing of the nanoparticles takes place within 20 hours at 50 °C or 1 hour at 100 °C (Figure 1.6). The difference in duration for the completion of NKE reveals the temperature dependence of the mobility of both copper cations and oxygen anions. Likewise, the temperature dependency of the diffusion coefficients as well as the size-dependency of the kinetics of oxidation have been noted by Rice et al. [64]. During the hollowing of the nanoparticles, their volume increases by about 2.5 times the initial volume of the metallic copper [68]. Tokozakura et al. also observed that the early stage of oxidation proceeds very rapidly until a thickness of 2.5 nm of Cu_2O is reached [68]. In the study of Tokozakura, the authors followed the oxide growth kinetics and found that the Cu_2O layer thickness increases slowly before reaching a maximum value. It was concluded that the growth rate in smaller nanoparticles is slower than that of the larger nanoparticles due to

the large fraction of void to copper in the smaller nanoparticles which hinders the outward diffusion of copper cations, which thus becomes the rate-limiting step of the reaction.

Also, the final morphology of the oxide nanoparticles is determined by the temperature of oxidation. Both Nakamura et al. [57] and Rice et al. [64] have demonstrated collapsing of the hollow nanoparticles when they are subjected to higher temperatures of oxidation. After hollow Cu_2O NP formation at 150 °C, an increase in temperature to 300 °C led to complete phase transformation to CuO within 1 hour of oxidation. However, when oxidised at a temperature of 400 °C the inner void starts to get filled from the inner surface of the shell. Further heating at 500°C results in complete compacting of the nanoparticles within a duration of 1 hour [57]. The sequence of transformation is presented in Figure 1.7.

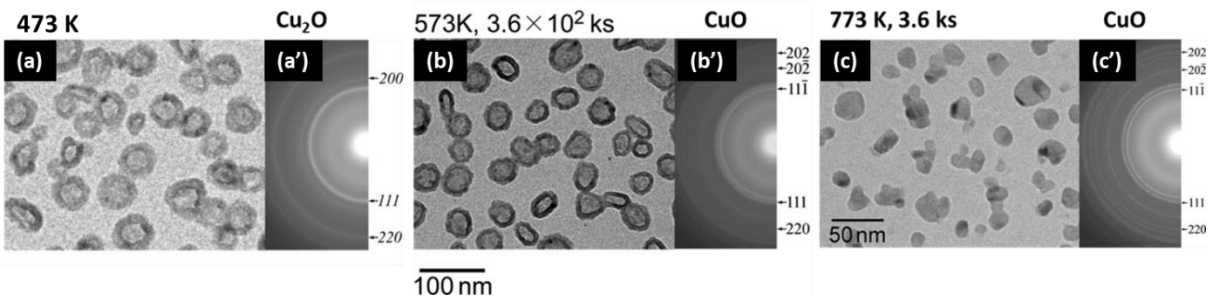

Figure 1.7: Bright-Field images of hollow Cu_2O nanoparticles (a) before and after oxidation at 573 K in air for (d) 360 ks and (c) hollow Cu_2O nanoparticles after oxidation at 773 K for 3.6 ks and their corresponding SAED patterns (a') and (b'). [57].

The dynamic changes during the oxidation using *in situ* STEM is monitored by LaGrow et al.; the authors conducted oxidation of 6-80 nm sized Cu NP in presence of 2 - 10 Pa O_2 at 300 – 500 °C [63]. While the majority of the previous studies reported oxidation via a thin layer oxide growth followed by Kirkendall void formation at a temperature of up to 400 °C, in their observation LaGrow et al. reported unidirectional oxidation growth on Cu to form compact Cu_2O NP independent of the variation in temperature. Once a nucleation site is formed, it seems to create a zone of capture for further oxygen diffusion eventually leading to layer by layer growth of the oxide phase. The difference in the final morphology of the oxide seems to be an O_2 partial pressure dependent phenomenon since hollowing of NP was observed at an O_2 partial pressure of 10 Pa after a long duration of exposure to oxygen [63]. Although the authors did not explicitly mention the mechanism leading to void formation, based on the contrast difference between the Cu and Cu_2O phases one can

deduce that the typical Cu_2O shell formation did not occur for this particular set of nanoparticles. Instead, multiple oxidation nucleation sites are visible with inhomogeneous propagation of oxidation resulting in hollowing, as a function of exposure [63]. This however could be related to low oxygen partial pressure resulting in lower adsorption of oxygen leading to preferential nucleation at defect sites as reported for the case of copper thin film [69].

To summarise, the reaction mechanism, morphology and the oxidation state of the copper oxide depends on the temperature, nanoparticle size as well as the O_2 partial pressure.

4.2 REDUCTION OF COPPER OXIDE

The reduction of an oxide is achieved by removal of lattice oxygen atoms or by dissolution of the reductant into the lattice to form metastable hydrides [70]. The reduction of oxides proceeds via adsorption of the reducing agent such as H_2, CO or other fuel as hydrocarbons followed by reaction with the lattice oxygen to form CO_2 and/or H_2O. The formation of the gas molecules is the thermodynamic driving force for the reduction of metallic oxides. Subsequently, the gas molecules desorb from the surface inducing phase and microstructural transformations. The mechanism of the reduction reaction is strongly influenced by the size and geometry of the system, exposed facets, surface defects, defect concentration, grain boundaries as well as the nature of the support and presence of other metals [71].

For the reduction of bulk and thin film CuO, a typical disagreement in literature revolves around the presence of intermediate species. While in some cases XANES data displayed the presence of Cu^+ during the reduction of CuO supported on ZnO [72], *in situ* XRD as well as XANES on powdered CuO sample showed direct reduction to metallic copper [73,74]. Nevertheless, the authors of the latter study also reported that the presence of Cu^+ can be detected when low H_2 partial pressure is used. Kim et al. concluded that the reduction of CuO is more facile compared to that of Cu_2O [74]. Both Kim et al. and Rodriguez et al. reported a period of induction prior to the reduction reaction [73,74]. This induction period is likely to be related to the production of sites on the oxide surface to facilitate the adsorption of H_2. Moreover, the induction period is shortened in the presence of large

defect concentration as well as an increase in the H_2 partial pressure [73,74]. Meanwhile, Imtiaz et al. reported both sequential and direct reduction of CuO on Al_2O_3, at 750 °C during redox reactions [75]. The mechanism shifts from sequential (at the beginning) to direct (after 50 redox cycle). The author attributed this shift to increase in structural disorder induced by the redox reactions. Seemingly, sequential reduction results from the slow removal of oxygen.

Recently, LaGrow et al. conducted *in situ* TEM reduction of Cu_2O in the presence of 2 Pa H_2 partial pressure at a temperature of 300 – 500 °C [63]. The reduction of Cu_2O directly led to metallic copper and the reaction progressed unidirectionally once a nucleation site was formed. Moreover, the reaction proceeded preferentially at the interface between Cu_2O and Cu which is in agreement with the reduction mechanism in copper oxide thin films [71]. Nevertheless, information on morphological transformation during the reduction of CuO or Cu_2O NP in presence of increased H_2 partial pressure is missing.

Other metallic oxide nanoparticles such as NiO or Co_3O_4 exhibits different shape evolution during the reduction process [76–78]. The observations from these studies are discussed within the scope of the present study, in Chapter 5.

Alike the oxidation reaction, the reduction of copper oxide may depend on the temperature, H_2 partial pressure as well as the structural defects present in the oxide particles.

4.3 MOBILITY AND GROWTH OF COPPER-BASED NANOPARTICLES

Particle growth is a very important phenomenon leading to the loss of activity of supported metal phases due to the increase in size or the decrease in surface area of the active metallic phase. In oxygen carriers, particle growth leads to phase segregation and increased porosity in the support grain thus deteriorating the mechanical strength of the material over time. Moreover, in copper-based OC, decreased methane conversion has been associated with the increase in the size of the CuO particles [10]. The growth process is governed by multiple factors such as initial size/shape/dispersion of the nanoparticles, type of metal, temperature, type and pressure of gaseous environment and the nature/roughness of the support. Many studies and review articles have been dedicated to the understanding of particles' growth mechanism [79-82], leading to two main mechanisms: 1. Particle

migration and Coalescence (PMC) and 2. Ostwald Ripening (OR) (Figure 1.8). In PMC, the whole nanoparticle (NP) diffuses on the support surface and fuses with another NP when they are proximate enough to overcome the activation barrier, whereas OR involves atomic migration via detachment of metal atoms or molecular metal clusters from a smaller NP to a bigger NP. Larger particles grow at the expense of smaller particles driven by the Gibbs-Thomson relation (difference in surface energy and local adatom concentration on the support surface). The transportation of atoms between the nanoparticles can take place via surface diffusion, subsurface diffusion or via the gas phase.

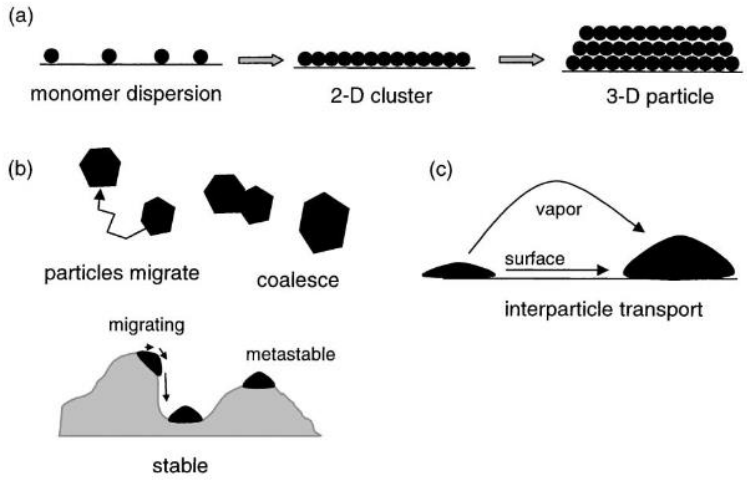

Figure 1.8: Particle growth (a) from single atom, (b) via PMC mechanism and (c) OR mechanism [82].

Ostwald ripening is deemed to be the most important sintering mechanism which can occur via hopping movement or via surface diffusion. Besides atomic diffusion on the support, solid state reaction via diffusion inside the support can also take place [6,83].

The mobility of the atomic species or whole clusters increases with increasing temperature and it is related to the melting point of the materials. It can be predicted using the semi empirical relation of Hüttig (0.3 $T_{melting}$) and Tamman (0.5 $T_{melting}$) temperatures [84–86]. At Hüttig temperature, atoms at defect sites and upon reaching Tamman temperature atoms from the bulk phase will become mobile. The Hüttig and Tamman temperatures of metallic copper and oxides of copper are provided in Table 1.1.

Table 1.1: Values of Melting, Tamman and Hüttig temperatures of copper and copper oxides [79].

Copper phase	Melting temperature (° C)	Tamman temperature (° C)	Hüttig temperature (° C)
Cu metal	1083	405	134
Cu_2O	1235	481	179
CuO	1326	527	207

One of the earliest studies conducted in environmental Transmission Electron Microscopy (eTEM) to understand the effect of gas atmosphere on the dynamic behaviour of copper nanoparticles on model alumina support was by Gai et al in 1990 [87]. Using *in situ* observation of the microstructural evolution under oxidative atmosphere (at 200 °C and 0.2 atm), the authors concluded that the diffusion process involves mobility of metal atoms both across and into the alumina substrate as opposed to only surface mobility. The diffusion of copper ions into the substrate is promoted by the presence of oxygen atmosphere, in contrast with reductive environment of H_2 or CO where bulk diffusion of copper is not observed. The authors believe the volume change resulting from reduced to oxidised phase and decrease in surface energy between metal NP and gas phase contributes to the driving force of the bulk diffusion. However, the interaction of copper with its substrate is influenced by the presence of H_2 (higher surface energy) or CO as they have different adsorption energy on the copper surface. CO is adsorbed more strongly compared to H_2 and under these reducing condition, sintering occurs via Oswald Ripening (OR) mechanism.

Martin et al. combined eTEM with kinetic models to understand the catalytic deactivation due to NP sintering. The study concerns the determination of sintering of Cu NP supported on Si_3N_4 and Al_2O_3 substrates at 500 °C under H_2 at 3 Pa. Under these conditions, the sintering is mainly driven by OR mechanism which seems to be increased by the presence of H_2 in comparison to the rate observed under high vacuum $1.2 \cdot 10^{-7}$ mbar, as shown in Figure 1.9. This could occur due to few proposed hypotheses like weakening of Cu-Cu bonds, enhanced diffusion of Cu adatoms or change in surface energy/wetting behaviour [87,88].

Similar conclusion regarding the effect of gas pressure on the increase in particles sintering has been made by Sun et al. [89,90].

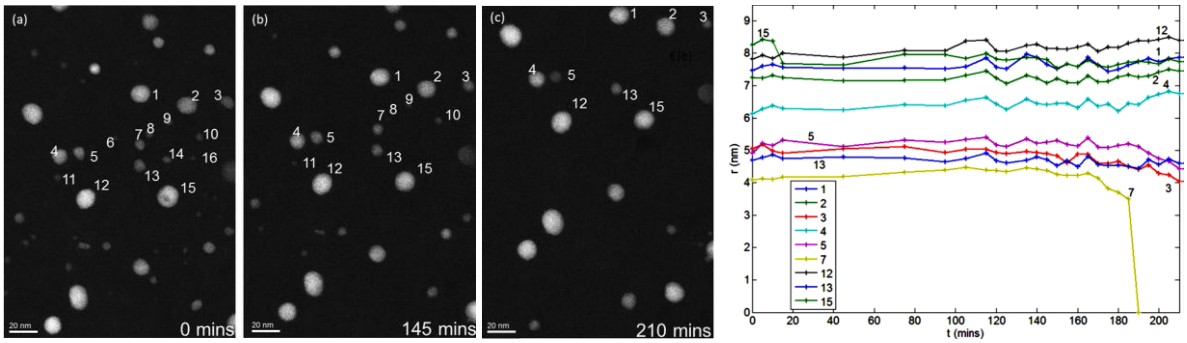

Figure 1.9: Cu/Si_3N_4 sintering by the OR mechanism in 3 Pa at 500 °C a) after 0 min, b) 145 min, c) 210 min, d) Experimental particle radius for r(t=0) < 3.5 nm (for particles 1-5, 7, 12, 13, 15) error in the measurement of r = ± 0.14 nm [91].

To summarize, the migration of copper can occur via surface, grain boundary or bulk diffusion depending on the temperature and the support. The extent of mobility is defined by several factors: temperature, particle size, metal-support interaction, the gas phase and the proximity to other particles. Moreover, the nanoparticles may undergo particle growth via Ostwald Ripening or particle migration and coalescence mechanisms.

4.4 CONCLUSIONS

Oxygen carrier materials are subjected to three key phenomena: oxidation, reduction and sintering during their high temperature operation. The oxidation of copper nanoparticles is affected by the reaction conditions as well as the microstructure of the starting metallic phase. Typically at intermediate temperatures (100-300 °C), the process of copper oxidation can be considered as a two steps process: the initial step involves formation of a thin layer of Cu_2O oxide encapsulating the metallic copper core followed by the genesis of hollow nanoparticles due to nanoscale Kirkendall effect. Nevertheless, with increasing temperature the nanoshells collapse to form compact nanoparticles and Cu_2O undergoes phase transition to form CuO.

Similarly, the reduction of copper oxide and associated mechanism of reaction is dependent on the size and defect concentration in the nanoparticles. The phase transition of CuO nanoparticles leading to metallic copper either occurs directly when the oxide phase contains some structurally disorder or otherwise via an intermediate of Cu_2O.

The behaviour of mobility and particle growth is strongly influenced by the metal-support interaction. In addition to that, the reaction atmosphere also plays an important role in the stability of the metal or metal oxide phases. Both particle migration and coalescence (PMC) and Ostwald ripening have been observed for copper based nanoparticles.

The oxidation, reduction and the particle mobility and growth mechanisms are defined by the studied system for example, the nanoparticle size, defect concentration, the nature of the support, temperature and reaction gas pressure. Therefore, it is crucial to understand the morphological evolution of the relevant nanoparticle/support as a function of the reaction parameters of interest.

5 CONCLUSIONS AND STRATEGIES

The mitigation of climate change demands for an array of solutions including emerging technologies such as Chemical Looping Combustion (CLC). In order for CLC technology to be economically feasible, special attention should be given to the development of the oxygen carrier material which is at the core of the CLC process. Among the several types of materials proposed and studied, supported copper based oxygen carriers received particular consideration due to their relatively low cost, acceptable environmental impact and flexible redox behaviour making them ideal candidates for industrial utilisation.

In particular, CuO/Al_2O_3 materials displays promising outcome as a potential commercial oxygen carrier. Despite the suitability of CuO/Al_2O_3 as an oxygen carrier, some drawbacks have been reported regarding the degradation of the material and loss of reactivity, especially at 900 °C or above. Attrition, fragmentation and sintering of the copper oxides are identified as the main mechanisms resulting in the loss of reactivity. Attrition leads to loss of copper phase due to the generation of copper-rich fines. After multiple redox cycles, oxygen carrier particles are subjected to fragmentation with the increase of support porosity. While the copper-rich fines formed by attrition are related to the outward migration of the copper, the increased porosity in the particles is associated to the alumina phase transition. At the same time, the copper/copper oxide phases undergo sintering resulting in further loss of reactivity.

Lambert et al. have suggested a comprehensive mechanism based on macroscopic *ex situ* characterisation of copper migration, sintering and various phase transitions in the CuO-Al_2O_3 system submitted to long term redox cycling at 900 °C. This mechanism emphasised two aspects which formed the basis of the current work: understanding the copper migration mechanism and the CuO-Al_2O_3 phase interactions as a function of cycling at different reaction temperatures. Most of the studies on the CuO/Al_2O_3 oxygen carriers are based on the macroscopic overview of post-mortem samples, after cycling. With post-mortem characterisations it is difficult to obtain information on the mobility especially if it encompases several scales. It is therefore essential to correlate the evolution of the copper phases at multiple scales and *operando* to have a global understanding of the phenomena at play in order to uncover the mechanisms involved in OC ageing.

To date, a negligible number of studies has been dedicated to understanding the dynamic behaviour of CuO/Al_2O_3 under CLC conditions (*i.e*. high temperature and atmospheric pressure) at the nanometric scale and its correlation to the macroscopic properties. The present work attempts to address these two issues – characterisation of the oxygen carrier in real-time and multi-scale to achieve a better understanding of the migration and phase transformation of alumina supported copper-based oxygen carriers. To achieve that, a multiscale and multi technique approach will be used including *in situ* STEM, STXM-XANES, *in situ* XRD and *in situ* XAS.

A range of materials has been chosen for specific studies, including 13 wt% CuO supported on commercial alumina support (main material), as well as model systems composed of copper nanoparticles supported on SiN_x and amorphous Al_2O_3 substrates, and impregnated alumina nanospheres.

In Chapter 3, the interaction of the copper phases with the alumina support as a function of the number of redox cycles at different temperatures will be investigated. The spatial distribution of the different chemical and polymorphic phases located within the support will be studied to provide a global idea of the possible interactions, and also to identify the possible migration pathways of the copper phase within the support grain.

In the following part (Chapter 4), the dynamic evolution of copper species over cycling will be studied employing XAS technique. The changes will be correlated to the morphology of

the oxygen carrier at different stages of cycling, to suggest possible pathways for the alumina phase transition.

In Chapters 5 and 6, the nanoscale evolution of the material will be characterised in real-time using *in situ* STEM. The first study will be carried out on a model system of made of copper nanoparticles deposited on inert SiN_x substrate (TEM echip membrane) allowed to achieve a fundamental outlook of the behaviour of copper nanoparticles under CLC reaction conditions without the influence of the support. In particular, morphological/phase transformations of the copper nanoparticles during their oxidation and reduction. Furthermore, Cu nanoparticles deposited on amorphous Al_2O_3 substrate will be investigated to achieve a better understanding of the migration behaviour under different gas environments. Finally, two CuO/Al_2O_3 supported samples will be observed in CLC reaction conditions using *in situ* STEM to study the mobility of the copper phase at the nanoscale as well as the first steps of the phase transitions.

6 REFERENCES

[1] G.C. Hergerl 2005 Climate change detection and attribution- Beyond mean temperature signal.

[2] Intergovernmental Panel on Climate Change. *Climate Change 2014 Synthesis Report: Summary for Policymakers : IPCC*, 2014.

[3] International Energy Agency. Energy Technology Perspectives 2017.

[4] L. Kohl and Richard B. Nielsen. *Gas Purification*. Elsevier, 1997.

[5] A. Lyngfelt. Chemical Looping Combustion: Status and Development Challenges, *Energy & Fuels*, 2020, **34**, 9077-3093.

[6] J. Adanez, A. Abad, F. Garcia-Labiano, P. Gayan and L. F. De Diego. Progress in Chemical-Looping Combustion and Reforming technologies, *Progress in Energy and Combustion Science*, 2012, **38,** 2, 215-282. DOI: 10.1016/j.pecs.2011.09.001.

[7] M. Matzen, J. Pinkerton, X. Wang, Y. Demirel. Use of natural ores as oxygen carriers in chemical looping combustion: A review, *International Journal of Greenhouse Gas Control*, 2017, **65**, 1-14.

[8] Protasova L., Snijkers F. Recent developments in oxygen carrier materials for hydrogen production via chemical looping processes, *FUEL*, 2016, **181**, 75-93. DOI: 10.1016/j.fuel.2016.04.110.

[9] Cheng Z., Qin L., Fan J.A., Fan L.-S. New Insight into the Development of Oxygen Carrier Materials for Chemical Looping Systems, *Engineering*, 2018, **4,** 3, 343-351. DOI: 10.1016/j.eng.2018.05.002.

[10] A. Lambert, A. Tilland, W. Pelletant, S. Bertholin, F. Moreau, I. Clemençon and M. Yazdanpanah. Performance and degradation mechanisms of CLC particles produced by industrial methods, *FUEL*, 2018, **216**, 71-82. DOI: 10.1016/j.fuel.2017.11.115.

[11] S. Sharna, M. Bahri, C. Bouillet, V. Rouchon, A. Lambert, A.-S. Gay, D. Chiche and O. Ersen. In situ STEM study on the morphological evolution of copper-based nanoparticles during high-temperature redox reactions, *Nanoscale*, 2021, **13,** 9747-9756.

[12] B. D Santer, K. E. Taylor, T. M. L Wigley, T.C. Johns, P.D. Jones, D.J. Karoly, J.F.B. Mitchell, A.H. Oort, J.E. Penner, V. Ramaswamy, M.D. Schwarzkopf, R.J. Stouffer & S. Tett. A search for human influence on the thermal structure of the atmosphere, *Nature*, 1996, **382**.

[13] G.C. Hegerl, H. von Storch, K. Hasselmann, B.D. Santer, U. Cubasch & P.D. Jones. Detecting Greenhouse-Gas-Induced Climate Change with an Optimal Fingerprint Method, *Journal of Climate*, 1996, **9,** 10.

[14] V. Ramaswamy, M. D. Schwarzkopf, W. J. Randel, B. D. Santer, B. J. Soden, G. L. Stenchikov. Anthropogenic and Natural Influences in the Evolution of Lower Stratospheric Cooling, *Science*, 2006, **311,** 5764, 1138-1141.

[15] S. Arrhenius. On the influence of carbonic acid in the air upon the temperature of the ground, *Philosophical Magazine*, 1896, **41**, 237-276.

[16] Alan Buis. A degree of concer: Why global temperatures matter?

[17] Scripps CO2. Keeling Curve Lessons: Lessons for long-term earth observations.

[18] Bernstein L. *Climate Change 2007: Synthesis report : [a report of the Intergovernmental Panel on Climate Change]*. IPCC, Geneva, 2008, 73 p.

[19] A. David. Fate of fossil fuel CO2 in geologic time, *Journal of Geophysical Research*, 2005, **110,** C9, 1769. DOI: 10.1029/2004JC002625.

[20] B. Metz, O. Davidson, H. de Coninck, M. Loos, L, Meyer. IPCC Carbon dioxide storage and capture, 2005.

[21] D. Thomas S. B. *Carbon Dioxide Capture for Storage in Deep Geologic Formations - Results from the CO2 Capture Project : Capture and seperation technology gaps and priority reserach needs*. Elsevier, 2005.

[22] CO2 Capture, transport and storage, *Parlamentary Office of Science and Technology*, 2009, **335**.

[23] Gauthier T., Yazdanpanah M., Forret A., Amblard B., Lambert A., Bertholin S. CLC, a promising concept with challenging development issues, *Powder Technology*, 2017, **316**, 3-17. DOI: 10.1016/j.powtec.2017.01.003.

[24] M. Ishida H.J. A novel combustor based on CLC reactions and its kinetics, *Journal of Chemical Engineering of Japan*, 1994, **27,** 3, 296-301.

[25] Abad A., Adánez J., García-Labiano F., Diego L.F. de, Gayán P., Celaya J. Mapping of the range of operational conditions for Cu-, Fe-, and Ni-based oxygen carriers in chemical-looping combustion, *Chemical Engineering Science*, 2007, **62,** 1-2, 533-549. DOI: 10.1016/j.ces.2006.09.019.

[26] García-Labiano F., Gayán P., Adánez J., Diego L.F. de, Forero C.R. Solid waste management of a chemical-looping combustion plant using Cu-based oxygen carriers, *Environmental science & technology*, 2007, **41,** 16, 5882-5887. DOI: 10.1021/es070642n.

[27] Lyngfelt A. Oxygen Carriers for Chemical Looping Combustion - 4 000 h of Operational Experience, *Oil & Gas Science and Technology – Revue d'IFP Energies nouvelles*, 2011, **66,** 2, 161-172. DOI: 10.2516/ogst/2010038.

[28] L. F. de Diego, F. Garcia-Labiano, P. Gayan, J. Celaya, J. K. Palacios, J. Adanez. Operation of a 10 kWth Chemical-Looping Combustor during 200 h with a CuO-Al2O3 Oxygen Carrier, *FUEL*, 2007, **86**, 1036-1045.

[29] Cho P., Mattisson T., Lyngfelt A. Carbon Formation on Nickel and Iron Oxide-Containing Oxygen Carriers for Chemical-Looping Combustion, *Industrial & Engineering Chemistry Research*, 2005, **44,** 4, 668-676. DOI: 10.1021/ie049420d.

[30] Mattisson. T, Johansson. M, Lyngfelt. A. The use of NiO as an oxygen carrier in chemical-looping combustion, *FUEL*, 2006, **85,** 5-6, 736-747. DOI: 10.1016/j.fuel.2005.07.021.

[31] Gayán P., Forero C.R., Abad A., Diego L.F. de, García-Labiano F., Adánez J. Effect of Support on the Behavior of Cu-Based Oxygen Carriers during Long-Term CLC Operation at

Temperatures above 1073 K, *Energy & Fuels*, 2011, **25,** 3, 1316-1326. DOI: 10.1021/ef101583w.

[32] Diego L.F. de, Gayán P., García-Labiano F., Celaya J., Abad A., Adánez J. Impregnated CuO/Al 2 O 3 Oxygen Carriers for Chemical-Looping Combustion : Avoiding Fluidised Bed Agglomeration, *Energy & Fuels*, 2005, **19,** 5, 1850-1856. DOI: 10.1021/ef050052f.

[33] Adánez J., Gayán P., Celaya J., Diego L.F. de, García-Labiano F., Abad A. Chemical Looping Combustion in a 10 kW th Prototype Using a CuO/Al 2 O 3 Oxygen Carrier : Effect of Operating Conditions on Methane Combustion, *Industrial & Engineering Chemistry Research*, 2006, **45,** 17, 6075-6080. DOI: 10.1021/ie060364l.

[34] Fan. Liang-Shih, ed. *Chemical Looping Systems for Fossil Energy Conversions*. Wiley, USA, 2010, 437 p.

[35] F. Li, Z. Sun, S Luo and L-S. Fan. Ionic diffusion in the oxidation of iron—effect of support and its implications to chemical looping applications : Li et al. Energy Environ. Sci., 2011, 4, 876–880, *Energy & Environmental Science*, 2011, **4**, 876-880.

[36] Sun Z., Zhou Q., Fan L.-S. Formation of core-shell structured composite microparticles via cyclic gas-solid reactions, *Langmuir : the ACS journal of surfaces and colloids*, 2013, **29,** 40, 12520-12529. DOI: 10.1021/la4029832.

[37] Zhao X., Zhou H., Sikarwar V.S., Zhao M., Park A.-H.A., Fennell P.S., Shen L., Fan L.-S. Biomass-based chemical looping technologies : The good, the bad and the future, *Energy & Environmental Science*, 2017, **10,** 9, 1885-1910. DOI: 10.1039/C6EE03718F.

[38] García-Labiano F., Diego L.F. de, Adánez J., Abad A., Gayán P. Reduction and Oxidation Kinetics of a Copper-Based Oxygen Carrier Prepared by Impregnation for Chemical-Looping Combustion, *Industrial & Engineering Chemistry Research*, 2004, **43,** 26, 8168-8177. DOI: 10.1021/ie0493311.

[39] Gayán P., Forero C.R., Abad A., Diego L.F. de, García-Labiano F., Adánez J. Effect of Support on the Behavior of Cu-Based Oxygen Carriers during Long-Term CLC Operation at Temperatures above 1073 K, *Energy & Fuels*, 2011, **25,** 3, 1316-1326. DOI: 10.1021/ef101583w.

[40] Diego L.F. de, García-Labiano F., Adánez J., Gayán P., Abad A., Corbella B.M., María Palacios J. Development of Cu-based oxygen carriers for chemical-looping combustion, *FUEL*, 2004, **83,** 13, 1749-1757. DOI: 10.1016/j.fuel.2004.03.003.

[41] Adánez J, de Diego LF, García-Labiano F, Gayán P, Abad A. Selection of oxygen carriers for chemical-looping combustion, *Energy & Fuels*, 18, **18**, 371-377.

[42] Zafar Q, Mattisson T, Gevert B. Redox investigation of some oxides of transition-state metals Ni, Cu, Fe, and Mn supported on SiO2 and MgAl2O4., *Energy & Fuels*, 2016, **20**, 34-44.

[43] Liu Y., Kirchesch P., Graule T., Liersch A., Clemens F. Development of oxygen carriers for Chemical Looping Combustion : The chemical interaction between CuO and silica/γ-alumina granules with similar microstructure, *FUEL*, 2016, **186**, 496-503. DOI: 10.1016/j.fuel.2016.08.090.

[44] N. van Garderen, E. H. Otal, C. G. Aneziris, T. Graule and F. J. Clemens. Influence of porous substrate on copper based oxygen carrier efficiencyfor chemical-looping combustion, *Microporous and Mesoporous Materials*, 2014, **190**, 362-370.

[45] Corbella B.M., Diego L. de, García F., Adánez J., Palacios J.M. The Performance in a Fixed Bed Reactor of Copper-Based Oxides on Titania as Oxygen Carriers for Chemical Looping Combustion of Methane, *Energy & Fuels*, 2005, **19,** 2, 433-441. DOI: 10.1021/ef049832z.

[46] Cho P., Mattisson T., Lyngfelt A. Comparison of iron-, nickel-, copper- and manganese-based oxygen carriers for chemical-looping combustion, *FUEL*, 2004, **83,** 9, 1215-1225. DOI: 10.1016/j.fuel.2003.11.013.

[47] Mattisson T., Järdnäs A., Lyngfelt A. Reactivity of Some Metal Oxides Supported on Alumina with Alternating Methane and OxygenApplication for Chemical-Looping Combustion, *Energy & Fuels*, 2003, **17,** 3, 643-651. DOI: 10.1021/ef020151i.

[48] M. Pishahang 1, Y. Larring *, R. E. Stensrød, K. A. Andreassen and A. I. Spjelkavik. 3kW circulating fluidised bed chemical looping reactor - A thermochemical and

chemomechanical investigation on the performance of Cuimpregnated Al2O3 as an oxygen carrier material, *International Journal of Greenhouse Gas Control*, 2021, **109**.

[49] M.T. Izquierdo, F. García-Labiano, A. Abad, A. Cabello, P. Gayan, L.F. de Diego and J. Adanez. On the optimization of physical and chemical stability of a Cu/Al2O3 impregnated oxygen carrier for chemical looping combustion, *Fuel Processing Technology*, 2021, **215**.

[50] Forero C.R., Gayán P., García-Labiano F., Diego L.F. de, Abad A., Adánez J. High temperature behaviour of a CuO/γAl2O3 oxygen carrier for chemical-looping combustion, *International Journal of Greenhouse Gas Control*, 2011, **5,** 4, 659-667. DOI: 10.1016/j.ijggc.2011.03.005.

[51] A. Boumaza, L. Favaro, J. Lédion, G. Sattonnay, J.B.Brubach, P.Berthet, A. M. Huntz, P. Roy and R. Tétota. Transition alumina phases induced by heat treatment of boehmite: An X-ray diffraction and infrared spectroscopy study, *Journal of Solid State Chemistry*, 2009, **182,** 5, 1171-1176.

[52] I. Levin and D. Brandon. Metastable Alumina Polymorphs: Crystal Structures andTransition Sequences, *Journal of the American Ceramic Society*, 1998, **81**, 1995-2012.

[53] W. Hu, F. Donat, S. A. Scott and J. S. Dennis. The interaction between CuO and Al2O3 and the reactivity of copper aluminates below 1000 C and their implication on the use of the Cu–Al–O system for oxygen storage and production, *RSC Advances*, 2016, **6**, 113016-113024.

[54] Zafar Q, Mattisson T, Gevert B. Integrated hydrogen and power production with CO2 capture using chemical-looping reforming-Redox reactivity of particles of CuO, Mn2O3, NiO, and Fe2O3 using SiO2 as support, *Industrial Engineering Chemistry Research*, 2005, **44**, 3485-3496.

[55] Zeng L., Cheng Z., Fan J.A., Fan L.-S., Gong J. Metal oxide redox chemistry for chemical looping processes, *Nature Reviews Chemistry*, 2018, **2,** 11, 349-364. DOI: 10.1038/s41570-018-0046-2.

[56] Q. Zhu, L. Zou, G. Zhou, W. A. Saidi and Y. C. Judith. Early and transient stages of Cu oxidation : Atomistic insights from theoretical simulations and in situ experiments, *Surface Science*, 2016, **652**, 98-113. DOI: 10.1016/j.susc.2016.03.003.

[57] R. Nakamura, D. Tokozakura, J. G. Lee, Mori and H. Nakajima. Shrinking of hollow Cu2O and NiO nanoparticles at high temperatures, *Acta Materialia*, 2008, **56,** 18, 5276-5284. DOI: 10.1016/j.actamat.2008.07.004.

[58] R. Nakamura, D. Tokozakura, H. Nakajima, J-G Lee, H. Mori. Hollow oxide formation by oxidation of Al and Cu nanoparticles, *Journal of Applied Physics*, 2007, **101,** 7, 74303. DOI: 10.1063/1.2711383.

[59] R. Nakamura, G. Matsubayashi, H. Tsuchiya, S. Fujimoto, H. Nakajima. Transition in the nanoporous structure of iron oxides during the oxidation of iron nanoparticles and nanowires, *Acta Materialia*, 2009, **57,** 14, 4261-4266. DOI: 10.1016/j.actamat.2009.05.023.

[60] R. Nakamura, D. Tokozakura, J. G. Lee, H. Mori, H. Nakajima. Oxidation Behavior of Cu Nanoparticles and Formation of Hollow Cu_2O Spheres, *Materials Science Forum*, 2007, **561-565**, 1703-1706. DOI: 10.4028/www.scientific.net/MSF.561-565.1703.

[61] A. Yabuki and S. Tanaka. Oxidation behavior of copper nanoparticles at low temperature, *Materials Research Bulletin*, 2011, **46**, 2323-2327.

[62] M. Mansoor, L. Favergeon and M. Pijolat. Kinetic modeling of low temperature oxidation of coppernanoparticles by O2, *Thermochimica Acta*, 2013, **570**, 41-50.

[63] A. P. LaGrow, M. R. Ward, D. C. Lloyd, P. L Gai, E. D. Boyes. Visualizing the Cu/Cu2(O) Interface Transition in Nanoparticles with Environmental Scanning Transmission Electron Microscopy, *Journal of the American Chemical Society*, 2017, **139,** 1, 179-185. DOI: 10.1021/jacs.6b08842.

[64] K. P. Rice, A. S. Paterson and M.P Stoykovich. Nanoscale Kirkendall Effect and Oxidation Kinetics in Copper Nanocrystals Characterised by Real-Time, In Situ Optical Spectroscopy, *Particle & Particle Systems Characterisation*, 2015, **32,** 3, 373-380. DOI: 10.1002/ppsc.201400155.

[65] M. D. Susman, Y. Feldman, T. A. Bendikov, A. Vaskevich and I. Rubinstein. Real-time plasmon spectroscopy study of the solid-state oxidation and Kirkendall void formation in copper nanoparticles, *Nanoscale*, 2017, **9,** 34, 12573-12589. DOI: 10.1039/c7nr04256f.

[66] G. J. Cheng and A. R. H. Walker. Transmission electron microscopy characterisation of colloidal copper nanoparticles and their chemical reactivity, *Anal Bioanal Chem*, 2010, **397**, 1057-1069.

[67] Anderson B.D., Tracy J.B. Nanoparticle conversion chemistry : Kirkendall effect, galvanic exchange, and anion exchange, *Nanoscale*, 2014, **6,** 21, 12195-12216. DOI: 10.1039/c4nr02025a.

[68] D. Tokozakura, R. Nakamura, H. Nakajima, J. G. Lee and H. Mori. Transmission electron microscopy observation of oxide layer growth on Cu nanoparticles and formation process of hollow oxide particles, *Journal of Material Research*, 2007, **22**, 2930-2935.

[69] Gattinoni. C. M.A. Atomistic detailsofoxidesurfacesandsurfaceoxidation:theexample of copperanditsoxides, *Surface Science Reports*, 2015, **70**, 424-447.

[70] Harold H. Kung. *Studies in Surface Science and Catalysis : Chapter 6 Reduction of Oxides*, 1989.

[71] X. Chen, D. Wu, L. Zou, Q. Yin, H Zhang, D. N. Zakharov, E.A. Stach and G. Zhou. In situ atomic-scale observation of inhomogeneous oxide reduction, *Chem. Commun*, 2018, **54,** 7342.

[72] T. L. Reitz, P. L. Lee, K. F. Czaplewski, J. C. Lang, K. E. Popp, and H. H. Kung. Time-Resolved XANES Investigation of CuO/ZnO in the Oxidative Methanol Reforming Reaction, *Journal of Catalysis*, 2001, **199**, 193-201.

[73] J. A. Rodriguez, J. Y. Kim, J.C. Hanson, M. Perez and A. I. Frenkel. Reduction of CuO in H2: in situ time-resolved XRD studies, *Catalysis Letters*, 2003, **85**, 247-254.

[74] J. Y. Kim, J. A. Rodriguez, J. C. Hanson, A. I. Frenkel and P. L. Lee. Reduction of CuO and Cu2O with H2: H Embedding and Kinetic Effects in the Formation of Suboxides, *Journal of the American Chemical Society*, 2003, **125**, 10684-10692.

[75] Q. Imtiaz, P. M. Abdala, A. M. Kierzkowska, W. van Beek, S. Schweiger, L. M. Rupp and C. R. Muller. Na+ doping induced changes in the reduction and charge transport characteristics of Al2O3- stabilized, CuO-based materials for CO2 capture, *Phys. Chem. Chem. Phys*, 2016, **18**, 12278-12288.

[76] J. A. Medford, C. A. Johnston-Peck and J. B. Tracy. Nanostructural transformations during the reduction of hollow and porous nickel oxide nanoparticles, *Nanoscale*, 2013, **5,** 1, 155-159. DOI: 10.1039/c2nr33005a.

[77] Chenna S., Banerjee R., Crozier P.A. Atomic-Scale Observation of the Ni Activation Process for Partial Oxidation of Methane Using In Situ Environmental TEM, *ChemCatChem*, 2011, **3,** 6, 1051-1059. DOI: 10.1002/cctc.201000238.

[78] C. J. Weststrate, M. M. Hauman, D. J. Moodley, A. M. Saib, E. van Steen and J. W. Niemantsverdriet. Cobalt Fischer–Tropsch catalyst regeneration: The crucial role of the Kirkendall effect for cobalt Redispersion, *Top Catalysis*, 2011, **54**, 811-816.

[79] M. Argyle C.B. Heterogeneous catalyst deactivation and regeneration: a review, *Catalysts*, 2015, **5**, 145-269.

[80] E.D. Goodman, J.A. Schwalbe, M. Cargnello. Mechanistic understanding and the rational design of sinter- resistant heterogeneous catalysts, *ACS Catalysis*, 2017, **7,** 7156-7173.

[81] T.W. Hansen, A.T. Delariva, S. R. Challa, A.K. Datye. Sintering of Catalytic Nanoparticles: Particle Migration or Ostwald Ripening?, *Accounts of Chemical Research*, 2013, **46,** 8, 1720-1730.

[82] F. Grillo, J.A. Moulijn, M.T. Kreutzer, R. van Ommen. Nanoparticle sintering in atomic layer deposition of supported catalysts: Kinetic modeling of the size distribution, *Catalysis Today*, 2018, **316**, 51-61.

[83] Q. Imtiaz, D. Hosseini and C. R. Müller. Review of Oxygen Carriers for Chemical Looping with Oxygen Uncoupling (CLOU) : Thermodynamics, Material Development, and Synthesis, *Energy Technology*, 2013, **1,** 11, 633-647. DOI: 10.1002/ente.201300099.

[84] Baker R.T. K. The Relationship between Particle Motion on a Graphite Surface and Tammann Temperature, *Journal of Catalysis*, 1982, **78**, 473-476.

[85] Helmut Mehrer. *Diffusion in Solids*. Springer, 2007.

[86] Hansen T.W., Delariva A.T., Challa S.R., Datye A.K. Sintering of catalytic nanoparticles : Particle migration or Ostwald ripening?, *Accounts of Chemical Research*, 2013, **46,** 8, 1720-1730. DOI: 10.1021/ar3002427.

[87] P. L. Gai, B. C. Smith and G. Owen. Bulk diffusion of metal particles on ceramic substrates, *Nature*, 1990, **348**, 430-432.

[88] Ouyang R., Liu J.-X., Li W.-X. Atomistic theory of Ostwald ripening and disintegration of supported metal particles under reaction conditions, *Journal of the American Chemical Society*, 2013, **135,** 5, 1760-1771. DOI: 10.1021/ja3087054.

[89] Sun J.T., Metcalfe, Ian. S and Sahibzada, Mortaza. Deactivation of Cu/ZnO/Al2O3 Methanol Synthesis Catalyst by Sintering, *Industrial & Engineering Chemistry Research*, 1999, **38,** 10, 3868-3872.

[90] Kuechen. C, Hoffmann. U. Investigation of simultaneous reaction of carbon monoxide and carbon dioxide with hydrogen on a commercial copper/zinc oxide catalyst, *Chemical Engineering Science*, 1993, **48,** 22, 3767-3776.

[91] T. E. Martin, P. L. Gai, and E. D. Boyes. Dynamic Imaging of Ostwald Ripening by Environmental Scanning Transmission Electron Microscopy, *ChemCatChem*, 2015, **7,** 22, 3705-3711. DOI: 10.1002/cctc.201500830.

Chapter 2:
Experimental part

This chapter presents the preparation and synthesis of the oxygen carrier materials, the methodology used to carry out the oxidation-reduction cycles and the characterisation techniques used throughout the course of this project.

1 MATERIAL PREPARATION

1.1 PREPARATION OF THE OXYGEN CARRIERS

In this study, three types of materials were used as oxygen carriers, ① supported oxygen carriers made of CuO supported on commercial gamma alumina (γ-Al_2O_3), ② a model system composed of nanoparticles of copper and ③ a model system composed of 13wt% CuO supported on lab-made γ-Al_2O_3 nanoparticles. Only the synthesis protocol of ① supported oxygen carriers (CuO over alumina) is presented in this chapter. The mains tests were carried out on 13wt% CuO on Al_2O_3 materials, the results of which are discussed in chapters 3, 4 and 6.

The synthesis of ② and ③ are presented in chapters 5 and 6, respectively.

For sample ①, a commercial γ-Al_2O_3 support from Puralox SCFa series (made by Sasol, Germany) was selected. The support is mesoporous with a pore diameter of 8-9 nm and a grain size of 100 to 250 µm. Two different concentrations of copper were studied, mainly 13wt% of CuO and 22wt% of CuO in the final oxygen carrier.

The choice of 13wt% CuO is linked to the following factors:

Constraint of agglomeration posed by the higher concentration of CuO in the CuO/Al_2O_3 oxygen carriying capacity, as addressed by the study of de Diego et al. [1] and outlined in chapter 1, section 3.2.2.1.

To be consistent with the literature where 10-15wt% CuO is used.

To achieve a $R_0\Delta X$ value of 2% set for the operating conditions used in IFPEN's pilot plant, where $R_0\Delta X$ defines the quantity of oxygen released by the OC, R_0 is the oxygen carrying capacity and ΔX is the conversion of the oxygen carrier in the fuel reactor.

The concentration of 22wt% was chosen to achieve half of the stoichiometric amount of copper compared to the copper-aluminate ($CuAl_2O_4$) phase. This material was only used in the *in situ* STEM experiment (chapter 6), where the goal was to observe whether the copper concentration has an impact on the migration behavior of the copper phase. For the facility in understanding other reasons are highlighted in chapter 6.

The supported oxygen carriers were prepared by incipient wetness impregnation method. The protocol used here was adapted from Adanez et al. with few modifications on the temperature and duration of calcination [16]. In a typical preparation, an aqueous solution of copper nitrate ($Cu(NO)_3.3\ H_2O$, from Sigma Aldrich) corresponding to the total pore volume of the support was slowly added to the support grains at room temperature under constant stirring. Afterwards, the mixture was kept aside for a 3 hours period of maturation. The mixture was then dried overnight at a temperature of 120 °C. Finally the impregnated supports were calcined for 12 hours to produce the supported oxygen carriers. Material samples were calcined at 700 °C, 800 °C and 900 °C respectively to determine the effect of calcination temperature on the chemical composition, and later on, on the aging of the oxygen carriers. The samples are called 13wt%CuO/Al_2O_3 – T, where T is the calcination temperature.

The 22wt% CuO/Al_2O_3 sample was prepared in similar manner by incipient wetness impregnation, in 3 steps of impregnation to achieve a homogeneous diffusion and dispersion of the copper phase. In the first two steps the calcination was carried out at 600 °C for 12 hours to avoid the formation of α-Al_2O_3 and the last step of calcination was carried out at 900 °C for 12 hours.

1.2 SYNTHESIS OF THE REFERENCE SAMPLES

In addition to the oxygen carriers, three copper aluminate samples were synthesised, to be used as references for XAS and STXM analysis. The three samples are $CuAl_2O_4$, $CuAlO_2$ and non-stoichiometric $CuAlO_2$.

The $CuAl_2O_4$ sample was prepared by mechanically mixing and grinding 1:1 molar ratio of CuO powder (from Sigma Aldrich) and Al_2O_3. The mixture was calcined at 600 °C for 12 hours, to avoid the formation of alpha Al_2O_3. The process of grinding and calcination was repeated one more time at 600 °C and finally at 900 °C for 12 hours.

The $CuAlO_2$ sample was synthesized by calcination of $CuAl_2O_4$ at 950 °C, under an inert atmosphere of N_2 for 10 hours.

The non-stoichiometric $CuAlO_2$ was prepared by the calcination of the 13wt% CuO/Al_2O_3-900 °C at 950 °C under an inert atomosphere of N_2 for 10 hours.

2 MATERIAL AGEING

A thermogravimetric analysis (TGA) device was used to carry out the aging of the oxygen carrier material. The TGA device used in this study is a symmetric SETARAM TAG 24 thermobalance.

During a typical run, 20-30 mg of sample is placed in a Pt crucible. To avoid temperature fluctuation and overheating of the furnace, the sample is heated under air in two stages: at a rate of 40 °C/min from room temperature to 100 °C below the temperature set, and then at 10 °C/min up to the reaction temperature. Materials reaction and ageing is operated by redox cycles with alternating reducing (10 % H_2, 90 % N_2) and oxidizing (air) gases. To avoid mixing of H_2 and air, the TGA system is purged under N_2 gas flow in between reduction and oxidation steps. The flowrate of the gases are set to 150 mL/min. *Figure 2.1*, showing sample weight evolution measured in the TGA along the process, demonstrates a typical reduction–oxidation cycle at 900 °C. Under nitrogen gas, a slight decrease in mass is observed (pointed with a black arrow) which is related to the reduction of Cu^{2+} into Cu^{+} [2]. Further decrease in mass corresponds to the reduction to metallic copper when H_2 is introduced. The red area in the *Figure 2.1* represents the introduction of oxygen gas, during which increase in mass corresponds to the oxidation of metallic copper. The slight increase in mass passing from H_2 to N_2, is due to a slight deviation in the equilibration of the symmetrical TGA system.

For the ageing test of the material, typically a temperature of 700 to 1000 °C was used to understand the effect of the reaction temperature and number of cycles on the ageing of the oxygen carriers.

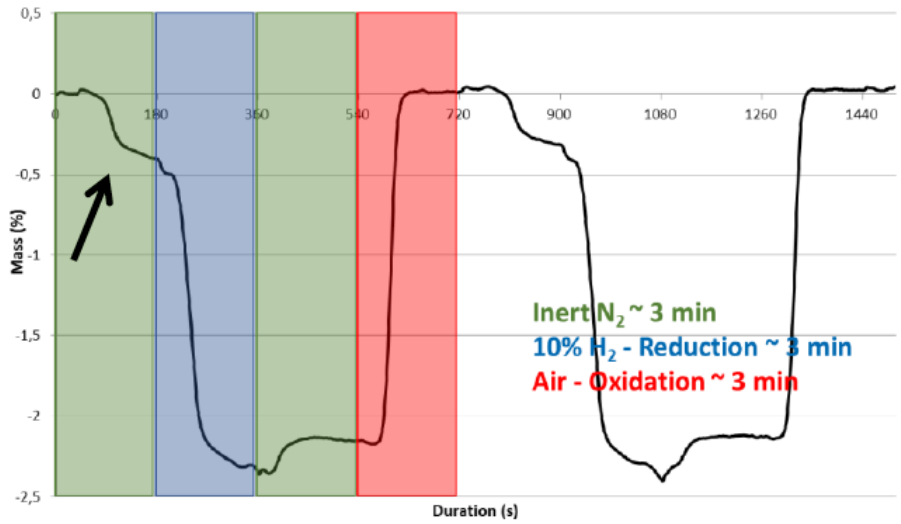

Figure 2.1 : CuO/Al2O3–900 °C undergoing oxidation–reduction reactions during redox cycle in a TGA device.

The TGA cycling can provide information on the oxygen carrying capacity of the sample from the loss of the sample mass during the reduction steps. Any changes in the value of the mass loss over the period of the redox cycling is a result of incomplete reaction due to the sintering or slower reaction kinetics of the copper phase.

Comparison of the CuO/Al_2O_3 – 900 °C cycled 200 times at 900 °C, bulk CuO powder cycled 5 times at 900 °C, and CuO/Al_2O_3 – 900 °C cycled 50 times at 1000 °C display significant differences. For the CuO/Al_2O_3 – 900 °C sample cycled at 900 °C, no significant mass loss was observed at the end of the 200 cycles compared to the beginning of the cycles. On the contrary, bulk CuO powder displayed gradual decrease in the value of mass loss as a function of the cycling. The CuO sample recovered after the cycling was a few mm in size. Without the presence of the support, the powdered CuO sample sustained considerable thermal sintering. The CuO/Al_2O_3 – 900 °C sample cycled at 1000 °C also presented a gradual decrease in the mass loss over the period of 50 cycles. During the oxidation the sample was not fully oxidized and underwent a gradual decrease in the mass loss in the subsequent cycles, possibly due to the formation of a copper phase exhibiting slow reaction kinetics [3].

3 MATERIAL CHARACTERISATIONS

A range of characterisation techniques has been employed to correlate the nanoscale evolution of the supported materials to its macroscopic properties. Table 2.1 and Table 2.2 display the *ex situ* and *in situ* characterisations performed on the different materials.

The operation procedure of all the characterisation techniques are outlined in the following paragraphs. It should be noted that the Hg-porosimetry and N_2 physisorption have only been carried out for the puralox support and the fresh oxygen carriers calcined at 800 and 900 °C. The analysis of the cycled materials could not be achieved as the amount of material used in the TGA cycle is significantly lower (about 20 – 30 mg) compared to the amount of material required to carry out the porosimetry and physisorption analysis (about 1-2 g).

Furthermore, due to constraints such as availability of the specific techniques some of the samples could not be characterized. The standard characterisation (Hg porosimetry and N_2 absorption) of the 13wt% CuO/Al_2O_3 are provided in Appendix A.

Table 2.1 : List of 13wt% CuO/Al_2O_3 samples calcined at different temperatures and related ex situ characterisations carried out.

	Fresh-700 °C	700 °C – 50 cycles	700 °C – 200 cycles	Fresh 800 °C	800 °C – 50 cycles	800 °C – 200 cycles	Fresh 900 °C	900 °C – 50 cycles	900 °C – 200 cycles
Hg Porosimetry				X			X		
N_2 Physisorption				X			X		
SEM	X	X	X	X	X	X	X	X	X
XRD		X	X	X	X	X	X	X	X
STXM				X			X	X	X
XAS	X	X		X	X	X	X	X	X
STEM		X		X			X	X	X

Table 2.2 : List of copper based samples calcined at different temperatures and related in situ characterisations carried out.

	CuO/Al_2O_3 – 800 °C	CuO/Al_2O_3 – 900 °C	Cu NP	CuO/Al_2O_3 NP – 800 °C	CuO/Al_2O_3 NP – 900 °C
XRD	Calcination in air	3 redox cycles at 700 °C			
XAS		40-50 redox cycles 1. $2.5\%H_2 – 2.5\%O_2$ 2. $2.5\%CO – 2.5\%O_2$ 3. $5\%CH_4 – 2.5\%O_2$ 4. $2.5\%H_2$ – air			
STEM	Redox cycle	Redox cycle up 900 °C	Redox cycles	Redox cycles, Calcination in O_2	Redox cycles, Calcination in O_2

3.1 HG POROSIMETRY

Mercury porosimetry is widely used for the characterisation of supported materials and catalysts to determine their porosity, pore size distribution and pore volume. The porosimeter utilizes a pressurized chamber where mercury (a non-wetting liquid) is forced into the voids of the porous material. With the application of pressure, mercury fills up the larger pores first, then further increase in pressure leads to filling up of the smaller pores. Intrusion pressure values are converted to pore radius using the Washburn equation [4,5].

Both inter-particle pores and intra-particle pores can be evaluated in the range of 3 to 11000 nm. For the supported samples used in this study the porosity of Al_2O_3 is 8.5 nm.

The analyses were conducted in AutoPore IV equipment by Micrometrics. The sample were treated for 2 hours at 250 °C. Intrusion curves were measured up to a maximum pressure of 400 MPa using a mercury surface tension of 485 dyne/cm and a contact angle of 140 °.

3.2 NITROGEN PHYSISORPTION

Nitrogen physisorption is another widely used textural analysis to characterize supported and catalytic material. It employs N_2 as gaseous adsorbate at its boiling temperature (77 K) on the surface of the sample [4,5]. It can be used to evaluate microporosity (< 2 nm) and mesoporosity (2 – 50 nm), as well as specific surface area greater than 1 m^2/g. For catalyst support or supported materials, specific surface area or S_{spe} measurement is typically used as an indicator for catalytic activity or active phase dispersion. The S_{spe} is based on Brunauer-Emmett-Teller (BET) theory which relates to the physical adsorption of gas molecules on a solid surface.

The analyses were performed in a ASAP 2420 apparatus by Micrometrics. To remove any physisorbed species from the sample surface, the samples were pretreated at 350 °C for 3 hours under secondary vacuum (10^{-6} mm Hg).

3.3 POWDER X-RAY DIFFRACTION

X-ray diffraction is a widely available technique for the determination of the crystalline phases present in a sample, following Bragg's law. XRD characterisations were performed using a PANalytical X'Pert Pro Diffractometer in Brag-Brentano configuration with CuKα radiation (λ = 1.54 nm) fitted with X'célérator detector.

For the data acquisition the samples were grounded into powder and compacted in a sample holder. An angle range of 5 to 70 ° 2θ with a step size of 0.033 °, dwell time of 5 s/step were set for the measurements.

The assignments of the crystalline phases were carried out using DIFFRAC.EVA software supported by Crystallographic Open database (COD). The following crystallogaphic information files were used for the phase identifications:Powder diffraction files, PDF 03-065-9026 for metallic copper, PDF 04-007-9767 for Cu_2O, PDF 00-010-0425 for gamma alumina, PDF 04-007-0518 for CuO, PDF 04-015-0578 for $CuAl_2O_4$, PDF 00-035-1401 for $CuAlO_2$ and PDF 01-070-5679 for alpha alumina.

3.4 IN SITU XRD

The *in situ* XRD experiments were conducted using the apparatus "XRK 900" from Anton Paar, available at IFPEN. The presentation of the equipment and the reactor configuration is given in *Figure 2.2*. For the data acquisition the samples were grounded into powder and compacted in a special reactor bed. The data acquisition was carried out in the 30 – 50 ° 2θ range with a step size of 0.033 ° and 0.4 s/step. One diffractogram recording took 4 min.

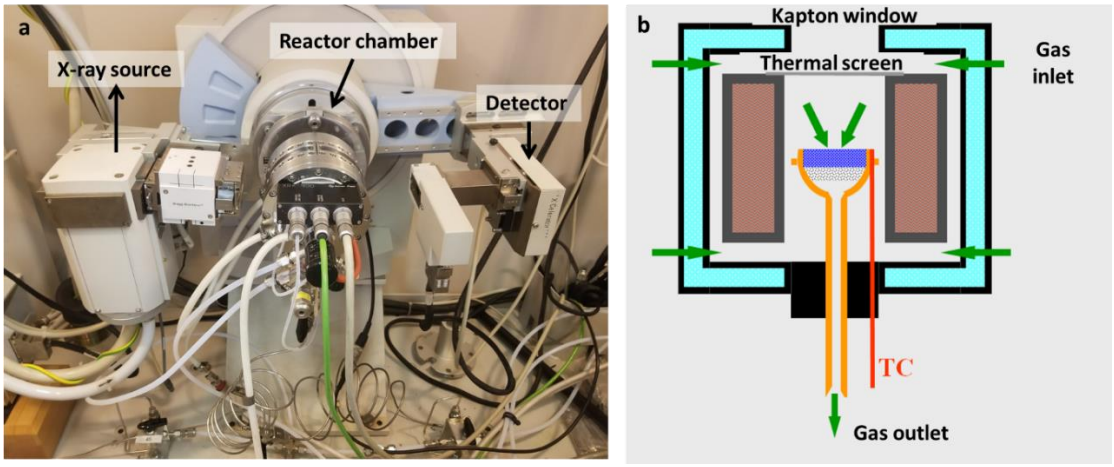

Figure 2.2 : a) presentation of the in situ XRD setup and b) schematic representation of the reactor.

To carry out oxidation and reduction cycles, air and H_2 (100vol%) with a flow rate of 2 L/hour and 1 L/hour were used, respectively. The mixing of the two gases was avoided by purging the system in between the two reactions. With the current reactor setup, it is possible to reach a temperature of 700 °C under hydrogen and a temperature of 1000 °C under N_2 and air.

For ease of understanding, the detail of the experimental parameters and the reaction conditions are provided with the respective experiments and results in chapter 3.

3.5 SCANNING ELECTRON MICROSCOPY

For the analysis of the morphology and the distribution of the copper phase within the support grain, Scanning Electron Microscope (SEM) observations with semi-quantitative elemental phase analysis have been performed. The sample was probed with an accelerated electron beam causing the emission of X-rays, heat and electrons which allows

the imaging of the sample and the determination of the elemental composition. The observations were made in backscattered mode to highlight the chemical contrast. For the semi-quantitative elemental phase analysis, relative measurements uncertainty was calculated on reference minerals. It was estimated at 15 to 20% by mass for contents below 10% and 5 to 15% for contents above 10%.

To image the cross-section of the sample, samples (in form of alumina grains) were embedded in an epoxy resin and polished with a SiC sheet and water. The polished samples were then coated with carbon and painted with silver glue on the side to achieve good conductivity.

The equiment used for these analysis is FEI Nova nanoSEM 450 SEM equipped with Oxford XMAX 80 EDS detector operating at 5 - 15 KeV.

3.6 X-RAY ABSORPTION SPECTROSCOPY (XAS)

Synchrotron based XAS experiments were carried out in two runs employing two techniques. The first set of experiments was carried out in February 2020 using Scanning transmission X-ray Microscopy (STXM). The second set of experiments was carried out in February 2021 using quick X-ray absortion spectrocopy (XAS) technique. Both of the characterisations are based on the priniciple of absorption spectroscopy and excitation of the core-level electron of the probing atom.

The principle of the XAS is presented in Appendix B.1.

3.6.1 Scanning Transmission X-ray Microscopy (STXM)

The STXM-XANES (Scanning Transmission X-ray Microscopy coupled with X-ray Absorption Near Edge Structure) experiments were carried out at the HERMES beamline in SOLEIL snychrotron. It is a spectro-microscopy technique which allows the visualization of the spatial distribution of the chemical and polymorphic phases of the material. The soft X-ray beamline is well adapted to characterize the morphology and the chemistry of both alumina and copper-based samples [6]. The analysis was carried out at Cu L-edge (930 – 960 eV) and Al K-edge (1560 – 1580 eV).

The introduction of the beamline, data acquisition and data treatment protocols are described in chapter 3.

3.6.2 Quick X-ray Absorption Spectroscopy (XAS)

The quick XAS experiments were carried out at the ROCK beamline at the SOLEIL synchrotron. The ROCK beamline is adapted to study the fast chemical reaction with milli second time resolution. The dynamic evolution of the reaction was observed during *operando* experiments, and was completed by post-mortem characterisations conducted on the aged samples. The data acquisitions were carried out at Cu K-edge (8980 – 8990 eV).

The presentation of the beamline, data acquisition and data treatment protocols are described in chapter 4.

3.7 TRANSMISSION ELECTRON MICROSCOPY (TEM)

Nanoscale evolution of the oxygen carriers was characterized *ex situ* and *in situ* using Transmission Electron Microscopy (TEM) and Scanning TEM (STEM). Various imaging, spectroscopic and diffraction modes of TEM were used, encompasing STEM-Bright Field (BF), STEM-High Angular Annular Dark Field (HAADF), Energy Dispersive Spectroscopy (EDS), and Selected Area Electron Diffraction (SAED).

3.7.1 Principle of TEM

The principle of Transmission Electron Microscopy (TEM) is to observe specimens using a highly accelerated beam of electrons as a probe. Indeed, according to the Rayleigh criterion, a specimen can be observed down to its atomic resolution owing to the smaller de Broglie wavelength of electrons (for 200 KeV acceleration voltage the wavelength of the electron beam is in the 1-3 pm range) [7].

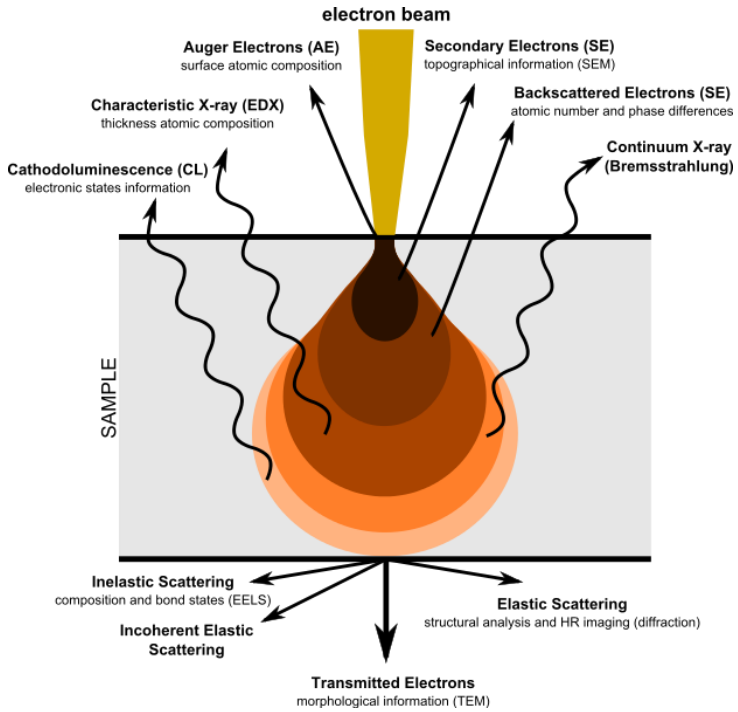

Figure 2.3: Schematic illustration of the phenomena resulting from matter-electron interactions.

The interactions between matter and electrons generate a range of characteristic phenomena. As the electrons pass through the matter, the following interactions take place: direct transmission, scattering, and absorption (*Figure 2.3*). The electrons are either scattered elastically or inelastically. While the elastic scattering is the most dominant phenomenon in TEM when the sample is considerably thin, the effect of inelastic scattering should be taken into account when the sample is thicker (~10 nm or thicker). In an elastic scattering the incident electron beam does not lose energy, whereas inelastic scattering induces loss of energy during the interactions with the specimen. Different interactions give information about the sample; for instance, the morphology of the sample can be formed from the transmitted beam, and structural analysis can be given by the elastic scattering. Furthermore, inelastic scattering gives a range of information due to a multitude of phenomena like ionization, emission of X-rays, secondary electrons, Auger electrons, phonon and plasmon vibrations. Consequently, all these different informations can be collected using dedicated detectors within the electron microscope. Moreover, TEM does not only provide morphological details of a specimen via imaging, but knowledge of its chemical composition, phase analysis, and local structure down to sub-nanometric scale can also be obtained [7].

3.7.2 Conventional TEM and STEM setup

The operational setup of TEM is provided in Appendix B.2. Two imaging modes are typically used: transmission and scanning transmission modes. In a conventional TEM setup, the sample is illuminated by a parallel beam. However, unlike conventional TEM, in STEM the electron beam is focused to a fine spot (with the typical spot size 0.05 – 0.2 nm) which is then scanned over the sample in a raster (*Figure 2.4*).

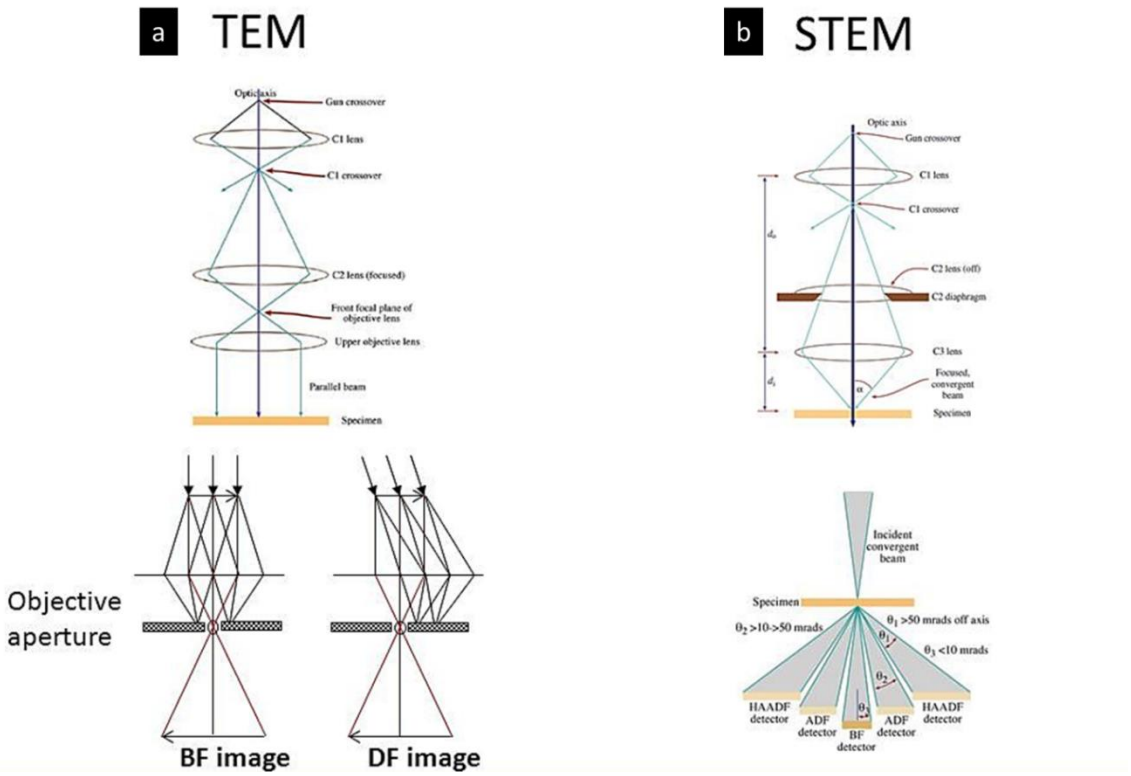

Figure 2.4: Microscope configuration and schematic representation of a) TEM mode with Bright-field (BF) and Dark-field (DF) imaging modes and b) STEM mode and the available detectors for various imaging modes [7].

3.7.3 Imaging Modes

3.7.3.1 Bright-Field (BF) imaging

BF images are formed by selecting the unscattered electron beam using an objective aperture. Therefore, the specimen appears darker where diffraction takes place and location where there is no diffraction appears brighter (*Figure 2.5*).

3.7.3.2 Dark-Field (DF, ADF and HAADF) imaging

DF images are produced using a primary aperture where the unscattered beam is excluded from forming the image. The image contrast comes from the crystallinity, atomic number and thickness of the sample. As a result only scattered electrons are used to produce the images. Only selected electrons are collected depending on the type of detector used such as ADF (annular dark field) where electrons are detected at an angle between 10 and 50 mrad, and HAADF (high angle annular dark field) where the electrons are detected at an angle greater than 50 mrad (*Figure 2.5*). The HAADF contrast is due to the mean atomic number Z of the scanned area. Intensity is proportional to Z^2. Contrast between metallic nanoparticles and oxide supports is enhanced.

3.7.3.3 Electron diffraction

Diffraction images result from Bragg scattering when the beam passes through a crystalline sample. For selected area electron diffraction (SAED) a selected area diffraction aperture is used, which delimits the area of interest, and a diffraction pattern is formed on the back focal plane of the objective lens as an array of dots or a set of diffused rings (*Figure 2.5*). Electron diffraction patterns provide information on the crystalline structure and orientation of the analysed area.

3.7.3.4 Energy dispersive X-ray spectroscopy (EDS)

EDS is used to analyse the elemental composition of a sample. The principle is based on detecting the characteristic X-ray generated from a specimen when the material undergoes interaction with the electron beam.

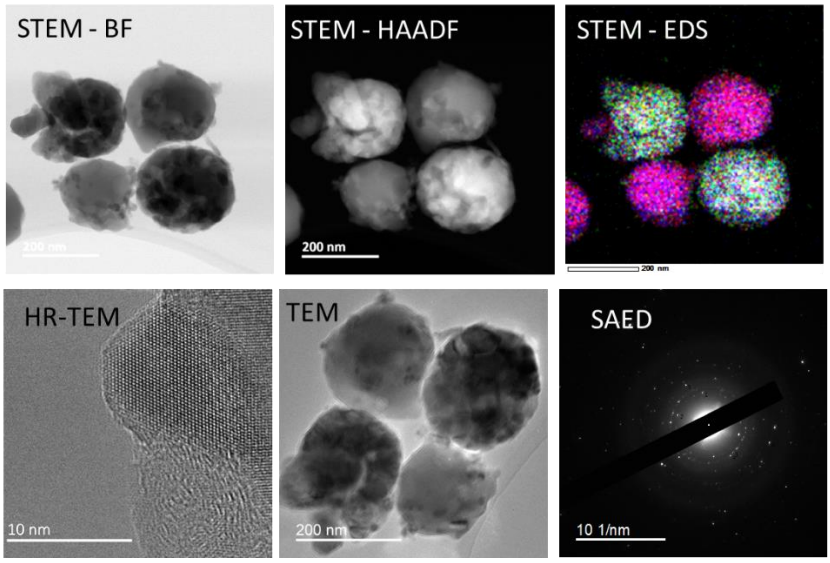

Figure 2.5: Images carried out in different modes of the TEM: From top left to bottom right: STEM-BF, STEM-HAADF, STEM-EDS, HR-TEM, TEM and SAED.

3.7.4 *Ex situ* and post-mortem STEM protocol

The ex situ characterisations were carried out at IFPEN using JEOL JEM-2100 microscope equipped with FEG (Field Emission Gun), high resolution objective lens pole piece and an UltraScan2 detector from Gatan. Post-mortem characterisations were carried out either on the ultramicrotomy-cut samples (described in chapter 3) or by standard TEM sample preparation protocol. The samples were simply grinded, suspended in ethanol and drop-casted on carbon-coated Au or Mo grid.

3.7.5 *In situ* STEM protocol

The dynamic behavior of the oxygen carrier under relevant CLC operating conditions can be monitored using TEM. Two technologies are available to conduct *in situ* STEM obervation in different gaseous environments: 1) the column of the microscope is modified to allow gas environment and 2) the sample is enclosed within a MicroElectroMechanical (MEMs) based cell. The description of the 1st technique is presented in Appendix B.4.

In this study the 2nd technique is used. The *in situ* STEM experiments were mainly carried out using JEOL JEM-2100F microscope (at IPCMS) operating at 200 kV voltage. The electron source is a Schottky type FEG with ZrO-W tip. The microscope is equipped with an electronic probe corrector to correct the spherical aberration, high resolution objective lens pole piece

and an UltraScan 1000 CCD array detector from Gatan. Elemental analysis was performed using Energy Dispersive X-ray Spectroscopy (EDS) probe equipped with silicon drift detector (SDD) with a sensor size of 60 mm^2.

For in situ observations, the Atmosphere system by Protochips was used [8]. The system is composed of the following items:

1. Atmosphere holder
2. Advanced SiC based sample support E-chips
3. Automated gas manifold
4. Clarity Workflow based software package

The Atmosphere sample holder with all the assembling components are presented in *Figure 2.6*. Two O-rings are initially deposited in the tip of the titanium object holder, which stabilize the two chips and ensure the confinement of the cell. Then, the cell is isolated from the microscope by putting the lid (A) secured with three screws. The pair of e-chips where the sample is placed for observation acts as sample support, heating device as well as sealed gas chamber [9,10]. The e-chips are made up of amorphous SiN windows with SiC ceramic thin film heating membrane. The SiC membrane is heated via Joule effect by the gold electrical leads patterned with the flexible circuit on the holder (*Figure 2.6 E*).

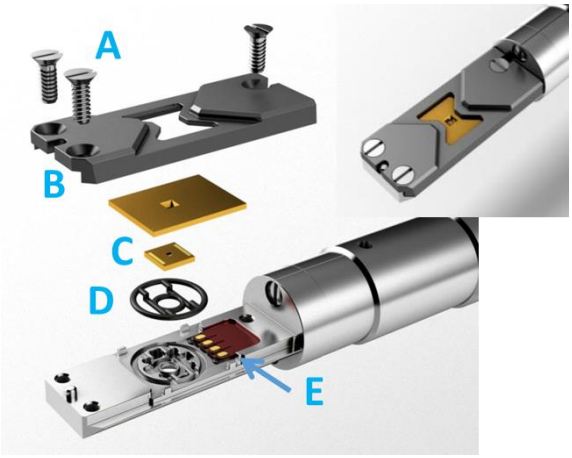

Figure 2.6: Atmosphere holder tip A) lid screws, B) lid, C) small/large e-chip pair, D) o-ring (gasket), E) flex-circuit. Top right inset shows assembled tip [8].

Figure 2.7a displays a schematic view of the enclosed membrane setup. *Figure 2.7b* shows a typical e-chip with 6 transparent holes for observations. 6 holes of ~9 µm diameter are pattered to maximize electrons transparency. The SiN membrane covers the SiC ceramic

membrane to provide vacuum barrier. Besides that, the 6 holes are within the limit of heating area (~90 µm diameter) and the sample must be placed in these holes within the heating region.

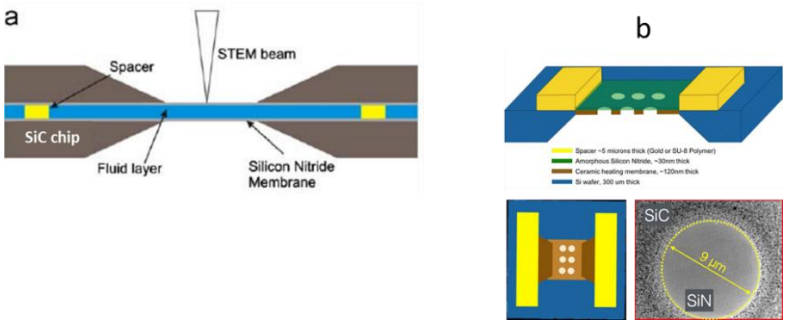

Figure 2.7: Schematic representation of (a) the in situ setup, (b) the thermal membrane (top), e-chip with 6 transparent windows (left), and the BF-TEM image of a transparent "hole" in the SiC ceramic membrane. The hole is covered with the continuous SiN_x membrane where the imaging is performed.

A manifold (*Figure 2.8*) containing three gas tanks is used to receive the purge and reaction gases. A pump is used to purge gases from the reservoirs and the microscope cell. Two experimental tanks from the collector allow the storage and sending of the gases of interest to the sample located in the cell. A third gas tank, which is connected to the cell outlet and the pump, provides a differential pressure to control and adjust the pressure in the experimental tanks. Dedicated software, called "Atmosphere", allows the user to enter pressure / temperature set points and transfer gases from experimental tanks to the cell and remove them. Sending the gases to supply the cell is accomplished through a capillary tube (~ 175 µm internal diameter) made of 316 stainless steel. At the cell outlet, the gases pass through a PEEK polymer tube (PolyEtherEtherKetone). The latter ensures electrical neutrality between the microscope and the sample-holder.

It is possible to work under different neutral (Ar, N_2, He) or reactive (H_2, CO, CO_2, O_2, etc.) atmospheres, both in static and dynamic modes. The operating pressure can be varied from 3 torr (4 mbar) to 760 torr (1 bar).

A maximum temperature of 1000 °C can be reached is this system. The calibration of the individual chips, the heating is controlled with a temperature accuracy of the order of ± 3 °C.

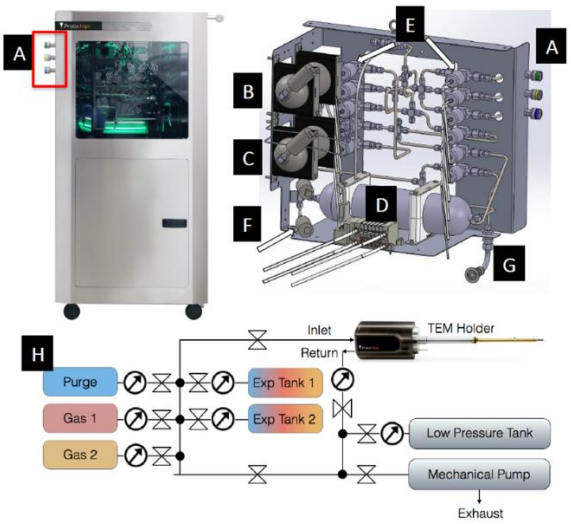

Figure 2.8: Gas feed preparation section: A) 3 gas input ports, B,C) experiment tank 1 and experiment tank 2, D) vacuum tank, E) pressure control valves (11), F) pressure sensor (4), G) gas entry module for control valves, H) vacuum diagram of the gas handling manifold.

Typically the sample preparation step involves first the cleaning of the e-chip in an Ar/O_2 plasma environment for 20 s using a Plasma Cleaner from Gatan. Plasma cleaning helps to get rid of the surface contaminants and to increase the hydrophilicity of the surface for the ease of sample deposition and stabilisation during the reaction. The sample is crushed carefully to achieve a very fine grind which is a requisite in order to reduce the undesired sample-electron interactions and to prevent the rupturing of the SiN_x membrane. The grinded sample is then suspended in cyclo-hexane and sonicated for 10-15 minutes. Achieving the optimum sample concentration in the solution is a crucial step. Too much sample may pierce the SiN_x membrane during the sealing or block the tranmission of the electron beam. Too little quantity reduces the chance of finding the sample in the transparent membrane areas. A range of solvents has been tested, and cyclo-hexane was found to be optimum in terms of surface wetting and drying. About 1 – 2 µL of the solution was deposited on the chip and dried under air for 10-15 minutes. During the preparation step the e-chip was checked multiple times for any cracks or fissures. Once the e-chips are assembled in the sample holder, the sample holder is introduced in the microscope column and checked for any possible gas leakage. The system is purged 2-3 times with Ar at 1.33 mbar to remove any contamination.

In the next four chapters various characterisation of the materials are presented along with their interpretations.

4 REFERENCES

[1] Diego L.F. de, García-Labiano F., Adánez J., Gayán P., Abad A., Corbella B.M., María Palacios J. Development of Cu-based oxygen carriers for chemical-looping combustion, *FUEL*, 2004, **83,** 13, 1749-1757. DOI: 10.1016/j.fuel.2004.03.003.

[2] A. Lambert, A. Tilland, W. Pelletant, S. Bertholin, F. Moreau, I. Clemençon and M. Yazdanpanah. Performance and degradation mechanisms of CLC particles produced by industrial methods, *FUEL*, 2018, **216**, 71-82. DOI: 10.1016/j.fuel.2017.11.115.

[3] M.T. Izquierdo, F. García-Labiano, A. Abad, A. Cabello, P. Gayan, L.F. de Diego and J. Adanez. On the optimization of physical and chemical stability of a Cu/Al2O3 impregnated oxygen carrier for chemical looping combustion, *Fuel Processing Technology*, 2021, **215**.

[4] DavorLončarević Ž. *Industrial Applications of Nanomaterials*. Elsevier, 2019.

[5] J. Lynch. *Physico-chemical Analysis of Industrial Catalysts: A practical guide to characterisation*, 2003.

[6] X. Ye, J. E. Schmidt, R-P. Wang, I. K. van Ravenhorst, R. Oord, T. Chen, F. de Groot, F. Meirer and B. M. Weckhuysen. Deactivation of Cu-Exchanged Automotive-Emission NH3-SCR Catalysts Elucidated with Nanoscale Resolution Using Scanning Transmission X-ray Microscopy, *Angewandte Chemie (International ed. in English)*, 2020, **59**, 2-10.

[7] D. B. Williams and C. B. Carter. *Transmission Electron Microscopy : A textbook for material science*.

[8] Protochips. Protochip Atmosphere. https://www.protochips.com/products/atmosphere/.

[9] L. F. Allard, W. C. Bigelow, M. Jose-Yacaman, D. P. Nackashi, J. Damiano, S. E. Mick. A new MEMS-based system for ultra-high-resolution imaging at elevated temperatures, *Microscopy research and technique*, 2009, **72,** 3, 208-215. DOI: 10.1002/jemt.20673.

[10] L. Allard, S. Overbury, W.C. Bigelow, M. Katz, D. Nackashi and J. Damiano. Novel MEMS-Based Gas-Cell/Heating Specimen Holder Provides Advanced Imaging Capabilities for In Situ Reaction Studies, *Microscopy and Microanalysis*, 2012, **18,** 4, 208-215.

Chapter 3:
Grain-scale migration of copper

1 INTRODUCTION

CuO supported on Al_2O_3 has been studied as an oxygen carrier for CLC and other looping processes. Much of the initial problem related to the agglomeration of the OC and de-fluidisation of the reactor bed has been resolved by adjusting the preparation step, reaction conditions and most importantly an optimum CuO content of 10-20 wt% for the CuO/Al_2O_3 oxygen carriers [1]. Nevertheless, fines formation and eventual fragmentation of the material remains a challenge to achieve a longer lifetime of the CuO/Al_2O_3 OC. As mentioned in chapter 1, section 3.2.2, these two degradation phenomena have been linked to the migration of the copper phases within and in/out of the support. The migration of copper inside the oxygen-carrier particles during CLC cycles is not well understood, especially considering the variations in the reaction parameters used in different studies. Therefore, it is important to carry out a systematic study to understand the material ageing by varying only the temperature and the number of cycles, keeping constant all the other reaction parameters. Furthermore, little is known regarding the stepwise evolution of the material as most of the studies report the bulk phases characterised by XRD and the texture and copper repartition by SEM, coupled eventually with EDS. However, no information on the nature of the phases is achieved by SEM.

The knowledge of the spatial distribution of the chemical elements and the polymorphic phases within the support can help us understand the underlying mechanism by which the evolution in the material occurs. It is crucial to make an association between the different phases and how their transformation affects the overall morphology of the oxygen carrier and vice versa. To that end, the simultaneous realization of the phases and the morphology was achieved by employing STXM, and complemented by SEM, STEM, XRD and XAS analyses.

The objective of the STXM characterisation is to understand the redox cycling dependent phase transition in the CuO/Al_2O_3 oxygen carrier. The identification of copper coordination states and of the spatial distribution of copper in the alumina grain aim to achieve better insights into the interaction between the active phase and the support as a function of material ageing (number of redox cycles). One of the goals was to correlate the different alumina and copper species with their respective morphologies perceived through the SEM and STEM characterisation. Eventually, this investigation aims to track the migration of the copper phases and identify the underlying mechanism concerning the phase transitions induced by the temperature-dependent oxidation, reduction as well as the number of redox cycles.

2 EXPERIMENTAL APPROACH

First, the fresh 13 wt% CuO/Al_2O_3 oxygen carriers calcined at 700, 800 or 900°C were characterised thoroughly using various standard techniques. The samples were then cycled in the TGA 50 and 200 times at their respective calcination temperatures.

The morphological and copper concentration changes were followed using SEM, and STEM. The information on phase transitions was obtained using XRD and STXM-XANES at Cu L and Al K-edge Table 2.1 in chapter 2 presents the list of samples and the techniques used to characterise the samples.

2.1 SCANNING TRANSMISSION X-RAY MICROSCOPY: PRINCIPLE AND EXPERIMENTAL SET-UP

2.1.1 Principle

Scanning transmission X-ray microscopy (STXM) is a spectro-microscopic technique comprising a combination of spatially resolved spectroscopy and imaging with spectral sensitivity. A schematic diagram of the STXM is shown in Figure 3.1, consisting of the main components of the equipment. In STXM the focalization of the X-ray beam is achieved using Bragg-Fresnel lenses (Zone Plate) to a small spot. The first diffraction order is filtered by using an order sorting aperture (OSA). The size of the focal point depends on the properties

of the FZP ($\Delta r \sim 1.22\ \delta_r$, where δ_r is the width of the outermost zone), adjusted by changing the width of the zone plate. The size of the beam determines the spatial resolution. The sample is positioned and scanned through the focal spot of the X-ray beam using interferometrically controlled positioning and the transmitted beam is obtained in raster mode (in x,y direction), point by point. The transmitted beam (image) is measured by a detector composed of a phosphor converter of X-ray to visible light using a high-performance photomultiplier tube (PMT). The transmitted intensity is recorded for each pixel.

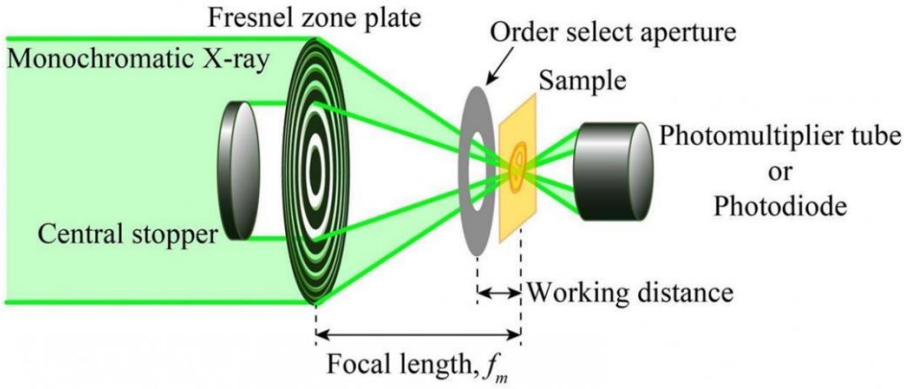

Figure 3.1: Schematic representation of the optical system of STXM. Image credit: National Institute of Natural Sciences Japan.

Absorption spectra were recorded for each sample position by recording images at a sequence of energies. The absorption spectra are in the XANES region of XAS. The imaging contrast in STXM is based on the relative intensity of the XANES peaks of the species present in the sample. Using Beer-Lambert's law, the transmitted photon intensity is converted to an optical density (OD), given by equation 3.1.

$$OD = \ln(I_0/I_t) \qquad \text{Equation 3.1}$$

Here, I_0 is the incident X-ray beam and I_t is the transmitted intensity through the sample. The OD is related to the sample thickness and the density, expressed by equation 3.2.

$$OD = \mu(E)\rho t \qquad \text{Equation 3.2}$$

where μ, E, ρ and t represent the mass absorption coefficient (inherent characteristics of material) at X-ray energy E, density, and thickness of the sample, respectively.

2.1.2 Beamline presentation

The STXM analyses were carried out on the HERMES beamline of the SOLEIL synchrotron [2]. The HERMES beamline contains two types of microscopes, STXM and XPEEM (X-ray photo emitted electron microscopy). The beamline utilises a beam in the energy range of 2.5 eV to 2.5 keV and covers the K-edge of light elements (C, N, O..), L-edge of transition metals, M-edge of rare earth and K-edge of Si, S and P. The beamline uses two undulators: for low energy of up to 600 eV and higher energy range of 0.5 - 2.5 keV.

The STXM equipment is presented in Figure 3.2. The energy range of the HERMES beamline is particularly advantageous to probe both the copper and aluminium environments, thus providing a complete picture of the sample's local environment. In the current experiments, the sample was probed at the Cu L-edge and Al K-edge. For the imaging a Fresnel zone width of 34 nm was used to provide a theoretical beam size of about 42 nm.

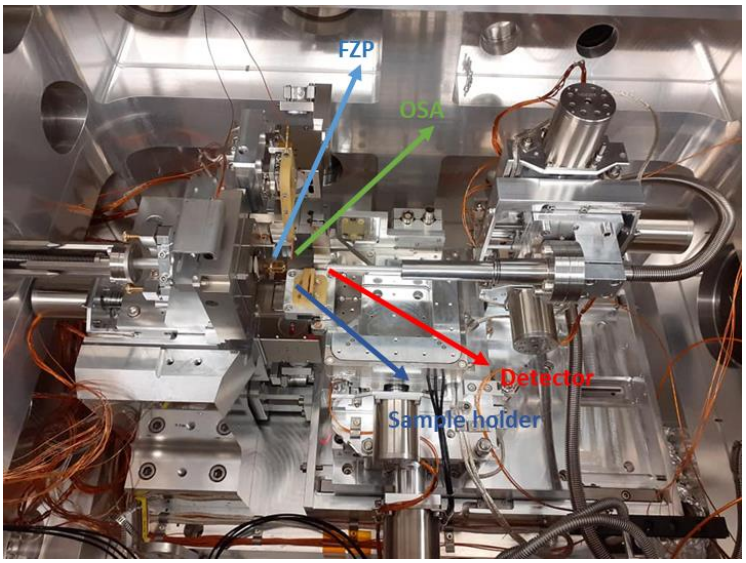

Figure 3.2: STXM, HERMES beamline, showing FZP (Fresnel Zone Plate), Order Sorting Aperture (OSA), sample holder and detector.

2.1.3 Data acquisition and analysis

Three types of scans were performed: lines, map (at specific energies) and stack (range of energies). The line scan mode records a line at a set of energy points specific to the sample, resulting in a spectrum at each data point along the line. The line scan mode was used for the reference materials.

For the samples, two modes of acquisition called “map” scan with a higher spatial resolution (10 x 10µm, 0.030 µm step-size) and “stack” (4 x 4 µm, 0.08 µm step-size) were used. The step size is the distance between the adjacent pixels that determines the spatial sampling of the image.

The mapping mode acquires images only at pre-selected energies.

A stack consists in a series of images acquired at a given energy range and allows to obtain a 3D dataset in x, y, and energy dimensions. Thus, each pixel contains a full spectrum.

The scan parameters for the different modes are provided in Table 3.1. The energy step Cu L-edge scan was adjusted to be faster at the beginning and end of the energy range, 0.5 eV for 920-929 eV and 960 – 970 eV. Between 929 and 960 eV which is the edge range, a shorter step-size was used: 0.15 eV from 929 – 940 eV, 0.35 eV for 940 – 950 eV and 0.15 eV for 950- 960 eV. For the Al K-edge, an energy step of 0.18 eV was used for the whole 1570 – 1600 eV energy range. For better statistical precision, a dwell time of 3 ms was used for both edges.

Table 3.1: Scan parameters used for the data acquisition in different scan modes.

Scan	Energy (eV)	Dimension (µm)	Step size (µm)	Dwell time (ms)	Total duration
Line	Cu: 920 – 970	5	0.1	1	14 min 30 s
	Al: 1570 – 1600	5	0.1	1	14 min
Map	Cu: 920, 933, 934, 936.6, 940.4 and 950	10 x 10	0.03	3	1 h 44 min
	Al: 1570, 1578, 1581, 1584 and 1591	10 x 10	0.03	3	1 h 27 min
Stack	Cu: 920 – 970	4 x 4	0.08	3	1 h 50 min
	Al: 1570 – 1600	4 x 4	0.08	3	1 h 30 min

Additionally, I_0 was measured during the acquisition of the line and stack. The I_0 area used for the I_0 acquisition was chosen without the presence of the feature of interest, typically, in an area with polymer resin of the sectioned samples.

Data treatment was carried out using AXis2000 software developed by Prof. Adam Hitchcock from McMaster University in Canada [3].

The line scan data was treated by taking the I_0 into account, to acquire the reference spectra.

Since the mapping was carried out at specific energies, typically at the absorption energy of the known phases, in order to provide images with absorption contrast corresponding to each component present in the sample, the individual maps can be compiled and presented in a colour composite map.

As demonstrated in Figure 3.3 the first step of stack data treatment involves drift correction by aligning the series of images, using a built-in function called “Jacobsen stack analyses” based on the Fourier cross-correlation method. Using the I_0 measurement as a reference point for the X-ray photon transmission, the transmission images are converted into optical density (OD) images. A typical stack contains about 2000-3000 spectra and usually less than 6 statistically significant species. In order to extract the principal components in the area of interest, spectra can be extracted as single component from an OD stack and used as a reference to generate the spatial distribution of the respective chemical components either using the Singular Value decomposition (SVD) or stack fit method. Both SVD and stack fit functions use the SVD algorithm.

Sets of component maps can be combined into colour composite maps displaying the relative spatial distribution of the individual components.

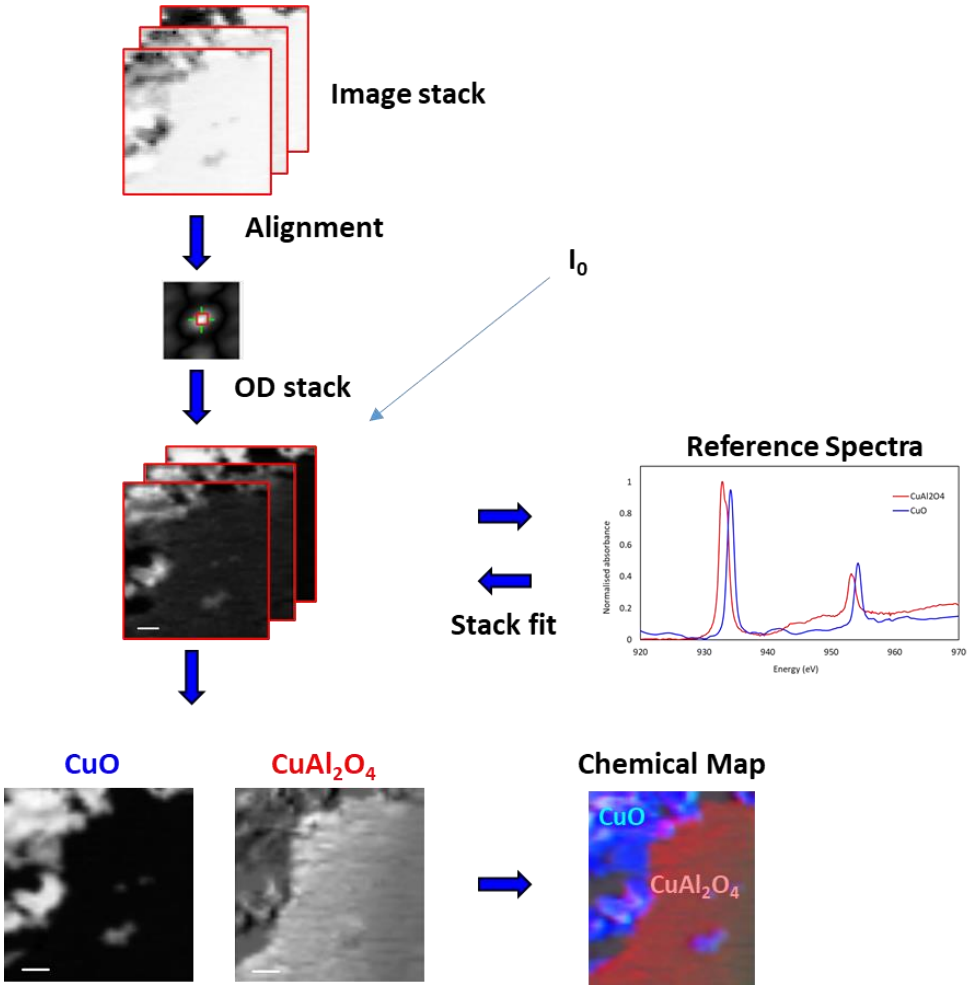

Figure 3.3: Outline of processing of a STXM stack process of CuO/Al_2O_3 sample. The image stack is measured in transmission mode by STXM at Cu L-edge (920 – 960 eV), stack alignment using "Jacobsen stack analysis" method, conversion to OD stack considering I0 background, generated component spectra from reference, stack fit using reference spectra, composite chemical map (blue is CuO, red is $CuAl_2O_4$).

2.1.4 Sample preparation

Soft X-rays are known to interact strongly with matter implying that the sample thickness is an important consideration. Strong absorption can modify the spectral shape and the apparent optical density due to non-linear absorption [4]. Therefore, the sample should be thin enough for the transmission of the beam and to avoid absorption saturation. The concentration of the sample, the choice of the edge and the edge energy determine the adequate thickness of the sample. For our samples the thickness was calculated to be less ~100 nm, using the Centre for X-ray Optics (CXRO) website [5].

Hence, ultramicrotomy sectioning was performed on capsules of impregnated bead powders in TEM resin to a thickness of 100 nm and placed on Au (200 mesh, carbon coated)

TEM grids. The region of interest was identified using SEM in STEM-HAADF imaging mode (~2 nm resolution @ 40kV) in SEM. In addition to the thickness, the sectioning of the sample preserved the structure of the support grain and the spatial information of the different copper-alumina phases.

Oxidation-sensitive samples such as reference metallic Cu, Cu_2O, and the cycled oxygen carrier in reduced state, were prepared inside a glovebox. The samples were crushed and deposited on a 50 nm thickness SiN_x membrane and sealed with another SiN_x membrane.

The other reference samples were simply crushed and deposited on an Au grid and glued to the sample holder with silver glue. An example of the sample holder is shown in Figure 3.4.

Figure 3.4: Sample holder with glued TEM grid.

2.1.5 Reference samples

As mentioned earlier, the copper-based phases present in OC are composed of Cu^0, Cu_2O, CuO, $CuAl_2O_4$, and $CuAlO_2$. In terms of Cu reference samples, we analysed Cu^0, CuO and $CuAl_2O_4$. At the time of the experimental run, pure $CuAlO_2$ compound had not been synthesised. Similarly, the spectrum of the Cu_2O sample could not be obtained due to high absorption by the SiN_x membrane and the atmosphere resulting from inadequate sample preparation. Nevertheless, the absence of Cu_2O or $CuAlO_2$ did not affect the data treatment protocol. The oxidised samples contained CuO and $CuAl_2O_4$. The reduced samples were composed of only metallic Cu, as deduced from the post-mortem and *in situ* XRD analysis (detailed in the result section dealing with *in situ* XRD).

For alumina phases, three references were considered: α-Al_2O_3, γ- Al_2O_3, and $CuAl_2O_4$ (synthesis protocol provided in Chapter 2). Other transition aluminas were not taken into account due to difficulties to acquire pure phases and most often these phases exist as mixtures [6,7].

2.1.5.1 Cu L-edge spectra

The reference spectra of CuO, $CuAl_2O_4$ and Cu^0 are shown in Figure 3.5.

The main peak of metallic copper is at 936.5 eV. The CuO phase where Cu is in the +2-oxidation state can be identified by the two main peaks at ~934.2 eV and ~954 eV assigned to $Cu2p_{3/2}$ (L_3) and $2p_{1/2}$ (L_2) electrons into empty d-states, respectively. The characteristic features of CuO include the broad peak at ~941.5 eV and a separation of about 19.8 eV between the L_3 and L_2 peaks [8]

For the $CuAl_2O_4$ reference sample, the intensities at 932.9 eV and ~953 eV correspond to the L_3 and L_2 transitions, respectively. $CuAl_2O_4$ is a spinel-like structure that contains both CuO_4 and CuO_6 species. Therefore, the L_3 peak displays a shoulder at ~933.6 eV which is assigned to the CuO_6 species [9].

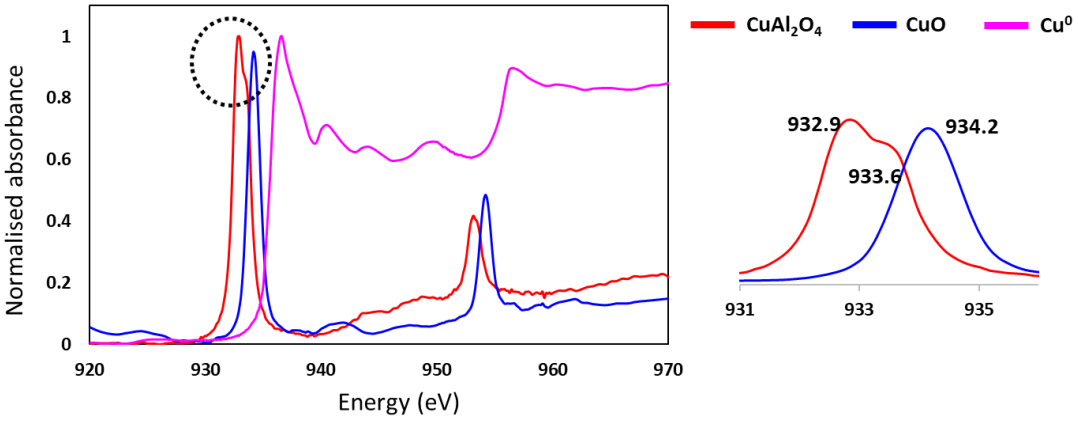

Figure 3.5: Spectra of the reference samples at Cu L-edge for CuO (blue), $CuAl_2O_4$ (red) and Cu^0 (pink).

The spectral features (number of peaks, distance between the peaks and the energy difference between two species) remain similar compared to the literature [10]. We only have a shift of a few eV, possibly resulting from the calibration of the detector. The spectral resemblance is deemed to be more important to identify the different species present. The difference between the L_3 peaks of $CuAl_2O_4$ and CuO is about ~1.3 eV. The difference

between the tetrahedral and the octahedral sites in $CuAl_2O_4$ is about 0.7 eV. The sensitivity of the XANES allows to distinguish the corresponding species.

2.1.5.2 Al K-edge spectra

For the Al-containing references, three distant peaks are observed corresponding to the tetrahedral (AlO_4) and octahedral (AlO_6) coordination environments [7]. Depending on the proportion of the coordination sites, the relative peak intensities will change. Therefore, the different Al-containing samples can be identified from the site-occupancy dependent peak intensities as shown for the Al-containing reference samples in Figure 3.6. The assignment of the peaks and the corresponding transitions are summarized in Table 3.2.

The α-Al_2O_3 only contains Al octahedrally coordinated with 6 oxygen atoms, displaying two prominent peaks at 1580.8 and 1584.9 eV [11].

The γ-Al_2O_3 phase is typically considered to have a spinel-type structure composed of octahedral and tetrahedral Al^{3+} coordination sites [12–14]. The first peak at 1579 eV displays the contribution from the tetrahedral occupancy. The peaks at 1581.0 and 1584.0 are assigned to similar transitions as those of α-Al_2O_3 arising from the octahedral environment [11].

For the $CuAl_2O_4$ sample, the peak assignments are like γ-Al_2O_3 transitions since both γ-Al_2O_3 and $CuAl_2O_4$ are spinel-type structures. The proportions of Al with octahedral vs tetrahedral coordination change since the spinel structure accommodates Cu-ions as well [7]. With regards to the AlO_4:AlO_6 species, in $CuAl_2O_4$ there is less AlO_4 compared to γ or θ-Al_2O_3.

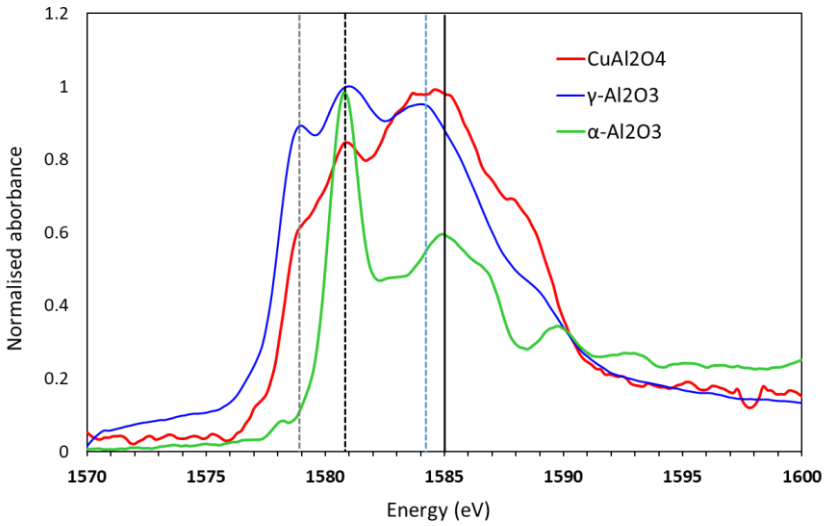

Figure 3.6: Spectra of the reference samples at Al K-edge for α-Al_2O_3 (green), γ-Al_2O_3 (blue) and $CuAl_2O_4$ (red).

Table 3.2: Al K-edge features and assignments of the energies.

Compound	Energy (eV)	Assignment
α-Al_2O_3	1578.0	1s → 2s-σ* (a_{1g})
	1580.8	1s → 3p-σ/π* (t_{1u})
	1584.9	1s → 3d-σ* (t_{2g})
γ- Al_2O_3	1579.0	1s → 3p-σ/π* (t_2)
	1581.0	1s → 3p-σ/π* (t_{1u})
	1584.0	1s → 3d-σ* (t_{2g})
$CuAl_2O_4$	1578.9	1s → 3p-σ/π* (t_2)
	1580.8	1s → 3p-σ/π* (t_{1u})
	1584.5	1s → 3d-σ* (t_{2g})

Our reference spectra are in good agreement with the XANES features of different alumina polymorphs and $CuAl_2O_4$ reported in the literature by Kato et al. [7]

The transition of the γ-Al_2O_3 phase to δ-Al_2O_3 and eventually θ-Al_2O_3 leads to increased occupancy of the tetrahedral sites by the Al^{3+} cation. The peak corresponding to the AlO_4 species, at ~1579 eV would display higher relative intensity as a function of the phase

transition. In contrast, the occupation of the Cu^{2+} ions in the spinel structure of the copper aluminate drives the Al^{3+} from the tetrahedral sites to the octahedral sites.

3 RESULTS AND DISCUSSIONS

3.1 FRESH 13 WT% CUO/AL_2O_3

3.1.1 Identification of the phases

3.1.1.1 Ex situ XRD analysis of fresh samples

The information on the possible phases present in the oxygen carrier calcined at 800 and 900°C are first provided by XRD (Figure 3.7).

The sample calcined at 800 °C contains a mixture of CuO, copper aluminate and transition alumina. The XRD spectra of the CuO/Al_2O_3 – 700 was not carried out but from literature and other characterisation (SEM and XAS), the sample should be composed of the same species as CuO/Al_2O_3-800. However, due to the diffusion-controlled nature of the reaction between CuO and Al_2O_3, at lower temperature of calcination it is expected to have higher a proportion of unreacted CuO.

In the sample calcined at 900 °C, no CuO peak was detected, indicating its full conversion into $CuAl_2O_4$ phase. A contribution from transition aluminas is observed but it is difficult to pin-point the exact polymorph present in the sample as γ-Al_2O_3 and δ-Al_2O_3 are difficult to distinguish [6]. The presence of α-Al_2O_3 is also detected at this calcination temperature.

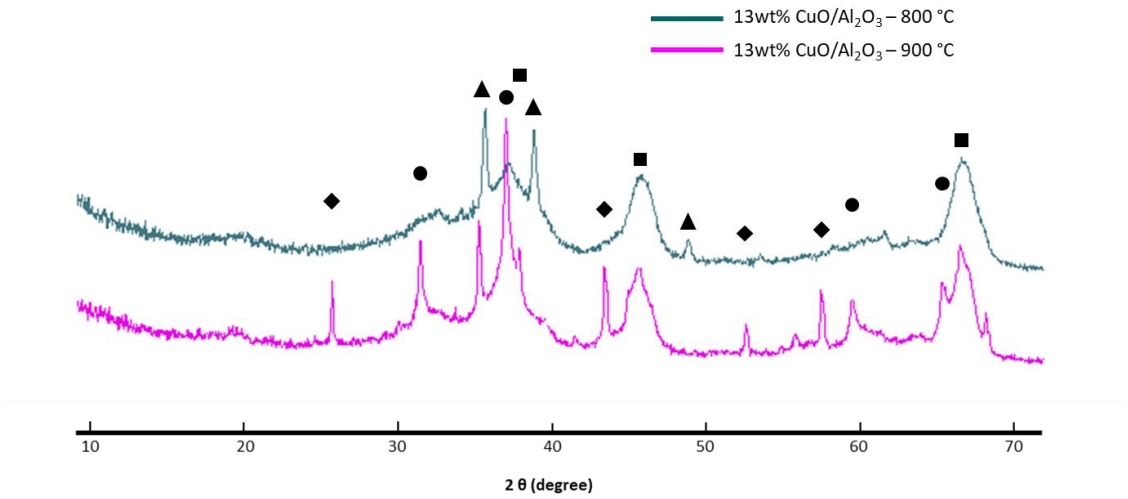

Figure 3.7: XRD patterns of CuO/Al_2O_3 samples calcined at 800 and 900 °C with CuO (▲), $CuAl_2O_4$ (●), γ-Al_2O_3 (■), and α-Al_2O_3 (◆).

Analysis of the as obtained diffractograms allows us to evidence significant differences with the copper aluminate features according to the calcination temperature. CuO/Al_2O_3-900 exhibits sharp peaks corresponding to well crystallized phases. In contrast, the main $CuAl_2O_4$ peaks in CuO/Al_2O_3-800 °C sample are much broader, indicating a much less crystalline phase..

The γ-Al_2O_3 phase is a defective spinel structure and, its diffraction pattern is similar to the cubic spinel structure of the $CuAl_2O_4$ phase [12]. The formation of $CuAl_2O_4$ results from the occupation of Cu^{2+} cations in the available positions in the structure of γ-Al_2O_3 [15,16]. The percentage of copper incorporated in the spinel structure of alumina will depend on the calcination temperature and its duration. In the CuO/Al_2O_3-900 °C sample, in which the CuO phase is not observed, we can consider that all the copper was incorporated in the alumina. The insertion of the Cu^{2+} increases the lattice parameter shifting the peak position towards lower 2θ value. Therefore, the peaks position relative to the $CuAl_2O_4$ would change depending on the amount of copper present in the copper aluminate.

As the total amount of copper during the impregnation amounts to 10.4 wt % compared to 35 wt% copper in the stoichiometric $CuAl_2O_4$, the copper aluminate in this study is non-stoichiometric, with theoretical formula $Cu_{0.24}Al_{2.51}O_4$. Since the sample is heterogeneous in composition, the sub-stoichiometric spinel will be referred to as $Cu_xAl_yO_4$

3.1.1.2 Effect of calcination from 800 to 900 °C – in situ XRD

To identify the origin of the α-Al_2O_3 formation, the CuO/Al_2O_3 – 800 °C sample has been subjected to calcination from room temperature to 900°C under air and the evolution was followed by *in situ* XRD to identify the possible phase transitions in the temperature range of 800 – 900 °C.

The sample was first heated from room temperature to 780 °C at a rate of 5 °C/min and, subsequently, at a rate of 1 °C from 780 °C to 800 °C. As the temperature reached 800 °C, heating was carried out in stages of 10 minutes of heating at every 10 °C, at 1 °C/min rate. X-ray diffraction acquisition was conducted from 25 to 70 ° in 2θ with a step size of 0.083 °/s. With this setup and experimental conditions, 1 diffractogram was acquired every 10 minutes.

Figure 3.8 displays the diffractograms obtained at every 10 °C, from 800 to 900 °C during the annealing of the oxygen carrier. As mentioned already in section 3.1.1.1, the sample is composed of CuO and a mixture of sub-stoichiometric $Cu_xAl_yO_4$ and transition aluminas. Above 830 °C, the peaks corresponding to the CuO phase start to decrease, disappearing completely as the temperature reached 860 °C. The disappearance of the CuO phase is linked to the diffusion of copper in the alumina matrix to form copper aluminate. The initial sample is composed of poorly crystalline Cu-aluminate and after the calcination at 900 °C, the peak positions of the (400) and (440) Miller indices of alumina (46 ° and 66 ° in 2θ, resp.) moved to lower 2θ, gradually reaching towards the peaks positions of the aluminate phase. The displacement of the peak position to lower 2θ is linked to the increase in the d-spacing and the lattice parameter due to the addition of the Cu^{2+} in the alumina spinel.

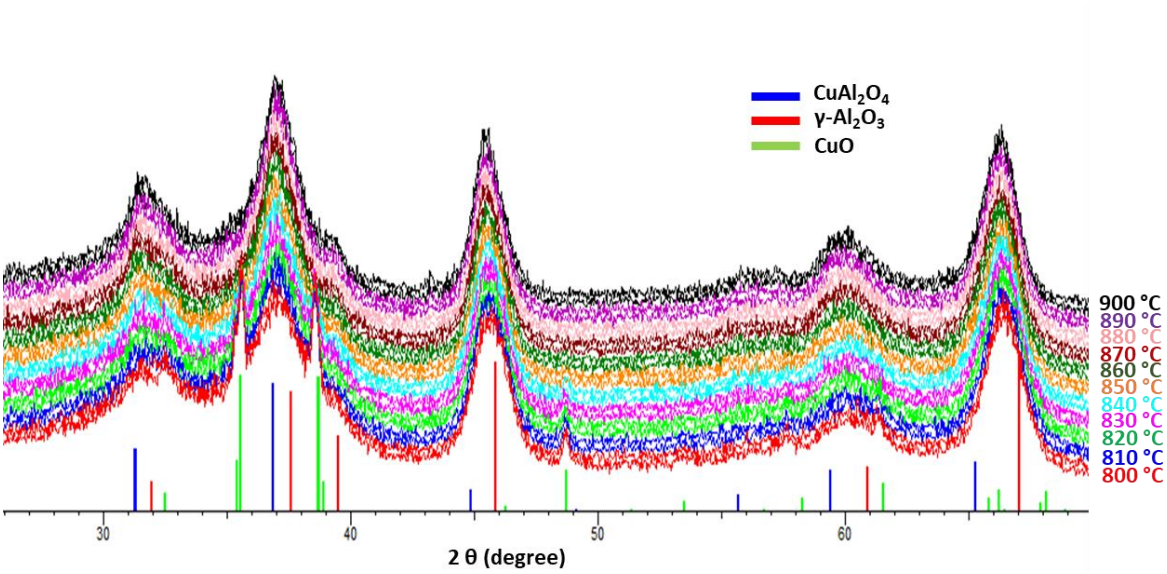

Figure 3.8: In situ XRD during the thermal annealing of the CuO/Al_2O_3-800 °C sample from 800 °C to 900 °C, under air.

The presence of α-Al_2O_3 phase was not observed in these conditions. To detect the α-Al_2O_3 phase by XRD, the sample should probably have been heated at 900°C for a longer duration.

3.1.1.3 XAS analysis at Cu K-edge of fresh samples

The three fresh samples calcined at 700, 800 and 900°C were characterised by XAS at Cu K-edge. The spectra were fitted with a linear combination fitting (LCF) algorithm, using CuO and $CuAl_2O_4$ as reference spectra (Figure 3.9). The details of XAS and LCF is presented in Chapter 4. An example of the LCF results is presented on Figure 3.10 (LCF of the fresh OC calcined at 800°C). From spectral deconvolution, it is possible to calculate the proportions of CuO and $CuxAl_yO_4$. As presented in Table 3.3, the proportion of $CuxAl_yO_4$ increases with the calcination temperature. The CuO/Al_2O_3-900 sample is solely composed of copper aluminate in terms of the copper phase. These quantitative results are in agreement with XRD analysis.

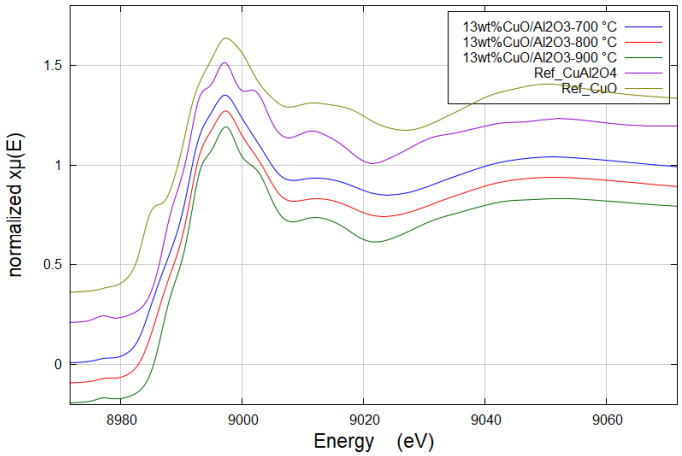

Figure 3.9: XAS spectra of fresh CuO/Al_2O_3 samples calcined at 700, 800 and 900 °C.

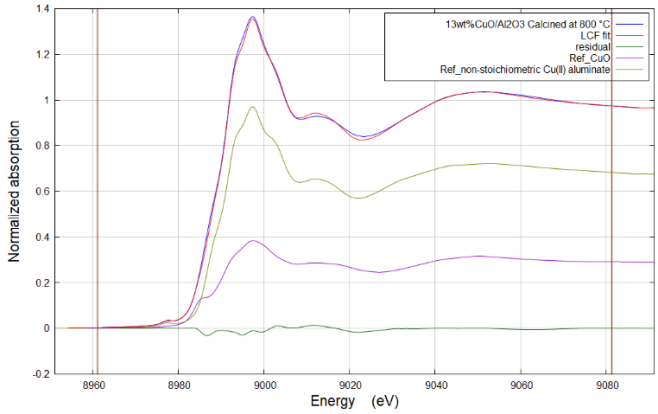

Figure 3.10: LCF fitting of the 13 wt%CuO/Al_2O_3 - 800 °C sample.

Table 3.3 provides a summary of the different phases identified from the XRD and XAS characterisation.

*Table 3.3: Presence of different copper and alumina phases in the calcined sample from XRD and XAS. * XRD of alumina not shown here.*

	Al_2O_3*	CuO/Al_2O_3–700 °C	CuO/Al_2O_3 – 800 °C	CuO/Al_2O_3 – 900°C
XRD	$\gamma - Al_2O_3$		CuO, $Cu_xAl_yO_4$, transition alumina	$Cu_xAl_yO_4$, transition alumina, α-Al_2O_3
XAS Cu K-edge	-	CuO: $Cu_xAl_yO_4$ = 45 : 55	CuO: $Cu_xAl_yO_4$ = 30:70	$Cu_xAl_yO_4$

3.1.2 Morphology and the spatial distribution of the components

SEM imaging with semi-quantitative elemental mapping was performed on the fresh samples to observe the morphology and the distribution of the copper-containing phase. The SEM images of the sample calcined at 700 °C are not shown as there is little difference with the sample calcined at 800°C.

3.1.2.1 Fresh sample calcined at 800°C

The cross-section SEM image and the corresponding Cu-concentration map of the CuO/Al_2O_3-800 are displayed in Figure 3.11a and b. Figure 3.11 c and d are representative areas of the edge and the interior of the grains, respectively.

Many Cu-rich crystals can be visualized at the periphery of the grains, as illustrated in Figure 3.11b and indicated within the blue circle in Figure 3.11c. These crystallites range from 2 to 10 µm in size, and the absence of aluminium signal in these Cu-rich areas indicates the presence of copper oxide.

The average percentage of copper inside the grain was estimated to be around 10 wt%, equivalent to the theoretical percentage of the impregnated copper. In the elemental map acquired on the whole grain, differences in the copper percentages indicate that the sample is not locally homogeneous. Higher resolution images (Figure 3.11c and d) display variations in the greyscale. The copper percentage appears to follow a concentration gradient from higher percentage at the edge of the grain (lighter grey area highlighted within the red circle, in Figure 3.11c) to lower percentage away from the edge (darker grey area indicated by the pink circle, Figure 3.11c).

In Figure 3.11d, spherical nanoparticles of 25 – 100 nm are observed in places located within the white circles. Speculated from the lighter grey/white shade, these nanoparticles contain a higher Cu concentration. Due to the presence of both Al and Cu phases, it is difficult to deduce whether these particles are CuO.

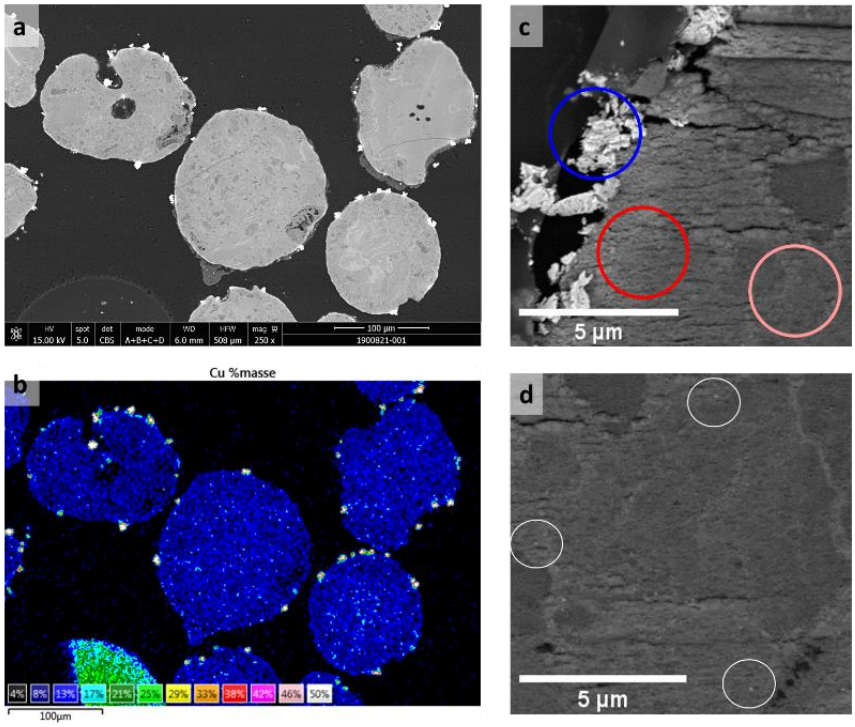

Figure 3.11: CuO/Al_2O_3-800 °C sample: SEM image of the cross-section (a) and the corresponding copper concentration map (b). STEM – HAADF (in SEM) images of the ultramicrotomy cut sample (same area as the STXM analysis), represents the edge (c) and the interior (d) of the grain.

Complementary information using STXM – XANES allowed the identification of phases. Figure 3.12 presents data extracted from a "stack". The extracted spectra at Cu L-edge from the different regions show the presence of CuO (in blue #1-3) with the L_3 peak at 934 eV and $Cu_xAl_yO_4$ (in red #6-8) at 933 eV. Areas in green shaded circles (#4 and 5) contain both phases.

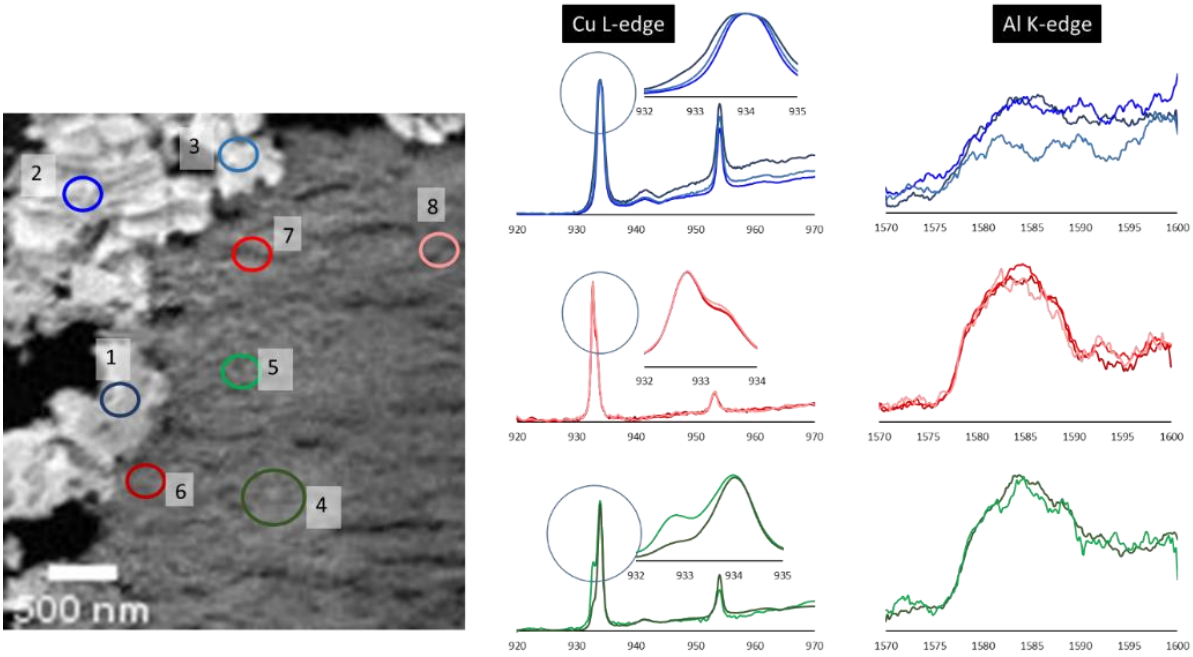

Figure 3.12: Spectral contribution from individual areas corresponding to the coloured circles in the SEM image of fresh CuO/Al_2O_3-800 °C sample. "stack" mode.

At Al K-edge, the blue spectra show absorption corresponding to the different alumina/aluminate phases, but the noise level is too high and is likely to arise from the proximity to the Cu-aluminate phase.

It is clear if we compare these CuO containing areas (blue) to the interior of the grain which is made of Cu-aluminate (red), the Al-spectra show features corresponding to the aluminate reference spectrum.

The reference spectra of the gamma alumina phase was used as component to solve the Energy dataset. However, no contribution from the gamma alumina phase was found. Hence, it can be concluded that the Al K-edge signal is solely coming from the Cu-aluminate phase and any discrepancies arising from one area to another is linked to the different proportions of copper within the alumina structure. The presence of different copper proportions can be visualized in the Cu L-edge features in Figure 3.12: the intensity of the shoulder peak at 933.6 eV (inset with red spectra at Cu L-edge) is relatively higher than the main peak at 933 eV for area-8 compared to areas 6 and 7.

The areas represented in green circles contain mixed phases of CuO and Cu-aluminate as seen from the relative peak intensities at 933 and 934 eV. They seem to contain particles of

CuO as observed from the blue areas within the aluminate matrix in the composite map in Figure 3.13. Due to the low spatial resolution of the SEM, these small CuO particles could not be observed.

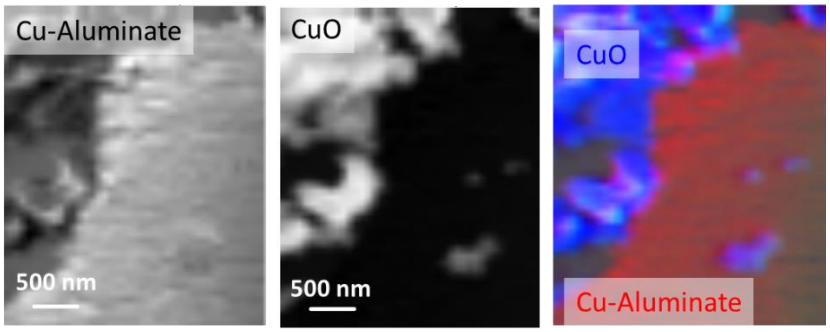

Figure 3.13: Coloured STXM map of fresh CuO/Al_2O_3-800 °C sample, with the spectral contributions pf the individual components mentioned on the image. "stack" mode.

3.1.2.2 Fresh sample calcined at 900°C

The sample calcined at 900 °C contains copper rich edges and areas in the centre with darker contrast according to the SEM image presented in Figure 3.14 a. The EDS elemental map in Figure 3.14 b displays a Cu-rich edge with 15 to 30 wt% copper. The interior of the grain contains an average of 8-10 wt% Cu. According to Figure 3.14 c and d), the edge of the grain contains higher porosity and denser areas with darker and lighter contrast, respectively. In comparison, the interior of the grain (Figure 3.14 e) appears to be dense with relatively uniform greyscale.

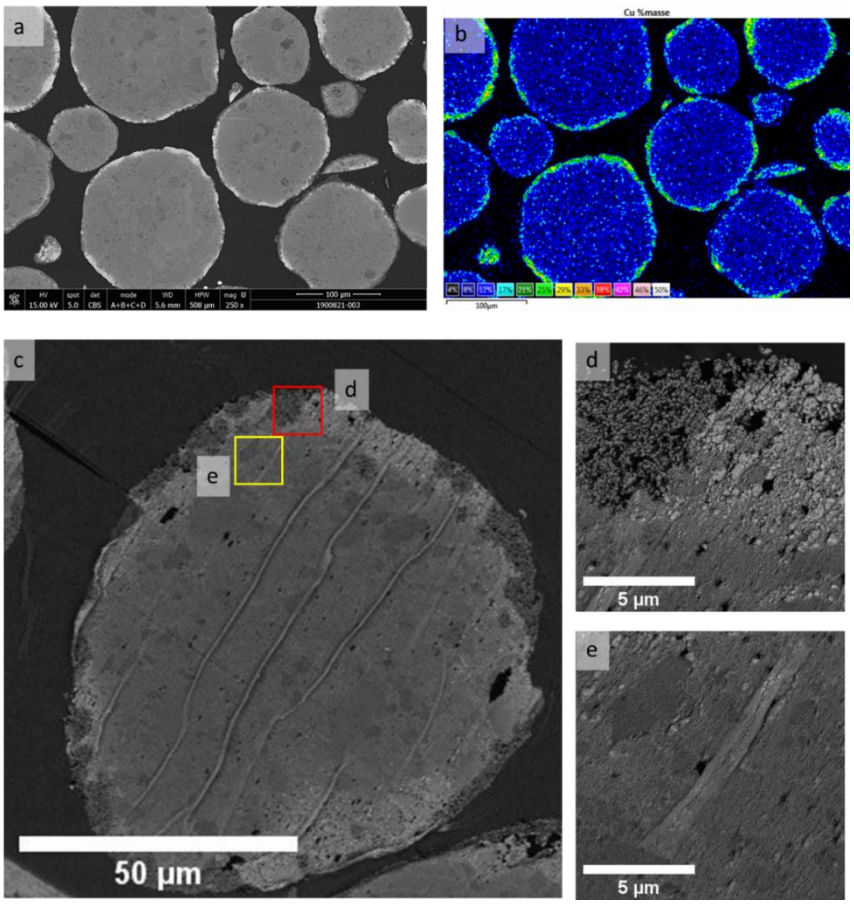

Figure 3.14: a) Cross-section SEM image of the CuO/Al_2O_3-900 °C sample and the corresponding Cu concentration map (b), c) STEM-HAADF (in SEM) image of the UMT cut fresh CuO/Al_2O_3-900 °C sample, where the STXM analyses have been carried out, d and e) higher magnification images of the areas marked in red and yellow in c).

From the STXM map in Figure 3.15, the alpha alumina phase is marked in green (also visible in darker contrast in the SEM image in Figure 3.15). The area in red is identified as Cu-aluminate phase (lighter contrast area in Figure 3.15 SEM).

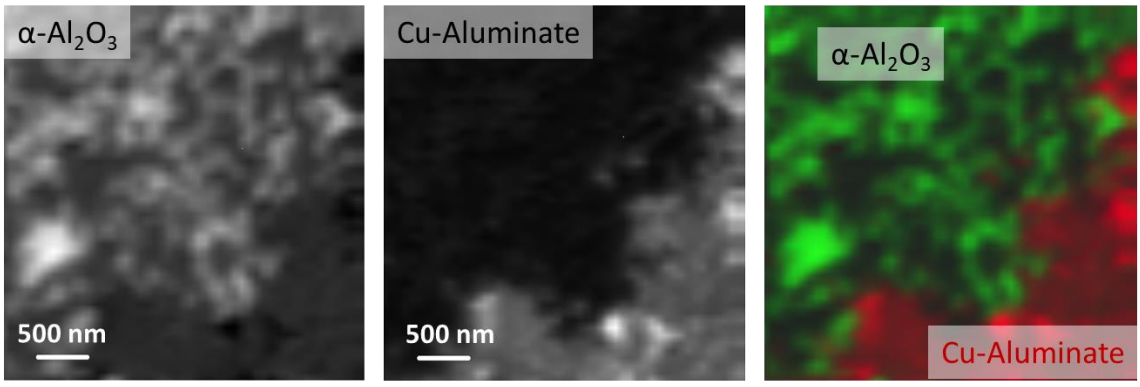

Figure 3.15: Coloured STXM map of fresh CuO/Al_2O_3-900 °C sample, with spectral contributions from the individual components mentioned on the image. Acquisition in the "stack" mode.

Figure 3.16 presents data extracted from a “stack”. Three types of areas seem to be present. For areas 1&2, the spectral feature at both Cu L-edge and Al K-edge show resemblance to the reference spectra of the aluminate phase.

For areas 3 & 4, the Al K-edge spectra show features corresponding to alpha alumina; at Cu L-edge the signal corresponding to the alpha alumina phase appears to be noisy, likely due to the proximity of the copper phase within the sample thickness.

Areas marked as 5 and 6 contain both Cu-aluminate and alpha alumina phases. The presence of the alpha phase is only noticeable in Al K-edge which is convoluted with the signal from the aluminate phase. The distinguishable features appear to be a shoulder at around 1579 eV, and relative higher intensity of the peak at 1584 eV (highest intensity peak of the aluminate phase) compared to the peak at 1581 eV (higher intensity peak for alpha phase).

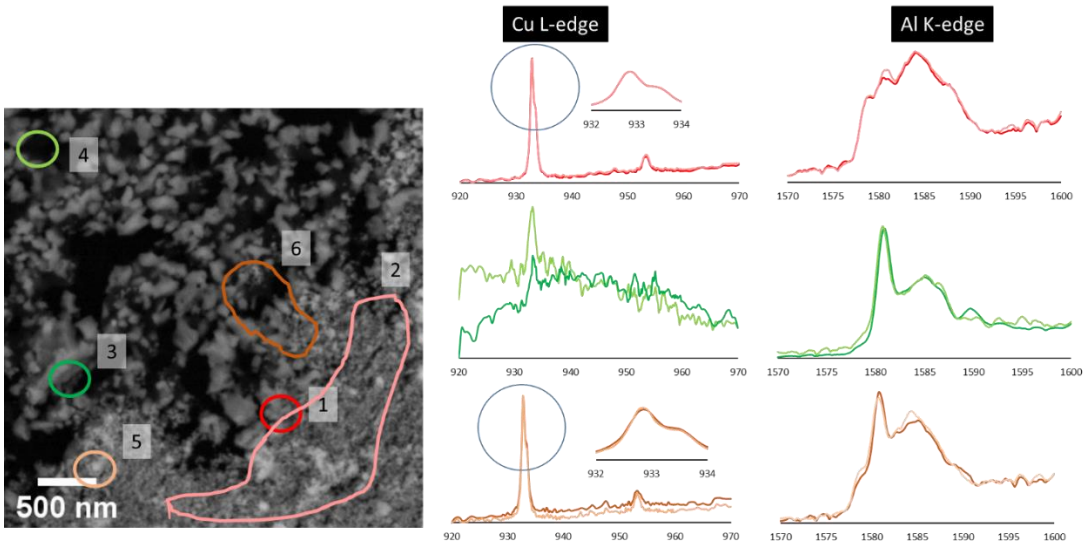

Figure 3.16: Spectral contributions from individual areas corresponding to the coloured circles in the SEM image of fresh CuO/Al_2O_3-900 °C sample. “stack” mode.

3.1.2.3 Comparison of fresh samples calcined at 800 and 900°C

The Cu L-edge spectral feature of the $Cu_xAl_yO_4$ phase of the fresh samples calcined at 800 and 900 °C is compared with the stoichiometric $CuAl_2O_4$ reference to estimate the proportions of octahedral and the tetrahedral Cu-environments. The spectra are presented in Figure 3.17. The ratio of the peak areas of the two peaks at 932.9 and 933.6 eV

corresponds to the amount of CuO_4 and CuO_6, respectively [9]. Visually, the relative intensity at 933.6 eV appears to be higher in the reference $CuAl_2O_4$ compared to the two samples. The two samples have similar spectral profiles; the calcination temperature of the samples does not seem to affect the relative intensities of the two peaks. The two L_3 peaks were fitted with Lorentzian function taking the range of 930 – 936 eV. The ratio of CuO_4:CuO_6 is estimated to be 55:45 for the $CuAl_2O_4$ sample. The percentage of CuO_6 is slightly higher in our reference compared to the typical ratio of 60:40 reported in the literature [9,15]. The 13 wt% CuO/Al_2O_3 samples display an average of 60:40 of CuO_4:CuO_6.

The values found in our study contradicts the observation of Shimizu et al. where they reported a CuO_4:CuO_6 ratio of 50:50 and 30:70 copper aluminate samples containing 16 and 8 wt% of copper [9].

The difference between the two studies could stem from the synthesis protocol used for the copper-aluminate synthesis. Nevertheless, the site occupancy by the Cu^{2+} cation may be significant in the light of Al occupancy and the ratio of AlO_4 and AlO_6 environments. The occupancy of both Cu^{2+} and Al^{3+} cations will be reviewed in section 3.3.

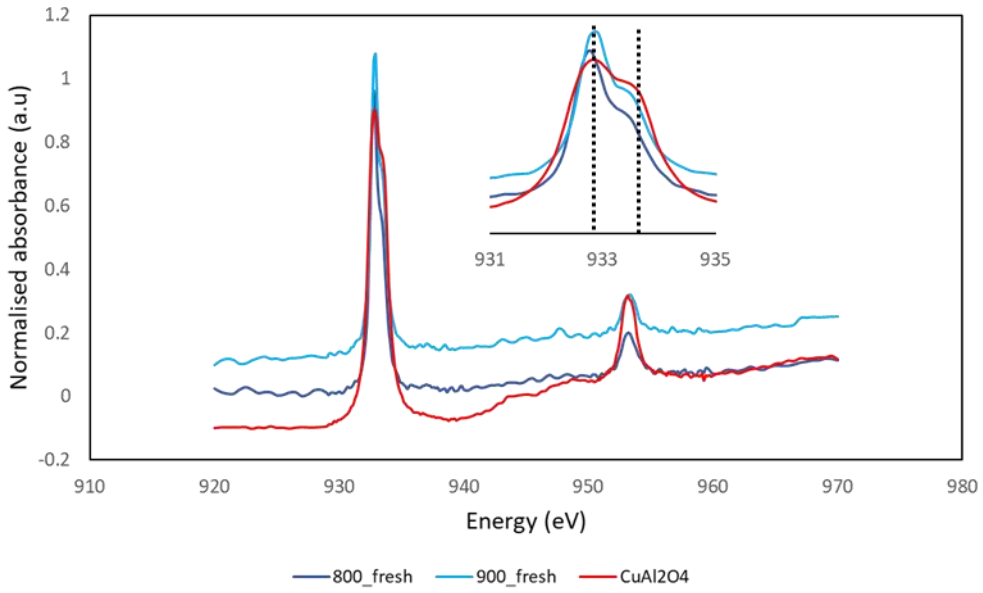

Figure 3.17: Cu L-edge spectra of the fresh and reference $CuAl_2O_3$.

3.1.3 Morphology of the fresh samples at nanoscale

The ultramicrotomy cut samples were characterised in STEM-EDS at IFPEN. Figure 3.18 a-b shows the overview of the support grain. Figure 3.18 c-d and e-f display the edge and the

interior of the grain, respectively. The edge contains large crystallites composed of Cu and Al. In some areas copper-rich particles are also observed. The inside of the grain is made of small particles containing both Cu and Al. The copper is found to be 8-10 wt%, similar to the value deduced by SEM.

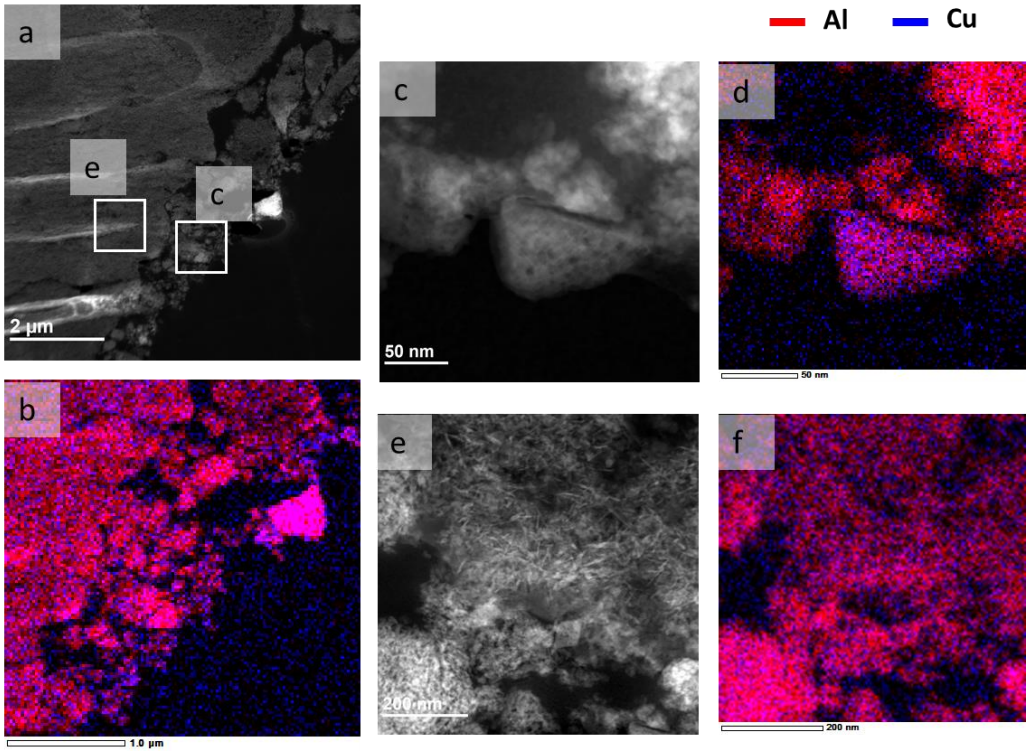

Figure 3.18: STEM-EDS of fresh CuO/Al_2O_3- 800 °C sample.

The STEM-EDS images of the fresh CuO/Al_2O_3-900 °C sample is presented in Figure 3.19. Three different areas are noted.

Figure 3.19 c (edge of the grain) depicts elongated particles containing both Cu and Al, occasionally rich in copper. This areas appears to be porous compared to the areas in Figure 3.19 e and g.

Area e contains a mixture of large Al-rich particles and Cu-Al particles of smaller size and less porosity. The Al-rich particles are α-Al_2O_3 as we know from the STXM characterisation the α-Al_2O_3 phase is located at the edge of the grain and it is porous. The α-Al_2O_3 particles have rounded edge shape.

In contrast, the interior of the grain (Figure 3.19 e) is less porous and composed of aggregated platelets of $Cu_xAl_yO_4$ phase.

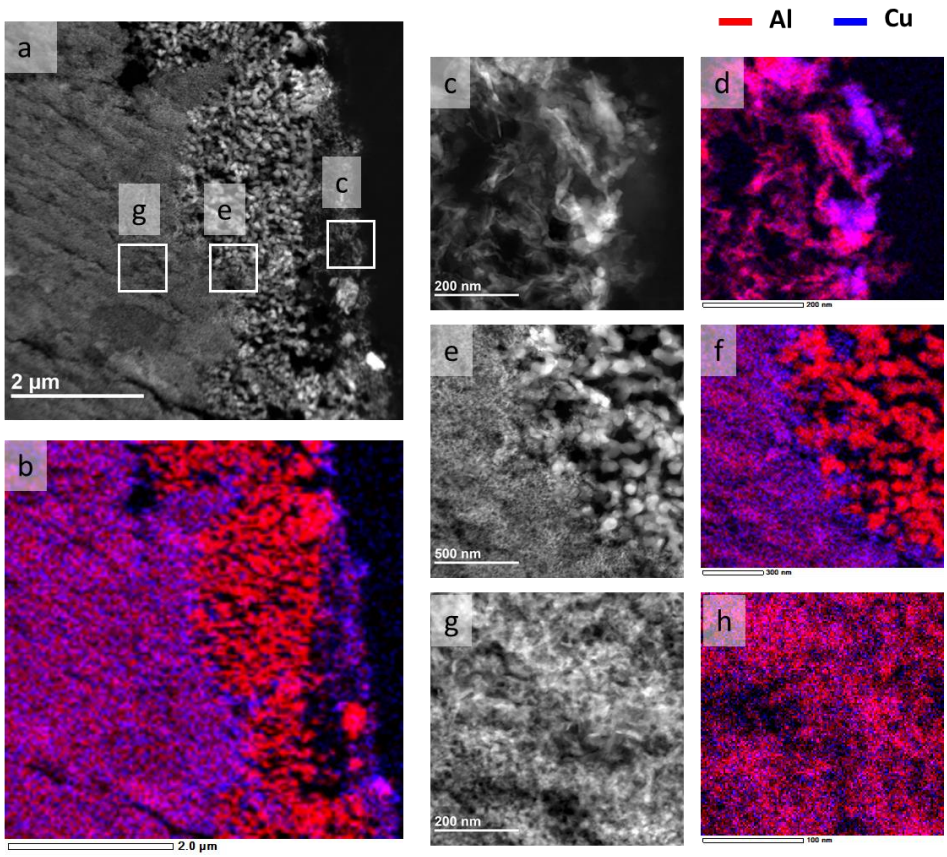

Figure 3.19: STEM-EDS of fresh CuO/Al_2O_3- 900 °C sample.

3.1.4 Conclusion

From the imaging techniques (STXM, SEM and TEM) performed on the fresh samples, we are now able to assign typical morphologies to the chemical phases.

Large particles with distinct tubular shape, exhibiting a porous structure, correspond to the α-Al_2O_3 phase. At the reaction temperature of up to 900 °C, the CuO or metallic copper do not interact with the α-Al_2O_3. The α-Al_2O_3 particles are mostly free of any copper, except for the existence of large Cu/CuO crystallites.

The alumina and copper aluminate matrices are composed of small aggregates of particles displaying a dense texture. The percentage of copper within the non-stoichiometric aluminate varies from one area of the sample to another.

3.2 EFFECT OF CYCLING TEMPERATURES

3.2.1 Redox cycles at 700 °C

For this set of samples, the SEM of the fresh sample CuO/Al_2O_3-700 is not shown in as much as its morphology is similar to that of fresh CuO/Al_2O_3-800 sample. The fresh sample was cycled in TGA at 700°C during 50 or 200 cycles.

3.2.1.1 After 50 cycles

After being subjected to 50 redox cycles at 700 °C, the oxygen carrier displays the presence of copper oxide, copper aluminate ($Cu_xAl_yO_4$) and transition alumina, according to XRD data, in Figure 3.20. According to LCF of the XAS data, the proportion of CuO and Cu_xAl_yO is 40:60.

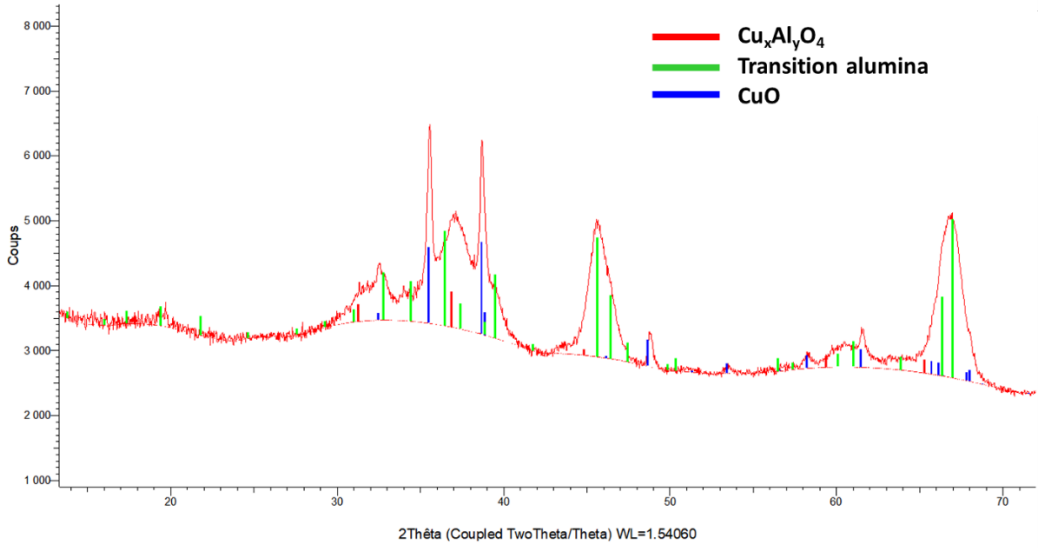

Figure 3.20: XRD of CuO/Al_2O_3-700 °C sample, after 50 cycles.

The SEM and STEM-EDS images of the cycled sample are presented in Figure 3.21. The oxygen carrier appears to be composed of a copper-rich grain edge with distinct presence of large CuO crystals (Figure 3.21c, particles in blue) and copper-aluminate with a high percentage of copper (Figure 3.21c, particles in purple with mixture of Al and Cu species). The interior of the grain contains a matrix of alumina with very small percentage of copper (<2 wt%). In this mixed Cu-Al matrix some dispersed copper-based particles and large aggregates of copper based particles are observed according to Figure 3.21d-e. The copper-rich particles range from 30 to 100 nm. The size of the aggregates is about 1-3µm. In some areas in the matrix, large pores of 50 – 100 nm are noted (for instance, Figure 3.21d-e). The

mixed Cu-Al particles appear to be sintered in those areas compared to the compact areas. The large porosity formation is presumably the result of particle sintering in those areas.

The exact composition of the Cu-rich aggregates could not be discerned since they are either found on or close to the alumina matrix, thus contribution of Al is inevitable in the EDS characterisation. However, from the morphology and concentration of the particles, they are likely to be CuO crystallites while the matrix is made of non-stoichiometric aluminate-transition alumina mixture. No alpha alumina is observed either in XRD or in the SEM characterisation.

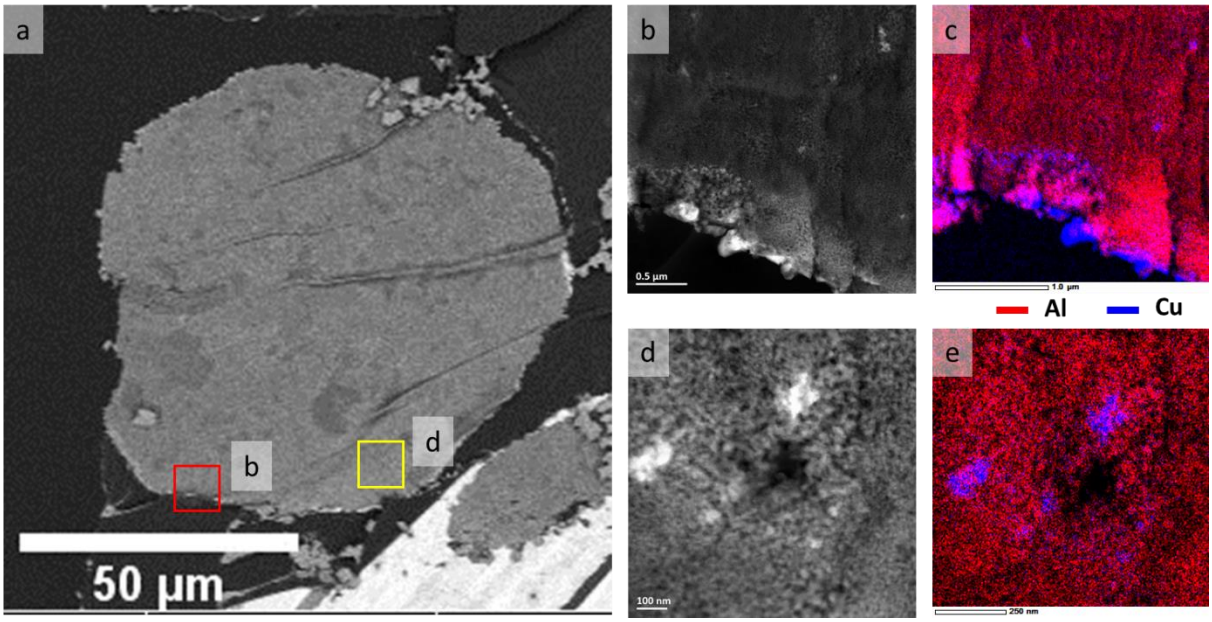

Figure 3.21: a) SEM image of the ultramicrotome cut sample cycles after 50 times at 700 °C. STEM-HAADF image (d and e) and EDS map (c and e) of the red and yellow squares marked on a, representing the edge and interior of the grain, respectively.

3.2.1.2 After 200 cycles

After 200 cycles at 700 °C, the material is composed of copper-aluminate, CuO and α-Al_2O_3 according to the diffractograms displayed in Figure 3.22.

The peaks corresponding to the $Cu_xAl_yO_4$ phase appear to be significantly sharper than the sample after 50 redox cycles. Additionally, the position of the aluminate peaks appears to be closer to that of the stoichiometric aluminate phase. Which means that Cu gradually moved to form a phase closer to $CuAl_2O_4$, while the remaining alumina turned into alpha phase. The longer duration of heating could cause the sintering of the copper-aluminate phase.

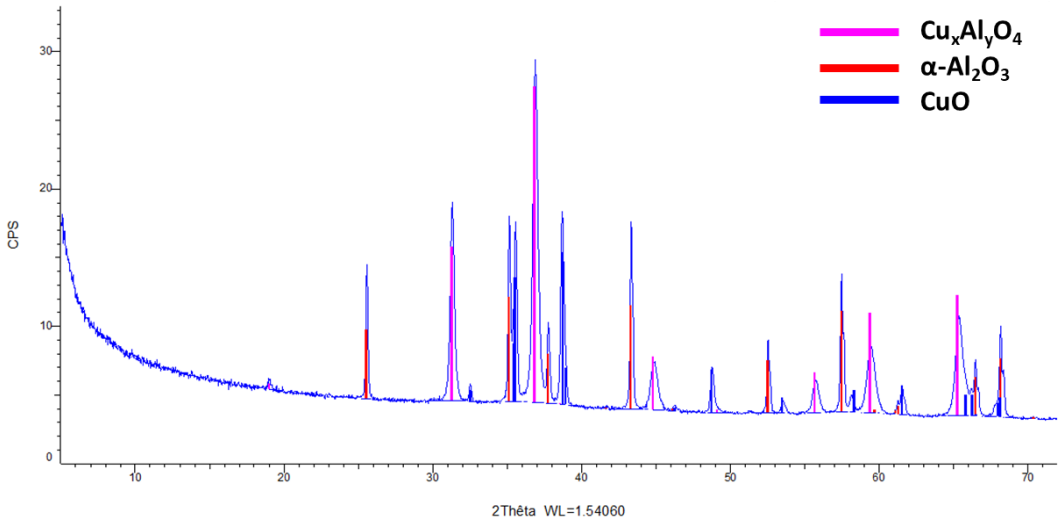

Figure 3.22: XRD of CuO/Al_2O_3-700 °C sample after 200 cycles.

Figure 3.23a-b displays the overall changes in the morphology and copper distribution in the oxygen carrier, after 200 cycles. Figure 3.23c shows the interior of the grain where four different features are seen:

Red circle: spherical regions of 1 – 2 µm diameter, with a 6-8 wt% copper concentration; inside these spherical regions some dense particles (pointed with white arrow) with 15-30 wt% copper are also noted. Likely, agglomerates of CuO particles. Blue circle: single particles of 60 – 200 nm diameter, possibly CuO. Yellow circle: support matrix with higher porosity compared to the rest of the grain matrix, presumably composed of α-Al_2O_3. The grey matrix containing 2-3 wt% of copper.

Figure 3.23d, displays the edge of the grain. Two areas are pointed in the grain, yellow arrow: contains numerous agglomerates of Cu-based crystals (CuO) in the size range of 5 to 20 µm. Red arrow: concentration gradient with high Cu content of 30 – 40 wt% to lower concentration, from the edge to the interior of the grain.

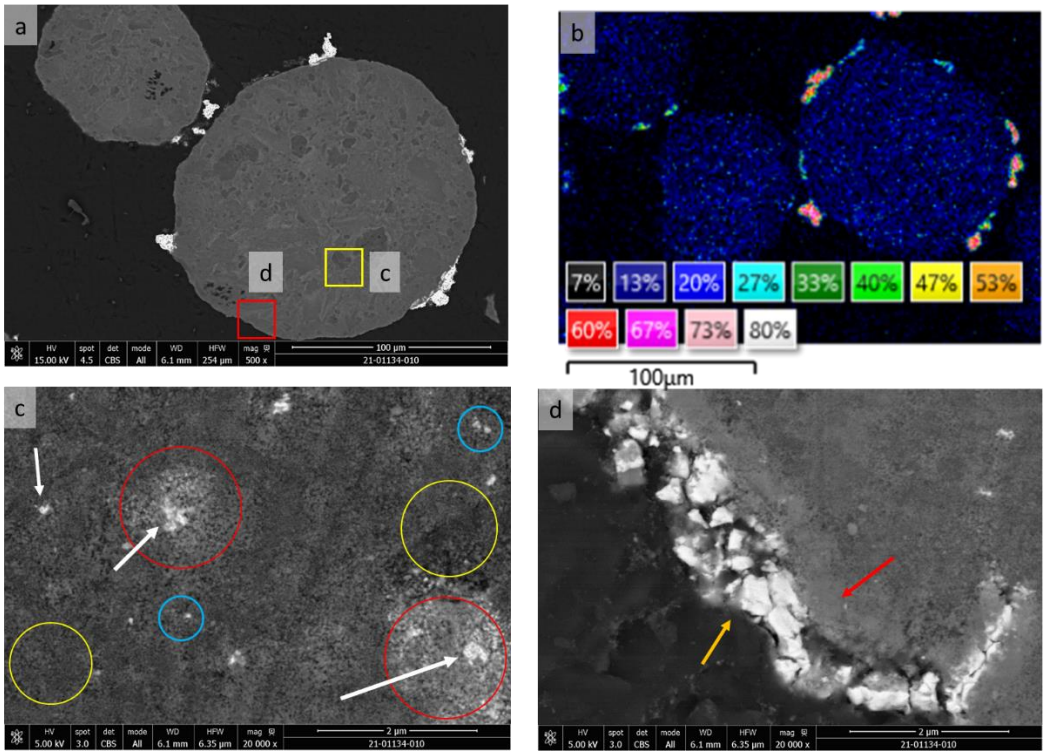

Figure 3.23: a) SEM image and b) EDS Cu-concentration map of the sample cycled at 700 °C, after 200 cycles. Red and yellow squares marked on the image is displayed in c and d, respectively.

3.2.1.3 Conclusion

The multiple redox cycling of the sample at 700 °C led to an overall increase in the sintering of the copper phase compared to the fresh sample. In terms of the microstructure, the size of the Cu-rich spherical areas appears to increase with the number of cycles. The quantitative analysis of the XAS spectra displayed a slight increase in the relative percentage of $Cu_xAl_yO_4$ from 55 % in the fresh sample to 60 %, after 50 cycles. Unfortunately, the relative percentage of the 200 cycles sample could not be estimated as XAS was not performed on this sample. However, from the XRD data and SEM data it can be deduced that the relative percentage of the $Cu_xAl_yO_4$ has increased. Furthermore, the porous structure in some areas could be linked to the formation of the α-Al_2O_3 phase which is confirmed by the XRD. Surprisingly, the alpha formation could occur at temperature as low as 700 °C.

3.2.2 Redox cycles at 800 °C

The fresh sample CuO/Al_2O_3-800 was cycled in TGA at 800 °C during 50 or 200 cycles.

3.2.2.1 After 50 cycles

According to the XRD analysis (Figure 3.24), after 50 redox cycles the sample contains CuO, $Cu_xAl_yO_4$ and transition alumina. Compared to the fresh sample at 800 °C, the $Cu_xAl_yO_4$ peaks appear sharper. The relative peak intensity of the CuO and the $Cu_xAl_yO_4$ points to an increase in the aluminate percentage. Using XAS, we get a relative amount of 23:77 for CuO:$Cu_xAl_yO_4$ phases. The peaks corresponding to the transition alumina are also observed which was not discernible in the fresh sample due to the overlapping of the broadened peaks. The transition alumina was identified as δ-Al_2O_3.

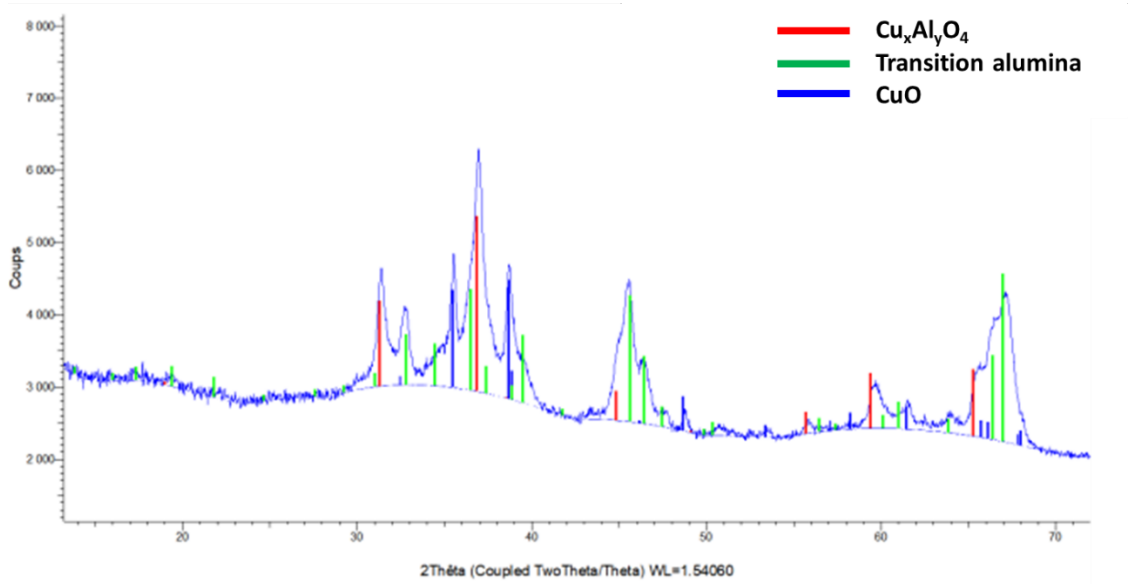

Figure 3.24: XRD of CuO/Al_2O_3-800 °C sample after 50 cycles.

After 50 cycles at 800°C, the copper is distributed in different forms as observed in the SEM imaging (Figure 3.25 a-b).

In the matrix in dark grey, it appears in the form of small agglomerates of homogeneously distributed particles, with a size of several tens of nm. The Cu concentration in the matrix is approximately 5-8 wt%.

Yellow circle, Figure 3.25d: Within the matrix there are areas with lighter contrast (marked in red square and in Figure 3.25d), with spherical shapes, containing higher concentrations of copper (about 15 to 25 wt%). These areas range from 1 to 10 µm in diameter. The particles in these zones are often denser and larger in size, compared to the particles in the

grey matrix. Some porosity and cracks can be observed as well within these copper-rich spherical zones.

Within some of these spheres some CuO particles of 20 to 500 nm size (circled in red, Figure 3.25b) are also noted.

On the outer periphery of the grains of the support, the Cu-rich phase is found either forming 5-10 µm sized particles or discontinuous layer of 1 to 2 µm thickness (circled in red, Figure 3.25c). The copper to oxygen ratio is about 80/20 wt% in the areas circled in red in Figure 3.25c and d. Between the white crust and grey matrix, a concentration gradient is observed from high to lower copper concentration from the outer edge towards the grain. The crust formation is likely to be due to the inward diffusion of the large copper crystallites (seen in the fresh sample), induced by the temperature during the cycling.

Also, as seen in Figure 3.25a, some sintered grains are observed to connect to the neighbouring grain by the white copper-rich areas. This phenomenon has been mentioned in the literature, arising due to the melting of the copper-based phase during the high temperature cycling and resulting in agglomeration due to the proximity of the grains.

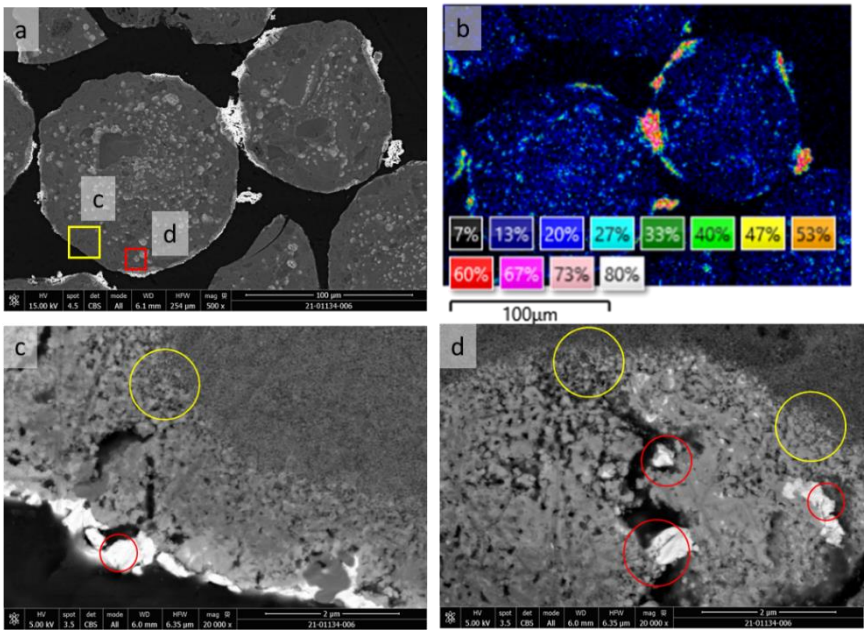

Figure 3.25: a) SEM image and b) EDS Cu-concentration map of the sample cycled at 800 °C, after 50 cycles. Red and yellow squares marked on the image are displayed in c and d, respectively.

3.2.2.2 After 200 cycles

After 200 redox cycle at 800 °C, the sample displays the presence of $Cu_xAl_yO_4$, CuO, transition alumina and α-Al_2O_3 (Figure 3.26). In terms of transition aluminas, both θ and δ phases can be identified in the diffractogram. From the relative intensity of the CuO and $Cu_xAl_yO_4$ peaks the concentration of CuO seems to have increased compared to the sample after 50 cycles.

The increase in CuO concentration was confirmed by from XAS and SEM-EDS analysis. Quantitative XAS estimates a ratio of 42:58 for the CuO: $Cu_xAl_yO_4$ phases.

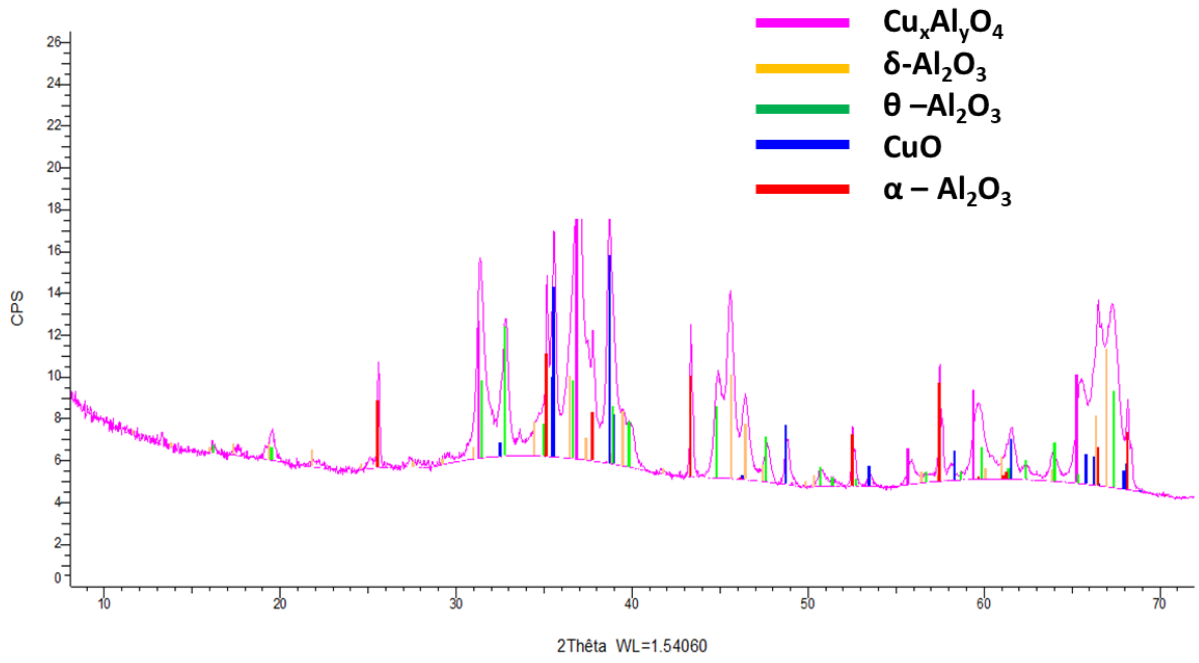

Figure 3.26: XRD of CuO/Al_2O_3-800 °C sample, after 200 cycles.

Indeed, this sample presents more Cu-enriched areas as seen in Figure 3.27. Like the previous sample, spherical copper-rich areas are noted with larger diameter ranging from 5 to 20 µm. A larger number of cracks is also observed within and outside of those spherical areas (Figure 3.27d). Within the cracks, CuO (60-80 wt% Cu content) either fills the cracks continuously (marked with yellow arrow in Figure 3.27c) or exists as individual particles (marked in yellow arrow in Figure 3.27d). The continuous white areas are a few microns in width and the individual particles are within the range of 50 to 200 nm. There is a Cu concentration gradient from the cracks to the matrix as shown with a red arrow in Figure 3.27d).

The areas circled in red are often denser, with a copper concentration of 10-25 wt%, corresponding to $Cu_xAl_yO_4$ phase. Large crystallites or crusts of Cu-rich phase are still observed on the outskirts of the grain for this sample. We can observe the presence of crystals of a few hundred nm to few µm on the outer periphery of the grains of the support, appearing in white in Figure 3.27c). The areas with visible white crystallites are made of CuO, with a Cu:O ratio of 80/20 wt%.

Apart from the Cu-rich spheres, the sample contains a dark grey matrix, rich in Al. The matrix in dark grey appears to be denser in some areas (white circle, Figure 3.27c), and porous in some of the areas (blue circle, Figure 3.27d). The white circled areas contain a very small concentration of copper varying from 0 to 3 wt%. The phase identification from XRD and the presence of copper-deficient, Al-rich matrix with different morphologies confirms the existence of different alumina polymorphs. While the dense areas (in white circle) might be made of the transition aluminas (δ and θ), the porous areas with larger particles (marked with blue circle) exhibit a morphology resembling that of the α-phase.

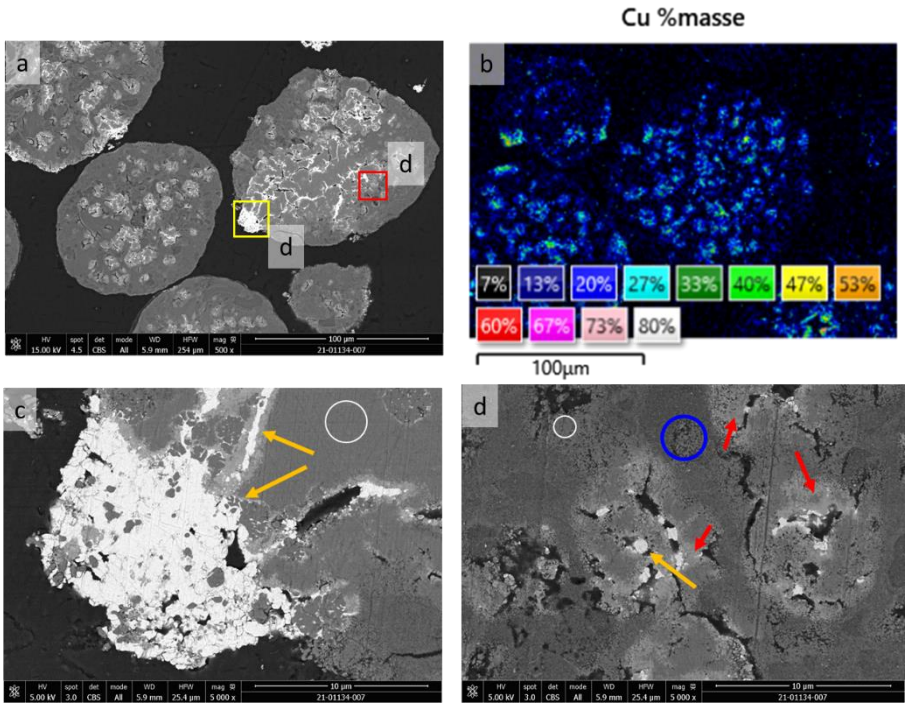

Figure 3.27: a) SEM image and b) EDS Cu-concentration map of the sample cycled at 800 °C, after 200 cycles. Red and yellow squares marked on the image is displayed in c and d, respectively.

3.2.2.3 Conclusion

In the sample calcined and cycled at 800°C, after 50 cycles the material displayed the presence of CuO, $Cu_xAl_yO_4$ and transition alumina. An increase in the proportion of $Cu_xAl_yO_4$ is observed after 50 cycles. The ratio of CuO:$Cu_xAl_yO_4$ was 30:70 and 23:77 in the fresh and 50 cycled samples, respectively. However, after 200 cycles, a drastic decrease in the $Cu_xAl_yO_4$ proportion is noted with respect to CuO; displaying a CuO:$Cu_xAl_yO_4$ ratio of 42:58. The phase change is complemented by the morphological change where an increasing proportion of CuO appears in the SEM images. The evolution at 800 °C is intriguing, especially considering the phase transitions and the presence of transition aluminas, $Cu_xAl_yO_4$, as well as α-Al_2O_3. The drastic change in the phase distribution could result from the phase transition of the aluminas.

3.2.3 Redox cycles at 900 °C

The fresh sample CuO/Al_2O_3-900 was cycled in TGA at 900°C during 50 or 200 cycles.

3.2.3.1 After 50 cycles

Figure 3.28 displays the XRD of the oxygen carrier after 50 redox cycles at 900 °C. The sample is mostly composed of CuO and α-Al_2O_3 with a small amount of copper aluminate. Transition alumina is almost non-existent. According to the XAS analysis, the relative percentage of CuO and $Cu_xAl_yO_4$ is 75:25.

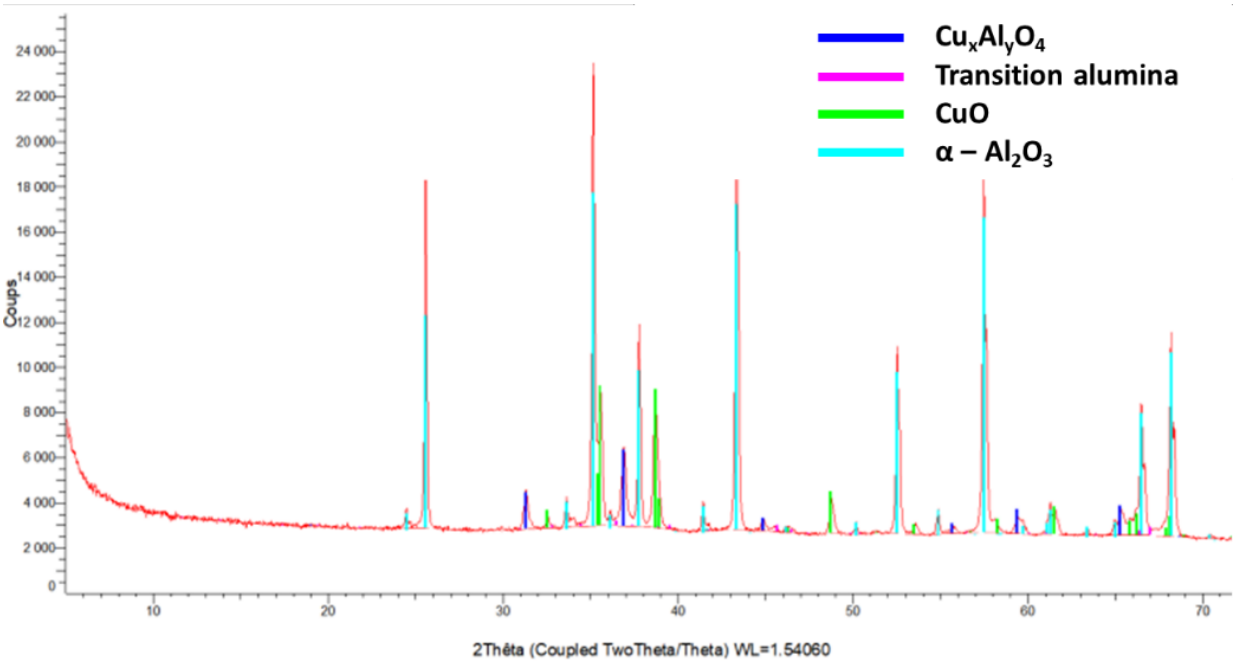

Figure 3.28: XRD of CuO-Al_2O_3-900 °C sample, after 50 cycles.

Figure 3.29 presents the SEM and STEM-EDS of the sample after 50 cycles at 900°C. As marked in Figure 3.29b and d the sample exhibits three different morphologies.

Area 1 contains a dense support matrix with a low concentration of copper (about 2-8 wt%). The morphology of area 1 is comparable to the inner part of the fresh sample.

Area 3, displayed in Figure 3.29 c is made of large Al-rich particles forming a porous network. These particles do not contain any copper and from the morphology they can be assigned to alpha alumina. The particles are in the range of above 100 nm in length and 100 to 200 nm in width. Within the α-Al_2O_3 matrix, large CuO particles were also found, depicting a wide size range of 50 to 500 nm.

Area 2 contains a higher concentration of Cu (20-30 wt%) and lies in between area 1 and area 3. In area 2, some porosity is observed, and the individual particles seem to be sintered compared to area 1. The white arrow in Figure 3.29 e indicates the existence of a Cu gradient. In the direction of the arrow, the concentration of copper increases from about 8 wt% in the far left to about 30 wt% at the border with area 3. Both area 1 and 2 are made of $Cu_xAl_yO_4$ with different proportions of copper.

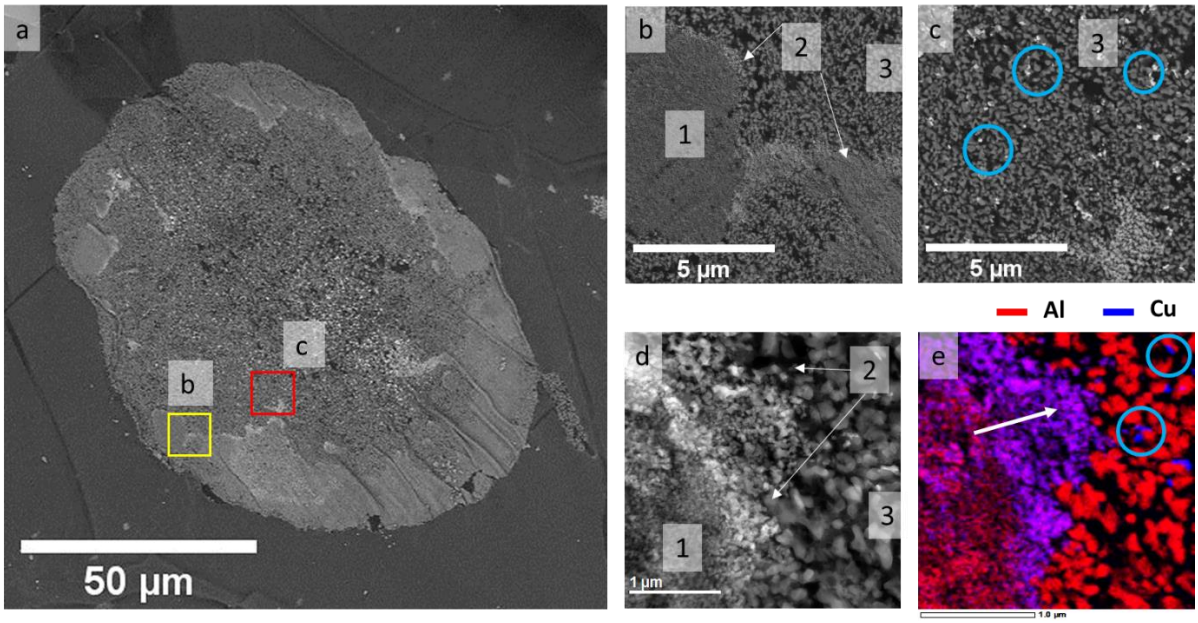

Figure 3.29:a) SEM image of UMT cut CuO-Al_2O_3-900 °C sample after 50 cycles. b and c, represents the area marked in red and yellow squares in a, where the STXM has been performed, d) STEM-HAADF image and the corresponding EDS map (e).

The spatial distribution of $Cu_xAl_yO_4$ with low and high copper concentration and the α-Al_2O_3 phase resolved by SVD of the STXM-XANES 3D stack is presented in Figure 3.30. The presence of such copper concentration gradient points towards a preferential migration pathway involving phase transitions.

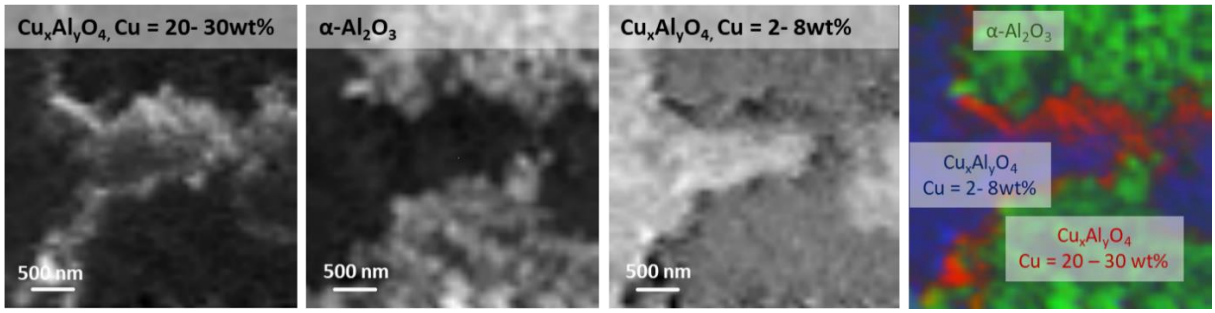

Figure 3.30: Coloured STXM map of the sample, after 50 cycles at 900°C, with spectral contribution from the individual components mentioned on the image.

In Figure 3.31, different areas characterised by STXM are shown: spectra corresponding the marked areas have been extracted to compare the local structural change in those areas, at both Cu L-edge and Al K-edge. In the red circle, the area corresponds to a high Cu-concentration. It displays a similar feature as the fresh sample, in particular the presence of

two L_3 peaks at ~933 and 933.6 eV belonging to the tetrahedral and octahedral Cu environments, respectively.

The spectra from the low Cu-concentration area (blue circle) displays a broad peak at about 933.6 eV at the Cu L-edge. The low signal to noise ratio confirms the presence of small amounts of copper. In terms of Al K-edge, both areas exhibit similar spectral features resembling that of the fresh sample at 900 °C and corresponding to $Cu_xAl_yO_4$ (Figure 3.12: Spectral contribution from individual areas corresponding to the coloured circles in the SEM image of fresh CuO/Al_2O_3-800 °C sample. "stack" mode.Figure 3.16). However, subtle differences can be noticed in the relative intensities of the 2nd peak at 1580.8 eV and the 3rd peak at 1584.5 eV. While in the fresh sample the 3rd peak is relatively higher than the 2nd peak, in this sample (after 50 cycles) the two peaks have relatively similar intensities (Figure 3.31). The relative peak intensities could either be influenced by the presence of the α-Al_2O_3 phase in the 3D volume or could originate from a change in the structural arrangement within the aluminate phase.

The area circled in green corresponds to α-alumina. In this particular area, no copper-phase is present.

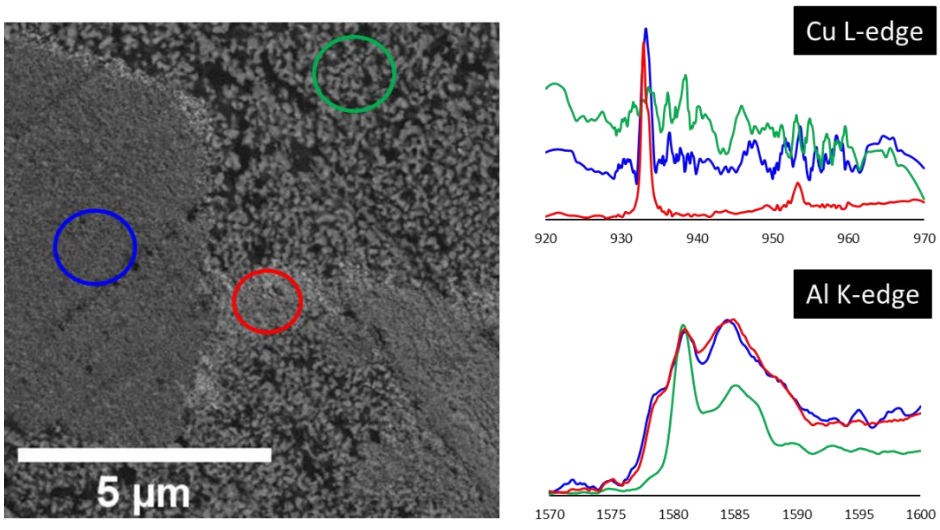

Figure 3.31: Spectral contribution from individual areas corresponding to the coloured circles in the SEM image of the sample cycled 50 times at 900 °C.

3.2.3.2 After 50 cycles: Reduced state

In order to study the oxygen carrier in the reduced state, the cycling in TGA was stopped after the reduction step followed by a temperature ramp from 900 °C to room temperature, under H_2. It is difficult to completely prevent exposure to air; during the sample preparation and before the data acquisition, the sample spent a significant amount of time in air. The room temperature oxidation of the sample is only likely to induce surface oxidation and should not affect the morphology of the particles. However, the morphology could be affected by sintering of the particles during the cooling down process. Metallic copper under hydrogen is known to be mobile and the oxygen carrier spent quite a few minutes at high temperature during the ramp down.

The aim of this observation was to locate the copper under reductive atmosphere, for a better understanding of the migration phenomenon occurring during the cycling, and thus to identify the origin of the Cu concentration gradient observed in the oxidised sample.

As observed from the SEM image in Figure 3.32, a and c represent two different grains with different overall morphology.

In Figure 3.32a, the grain seems to be composed of a mixture of higher porosity zone containing alpha alumina, denser areas made of alumina matrix without copper; between these two regions copper particles (between 50 nm to few µm) are found scattered within the porosity of the alpha alumina matrix. Some copper particles are also found in the denser matrix with a size range smaller than that in the α-Al_2O_3. At the interior of some of the grains (Figure 3.32a), sintered copper particles are found in large quantity, related to the presence of porosity.

In areas like Figure 3.32c, the grain is mostly composed of denser matrix and sintering of the copper particles appears to be less prominent. The particles are in the size range of few nm to few hundreds nm.

From the phase distribution, it can be assumed that during the reduction step, the migration and the eventual sintering of the metallic copper is facilitated by the porous α-Al_2O_3 matrix. During the oxidation step, the metallic copper migrates back to react with the available transition alumina to re-form copper aluminate. It is probable that due to limitation of

oxidation duration or long diffusion distances, homogeneous copper aluminate formation is hindered. Hence, a copper-concentration gradient is observed in between the two alumina regions.

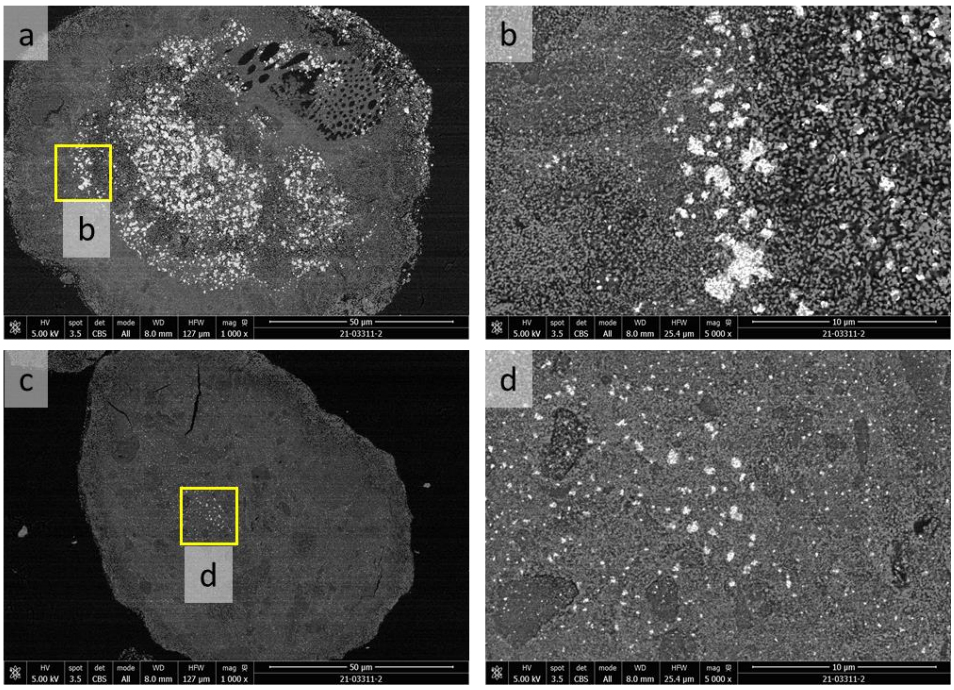

Figure 3.32: SEM image of CuO/Al_2O_3-900 °C sample, after 50 cycles – reduced state.

The chemical speciation, obtained by STXM, of the reduced sample is shown in Figure 3.33. In the characterised area, only the presence of metallic copper (red) and α-Al_2O_3 (green) is noted.

The "stack fit" data treatment leads to some residual absorption, indicating the presence of another alumina phase.

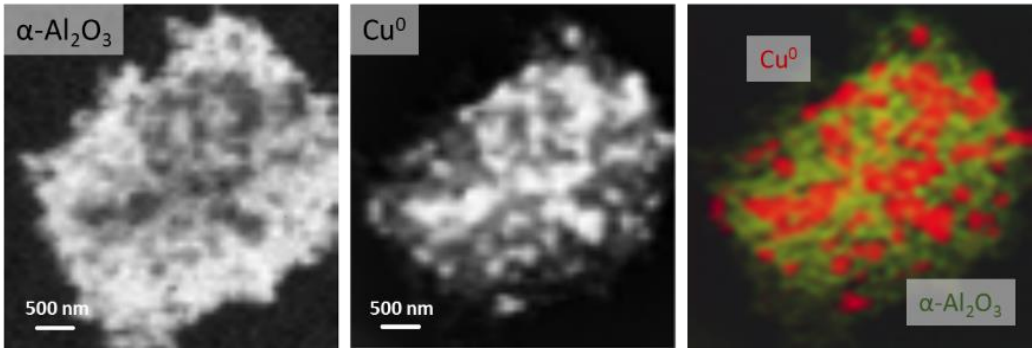

Figure 3.33: Coloured STXM map of the sample, after 50 cycles at 900° in reduced state, with spectral contribution from the individual components mentioned on the image.

Figure 3.34 shows the XAS spectra extracted from STXM stacks of some of the selected areas from the image. Some differences in the spectral features of Al K-edge are noted between the two areas marked in light green and dark green. The dark green spectrum resembles that of the α-Al_2O_3 reference spectra (section 2.1.5.2), whereas, the light green spectrum displays a slightly higher intensity shoulder peak at ~1579 eV. Additionally, the peak at ~1584 eV has a relatively higher intensity than that of the α-Al_2O_3 phase, thus, confirming the presence of another alumina phase.

Simulating the overall experimental spectra using gamma alumina or the copper aluminate, could not account for the unknown phase. Moreover, no significant contribution from the transition alumina phase was noted from the XRD of the oxidised sample either. Since no transition alumina is present, the only possibility is the presence of a copper-deficient aluminate phase, after the eviction of the metallic copper. Besides that, the spectral feature displays both octahedral and a small percentage of tetrahedral species, like that of copper-aluminate. Indeed, due to similar alumina framework the copper-deficient aluminate may display similar features as the copper-alumina.

Since the sample was grinded, the analysed area is likely to be a mixture of the two alumina phases rather than a pure Cu-deficient aluminate. Therefore, it is difficult to conclude anything more concerning any local structural difference between the Cu-deficient aluminate and copper-aluminate.

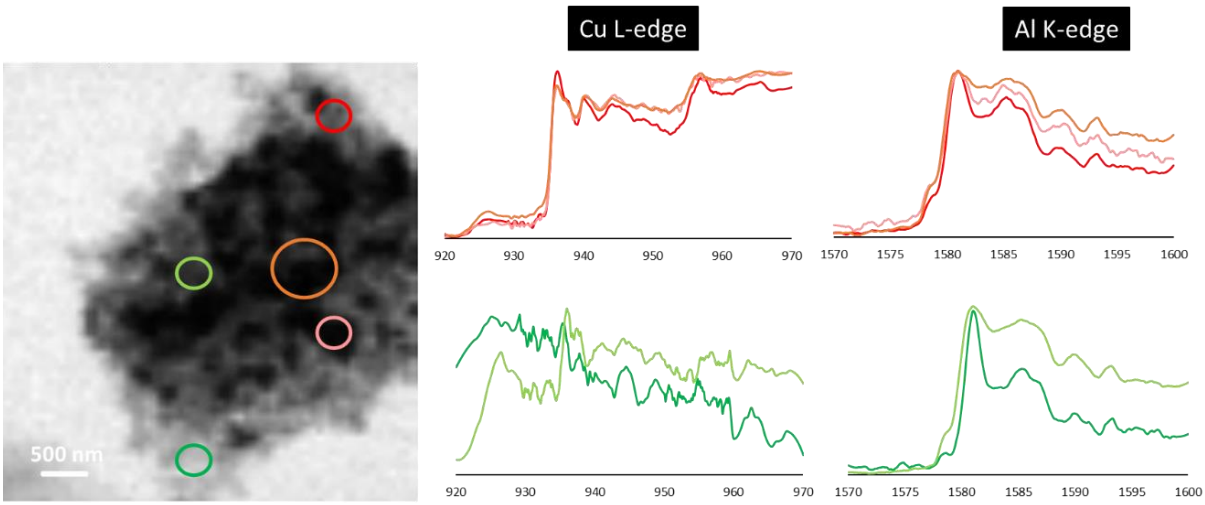

Figure 3.34: Spectral contributions from individual areas corresponding to the coloured circles in the SEM image of the sample cycled 50 times at 900 °C (in the reduced state).

3.2.3.3 After 200 cycles

According to the XRD data in Figure 3.35, 200 redox cycles at 900 °C led to the complete conversion of the alumina phase to α-Al_2O_3. The copper mainly exists as CuO with trace amounts of copper aluminate. The XAS speciation provides similar information in terms of copper species, with a relative spectral contribution of 91 % for CuO and 9 % for $Cu_xAl_yO_4$.

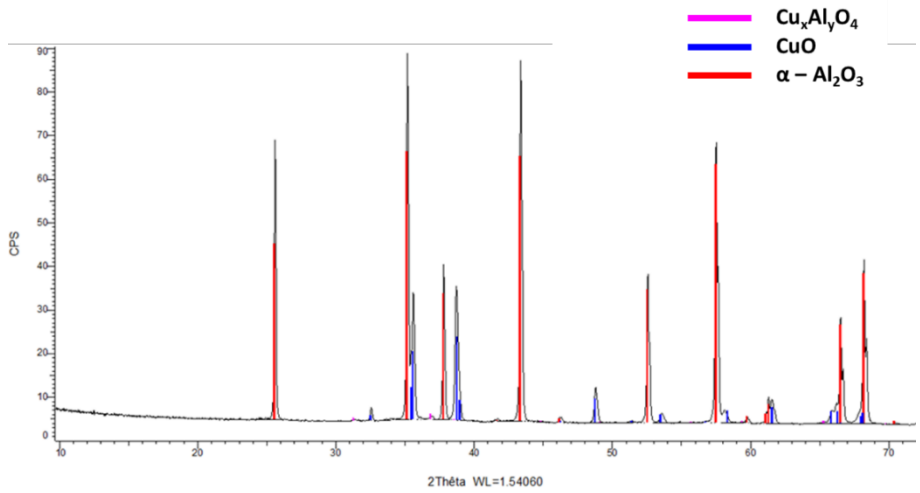

Figure 3.35: XRD of the CuO/Al_2O_3 – 900 °C sample, after 200 cycles.

From the SEM image, after 200 cycles, the sample is mainly composed of large crystallites of CuO and alpha alumina phase (Figure 3.36 a). The increased porosity in the alumina support is visible. The alpha alumina particles are in the size range of 500 nm and above in length, and above 300 to 500 nm in width (Figure 3.36 c). The size of the copper oxide particles is above 200 nm and they exhibit irregular shapes, mostly existing and moulding

into the alumina particles (Figure 3.36 b-e), where the white particles (CuO) are observed to be encompassing the grey particles (α- Al_2O_3).

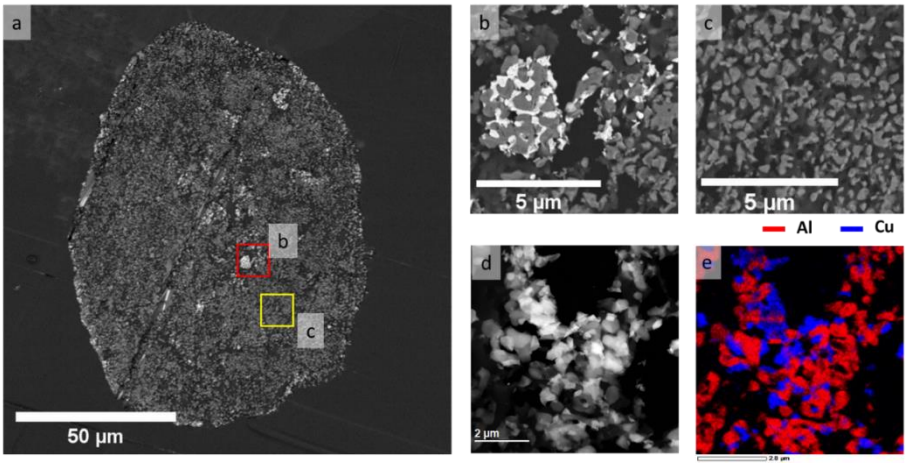

Figure 3.36: a) SEM image of UMT cut CuO-Al_2O_3-900 after 200 cycles. b and c, represents the area marked in red and yellow squares in a, where the STXM has been performed, d) STEM-HAADF image and the corresponding EDS map (e).

The chemical speciation from the STXM-XANES analysis is displayed in Figure 3.37 which displays the two dominant phases identified by the characterisation techniques.

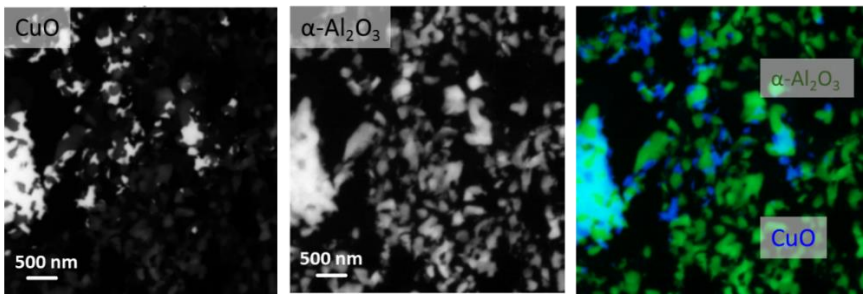

Figure 3.37: Coloured STXM map of the sample after 200 cycles at 900 °C, with spectral contribution from the individual components mentioned on the image.

In Figure 3.38, spectral features from specific areas confirm no deviations from the reference samples or any difference in the local speciation.

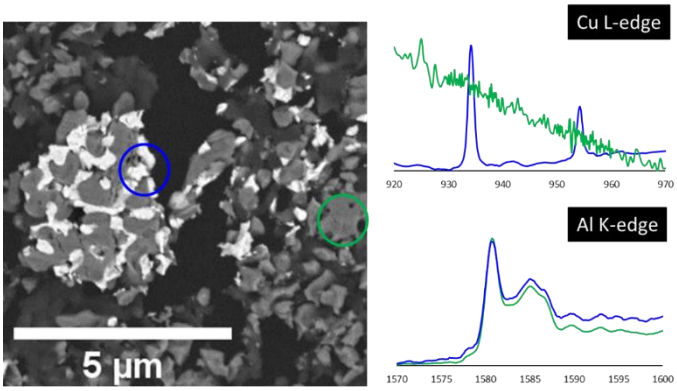

Figure 3.38: Spectral contributions from individual areas corresponding to the coloured circles in the SEM image of the sample after 200 cycles at 900 °C.

3.2.3.4 Conclusion

The redox cycling at 900°C leads to drastic changes in the material in terms of phase distribution and morphological evolution.

From an initial copper aluminate sample the material transforms into highly porous α-Al_2O_3 with large CuO crystallites within the porosity of the alumina. From the appearance of the intermediate cycled sample (after 50 cycles), it is reasonably speculated that the copper aluminate gradually transforms to α-Al_2O_3 phase during the reduction step. Followed by removal of copper during reduction, a Cu-deficient aluminate is formed. Structurally, the Cu-deficient aluminate structure resembles neither γ, nor any other transition alumina. The formation of the α-Al_2O_3 promotes the eventual CuO-alumina phase segregation as the cycling proceeds.

3.2.4 Effect of cycling temperature on the fresh material calcined at 900°C

The effect of the cycling at a temperature of 700 °C on the fresh oxygen carrier calcined at 900 °C, was monitored using *in situ* XRD. As mentioned previously, the sample is initially mainly composed of $Cu_xAl_yO_4$, transition alumina and α-Al_2O_3.

Using the *in situ* XRD setup mentioned in Chapter 2, three redox cycles were carried out at 700 °C using H_2 and air as the reducing and oxidising gas. The acquisition parameters and the reaction conditions are also described in Chapter 2.

The evolution of diffractograms as a function reaction gas is presented in Figure 3.39. At the first reduction step the initial $Cu_xAl_yO_4$ phase directly reduces to metallic copper, according to reaction 3.1. No intermediate of copper oxide phase is observed. The peak of the $Cu_xAl_yO_4$ is broadened with a gradual loss of intensity during the first few minutes.

Under H_2: $Cu_xAl_yO_4 + H_2 \rightarrow Cu^0 + H_2O$ + alumina Reaction 3.1

During the reoxidation, the copper is first oxidised to Cu_2O and then the Cu_2O slowly disappears to reform the $Cu_xAl_yO_4$ phase. The reformation of $Cu_xAl_yO_4$ occurs either directly from Cu_2O or via CuO phase according to reactions 3.2 and 3.3. The peak intensity and shape is relatively sharper than the Cu-deficient aluminate, after the reduction step. The CuO intensity is weak in the 1st redox cycle.

Re-oxidation: $2\ Cu^0 + O_2 \rightarrow Cu_2O + ½\ O_2$ + alumina $\rightarrow 2\ CuAl_2O_4$ Reaction 3.2

$2\ Cu^0 + O_2 \rightarrow Cu_2O + ½\ O_2 \rightarrow 2\ CuO$ + alumina $\rightarrow 2\ CuAl_2O_4$ Reaction 3.3

Similar reactions occur during the 2nd and 3rd redox cycles. With every reduction-oxidation reaction, the CuO peaks' intensity increase, while the $Cu_xAl_yO_y$ peaks' intensity fades, and the peaks' shape broaden. For the $Cu_xAl_yO_y$ phase, the peak positions slowly shifted to higher 2θ values (by 0.2° 2θ) or lower d-spacing values indicating a decrease in the lattice parameter values. With the conversion of copper from the aluminate phase to CuO, the concentration of copper in $Cu_xAl_yO_y$ phase is reduced. Additionally, due to the relatively low temperature of the reaction, the diffusion of copper might be hindered. The peak broadening could either stem from the low copper concentration and/or presence of structural defects. No change in the α-Al_2O_3 phase is noted.

Over these three cycles at 700°C, CuO accumulates, hence the Cu deficient spinel peaks move towards the position of a transition alumina (probably gamma). Since no alpha alumina is formed, the CuxAlYO4 slowly moves back to Al2O3.

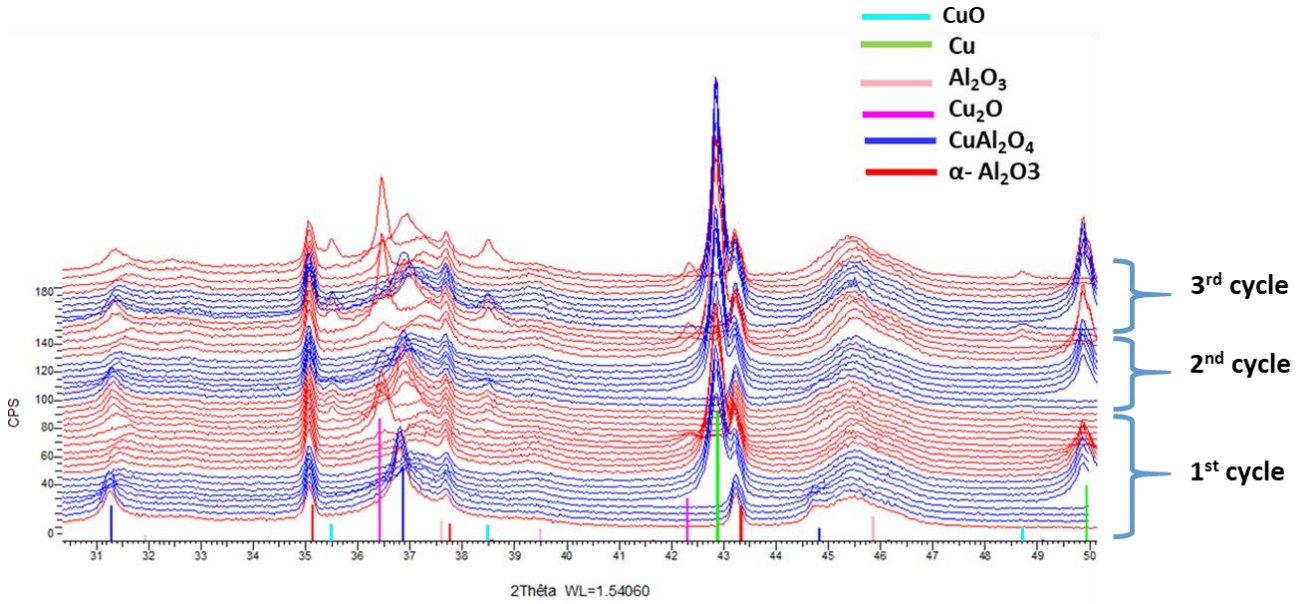

Figure 3.39: in situ *XRD of the redox cycling of CuO/Al_2O_3-900 °C sample at 700 °C. The blue and red spectra represent the sample during oxidation and reduction, respectively.*

The redox induced phase transition is determined by the temperature of redox cycling. Even if the initial sample is composed of $Cu_xAl_yO_4$ phase, the reformation of the copper aluminate from reduced copper is a diffusion-controlled reaction which would either require high reaction temperature or longer duration of heating. Bolt et al. specified that the grain boundary diffusion of copper in polycrystalline γ-Al_2O_3 is faster than the bulk diffusion [15]. Thus, the accumulation of copper oxide is more likely at 700 °C.

3.3 Discussion

The temperature and redox cycle dependent morphology evolution can be explained by three phenomena: formation of CuO vs $Cu_xAl_yO_4$, sintering of CuO and the transition to α-Al_2O_3. These phenomena are connected to each other by the temperature-dependant diffusion properties of CuO and the kinetics of the reactions and phase transitions. At higher temperatures, copper migration may procced via reactive-diffusion reaction between CuO and transition alumina, or if the reaction temperature is not high enough other diffusion mechanisms such as grain boundary, surface, and vapour phase diffusion may dominate.

$Cu_xAl_yO_4$ formation and CuO sintering

The formation of the metal aluminate occurs by reactive diffusion involving the counter diffusion of the divalent cations (Cu^{2+}) and Al^{3+} through an initially formed $CuAl_2O_4$ layer [15]. The kinetics of the growth is often described by a parabolic growth law where the growth occurs as a function of the square root of the annealing time. The growth of the aluminate layer might be hindered if the bulk diffusion is not sufficient due to diffusion barriers induced by the temperature or the mobility of the species on the surface or at the grain boundaries [17].

Indeed, as noted in this study (section 3.1), a higher calcination temperature increases the fraction of $Cu_xAl_yO_4$. Moreover, a higher calcination temperature results in relatively fast reaction between the residual CuO and transition alumina, as seen in section 3.1.1.2). In contrast, the initial sample containing only $Cu_XAl_yO_4$ phase gradually transformed to CuO during the redox cycling at 700 °C (section 3.2.4).

A comparison of the bulk diffusion rates of copper in alumina at different temperatures can help us to understand the extent of reaction between 700 and 900 °C. The diffusion coefficient of copper in α-Al_2O_3 is reported by Moya et al. using SIMS (Secondary Ion Mass Spectroscopy) [18]. The temperature dependent values are reported to be 9.7 x 10^{-22} $m^2.s^{-1}$ and 8.6 x 10^{-20} $m^2.s^{-1}$ at 800 and 900°C, respectively and an extrapolated value of 7 x 10^{-24} $m^2.s^{-1}$ at 700 °C. As diffusion data of copper in γ-Al_2O_3 is not available in the literature (to the best of our knowledge), the diffusion coefficient of Cu^{2+} in α-Al_2O_3 is useful to understand the feasibility of the reaction at different temperatures. The diffusion distance ($x = \sqrt{D_c t}$) is calculated for our reaction with t= 180 seconds. The distance at 700, 800 and 900 °C are estimated to be 0.001, 0.2 and 16 nm, respectively. Given the initial alumina platelet size of 15-20 nm, the $Cu_xAl_yO_4$ formation at 700 or 800 °C would be limited to the surface. Nevertheless, based on the faster reaction between γ-Al_2O_3 and Cu^{2+} at a lower temperature, the actual diffusion coefficient of copper in the γ-Al_2O_3 phase is likely to be higher [19,20]. Hence, we can see Cu-aluminate even at lower temperature.

The kinetics of the oxidation and the sintering of the copper oxide phase must be also considered. Based on the temperature, the reaction would either proceed through the formation of copper aluminate (at 900 °C) or the sintering of CuO as well as the copper aluminate formation (at 700 and 800 °C). The drastic difference between the aged sample

(especially after 200 cycles) at 700 and 800 °C, may originate from the increased rate of sintering at 800 °.

Alumina transition

Surprisingly, the 200 cycled samples contain α-Al_2O_3 at both 700 and 800 °C. Moreover, the θ-phase is only observed in the sample cycled 200 times at 800 °C. The fact that θ alumina is not identified in the other samples points out the possibility of different phase transition mechanisms: temperature-dependant (γ→δ→θ→α) and copper-promoted alumina transition.

As mentioned in section 3.1. the presence of copper has been identified to promote the phase transition in alumina, which has also been reported in the literature [16,21]. In the presence of copper, the phase transition to α-Al_2O_3 occurs at a temperature lower than the expected phase transition temperature (typically above 1000 °C) [6]. The phase transition temperature of the alumina is described to be affected by several factors such as surface properties, alumina particles size, presence of water, etc [22]. Hence, it was important to carry out a control experiment with the initial γ-Al_2O_3 (Puralox) support. To ensure fair comparison, a similar protocol of incipient wetness impregnation (only with water), maturation, drying and calcination at 900 °C for 12 hours was performed on the γ-Al_2O_3 support. The water impregnated Puralox alumina support was subjected to 50 redox cycles at 900 °C, which is equivalent to 20 hours of thermal treatment. From the XRD of the water-impregnated sample, no α-Al_2O_3 was found. Indeed, confirming the presence of copper lowers the phase transition temperature.

The exact role of the copper is debated, where some studies suggest the $CuAl_2O_4$ phase as a heterogenous nucleation site while other studies report the presence of a “Cu-modified” alumina structure, before the emergence of α-Al_2O_3 [16,21,22]. In this study, we are proposing a pathway based on the modification of the Al-O bonding environment. Figure 3.40, displays the Al K-edge spectra of reference γ-Al_2O_3, reference $CuAl_2O_4$, fresh oxygen carrier calcined at 900 °C and the sample cycled after 50 times. As mentioned earlier in section 2.1.5.2, the peak at 1579 eV corresponds to tetrahedral AlO_4 and the peaks at 1581 and 1584 eV are associated with the octahedral sites. The peak area ratio of 1579 and 1581 eV provides information on the percentage of the two environments [7]. The relative

difference in the two peaks for the γ-Al_2O_3 and the $CuAl_2O_4$ is evident from the graph. The AlO_4:AlO_6 is found to be 40:60 and 30:70 for the reference γ-Al_2O_3 and the $CuAl_2O_4$. From this difference, it can be deduced that the Cu^{2+} insertion in the alumina leads to the diffusion of Al^{3+} from a tetrahedral to an octahedral site. Furthermore, after 50 cycles, the tetrahedral to octahedral ratio is approximately 20:80. Clearly, the local structural organisation of the Al^{3+} started to resemble the α-Al_2O_3 spectral features, indicating the starting/progression of the phase transition, before the reconstruction of the *FCC* lattice to *HCP*. This slow shift towards the α-Al_2O_3 formation must be accompanied by the repeated re-insertion and de-insertion of the Cu^{2+} during the redox cycles.

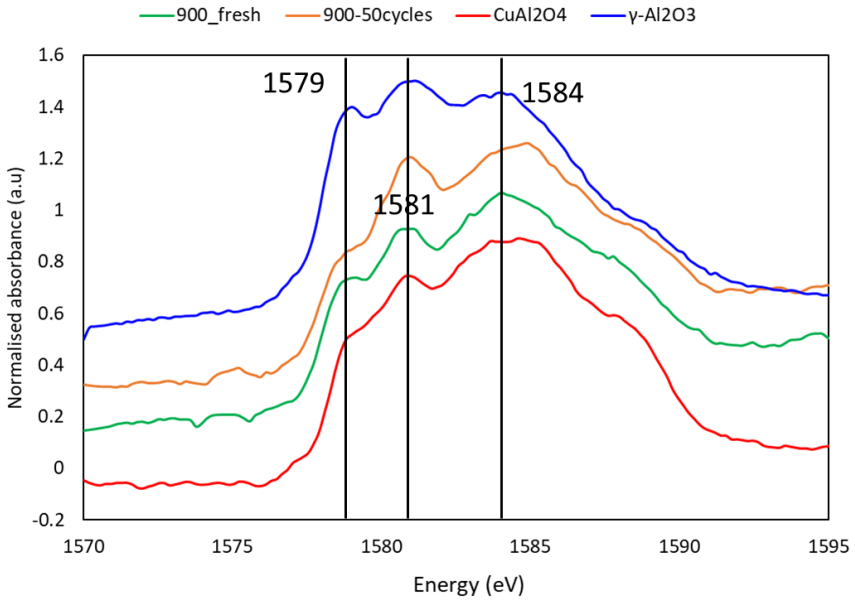

Figure 3.40: Al K-edge spectra of the fresh and reference $CuAl_2O_4$.

Possibly, the phase transition occurs from a Cu-deficient aluminate to α-Al_2O_3 via gradual structural reorganisation. In comparison, in pure samples, the γ-Al_2O_3 to α-Al_2O_3 occurs via a γ → δ→ θ → α-Al_2O_3 transition sequence [6]. In this sequence the percentage of the Al^{3+} ions in the tetrahedral configuration increases from γ-phase to θ-phase, reaching a 1:1 ratio of AlO_4:AlO_6. During the α-Al_2O_3 formation, the overall oxygen position has to be reconfigured from a FCC structure to HCP structure. This transition requires a high temperature (above 1000 °C), since, the movement of vacancies between two Al^{3+} sites requires a high activation energy [23]. The activation energy is calculated by Okada et al. which gives a value of 605 kJ/mol for the conventional alumina pathway, compared to the

activation energy of copper-promoted alumina transition (510 kJ/mol) [21]. Therefore, it can be deduced that the structural change induced by copper leads to the lowering of the overall phase transition energy barrier.

Effect of temperature and cycling

The phase evolution and the resulting morphology of the oxygen carriers depend on the number of redox cycles, the reaction temperature and the initial state of the material. Figure 3.41 summarizes the findings reported in the result section based on the multi-technique characterisation of the materials. Figure 3.42 summarizes the evolution of the proportion of the different phases of Cu.

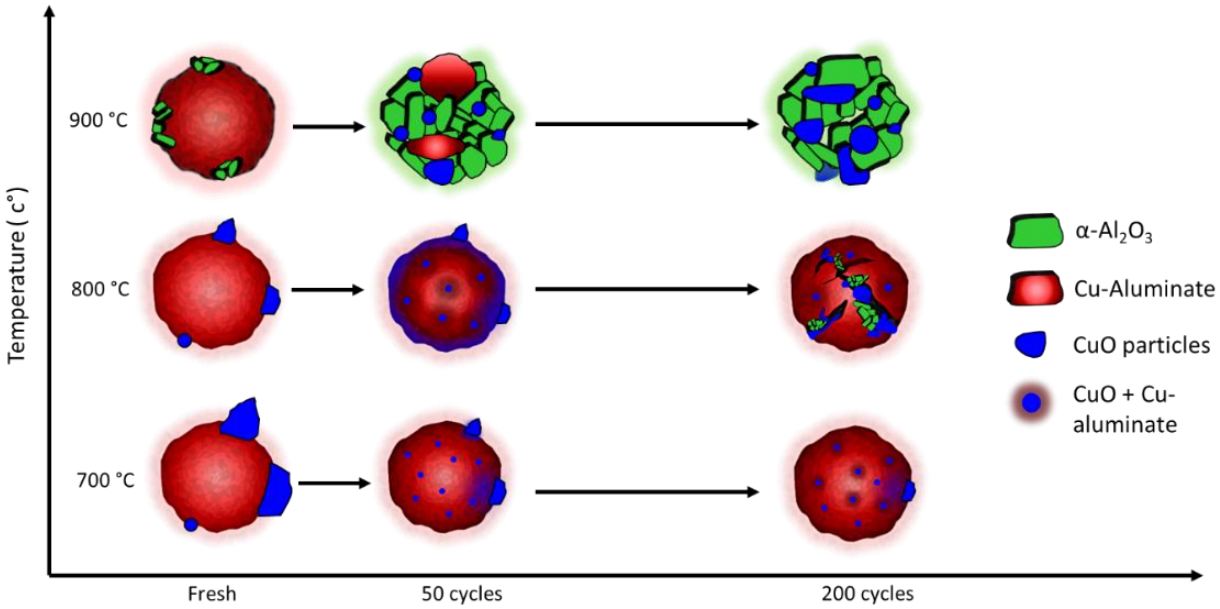

Figure 3.41: Schematic diagram depicting the phase and morphological evolution as a function of reaction temperature and the number of redox cycles.

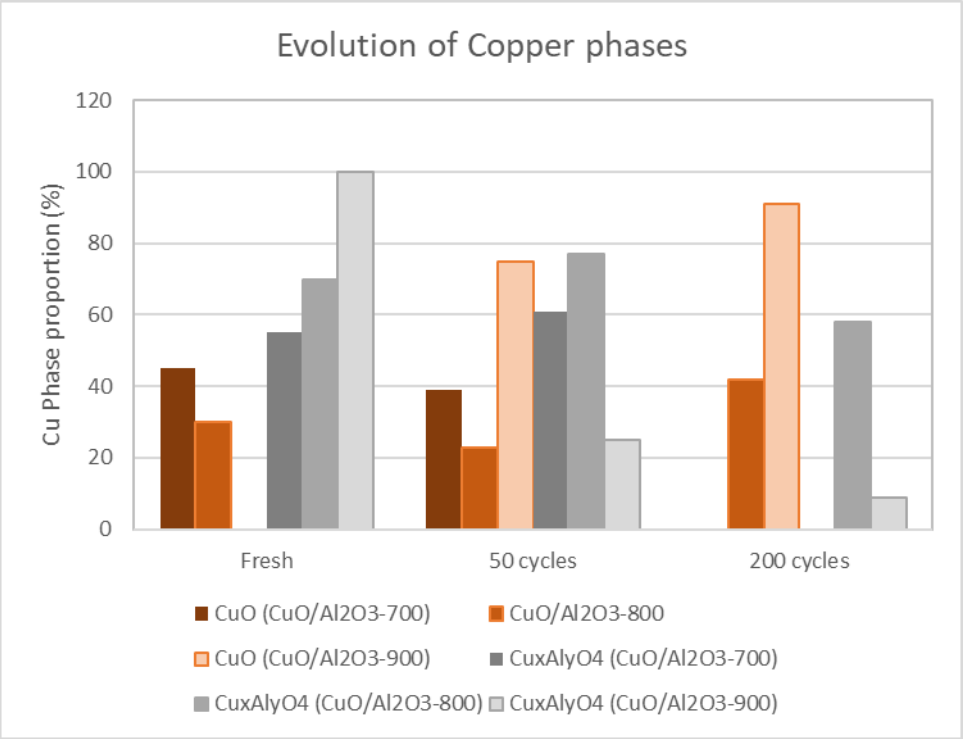

Figure 3.42: Evolution of the proportions of the different phases of Cu according to number of cycles.

The migration of the copper phase depends on temperature and on the alumina phase.

At low temperature (700 or 800 °C), during oxidation, both Cu sintering and Cu-aluminate formation take place. Most probably, there is a competition among the different migration processes. In one case, sintering occurs due to surface or grain boundary migration and in another case, solid-state reaction and bulk diffusion lead to formation of the aluminate phase. At 700 °C, the 1st process is prominent, leading to larger crystallites of CuO (see the SEM image) as a function of the number of cycles. At 800 °C, there is competition between both phenomena, and strong CuO sintering, as well as microstructural changes in the support grain is observed.

On the contrary, at 900 °C, the bulk diffusion is generally more prominent resulting in the formation of the copper aluminate. However, the presence of the Cu-aluminate phase promotes the transition of the support to α-Al_2O_3 phase. Indeed, the γ to α-Al_2O_3 transition should not occur below 1000 – 1100 °C, and atomic migration of copper in and out of the alumina during oxidation and reduction, respectively, might promote the γ to α-Al_2O_3 phase transition. It is suspected that the expelling of Cu from the spinel structure of $Cu_xAl_yO_4$ (during the reduction) favours the formation of the corundum structure of Cu-free Al_2O_3.

Reversely, the oxidative formation of spinel is possible in the Cu + γ-Al_2O_3 system, and strongly kinetically limited in the case of Cu + α-Al_2O_3. The mobility of copper on alumina during oxidation is sufficient to form (1) $CuAl_2O_4$ at the expense of γ-Al_2O_3, and (2) larger CuO particles on α-Al_2O_3 by sintering. Hence, with increasing number of cycles, the α-phase and the CuO segregate and eventually large CuO crystals are formed within a porous α-alumina support.

Thus, at lower temperature (< 800 °C) the sintering of the copper oxide will dominate while at higher temperature (> 900 °C) the α-Al_2O_3 formation and eventual phase segregation will be prevailed.

4 CONCLUSIONS

In this chapter, a multi-technique characterisation has been employed to understand the phase and morphological evolution of the CuO/Al_2O_3 oxygen carrier, cycled multiple times at different temperatures. The overall temperature-dependent phase interactions have allowed to propose an overall migration and phase interaction mechanism over the range of 700-900 °C. Three competitive and intertwined phenomena are involved, including the competition between CuO and $Cu_xAl_yO_4$ formation, the sintering of CuO and the phase transition to α-Al_2O_3. Whether CuO or $Cu_xAl_yO_4$ will be formed is determined by the temperature, reaction duration as well as the alumina polymorph. Meanwhile, the CuO sintering will be determined by the temperature and the available copper oxide after every redox cycles.

Finally, the α-Al_2O_3 formation is determined by the presence of copper and the reaction temperature. Based on the analysis of the Al K-edge spectral feature, a possible role of copper was identified, whereby Cu^{2+} insertion in the transition aluminas lattice increases the proportion of octahedrally coordinated aluminium ions in the structure, possibly lowering the overall phase transition barrier to α-Al_2O_3. However, it could not be deduced whether the α-Al_2O_3 formation is a gradual process or if there are other factors contributing to this phase transition.

5 REFERENCES

[1] Diego L.F. de, Gayán P., García-Labiano F., Celaya J., Abad A., Adánez J. Impregnated CuO/Al 2 O 3 Oxygen Carriers for Chemical-Looping Combustion : Avoiding Fluidized Bed Agglomeration, *Energy & Fuels*, 2005, **19,** 5, 1850-1856. DOI: 10.1021/ef050052f.

[2] Belkhou R., Stanescu S., Swaraj S., Besson A., Ledoux M., Hajlaoui M., Dalle D. HERMES: A soft X-ray beamline dedicated to X-ray microscopy, *Journal of synchrotron radiation*, 2015, **22,** 4, 968-979. DOI: 10.1107/S1600577515007778.

[3] A. P. Hitchcock. *AXis2000*. McMAster University, Canada.

[4] F. M. F. de Groot, E. de Smit, M. M. van Schooneveld, L. R. Aramburo, and B. Weckhuysen. In-situ Scanning Transmission X-Ray Microscopy of Catalytic Solids and Related Nanomaterials, *ChemPhysChem*, 2010, **11**, 951-962.

[5] https://henke.lbl.gov/optical_constants/atten2.html.

[6] A. Boumaza, L. Favaro, J. Lédion, G. Sattonnay, J.B.Brubach, P.Berthet, A. M. Huntz, P. Roy and R. Tétota. Transition alumina phases induced by heat treatment of boehmite: An X-ray diffraction and infrared spectroscopy study, *Journal of Solid State Chemistry*, 2009, **182,** 5, 1171-1176.

[7] Y. Kato, K-I. Shimizu, N. Matsushita,T. Yoshida, H. Yoshida, A. Satusuma and T. Hattori. Quantification of aluminium coordinations in alumina and and silica-alumina by Al K-edge XANES, *Phys. Chem. Chem. Phys*, 2001, **3**, 1925-1929.

[8] A. Sharma, M. Varshney, J. Park, T.-K. Ha, K.-H. Chae and H.J. Shin. XANES, EXAFS and photocatalytic investigations on copper oxide nanoparticles and nanocomposites, *RSC Advances*, 2015, **5**.

[9] K-I. Shimizu, H. Maeshima, H. Yoshida, A. Satsuma and T. Hattori. Spectroscopic characterisation of Cu–Al2O3 catalysts for selective catalytic reduction of NO with propene, *Phys. Chem. Chem. Phys*, 2000, **2**, 2435-2439.

[10] J. Everett, F. Lermyte, J. Brooks, V. Tjendana-Tjhin, G. Plascencia-Villa, I. Hands-Portman, J. M. Donnelly, K. Billimoria, G. Perry, X. Zhu, P. B. O'Connor, J. Collingwood and N. D. Telling. Biogenic metallic elements in the human brain?, *Science Advances*, 2021, **7,** 24.

[11] A. B. Altman, C. D. Pemmaraju, S. Alayoglu, J. Arnold, C. H. Booth, A. Braun, C. E. Bunker, A. Herve, S. G. Minasian, D. Prendergast, D. K. Shuh and T. Tyliszczak. Chemical and Morphological Inhomogeneity of Aluminum Metal and Oxides from Soft X-ray Spectromicroscopy, *Inorganic chemistry*, 2017, **56**, 5710-5719.

[12] K. Sohlberg, S.J. Pennycook, S.T. Pantelides. The bulk and surface structure of γ-alumina, *Chemical Engineering Communication*, 2000, **181,** 1, 107-135.

[13] X. Krokidis, P. Raybaud, A.-E. Gobichon, B. Rebours, P. Euzen, H. Toulhoat. Theoretical Study of dehydration process of boehemite to γ-alumina, *The Journal of Physical Chemistry B*, 2001, **105,** 55, 5121-5130.

[14] M. Rudolph, M. Motylenko and D. Rafaja. Structure model of γ-Al2O3 based on planar defects, *IUCrJ*, 2019, **6**, 116-127.

[15] Bolt, P. H., et al. Formation of Nickel, Cobalt, Copper, and Iron Aluminates from a- and c-Alumina-Supported Oxides: A Comparative Study.

[16] M. Ozawa, H. Toda, O. Kato and S. Suzuki. Solid-state thermal behavior of copper-modified alumina toward lean-burn exhaust NO removal catalyst, *Applied Catalysis B: Environmental*, 1996, **8**, 123-140.

[17] Helmut Mehrer. *Diffusion in Solids*. Springer, 2007.

[18] F. Moya, E.G. Moya, D.Juve, D. Tr6heux, C. Grattepain and M. Aucouturier. SIMS study of copper diffusion into bulk alumina, *Scripta Metallurgica et Materialia*, 1993, **28**, 343-348.

[19] K. T. Jacob and C. B Alcook. Thermodynamics of CuA102 and CuA120, and Phase Equilibria in the System Cu20-Cu0-Al2O3, *Journal of American Ceramic Society*, 1975, **58**, 192-195.

[20] W. Hu, F. Donat, S. A. Scott and J. S. Dennis. The interaction between CuO and Al2O3 and the reactivity of copper aluminates below 1000 C and their implication on the use of the Cu–Al–O system for oxygen storage and production, *RSC Advances*, 2016, **6**, 113016-113024.

[21] K. Okada, A. Hattori, T. Taniguchi, A. Nukui and R. N. Das. Effect of Divalent Cation Additives on the γ-Al2O3-to-α-Al2O3 Phase Transition, *Journal of American Ceramic Society*, 2000, **83,** 4, 928-932.

[22] I. Levin and D. Brandon. Metastable Alumina Polymorphs: Crystal Structures andTransition Sequences, *Journal of the American Ceramic Society*, 1998, **81**, 1995-2012.

[23] R. Prins. On the structure of γ-Al2O3, *Journal of Catalysis*, 2020, **392**, 336-346.

Chapter 4:
Phase evolution of oxygen carrier during redox cycling

1 INTRODUCTION

In Chapter 3, the structural and morphological transformation of the supported oxygen carrier after 50 and 200 redox cycles were discussed, based on SEM and STXM experiments. Notably, the spectro-microscopic study has enabled to identify and associate the different chemical and polymorphic phases to the morphology of the copper-alumina system. However, some open questions remain regarding the extent of phase transition occurring at each redox cycle. What are the intermediate species during the redox reaction? Does the presence of the intermediate species affect the final phases at the end of the material cycling? In terms of Al_2O_3 phase transition, does the phase transition to α-Al_2O_3 occur gradually with each redox cycle or does it occur after a certain number of cycles? Or, is copper phase transition related to the α-Al_2O_3 phase transformation?

This chapter starts by providing the SEM observation of the material cycled after 1, 5, 10, 20 and 50 cycles at 900 °C. From the morphological information, the appearance of porous α-Al_2O_3 phase is only evident after a certain number of cycles (section 2). This observation set the goal to perform real-time characterisation of copper species evolution, in order to understand the phenomena occurring at every cycle.

In situ Quick XAS has been employed to probe the bulk evolution of the material over a large number of cycles. The *in situ* Quick XAS allows to obtain time-resolved spectrum down to second time resolution. The combination of elemental sensitivity, time resolution and penetration depth of hard X-rays makes QXAS an indispensable tool to probe *operando* chemical reaction. It is especially valuable to track intermediate species during the reaction when the kinetics of a given chemical reaction is very fast. Imtiaz et al. performed *in situ* XANES to investigate the evolution of CuO/Al_2O_3 oxygen carrier over 3 redox cycles at

750 °C. From the identification of the intermediate species during the phase transitions, the authors highlighted the effect of the reaction kinetics on structural disordering of the oxygen carrier during redox cycling. This study highlighted the significance of *operando* characterisation.

Moreover, it is important to understand whether the type of reducing gas or O_2 concentration have any impact on the phase transition of the CuO/Al_2O_3 oxygen carrier, especially over a large number of cycles. In this chapter the relative spectral contributions of the different copper-based phases have been monitored over 50 redox cycles with different reducing gases such as, CH_4, CO and H_2 as well as the different concentrations of O_2, 2.5vol% and 21 vol%. To achieve complementary information on the morphological changes in the materials, post-mortem characterisations of the sample after the XAS run was carried out using SEM.

2 MORPHOLOGICAL EVOLUTION DURING TGA CYCLINGS

In this section, evolution of the morphology of the oxygen carrier as a function of cycle number is presented. The oxygen carrier 13wt% CuO/Al_2O_3 calcined at 900°C has been cycled in TGA. *Figure 4.1* displays the SEM image of the TGA cycled samples, after 1, 5, 10, 20 and 50 cycles respectively. In Chapter 3, the fresh and the 50 cycles samples have been presented and discussed in the light of the possible phase transition. Here, the goal was to try to map out the events occurring at each cycle. Particularly, understanding concerning the formation of the α-Al_2O_3 phase would provide insights into the trend in spectral evolution identified throughout this chapter.

In general, the material is composed of an alpha alumina rim and $Cu_xAl_yO_4$. The microstructure does not seem to change much from the fresh sample to the sample cycled 10 times, except, copper phase concentration seems to become homogeneous with the number of cycles. In the fresh sample, and in samples cycled 1 and 5 times, copper concentration follows a gradient from the rim to the interior of the spherical grain. For the sample after 10 cycles, the concentration of copper seems to be much more homogeneous. In terms of the individual aluminate particle, there is an overall coarsening with the number of cycles observed in the higher magnification images (Appendix D.1) The sintered particles

are found closer to alpha alumina rim in the 5 cycles sample and the interior of the grain in the 10 and 20 cycles samples.

The 20 cycles sample displays some dark grey areas appearance (marked by red squares). These areas are composed of alpha alumina and surrounded by Cu-rich aluminate phase. Such patches of alpha alumina are not observed in the interior of the samples cycled after 5 or 10 times. The sample cycled 50 times is mostly composed of porous alpha alumina and CuO and few denser areas made of aluminate phase (discussed in detail in chapter 3).

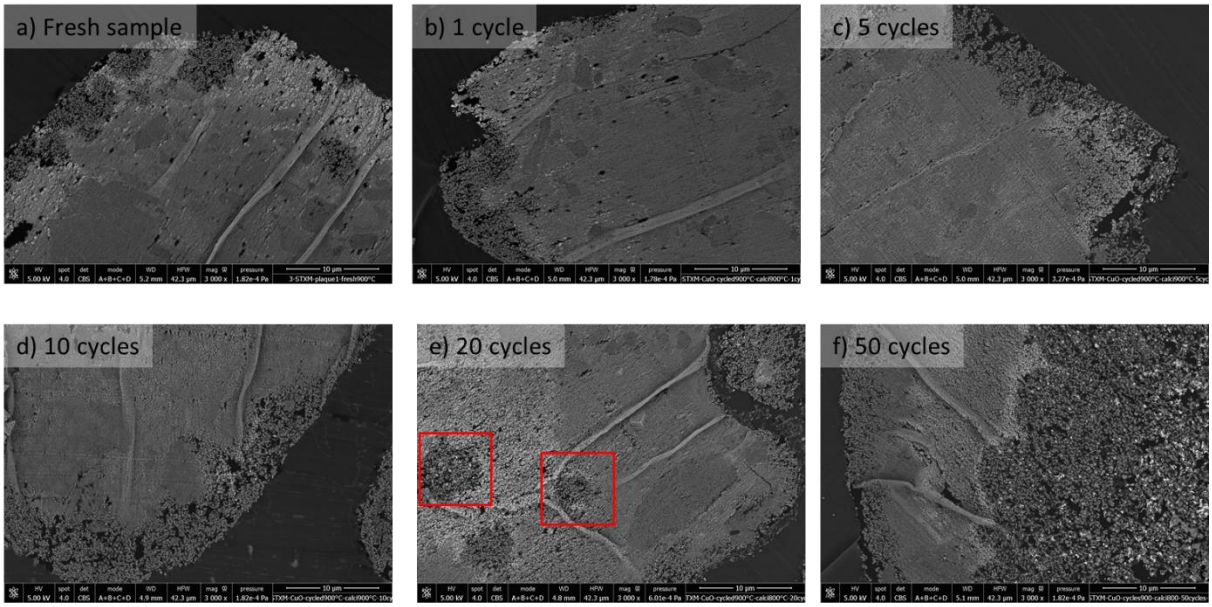

Figure 4.1: SEM image of samples in fresh condition (a) and after redox reactions at 900 °C, carried out in TGA after b) 1 cycle, c) 5, c) 10, d) 20 and e) 50 cycles.

The 20 cycles sample is further characterised in STEM-EDS. *Figure 4.2* reports the STEM-EDS imaging of the Cu-aluminate/α-Al_2O_3 interface of the "patches" areas in the 20 cycled sample. As observed from the *Figure 4.2b*, the copper aluminate phase exists as aggregation of small particles (circled in white) and large particles (pointed with a white arrow). Next to the copper aluminate phase, large particles of α-Al_2O_3 phase is observed in red (pointed with a green arrow). Provided that the reaction between CuO and α-Al_2O_3 occurs at a temperature higher than 950 °C to form $CuAl_2O_4$ [1], the appearance of the large $Cu_XAl_yO_4$ particles is likely to have resulted from the sintering of the small $Cu_XAl_yO_4$ particles.

Moreover, large particles of CuO are only found in the α-Al_2O_3 matrix (*Figure 4.2c* and d). No CuO is noted in the denser area which is mostly composed of copper alumina with carrying percentages of copper and possibly transition alumina.

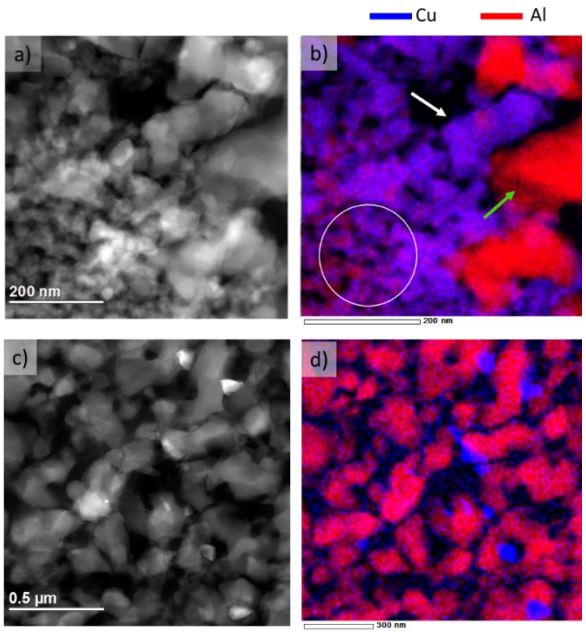

Figure 4.2: a,d) STEM and b,c) EDS of 13wt%CuO/Al_2O_3-900 sample cycled 20 times at 900 °C, displaying Cu-aluminate/α-Al_2O_3 phases.

The 20th cycle is an approximate threshold point after which the different copper phases undergo more drastic evolution. Besides that, the SEM images of the 20th cycle display patches of α-Al_2O_3, Thus, making the 20 cycled sample significant to correlate the spectral trend (in XAS) and the α-Al_2O_3 phase transition.

The prediction of the transition between the different copper species and the intermediate states during these transformations remains difficult from post-mortem analyses. Hence, it is pertinent to obtain dynamic phase transition information to understand the cycle-dependent behaviour of the oxygen carrier. It is the objective of the Quick XAS experiment detailed in the further parts of the chapter.

3 XAS EXPERIMENTAL AND DATA ANALYSIS PROTOCOL

The redox cycling of the 13wt% CuO/Al_2O_3-900 samples were carried out in Quick XAS. After the *in situ* experiment, the microstructure of the material was characterized using SEM. The working principle of XAS has been described in Appendix B.1. In this section the details of the experimental parameters and data treatment protocol are described.

3.1 EXPERIMENTAL SETUP

The operando experiments were performed at the ROCK beamline at Synchrotron SOLEIL in Saint-Aubin, France. The ROCK beamline uses a bending magnet source and can probe the samples at an energy range of 4.5 to 40 keV. The beamline is specifically dedicated to monitor fast kinetic processes and simultaneous characterisation of different chemical elements present in the material, thanks to a high level of automation to achieve fast changes of monochromators and optimization of mirrors and detectors. The Si (111) and Si (220) monochromators lie between a flat mirror and a collimating mirror made of Pd, Pt and B_4C for harmonic rejection. The detector is composed of ionization chambers (from OKEN) for detection in transmission or PIPS for fluorescence detection. The sample can be moved in *x* (horizontally) and *z* (vertically) directions. The probe size was adjusted to have a dimension of ~300 µm horizontally and ~500 µm vertically. *Figure 4.3* displays the experimental setup of the *in situ* experiment.

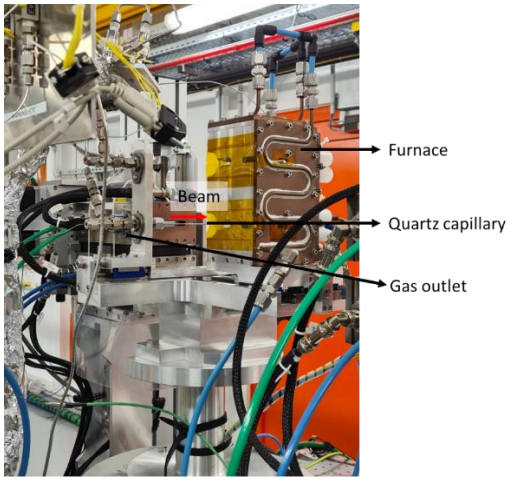

Figure 4.3: The experimental setup of the in situ XAS run, depicting the furnace, direction of the beam, the capillary reactor and the gas line.

The data acquisitions were carried out at Cu K-edge, collected in transmission mode using two ionization chambers filled with nitrogen gas. The second ionization chamber was used to measure the transmission in the sample and the third was dedicated to collect transmission data from a reference copper foil. The temporal resolution was set to collect 2 spectra per second with increasing angles and 2 spectra with decreasing angles.

Reactor configuration

The reactor is based on a plug flow configuration consisting of a 1.2 mm external diameter capillary with 20 µm wall thickness made of quartz. The sample was simply put inside the capillary without crushing or dilution in its original granular form (100 to 200 µm). The reactor bed was secured to avoid dispersion of the material during gas transport by putting 2-3 mm of rock wool on each side. The total mass of material used for the experimental run ranges from 7 – 10 mg with a bed thickness within 5 – 7 mm range. Special care has been taken during the filling of the tubes to avoid over or under densifying of the rock wool and the sample bed to ensure proper gas transfer. Once the capillaries were filled, they were attached to the sample holder horizontally (as shown by the white line in *Figure 4.4*) and a thermocouple was inserted through the right side of the capillary. The capillary was then glued to the sample holder ensuring proper sealing on both sides to avoid gas leakage. The setup sample holder was taken to the XAS experimental bench and attached to the gas inlet and outlet and the furnace. The sample was subjected to 1 atm of gas pressure. The furnace developed at the ROCK beamline can heat the sample up to 1000 °C. The outlet of the gas was connected to a mass spectrometer. At the end of each experiment, the sample was carefully collected by breaking the capillary, for further analyses.

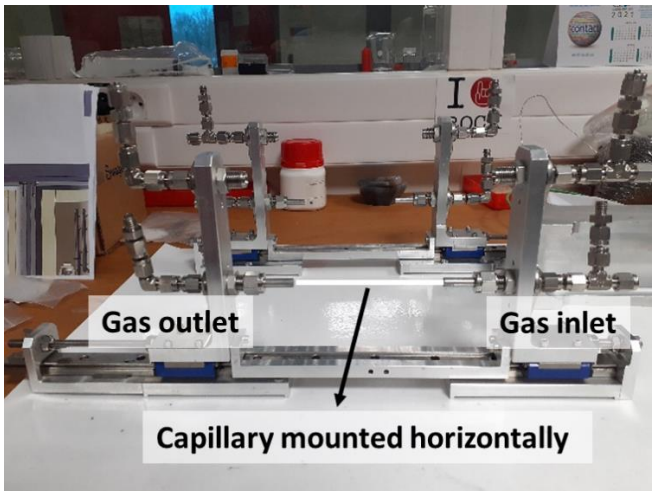

Figure 4.4: The sample holder where the capillary (shown with a white line) is mounted horizontally.

3.2 EXPERIMENTAL PROGRAM

Ex situ analysis were carried out on the of the fresh samples, after 50 and 200 cycles of CuO/Al_2O_3-700, CuO/Al_2O_3-800 and CuO/Al_2O_3-900 containing 13wt% of copper, according to the list of experiments provided in Chapter 2. The linear combination fitting of the *ex situ* samples has been discussed in Chapter 3.

The *ex situ* samples also included the reference samples. For the reference samples, the following five copper-based phases were considered: $CuAl_2O_4$, $CuAlO_2$, Cu_2O, CuO and metallic copper. The preparation of the copper aluminate reference samples is provided in Chapter 2. The spectral features and their associated transitions are presented in the following section.

In situ experiments were carried out on the sample calcined at 900 °C. Five *in situ* experiments were carried out at 900 °C, by either changing the type of reducing environments or by varying the concentration of the oxygen gas during the oxidation steps. To avoid mixing of the oxygen with the reducing gas, the reactor was purged with a step of inert gas. Hence, the redox cycles were composed of 4 steps: 1st step under inert gas with N_2 (after oxidation), reduction step, 2nd step under inert gas (after reduction) and oxidation step.

The theoretical duration of gas flow required to achieve full conversion for each sample during oxidation and reduction was calculated considering a sample mass of 7 mg, as a

function of reactive gases and respective molar flow rate (assuming STP condition). As samples were analysed roughly halfway across the reactor bed (related to beam position on the capillary), expected durations for completion of the reaction were divided by two as an additional assumption. Calculations results are reported in Table 4.1. For example, for H_2-O_2 experimental conditions, full conversion of material should be reached in 45 seconds of gas flow during oxidation and reduction, in the centre of the capillary. Therefore, a higher duration of 90 s was set for both oxidation and reduction. These durations were applied then for all experiments, in order to compare all experiments with a same ageing time.

However, considering the mass during the sample preparation, exact dilution of the gas and flow rate values, and eventual mass transfer limitations, some of the experiments might not have undergone complete reactions through the sample volume. This should be considered for further data analysis.

Table 4.1: Theoretical duration of oxidation and reduction for the given mass and experimental conditions.

Sample	Oxidation (seconds)	Reduction (seconds)
$H_2 – O_2$ 7 mg	44	44
$CO – O_2$ 10 mg	63	63
$CH_4 – O_2$ 8 mg	50	7
H_2 – air 7.5 mg	7	47

The details of the 5 experiments with their respective experimental parameters are presented in table 4.2

Table 4.2: The list of the in situ experiments and the parameters used to carry out the oxidation and reduction reactions at 900 °C.

Sample	Oxidation	Reduction	Inert gas	Mass, cycle duration, # cycles
$H_2 – O_2$	- 7 mL/min 2.5% O_2/N_2 - 90 seconds	- 7 mL/min 2.5% H_2/N_2 - 90 seconds	- N_2 - 7 ml/min - 90s	7 mg 6 min 50 cycles
$CO – O_2$	- 7 mL/min 2.5% O_2/N_2 - 90 seconds	- 7 mL/min 2.5% CO/N_2 - 90 seconds	- N_2 - 7 ml/min - 90s	10 mg 66 cycles
$CH_4 – O_2$	- 7 mL/min 2.5% O_2/N_2 - 90 seconds	- 7 mL/min 5% CH_4/10 % CO_2/N_2 - 90 seconds	- N_2 - 7 ml/min - 90s	8 mg 6 min 46 cycles
H_2 – air	- 7 mL/min 10.5% O_2/N_2 - 90 seconds	- 7 mL/min 2.5% H_2/N_2 - 90 seconds	- N_2 - 7 ml/min - 90s	7.5 mg 6 min 45 cycles

3.3 DATA TREATMENT

To treat the large volume of data generated during the experimental run, two graphical user interfaces (GUI) have been developed by the ROCK beamline – Extract-GUI and Normal_GUI. The Extract_GUI is used to convert the raw data (NEXUS files) into ASCII format containing 10 columns with 1) Energy, 2) Bragg Angle, 3) absorption of the sample, 4) absorption of the reference foil, 5 to 7) signal of the ionization chambers (I_0, I_1 and I_2), 8) monochromator direction, 9) fluorescence signal and 10) time of start of the experiment. In the extraction process, any angular offset is corrected.

In the Normal_GUI, the data previously extracted are calibrated and normalized for further analysis. *Figure 4.5* presents the GUI of the Normal_GUI with the available options to correct the energy offsets and the normalization of the dataset. Different options are available for the **Energy calibration** – the calibration can be carried out on the known references by offsetting the position of energy. The offset value is written on the **E0** box as shown on the right side of the window (*Figure 4.5)* and followed by “shift to E0” to calibrate the whole dataset. For experiment with low signal to noise for the reference sample, “align smooth reference” can be used for the calibration. Finally, energy calibration can be done within a selected energy range of the data using “align glitches”, which in the present study ranges from 9070 to 9110 eV.

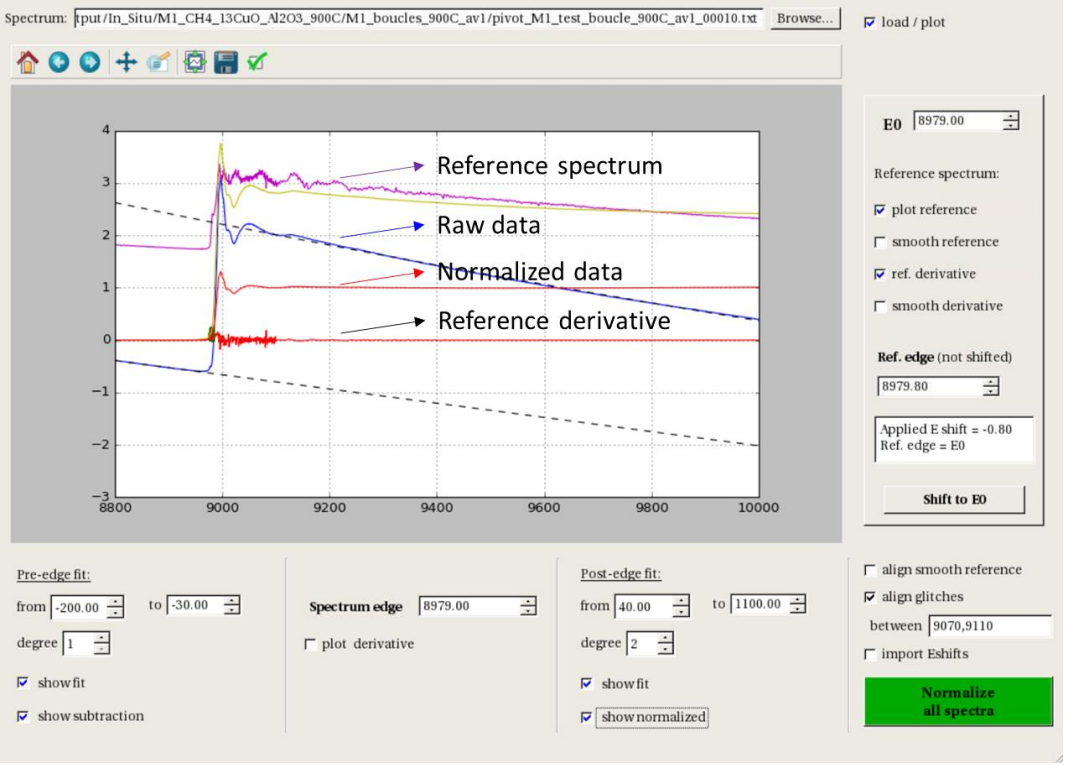

Figure 4.5: "Normal_GUI" graphical user interface, where the purple, blue and red spectra define the reference, raw and normalized data.

The normalization process helps to regularise the data with respect to the differences in the sample thickness, sample preparation, concentration of the absorber, detector and the amplifier settings, and any other experimental parameters that may have an impact on the absorption spectra. The normalization of the data involves 1) the removal of a linear function in the pre-edge region with respect to the edge energy of the spectrum (-200 to -30 eV, for the present sample) and 2) the calculation of a polynomial function in 1st or 2nd order to define the post-edge range of the spectrum (40 to 1100 eV).

Once the datasets are normalised, they are analysed using two chemometric methods, Principal Component Analysis – Singular Value Decomposition (PCA-SVD) and Multivariate Curve Resolution with Alternating Least Squares (MCR-ALS) to determine the species present in the datasets. The MCR-ALS GUI toolbox used in this study was developed by Tauler et al. in Matlab [2,3]. MCR-ALS is a method used to solve an unknown and unresolved mixture of a multicomponent system. The absorption spectra obeying Beer-Lambert law fulfil the requirement of linear dataset required to solve using MCR-ALS method. The experimental data are presented in a matrix form.

MCR methods are based on a bilinear model described by equation (1) $D = CS^T + E$. This equation is a multiwavelength extension of Beer-Lambert's law in a matrix form [3]. The *D* matrix are the spectra recorded at the given energies during the experiment. *C* matrix is the concentration profiles of the pure components, S^T is the transposed matrix of *S* containing the normalized XAS spectra of the pure components, and *E* is the residue such as experimental uncertainties. Equation 1 is solved iteratively using the ALS algorithm to calculate the concentration *C* and the pure spectra S^T matrices fitting the experimental dataset *D*. The optimization is carried out for a selected number of components and using initial estimates of either *C* or S^T. The initial estimate of ***C*** was obtained using Evolving Factor Analysis (EFA) in this study. The initial estimate of *C* can also be used either from the EFA or other methods described in the original papers [2,3]. For the data fitting several constraints such as non-negativity, unimodality or closure can be applied. The convergence is reached when the relative differences in the standard deviation of the residuals between the experimental data and the ALS fitting are less than a pre-selected value typically 0.1%.

In this study, EFA algorithm was used to find the spectral profiles of the components in each dataset. Several constraints are used for the *C*-matrix such as: non-negativity of the concentration and the sum of concentration should be equal to 100%. For the spectral matrix *S*, only non-negativity constraint was put in place.

To carry out the data treatment, several difficulties were encountered:

1) The spectra recorded at 900 °C are significantly different compared to the references collected at room temperature. At higher temperature, the mean square relative distance, or the Debye-Weller factor (σ^2) value is higher which broadens the spectral features [4].

2) At a given cycle the sample contains a mixture of several Cu-containing phases (CuO and copper aluminate with varying percentage of copper within the same sample).

3) The percentage of copper within the aluminate changes as a function of the redox cycles.

The phase changes during redox cycles make it difficult to refer to a particular $Cu_xAl_yO_4$ composition. The percentage of the different copper phases varied from one cycle to another, and as seen in Chapter 3, copper-aluminate content decreases and copper oxide content increases with the progression of the cycling. Moreover, the Cu-percentage in the

aluminate is critical since the spectral feature of the copper aluminate changes with the percentage of copper present in the spinel phase [5].

In terms of the spectral features it was difficult to match with the reference spectra or the features variation depending on the number of components chosen to solve the MCR-ALS, the volume of data chosen or even from one experiment to another. Hence, two approaches have been employed to consider the effect of temperature and the effect of the copper aluminate features evolution.

The copper aluminate is assumed to be constant and globally composed of 13wt% CuO. The copper-aluminate is referred to $Cu_xAl_yO_4$ and it is assumed to remain the same throughout the redox cycling, for all the samples.

It was decided to extract "reference" spectra at 900 °C (will be referred to as ref_900, such as Cu_2O_900) by considering all the experimental datasets, and not the reference samples. For example, the Cu_2O reference-900 spectrum has been extracted from CO-O_2 dataset as this sample has been cycled 66 times and at the end of the cycle the material was only composed of Cu_2O. Taking in account a possible heterogeneity in composition between samples used for the different experiments, the copper aluminate "reference" at 900 °C is extracted uniquely from each dataset.

Finally, these reference samples were imposed and solved by linear combination to fit the datasets to obtain the relative concentrations of the different species as a function of the number of redox cycles. It should be noted that the "relative concentration" is not the absolute concentration of the different copper species, rather the **relative spectral contribution** of the different copper phases. Hence, the values are expressed as %.

3.4 REFERENCE SAMPLES

In this section, the reference samples spectra collected at room temperature and the reference spectra extracted from the experimental data at 900 °C using the MCR-ALS algorithm are discussed. The identification, choice and justification for the high temperature reference spectra are presented in *Figure 4.6* and are also discussed in detail.

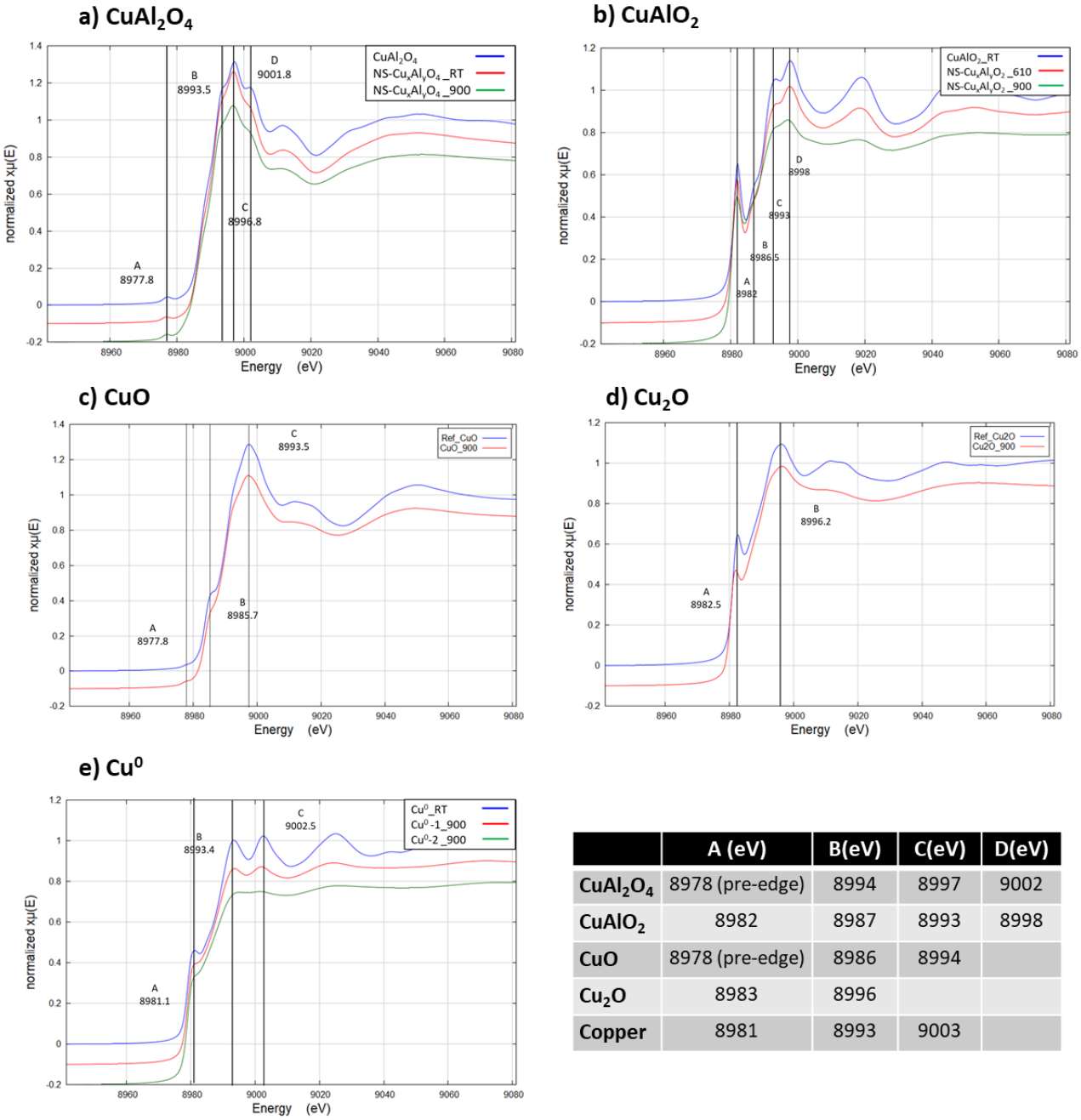

	A (eV)	B(eV)	C(eV)	D(eV)
$CuAl_2O_4$	8978 (pre-edge)	8994	8997	9002
$CuAlO_2$	8982	8987	8993	8998
CuO	8978 (pre-edge)	8986	8994	
Cu_2O	8983	8996		
Copper	8981	8993	9003	

Figure 4.6: Reference spectra collected at room temperature and extracted from the experimental dataset used as reference at 900 °C for a) stoichiometric $CuAl_2O_4$ reference at room temperature (ref-$CuAl_2O_4$) in blue, non-stoichiometric $Cu_xAl_yO_4$ reference at room temperature (NS- $Cu_xAl_yO_4$_RT) in red, non-stoichiometric $Cu_xAl_yO_4$ reference at 900 °C ($Cu_xAl_yO_4$_900) in green, b) stoichiometric $CuAlO_2$ reference at room temperature (ref-$CuAlO_2$) in blue, non-stoichiometric $Cu_xAl_yO_2$ reference at 610 °C ($Cu_xAl_yO_2$_610) in red, non-stoichiometric $Cu_xAl_yO_2$ reference at 900 °C ($Cu_xAl_yO_2$_900) in green, c) reference CuO at room temperature (in blue) and CuO at 900 °C in red, d) reference Cu at room temperature (in blue), reference Cu at 900 °C in red and green, extracted from the experimental data and the tabulated values of the main peaks.

3.4.1 $CuAl_2O_4$

*Figure 4.6*a displays the stoichiometric $CuAl_2O_4$ reference at room temperature in blue, the non-stoichiometric $Cu_xAl_yO_4$ reference at room temperature in red and the non-stoichiometric $Cu_xAl_yO_4$ "reference "at 900 °C in green.

The stoichiometric reference was collected *ex situ* using a synthesized sample (synthesis protocol provided in Chapter 2).

The $Cu_xAl_yO_4$ is the 13wt% CuO fresh sample which was calcined at 900 °C (also, provided in Chapter 2). Two $Cu_xAl_yO_4$ "references" were extracted by solving the temperature ramp data of the respective experimental data set by using the MCR-ALS method. The first one is $Cu_xAl_yO_4$_RT representing the room temperature feature (similar to the *ex situ* reference sample), and the second one is $Cu_xAl_yO_4$_900 representing the broadened spectral features at higher temperature.

For all the three spectra, the 4 distinct peaks are noted. Peak A at about 8978 eV is a pre-edge peak resulting from 1s → 3d transition, similar to CuO [5]. Peaks B to D result from the different Cu atoms environments (tetrahedral and octahedral sites) present in the copper aluminate phase [6].

3.4.2 $CuAlO_2$

Figure 4.6b, displays the stoichiometric $CuAlO_2$ at room temperature (in blue), non-stoichiometric $Cu_xAl_yO_2$ data collected at 610 °C ($Cu_xAl_yO_2$_610) in red and non-stoichiometric $Cu_xAl_yO_2$ spectra extracted at 900 °C ($Cu_xAl_yO_2$_900) in green. The synthesis of the reference stoichiometric $CuAlO_2$ and the non-stoichiometric $Cu_xAl_yO_2$ samples are described in Chapter 2.

The extraction of the reference spectra for the $Cu_xAl_yO_2$ phase was difficult since this phase is sub-stoichiometric, with composition probably varying during cycles, and exists as an intermediate specie, possibly mixed with CuO, Cu_2O and $Cu_xAl_yO_4$.

The spectra of the different $CuAlO_2$ display features of both Cu(i) at 8983 eV and 8997 eV and Cu(ii) at 8986 eV and 8994 eV [7].

3.4.3 CuO

The spectra of the reference CuO phase at room temperature and the extracted reference at 900 °C are presented in blue and red, respectively in *Figure 4.6c*. The reference used for the CuO phase is analysed using a commercial CuO powder from Sigma Aldrich. The CuO "reference" at 900 °C was extracted from the H_2-air dataset where CuO is expected to form during oxidation rather than Cu_2O

The CuO K-edge spectrum is characterized by three peaks representing the pre-edge (A at 8978 eV) for the 1s → 3d transition, B (8986 eV) is due to the 1s→ 4 p shakedown and C (8994 eV) is due to 1s → 4p continuum transition [4,8]. The pre-edge peak is specific to Cu(ii) species due to the presence of $3d^9$ configuration.

3.4.4 Cu_2O

Similarly, *Figure 4.6d* presents the reference of Cu_2O at room temperature and the extracted reference at 900 °C.

Here, two peaks are noted, the first peak at 8983 eV corresponds to the electric dipole allowed 1s → $4p_{xy}$ and the second peak B at 8996 eV is assigned to 1s to $4p_z$ [4,8]. The first peak is a characteristic peak of Cu(i) species.

3.4.5 Metallic copper, Cu^0

The reference of metallic copper *Figure 4.6e* shows three prominent peaks A (at 8981.1 eV) , B (at 8993.4 eV) and C (at 9002.5 eV). The feature at A results from the 1s to 4p transition in a $3d^{10}$ configuration [8]. The reference metallic copper at room temperature was carried out on the copper metallic foil used for the data acquisition. The difference between the RT and Cu-1_900 arises from 1) difference in the size, while Cu^0_RT is a foil, Cu-1_900 collected from the experimental data is composed of nanoparticles and 2) the broadening of the spectral feature due to the effect of temperature. For the extracted reference at 900 °C, two spectra are presented and termed as Cu-1 and Cu-2. The ambiguity in the naming is done purposefully since the difference could arise from several possible reasons. The two peaks B and C are discernible in Cu-1_900 but they are not very pronounced for Cu-2_900. The presence and the contribution of these two different spectra varied within the same set of experimental data as well as from one experiment to another.

Three possible reasons are identified. It could be due to a change in the particle size, big particles at the beginning of the experiment leading to Cu^0-1_900 spectral feature, and smaller particles with the progression of the reaction leading to Cu^0-2_900. The interpretation of the effect of particle size is based on the broadening of the resonances in the XANES spectra for the metallic phase systematically observed for the different samples upon cycling indicating that the medium range order around Cu is decreasing with cycles [9]. However, this hypothesis contradicts the observation of copper/copper oxide sintering, identified using SEM (presented in Chapter 3).

A loss of signal might also occur due to the formation of porosity in the alumina support, which should be manifested in the spectral feature of both the oxidised and the reduced phases. In the reduced sample presented in Chapter 3 no significant porosity is noted. Besides, the broadening of the peak is only noted for the reduced phase.

Another possibility is the incomplete reduction of the oxide phase giving rise to a core-shell like structure with an oxide core and metallic Cu shell. This hypothesis is the mostly likely as the idea of incomplete reaction corroborates with the experimental program. Both Cu^0_1 and Cu^0_2 features contribute in the oxidation and reduction steps. These hypotheses will be discussed in the light of individual experiments, in the results section.

3.4.6 Conclusion

The high temperature references were used to determine the concentration profiles using the linear-combination feature of the MCR-ALS. The high temperature references that were used to solve the *in situ* redox cycling datasets are $Cu_xAl_yO_4$_900 for the copper (ii) aluminate, $Cu_xAl_yO_2$_900 for the copper (i) aluminate ($CuAlO_2$), CuO_900 for copper (ii) oxide, Cu_2O_900 for the copper (i) oxide and Cu-1_900 and Cu-2_900 for the metallic copper.

4 RESULTS AND DISCUSSIONS

In the result section, the H_2-O_2 sample is discussed in detail in the light of the possible chemical reactions occurring during each step of a cycle. Then an overview of the changes of the copper phases as a function of the number of redox cycles is presented separately

for oxidation and reduction reactions. In the following sections, the effect of the reducing gas and the O_2 concentration on the relative spectral contributions is explained and discussed in relation to phase variations.

4.1 *IN SITU* REDOX CYCLES, CASE STUDY H_2-O_2

Each *in situ* experiment is composed of 3 steps: temperature ramp up from room temperature to 900 °C, the oxidation-reduction cycles, and the ramping down of the temperature.

Before discussing the result, it is first important to discuss the phase stability of the Cu-Al-O and Cu-O systems as the concentration of the O_2 would affect the oxidation state of the copper oxide or copper aluminium oxide. Thermodynamic phase diagrams of CuO-Al_2O_3 at isobaric condition and pressure vs temperature are presented in *Figure 4.7a* and *Figure 4.7b*, respectively.

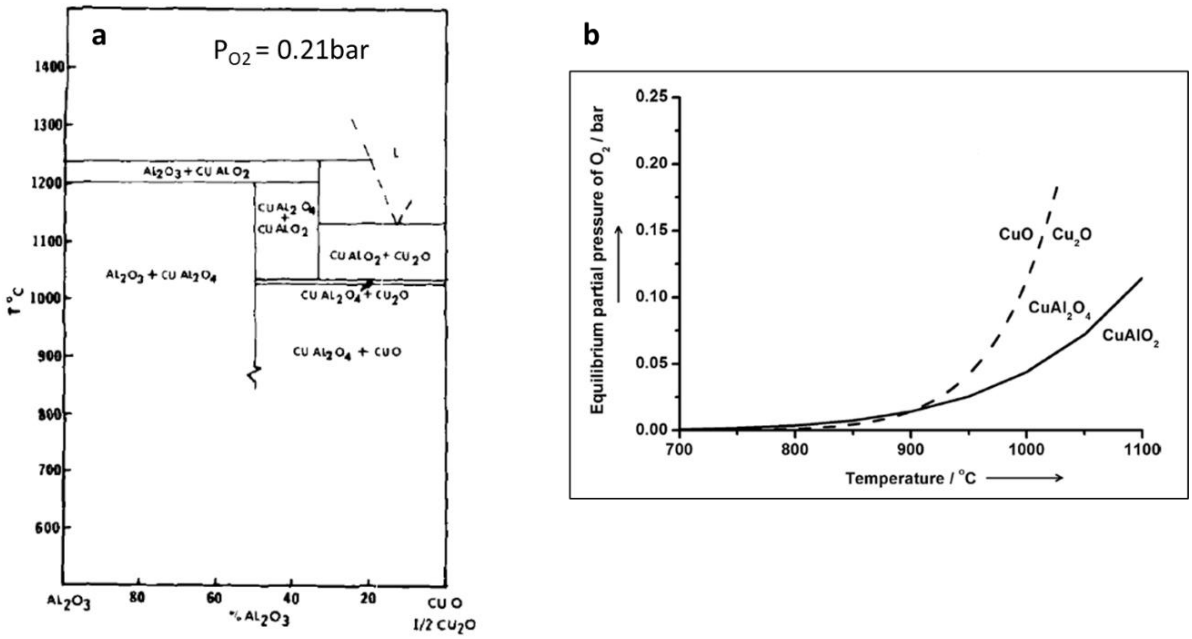

Figure 4.7: a) Isobaric section of ternary system Cu_2O-CuO-Al_2O_3 at P_{O2} = 0.21 bar and b) Equilibrium partial pressure of O_2 as a function of temperature for $CuAl_2O_4$/$CuAlO_2$ (in solid line) and CuO/Cu_2O (dashed line) taken from [10].

The stability of the $CuAl_2O_4$ depends on temperature and oxygen partial pressure as demonstrated in *Figure 4.7b*. Some studies reported that decomposition of $CuAl_2O_4$ takes place according to Reaction 4.1, to form $CuAlO_2$ and alumina. Other studies have reported

the formation of Cu_2O phase as well via reaction 4.2. Regarding pure CuO, it decomposes according to 4.3 [11]. In XAS experiment conditions, at 900°C under air, $CuAl_2O_4$ and CuO phases are most stable copper phases. However, it should be noted that the phase diagram in *Figure 4.7b* is based on bulk metal oxide phases. For nanosized particles, the equilibrium temperature of Reaction 4.1 is estimated to be lower [12]. The nano-size effect is also valid for the mixed copper-alumina phases.

$4\ CuAl_2O_4 \leftrightarrow 4\ CuAlO_2 + 2\ Al_2O_3 + O_2$ Reaction 4.1

$4\ CuAl_2O_4 \leftrightarrow 2\ Cu_2O + 4\ Al_2O_3 + O_2$ Reaction 4.2

$4\ CuO \leftrightarrow 2\ Cu_2O + O_2$ Reaction 4.3

4.1.1 Heating from 25 °C to 900 °C

The temperature ramp was carried out either under 2.5 vol% oxygen for all the experiments except H_2-air which was heated under air. The temperature was increased from room temperature to 500 °C at a rate of 20 °C/min, then at 15 °C/min from 500 °C to 700 °C and at 10 °C/min from 700 °C to 900 °C. Changes in the spectral features from room temperature to 900 °C are presented in *Figure 4.8a* and b for two sets of data, H_2 - O_2 and H_2 – air, respectively. At room temperature, the sample is composed of the $Cu_xAl_yO_4$. With the increase in temperature, as shown in both graphs, there is a decrease in the intensity of the main peak at 8996 eV along with damping in the multiple scattering zone. In addition, there is a significant peak broadening along the rising edge, right after the pre-edge feature at 8977 eV.

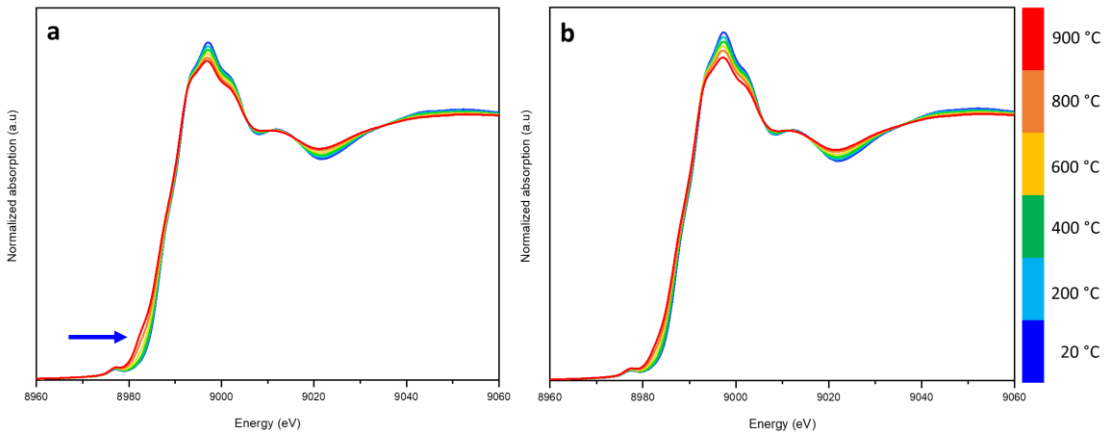

Figure 4.8: Spectral evolution during ramp up for H_2-O_2.

For the H_2 – O_2 dataset (*Figure 4.8a*) the area marked by a blue arrow displays the appearance of a bump-like feature starting a temperature of 600 °C. This feature becomes clearer with further increase in temperature. The position of the bump is at about 8982 eV which corresponds to the edge feature of either Cu_2O or $CuAlO_2$ phase. MCR-ALS fitting was carried out by imposing the spectra of $Cu_xAl_yO_4$, $Cu_xAl_yO_2$, Cu_2O, CuO and Cu^0 at high temperature points to the presence of mainly non-stoichiometric $Cu_xAl_yO_4$, Cu_2O and a very small percentage of metallic copper. The changes in the relative percentage of the three components with respect to the temperature change is presented in *Figure 4.9*. At the end of the 900 °C heating, the percentage of $Cu_xAl_yO_4$ and Cu_2O reached a value of ~85 % and ~15 %, respectively. No contribution from $Cu_xAl_yO_2$ specie was observed.

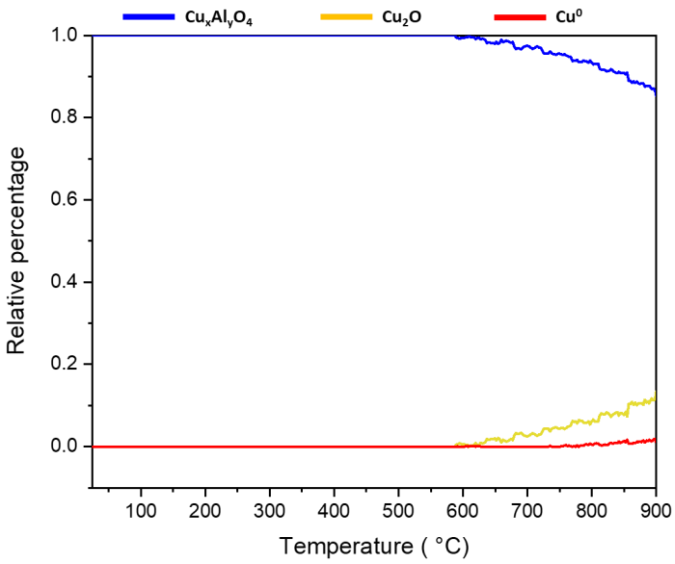

Figure 4.9: Change in the concentration of the species present during the ramping of sample H_2-O_2.

For the H_2 – air dataset, no contribution from neither Cu_2O nor metallic copper was observed, indicating that the sample is composed of $Cu_xAl_yO_4$ throughout the heating process. The difference between the two datasets can be attributed to the stability of the copper-alumina phases as a function of the oxygen partial pressure and the temperature as presented in section 1.

4.1.2 Reaction steps

Figure 4.10 displays the evolution of the spectral profile from oxidized state (blue line) to reduced state (red line) during the first reduction step and towards the end of the redox cycling, at the 40th cycle. Before presenting the concentration profile over the course of 50 redox cycles, it is important to first understand what is happening at each step of the reaction.

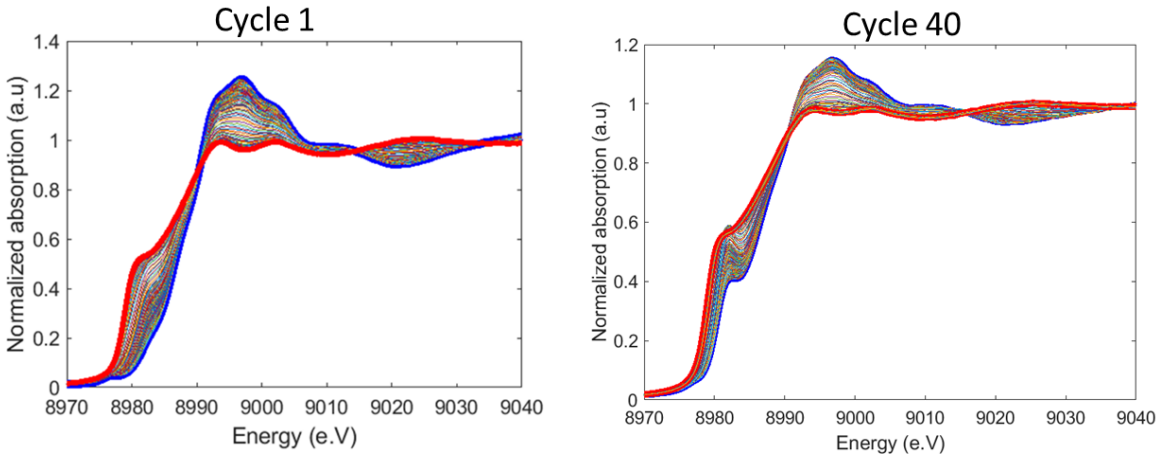

Figure 4.10: Spectral evolution during the oxidation (blue spectrum) to reduction (red spectrum) reaction at 900 °C for cycle 1 (left) and cycle 40 (right).

To illustrate the step of one redox cycle (inert gas with N_2, reduction, inert gas, and oxidation), the example of the $H_2 – O_2$ experiment is used. In *Figure 4.11*, the evolution of the concentration of the different copper phases as a function of the reaction gas during one cycle is presented. Cycle 1 (left) and Cycle 40 (right) display the concentration profiles for the first redox cycle and at the 40th cycle, with the following sequence $N_2 – H_2 – N_2 – O_2$.

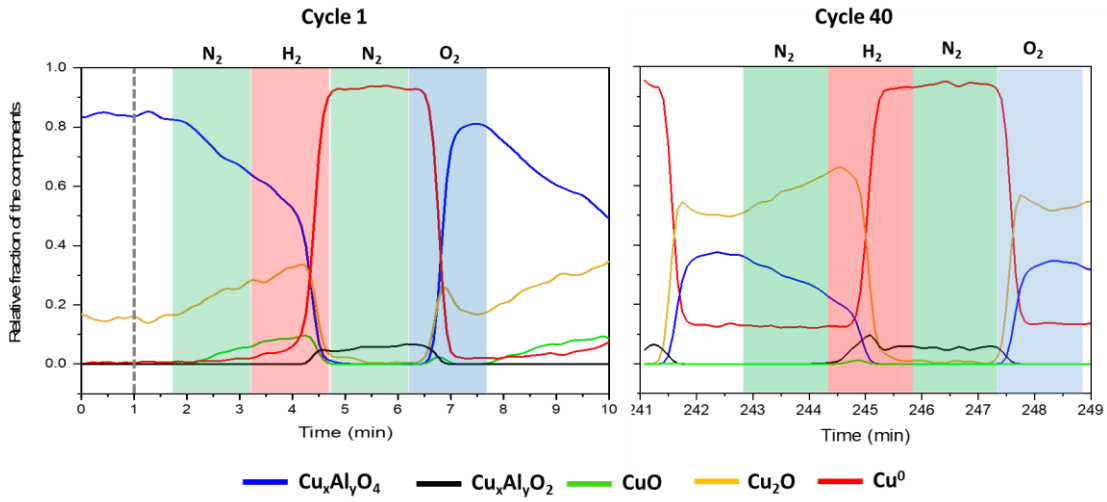

Figure 4.11: Change in the relative percentage of the copper-phases as a function of the four steps of the redox cycle – each step makes up 1.5 min. The duration and presence of the N_2, H_2 and O_2 are presented by green, red, and blue coloured areas, respectively.

Inert gas: At the start of the 1st cycle, the sample is still under 2.5% O_2. N_2 gas is introduced during 90 sec, as displayed by the green area in *Figure 4.11*. The decrease in the amount of $Cu_xAl_yO_4$ is gradual and at the same time the amount of Cu_2O increases, possibly via Reaction 4.2. No presence of $Cu_xAl_yO_2$ is noted during the inert gas step, contrary to what could be expected according to the literature (Reaction 4.1). Jacob and Alcook [13] have proposed a mechanism based on Reaction 4.3 at low O_2 partial pressure which has also been reported by Arjmand et al [11] and Izquierdo et al [14]. The difference may be due to longer duration of heating in the study of Jacob and Alcook [13] and Arjmand et al [11]. Indeed, a long annealing under N_2 atmosphere at 1000 °C was used as the synthesis protocol to obtain a pure $CuAlO_2$ phase as the reference sample (details in Chapter 2).

There is appearance of CuO right after the formation of Cu_2O and a few seconds later, metallic copper is observed in very small percentages (> 5 spectral %). This could be due to the reaction between the newly formed Cu_2O and the oxygen released from the reaction. Nevertheless, 5 % is a small quantity and care must be taken in the interpretation of such low amount.

Overall, at the end of the N_2 step, the amount of $Cu_xAl_yO_4$, Cu_2O, and CuO makes up for 60-65 %, 25-30 % and less than 5 % compared to 80-85 %, 15 – 20 % and 0 %, respectively, at the end of the 2.5 vol% O_2 -step.

Reduction: With the introduction of H_2 for 90 sec, there is a gradual decrease in $Cu_xAl_yO_4$ phase content, which then rapidly decreases to zero at the end of the reduction. Meanwhile, the Cu_2O content reaches its peak after about a minute, contributing to about 35 % of the phase distribution. Afterwards, the Cu_2O phase content decreases until the end of the reduction step. During the fast decrease in the oxides' fractions, there is a rapid increase in the metallic copper concentration. At about the same time, the $CuAlO_2$ phase emerged in very small percentage of about 4-6 %. At the end of the reduction step, the amount of metallic Cu accounted for more than 90 % of the phases and the rest was composed of Cu_2O and $CuAlO_2$.

The possible reactions are:

$CuAl_2O_4 + H_2 \rightarrow Cu + H_2O + Al_2O_3$ Reaction 4.4

$2\ CuAl_2O_4 + H_2 \rightarrow Cu_2O + 2\ Al_2O_3 + H_2O$ Reaction 4.5

$Cu_2O + H_2 \rightarrow 2\ Cu + H_2O$ Reaction 4.6

$2\ CuO + 2\ H_2 \rightarrow Cu_2O + 2\ H_2O$ Reaction 4.7

$CuO + H_2 \rightarrow Cu + H_2O$ Reaction 4.8

$Cu_2O + Al_2O_3 \rightarrow 2\ CuAlO_2$ Reaction 4.9

For Reaction 4.9 to occur, it requires presence of alumina for copper or copper oxide to react with. It is much likely that $CuAlO_2$ phase forms due to the reaction between Cu_2O and Al_2O_3 phases, since upon the reduction of Cu_2O further increase in $CuAlO_2$ is not observed.

Inert gas: Under N_2 after reduction, the amount of metallic copper remains constant. The percentage of $CuAlO_2$ increases slightly while the Cu_2O content decreases until there are no contributions at all, after about 45 s of N_2. There is no trace of other phases.

Re-oxidation: At the beginning of the oxidation, there is a rapid decrease in the amount of metallic copper with simultaneous increase in Cu_2O and $CuAl_2O_4$ following Reactions 4.10 and 4.13. Cu_2O reaches a maximum of 25-30 % after about 45 s of oxidation, after that the fraction of Cu_2O decreases slowly while the percentage of $CuAl_2O_4$ increases gradually via Reaction 4.14. There is a slight increase in CuO content as well (Reactions 4.11 and 4.12), but it decreases down to zero within few seconds. Both Cu_2O and CuO phases appear to be

intermediate species before forming $CuAl_2O_4$. It is likely that the oxidation reaction is not complete as the full conversion to $CuAl_2O_4$ could not take place (this is discussed later in the chapter). The incomplete reaction is evidenced from the presence of remaining metallic copper at the end of the oxidation step.

The possible reactions occurring during the re-oxidation step:

$4\ Cu + O_2 \rightarrow 2\ Cu_2O$ Reaction 4.10

$2\ Cu + O_2 \rightarrow 2\ CuO$ Reaction 4.11

$2\ Cu_2O + O_2 \rightarrow 4\ CuO$ Reaction 4.12

$2\ Cu + O_2 + 2\ Al_2O_3 \rightarrow 2\ CuAl_2O_4$ Reaction 4.13

$Cu_2O + 0.5\ O_2 + 2\ Al_2O_3 \rightarrow 2\ CuAl_2O_4$ Reaction 4.14

$CuO + Al_2O_3 \rightarrow CuAl_2O_4$ Reaction 4.15

Similarly, $CuAlO_2$ can also undergo a series of oxidation reactions:

$2\ CuAlO_2 + 0.5\ O_2 \rightarrow CuAl_2O_4 + CuO$ Reaction 4.16

$2\ CuAlO_2 + Al_2O_3 + 0.5\ O_2 \rightarrow 2\ CuAl_2O_4$ Reaction 4.17

Compared to the first cycle, at the 40th cycle, there is an increased presence of Cu_2O and unreacted copper phases during the oxidation reaction. Other than that, the intermediate species remain the same.

4.1.3 Evolution of the species as a function of the number of cycles

The change in the relative concentration of the different species during the progression of the cycles over 50 redox reactions is presented in *Figure 4.12*. As seen from the figure, the traits of the spectra change with the number of cycles for both oxidized and reduced states. For the oxidized sample, the bump at around 8983 eV corresponding to Cu_2O becomes prominent with increased cycling. For the reduced state, the progression of the number of cycles induces a flatter profile to the metallic copper spectra, above the edge.

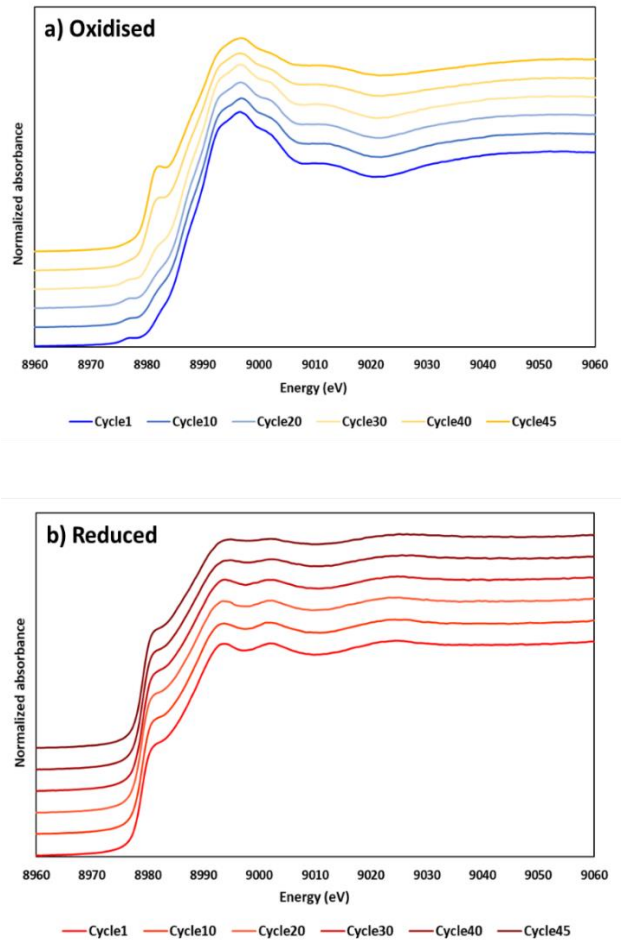

Figure 4.12: Change in spectral feature of the H_2-O_2 dataset at every 10 cycles during oxidation (a) and reduction (b). Cycle 1 (bottom) to cycle 45 (top) are presented in the graph.

In terms of the relative spectral contribution, *Figure 4.13* displays the change of the relative contributions of the different copper species at the end of each oxidation step from the beginning of the experiment to the 50th cycle. From the overall evolution during oxidation, only three species change – $Cu_xAl_yO_4$, Cu_2O and metallic copper. Overall, there is a decrease in the proportions of $Cu_xAl_yO_4$ and an increase in the percentages of the other two phases. While the metallic copper displays a steady increase of percentage by ~0.3 %/cycle, the change in $Cu_xAl_yO_4$ and Cu_2O contents depend on the number of cycles. We can divide the observation into two parts, from 0 to 26th cycle and from the 27th to 50th cycle. The rate of decrease of $CuAl_2O_4$ content is slow in the first part, decreasing at a rate of about ~-0.3 %/cycle. The Cu_2O content displays a slight decrease as well (~-0.3 %/cycle). Surprisingly, after the 26th cycle, the rate of decrease in the $Cu_xAl_yO_4$ percentage is 9 times faster, with a rate of ~-2.7 %/cycle,. The change in Cu_2O content displays a trend inverse to that of

$Cu_xAl_yO_4$ content decrease and exhibits an increase of ~2.5 %/cycle. There seems to be a threshold after which the system evolved rapidly and irreversibly.

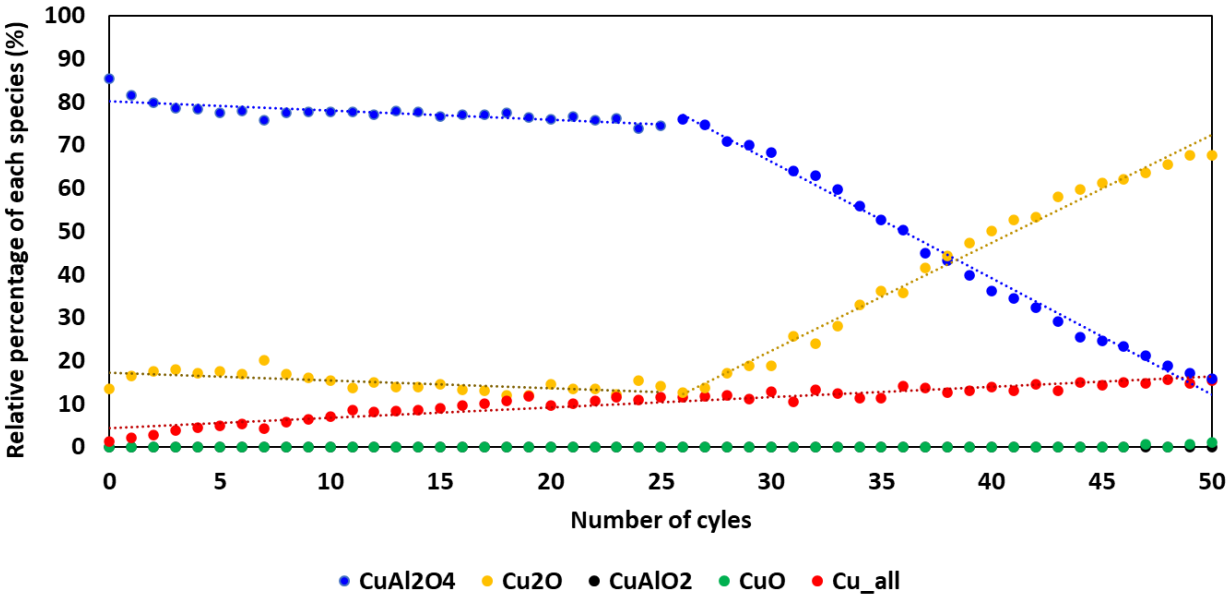

Figure 4.13: Relative percentages of the copper-species present at the end of the oxidation step throughout the 50 cycles.

Similarly, the breakdown of the proportions of the different copper phases at the end of each reduction step is presented in *Figure 4.14*. Here the main components are metallic copper and $Cu_xAl_yO_2$. No other copper oxides were discerned. Up to 45th cycle, metallic copper made up for 90 to 95 % with $Cu_xAl_yO_2$ making up for the remaining of the 5 to 10 % of the phases. After the 45th cycle, $Cu_xAl_yO_2$ content fell to almost zero.

It should be noted that in *Figure 4.14*, two metallic copper species are presented – Cu^0-1 and Cu^0-2. The Cu^0_all presented in the graph is the summation of the Cu^0-1 and Cu^0-2. It is evident from the graph that the two species are present in varying proportions through the 50 cycles, with Cu^0-1 decreasing and Cu^0-2 increasing with the number of the cycles.

Later in section 3.2, the presence of the two copper species in different samples will be compared and discussed.

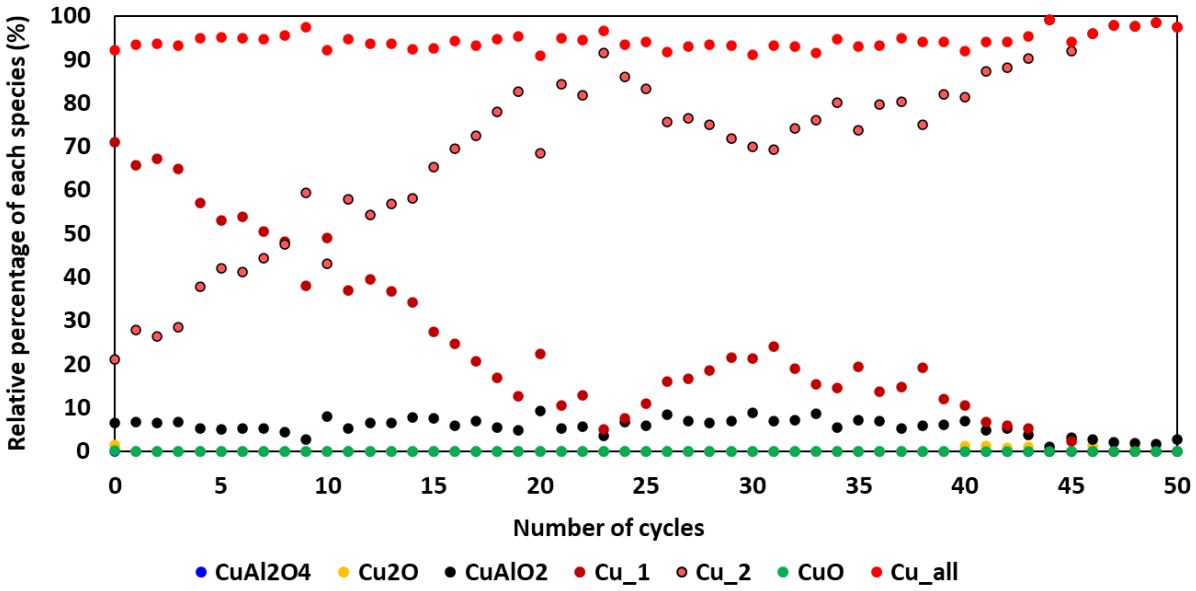

Figure 4.14: Relative percentages of the copper-species present at the end of the reduction step throughout the 50 cycles.

4.1.4 Ramp down

After the redox cycling, the temperature of the furnace was brought down to room temperature under O_2. *Figure 4.15* a and b display the spectral evolution and the contribution of the different species during the decrease in the temperature. Indeed, with the decrease in temperature, under low O_2 partial pressure, Cu_2O converts gradually to form CuO via Reaction 4.3 presented in section 1, as seen from the edge-energy shift in *Figure 4.15a*. The phase change starts to occur at a temperature of about 870 °C, and by 820 °C, the Cu_2O phase has been fully converted to CuO. The phase stability of the Cu_2O/CuO corroborates the finding in the literature discussed in section 1. The change is also evidenced from the concentration profile. Finally, at about 200 °C all the copper only exists as CuO according to the MCR-ALS fitting. However, the Linear Combination Fitting of the room temperature data displays a different phase proportion consisting of 90 % CuO and 10 % $Cu_xAl_yO_4$. The room temperature data were fitted with LCF algorithm using the Athena software.

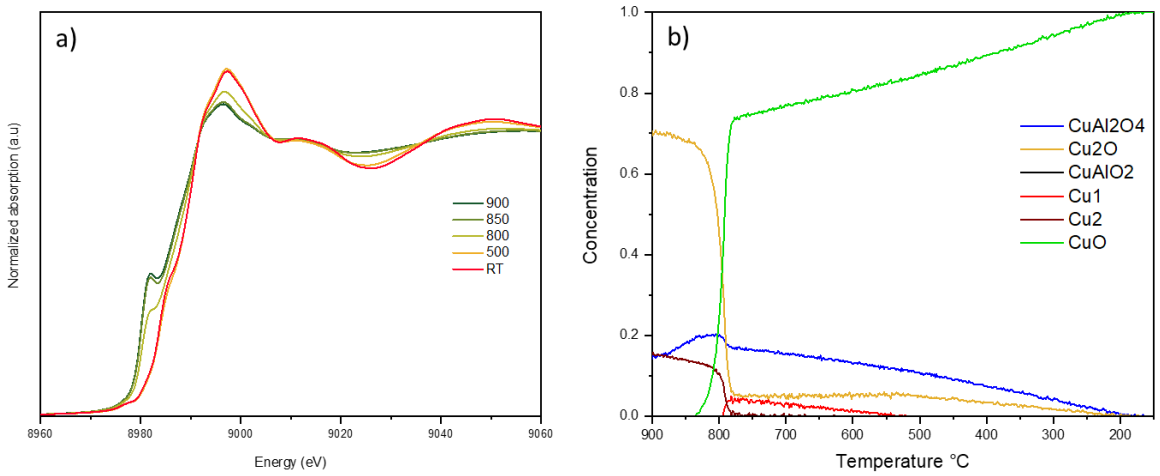

Figure 4.15: a) Change in the spectra during the cooling down from 900 °C to room temperature and (b) corresponding relative contributions of the different copper phases.

The phase percentage predicted by the evolving dataset especially during a temperature ramp might be misleading and difficult to fit, as the spectral feature is influenced by the temperature factor as well as the possible phase transition. Hence, verification of the analysis must be done with the room temperature data. Furthermore, characterisation of the sample with other techniques is pertinent.

To verify and complement the *in situ* XAS analysis, post-mortem characterisation of a cross-cut section of the sample has been carried out using SEM-EDS. *Figure 4.16* reveals the SEM image of the sample after the *in situ* XAS run with $H_2 – O_2$ gas. The support grains are found to be almost homogeneous within the sample (Appendix D). Two types of overall grain textures are visible according to *Figure 4.16 a*. The grains are mostly composed of α-Al_2O_3 (as identified in Chapter 3). Very few grains exhibit copper-containing matrix such as the grain on the left side of the image in *Figure 4.16 a*. Higher magnification image allows to identify 4 different textures: Copper aluminate with different proportions of copper: 1) lower content and 2) higher content, according to the SEM greyscale, 3) porous α-Al_2O_3, and 4) CuO. The identification of the different chemical and polymorphic phases were previously established based on the greyscale and the STXM-XAS characterisations (Cf Chapter 3).

Compared to the TGA-cycled sample after 50 cycles, the H_2-O_2 displays a higher proportion of porosity and phase segregation between the CuO and the α-Al_2O_3 phase. A comparison

of phase percentage and the morphology of the TGA cycled sample, H_2-O_2 and the H_2-air is presented in section 3.5

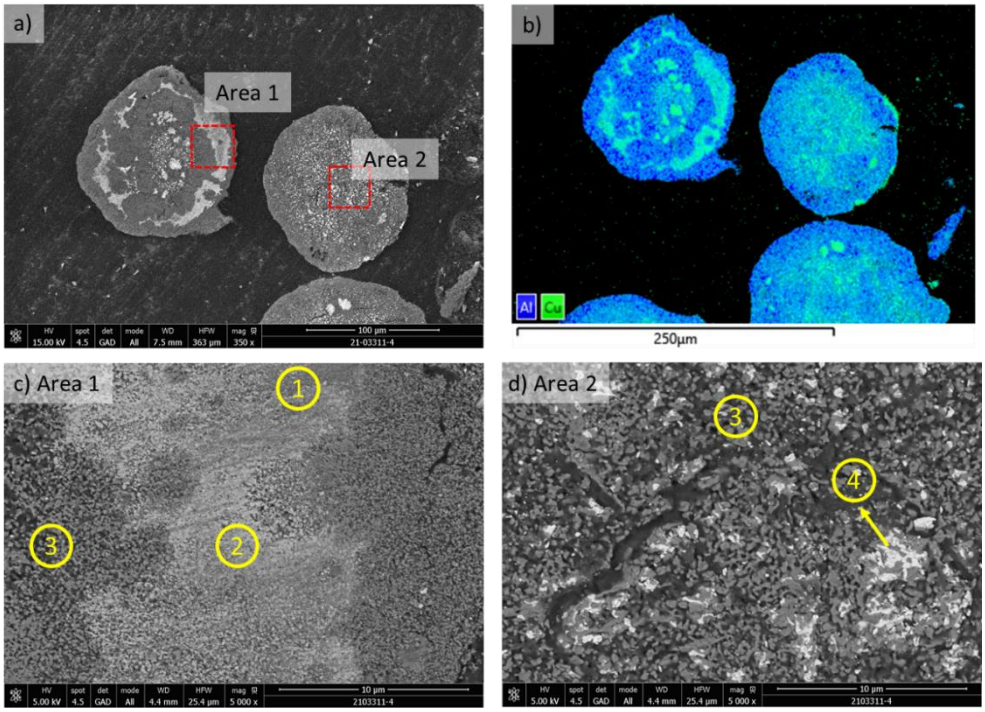

Figure 4.16: Post-mortem characterizations of the sample after the $H_2 – O_2$ experiment. a) SEM image of the sample, b) EDS elemental mapping of the SEM image and c-d) higher magnification image of area 1 and 2, respectively, marked with red square in (a).

4.1.5 Conclusion on the effect of the number of cycles

To summarize the effect of the number of redox cycles, the decrease in the $Cu_xAl_yO_4$ phase content and the increase in the Cu_2O phase follow two regimes: up to the 25th cycle, the change is gradual while afterwards the evolution occurs drastically. The drastic change can be confronted by the rapid transformation to the α-Al_2O_3 leading to the phase segregation and accumulation of the copper oxide phase. Meanwhile, residual metallic copper in the oxidized sample is found to accumulate and increase with the number of cycles which could be related to the incomplete oxidation.

The presence of CuO is only noted when the copper (I) oxide Cu_2O transforms to CuO during the decrease in the temperature, at the end of the experiment. The $Cu_xAl_yO_2$ phase only appears during the reduction/inert gas steps from the reaction between Cu_2O and Al_2O_3, which transforms to $Cu_xAl_yO_4$ upon oxidation.

4.2 EFFECT OF REDUCING GAS

In this section the effect of the reducing gas (CH_4, CO and H_2) on the phase transitions and the morphology of the material is illustrated and compared. Here, the individual steps are not elaborated as its already discussed in the previous sub-section. Only the relative percentages at the end of the oxidation and reduction steps are highlighted.

With the different gases the following reactions would take place:

$CH_4 + 4\ CuO\ (or\ 4\ CuAl_2O_4) \rightarrow CO_2 + 2\ H_2O + 4\ Cu^0\ (+\ 4\ Al_2O_3)$ Reaction 4.18

$CO + CuO\ (or\ CuAl_2O_4) \rightarrow CO_2 + Cu^0\ (+\ Al_2O_3)$ Reaction 4.19

$H_2 + CuO\ (or\ CuAl_2O_4) \rightarrow H_2O + Cu^0\ (+\ Al_2O_3)$ Reaction 4.20

As demonstrated in the reactions, CH_4 displays higher reduction potential (1:4 for CH_4:CuO) compared to the CO and H_2 gases. Experimentally, the CH_4 (5 vol%) was twice the content of CO and H_2 (2.5vol%). thereby the reduction potential of the experiment with CH_4 was 8 times higher than the other two reducing gases. Considering the theoretical duration of reduction with CH_4, the duration to reach full reduction is about 6 seconds assuming no kinetic and mass transfer limitations. However, with CO or H_2 the duration is about 60 and 45 seconds, respectively. Therefore, there is a possibility that the reaction might not be complete under CO and H_2. Furthermore, similar limitations might also occur for oxidation.

4.2.1 Reduction reaction

For the three datasets the changes in relative percentage of the relevant copper phases at the end of the reduction step are presented in *Figure 4.17.* At the end of the reduction only metallic copper and $Cu_xAl_yO_2$ phases are identified.

Metallic copper is the main component at the end of the reduction steps. The overall percentage of the metallic copper remains approximately constant throughout the cycles for all the experiments. The average percentage of the metallic copper in CO-O_2, H_2-O_2 and CH_4-O_2 are 95$\pm$ 3 %, 94 $\pm$2 %, 97 $\pm$1%, respectively. In terms of the distribution of the two features of the metallic copper (Cu^0_1 and Cu^0_2) , initially the copper exists as Cu^0_1 which gradually decrease and are replaced by Cu^0_2 species towards the end of the experiments. The Cu^0_2 is the dominant species in the CO and H_2 datasets compared to CH_4. The

prominent presence of Cu^0_1 in CH_4 dataset tends to validate the hypothesis based on the incomplete reduction at the origin of the two spectral features of metallic copper. Moreover, the decrease in the Cu^0_1 can be correlated to the increase in the Cu_2O phase, as the accumulation of the oxide phase during the oxidation step is expected to form large particles.

$Cu_xAl_yO_2$ phase exists together with metallic copper in varying percentages throughout the experiments. For CH_4-O_2 dataset, the value fluctuated in the range of 0-6% in the span of 42 cycles. There is no clear trend in the presence of $Cu_xAl_yO_2$. In H_2-O_2 and CO-O_2 experiments, the trend in change is similar – with a steady increase in $Cu_xAl_yO_2$ fraction with the number of cycles, reaching a peak value of ~9% at about 27^{th} and 20^{th} cycles, respectively. Afterwards, the contribution of $Cu_xAl_yO_2$ decreased gradually until becoming negligible after the 35^{th} and 44^{th} cycles for the CO-O_2 and the H_2-O_2 samples, respectively.

Evolution of $Cu_xAl_yO_2$ phase content might be consistent with the partial reduction reached during the CO and H_2 experiments. Additionally, as seen in section 3.1.2. the $Cu_xAl_yO_2$ formation results from the reaction between Cu_2O and alumina phases. Therefore, the alumina polymorph present in the sample during the cycling will also determine the percentage of $Cu_xAl_yO_2$.

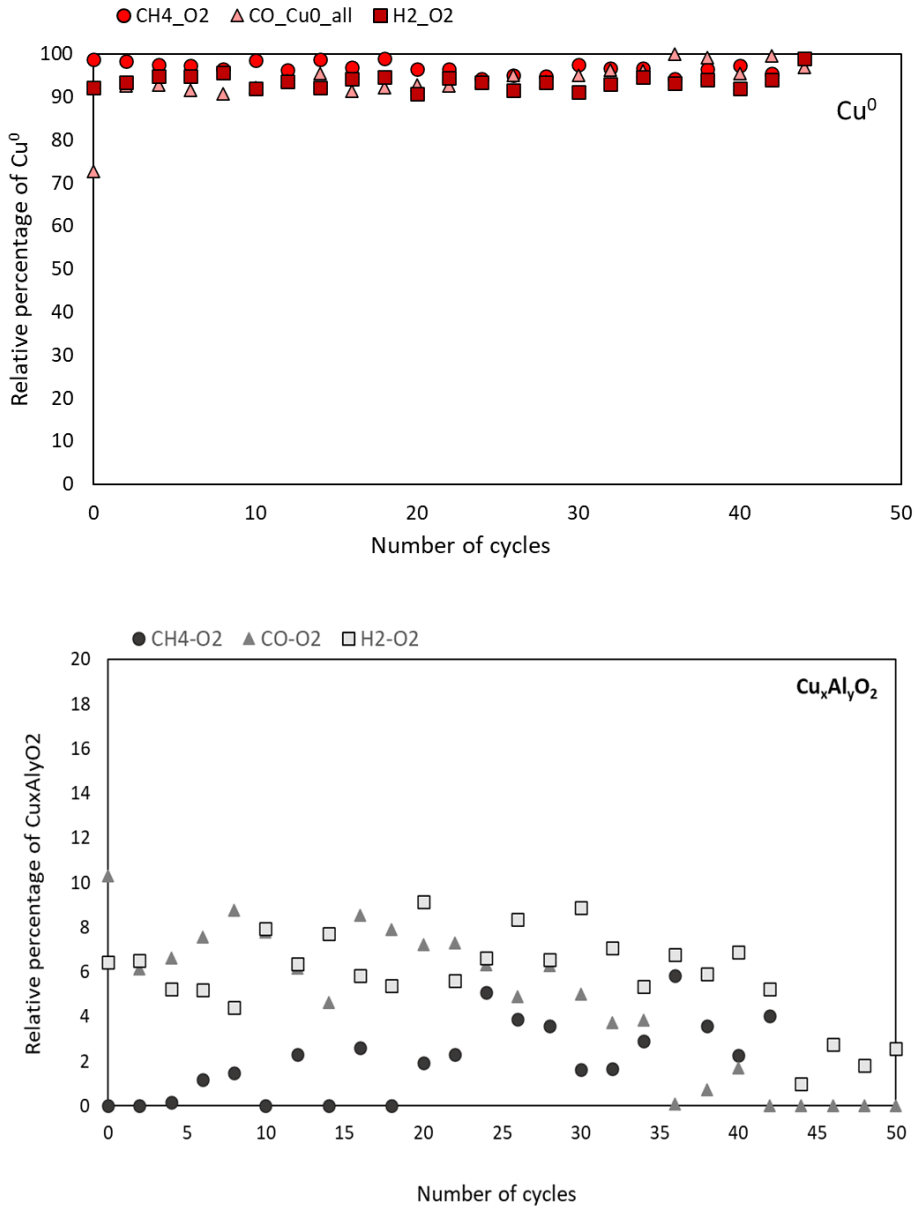

Figure 4.17: The relative percentage of the Cu and $Cu_xAl_yO_2$ (from top to bottom) at the end of the reduction step throughout the 50 cycles for the experimental datasets $CH_4 – O_2$, $CO – O_2$ and $H_2 – O_2$.

The $Cu_xAl_yO_4$, Cu_2O and CuO contents accounted for zero % for all the datasets in the reduction steps. Except for the first reduction step of $CO\text{-}O_2$, there a contribution of 11 %, which in the successive cycles displayed mostly zero %. Towards the end of the experiment between cycles 40 and 50, there is a fluctuation of Cu_2O contribution for the $CO\text{-}O_2$ and $H_2\text{-}O_2$ datasets, indicating the incomplete reaction.

4.2.2 Oxidation reaction

For the three datasets, the changes in relative percentage of $Cu_xA_yO_4$, Cu_2O and metallic copper at the end of oxidation are compared in *Figure 4.18*. There is a global decrease in the relative percentage of the $Cu_xA_yO_4$ and an increase in Cu_2O and metallic copper. However, the extent and the rate of decrease are not equal for all the experiments.

As already presented for dataset H_2-O_2, a similar trend is also oberved for the $Cu_xAl_yO_4$ and Cu_2O species in CO-O_2 dataset. Upto the 24th cycle, the decrease in the percentage of $Cu_xAl_yO_4$ follows a rate of -1 %/cycle, a value higher than the H_2-O_2 experiment. After the 24th cycle the decrease in $Cu_xAl_yO_4$ is about 2.5 times the initial rate of decrease. There is a slow increase in the relative percentage of Cu_2O in the CO-O_2 dataset of about 0.2 %/cycle until the 24th cycle. After the slow change in the percentage, there is a rapid increase of 2.1 % /cycle. For the metallic copper, the proportion of copper increases steadily up to the 25th cycle, afterwards the percentage remains at a constant value of ~16 %.

While the CO-O_2 and the H_2-O_2 datasets share common trends, the CH_4-O_2 experiment exhibits significant differences. Unlike the other two datasets, the rate of decrease of $Cu_xAl_yO_4$ and increase of Cu_2O follows a constant rate of -0.8 %/cycle and +0.5 %/cycle, respectively, while the increase in Cu makes up for +0.3 %/cycle. However, the copper species present in these two datasets are different. The metallic copper in the CH_4-O_2 experiment exhibits in the form of Cu^0_1, whereas, metallic copper in H_2-O_2 experiment is in Cu^0_2 form. Meaning, either the extent of oxidation is not the same in the different experiments or the size of metallic copper phase varies between the two experiments, as in the case of the H_2-O_2 dataset.

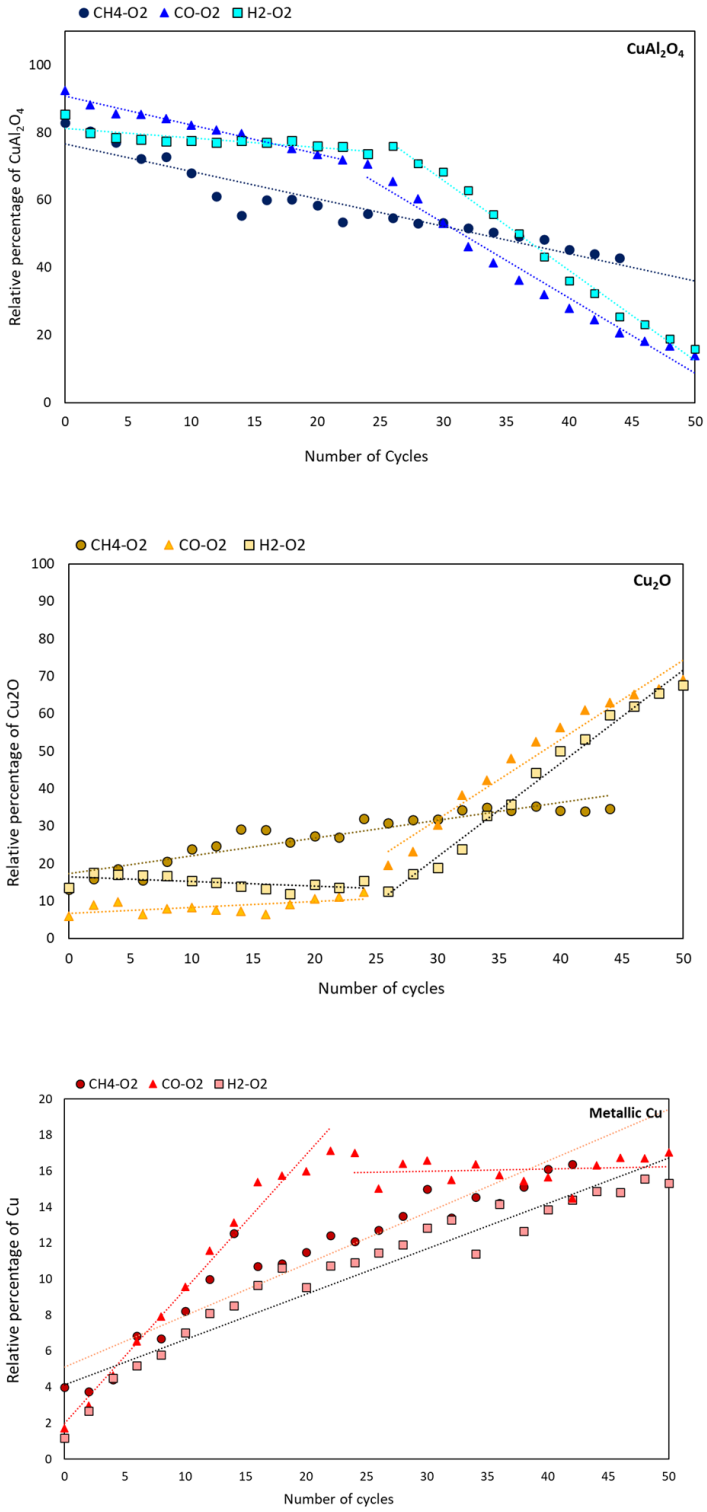

Figure 4.18: The relative percentage of the $CuAl_2O_4$, Cu_2O and Cu (from top to bottom) at the end of the oxidation step throughout the 50 cycles for the experimental datasets $CH_4 – O_2$, $CO – O_2$ and $H_2 – O_2$.

4.2.3 Post-mortem SEM characterisation

The grain morphology of the CO-O_2 sample after the XAS run is displayed in *Figure 4.19*. It is largely similar to H_2-O_2 dataset. The majority of the grains contains a mixture of α-Al_2O_3 (zone 3) and large crystallites of copper oxide (zone 4, pointed with an arrow) surrounding the α-Al_2O_3 particles (*Figure 4.19 d*), and very few areas contain copper aluminate phase (*Figure 4.19 c*, zone 2). The texture in zone 2 is not dense as observed in Chapter 3 for the fresh samples, these areas are rather composed of particle size similar to the α-Al_2O_3 grains but with no/less porosity and contains copper (from elemental analysis and phase contrast).

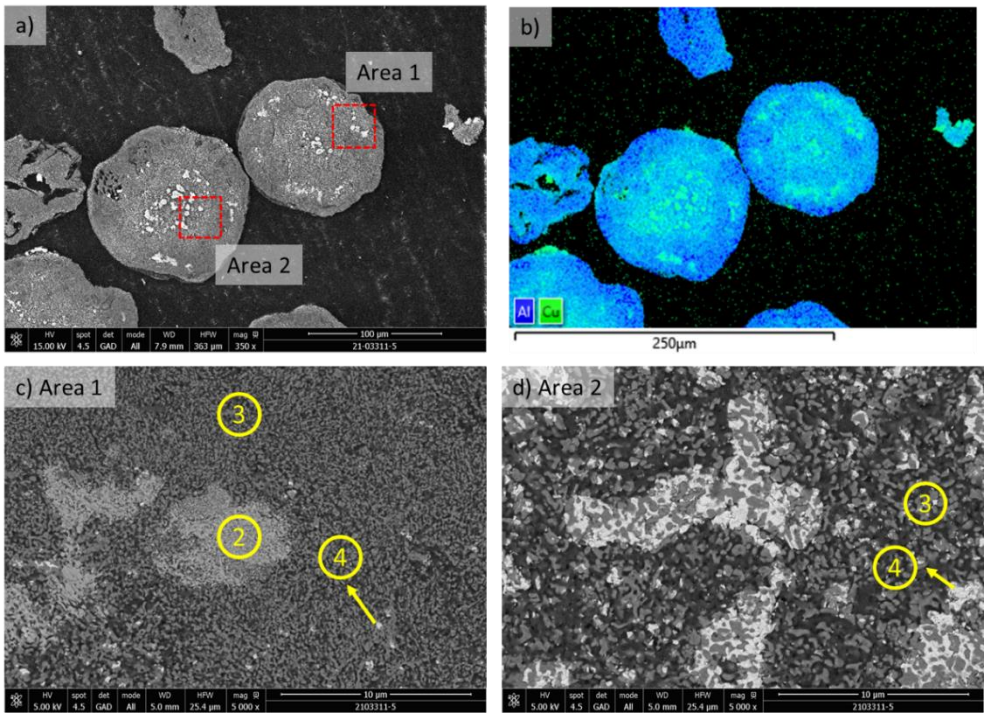

Figure 4.19: SEM of CO-O_2. a) SEM image of the sample, b) EDS elemental mapping of the SEM image and c-d) higher magnification image of area 1 and 2, respectively, marked with red square in (a).

Surprisingly, structure and morphology of the CH_4-O_2 sample are considerably different compared to the H_2-O_2 and CO-O_2 samples, as seen in *Figure 4.20*. All the grains have a similar structure and copper distribution. The edge of the grain is composed on α-Al_2O_3, sandwiched between a layer of CuO + Cu-rich aluminate on the outside and copper-rich alumina on the inside as shown in *Figure 4.20 d*. In the interior of the grain, the presence of few clusters (the two bigger grains in *Figure 4.20 a*) or in some cases one big cluster of copper-rich area (the small grain at the bottom of *Figure 4.20 a*) is observed. Higher magnification images of the copper-rich areas such as area 1 (in *Figure 4.20* c) reveals 5

zones with different texture and copper repartition. These zones are analogous to the ones presented in the H_2-O_2 dataset, except for zone number 5 which is not observed in the other samples. The texture is dense with relatively higher concentration of copper in copper aluminate form. Elemental analysis displayed a similar copper concentration between zone 2 and zone 5. They differ in terms of texture, while zone 2 is made of grains and contains porosity, zone 5 is dense, as typically observed in fresh samples.

Similar α-Al_2O_3 corolla and copper-rich nodules have been observed by Lambert et al. [15]. We believe the α-Al_2O_3 corolla formation is linked to the Cu-rich aluminate found in the fresh sample.

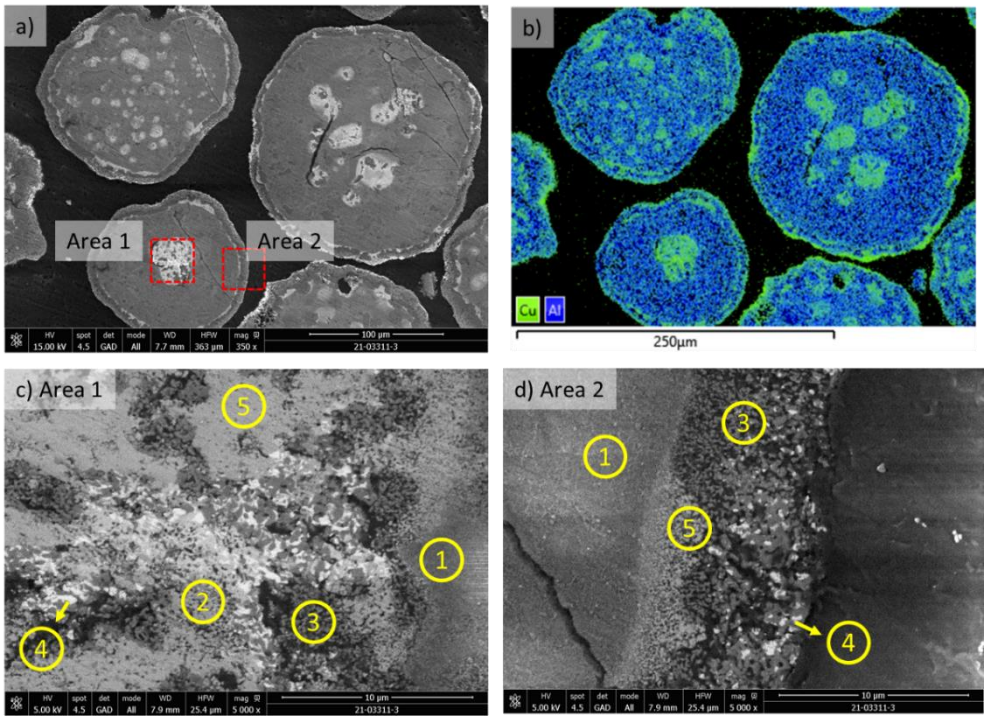

Figure 4.20: SEM of CH_4 – O_2. a) SEM image of the sample, b) EDS elemental mapping of the SEM image and c-d) higher magnification image of area 1 and 2, respectively, marked with red square in (a).

From the microstructure, the difference in the relative presence of the α-Al_2O_3 phase vs copper-aluminate is apparent in the three samples. While the CO-O_2 and H_2-O_2 samples are mostly composed of α-Al_2O_3, the CH_4-O_2 sample is composed of copper-aluminate with small percentage of the alpha alumina phase either forming an external shell or exhibiting patches of alpha alumina phase in the interior of the grains. However, the difference in the CH_4-O_2 is puzzling, one possible explanation could be related to carbon deposition on the

aluminate/alumina. Carbon deposition is known to lower the phase transition of transition alumina to α-Al_2O_3 [16]. However, the gas mixture of CH_4 contains CO_2 which should react with any carbon to form CO via reverse Boudouard reaction:

$C + CO_2 \rightarrow 2CO$ Reaction 4.21

Lambert et al. concluded that any carbon formed during the reaction would be consumed by this reaction as CO/CO_2 could not be detected in their air reactor [15]. Arjmand et al. suggested that the formation of a copper film (rather than particles) on the alumina for the delayed phase transition to form α-Al_2O_3, during the redox cycling with CH_4 [11]. Nevertheless, copper is formed in the other datasets as well. Unpublished *in situ* STEM studies at IPCMS carried out on the same system do not seem to reveal any differences in the copper phase morphology under CH_4 vs H_2 as a reducing gas. In both cases at about 600-700 °C, the supported nanoparticles exhibited spherical shape [17].

In brief, the general trend in phase distribution and the morphology of samples from CO-O_2 and H_2-O_2 experiments are comparable. Additionally, they display similar porous morphology with dispersed CuO. In contrast, the sample from CH_4-O_2 experiment displays a slower evolution trend in the different oxide phases and a less porous/denser morphological feature.

4.3 Effect of O_2 concentration

In this sub-section the datasets of H_2-O_2 with 2.5 vol% O_2 and H_2-air with 21 vol% O_2 are compared in terms of phase evolution over the 50 cycles and their post-mortem morphologies. As mentioned in the introduction, the O_2 partial pressure and the temperature determine the phases present in the Cu-Al-O and Cu-O systems. Under 2.5 vol% O_2 at 900 °C, the Cu_2O phase is the most stable between the CuO/Cu_2O pair and the $CuAl_2O_4$ phase seems to be more stable between the $CuAl_2O_4/CuAlO_2$ pair. Moreover, the phase percentage is also determined by whether the reaction undergoes completion. With air, the reaction is expected to be completed within 6 seconds while with 2.5 vol% O_2 the expected duration for completion is about 60 seconds, without considering the kinetics and/or eventual mass transfer limitations inside grains. In both cases, the complete oxidation of the whole sample volume is unlikely.

4.3.1 Oxidation reaction

For the two datasets with different O_2 concentrations, the changes in the percentages of the relevant copper phases ($CuAl_2O_4$, Cu_2O, metallic copper) at the end of the oxidation reactions are presented in *Figure 4.21.*

As visualised in the H_2-air dataset, the trends in the relative percentages of the different species are different from cycle 1 to 14 compared to the cycles afterwards. This is due to change in the sample position when a significant loss of signal was noted during the experimental run. It was assumed that the problem could arise from gas transport related dispersion of material within the capillary which could mean lower sample concentration and higher amount of void. The sample position was moved by ~80 µm in the z-axis. After the displacement of the sample, the relative concentrations of the species changed. From the difference in the concentration profiles, it can be assumed that the two areas had different gas exposure. Considering the grain size (100 – 200 µm) and the beam size (300 x 500 µm), the probe can analyse 3-5 grains, beam position shift of ~80 µm should not affect spectral signal unless area 1 contained dead volume.

To avoid confusion only area 2 is considered in the following text. Besides, evolution in the second area seemed more logical with previously observed as well as expected trend. No change in the relative percentages were observed from cycle 15 - 17 and copper aluminate phase was the only phase present. Therefore, it was hypothesized that area 2 displayed no change in the $Cu_xAl_yO_4$ from the starting of the experiment to the 17th cycle. After the 17th cycle, the fraction of $Cu_xAl_yO_4$ decreases rapidly with a rate of about 1.3 %/cycle.

In H_2-air datasets, the presence of Cu_2O is negligible as opposed to the H_2-O_2 dataset. Due to the P_{O2}- temperature effect on the equilibrium phase stability of the CuO/Cu_2O pair, CuO is present under air and Cu_2O is found during the H_2-O_2 dataset. No CuO was detected until the 17th cycle. After the 17th cycle the average rate of increase is about 1.1 %/cycle. At the oxidation step of the last cycle (42nd cycle), a maximum of 27 % of CuO was found.

The amount of metallic copper (Cu^0_2) displayed less than 10 % Cu at the end of last cycle for the H_2-air dataset. From the graph on *Figure 4.21* the accumulation of Cu has started after the 20th cycle. It is surprising to find metallic copper in the H_2-air sample as the expected completion is about 6 times faster than the experimental duration. However,

considering the presence of sintered particles observed in the SEM (presented later), reaching complete oxidation might be difficult due to kinetic limitation in some of the areas.

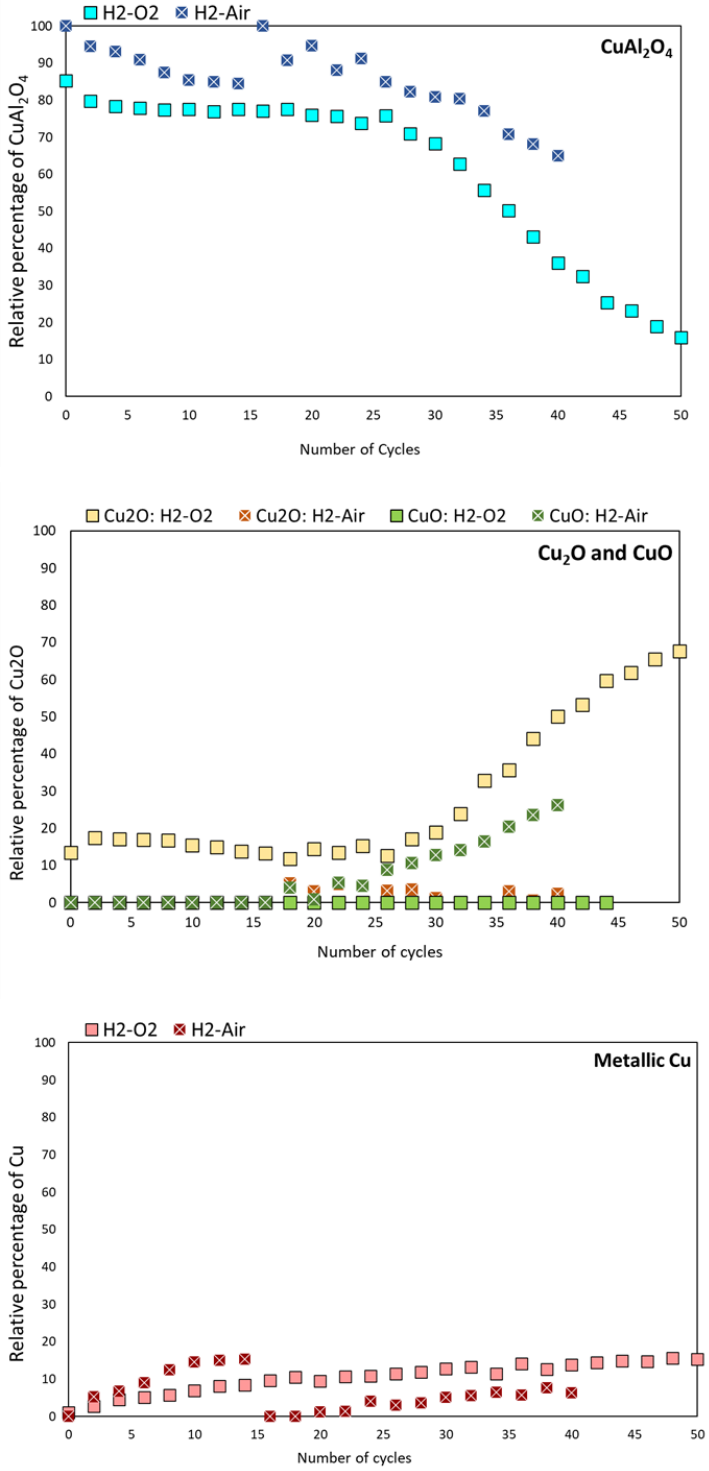

Figure 4.21: Changes in the relative percentages of $CuAl_2O_4$, Cu_2O and CuO and metallic copper phases (from top to bottom) at the end of the oxidation reactions from fresh sample to up to 50 cycles.

4.3.2 Reduction reaction

Metallic copper is the main component at the end of the reduction steps. The overall percentage of the metallic copper phase remains approximately constant throughout the cycles for all the experiments (*Figure 4.22*). In the first part of the H_2-air experiment, *i.e.* up to the 14th cycle, there is a steady rise in the relative percentage of metallic copper, reaching a maximum of about 92 % at the end of the 14th cycle. From the 15th cycle until the end of the experiment, the percentage remained constant with an average of 85 %. In terms of the distribution of the two copper species, Cu^0_2 features (attributed to incomplete reduction) made up for the majority towards the end of the experiments.

For the H_2-air dataset, there is an increase in $Cu_xAl_yO_2$ percentage as seen in *Figure 4.22*. The $Cu_xAl_yO_2$ reached a constant maximum of about 15 % after the 40th cycle.

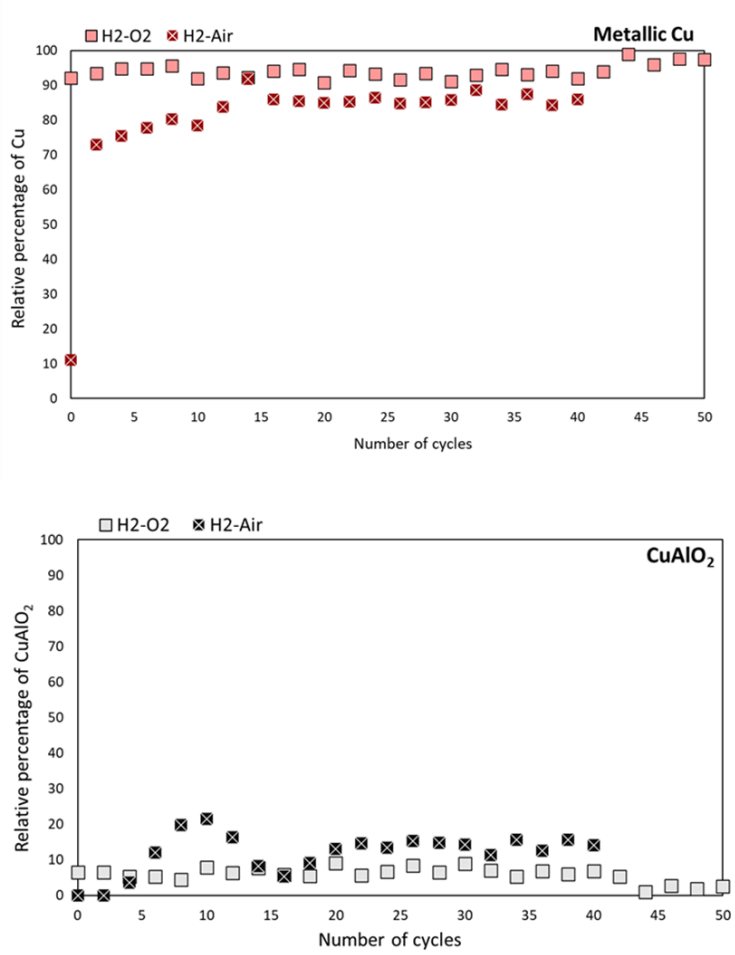

Figure 4.22: Changes in the relative percentages of metallic copper (top) and $Cu_xAl_yO_2$ at the end of the reduction reactions as a function of the number of cycles for the H_2-O_2 and H_2-air samples.

The $Cu_xAl_yO_4$, Cu_2O and CuO content accounted for zero for all the datasets, throughout the experiment. However, with an exception of the first reduction step of H_2-air dataset where residual values of about 40 % of $Cu_xAl_yO_4$ and 20 % of CuO were noted. The residual $Cu_xAl_yO_4$ content arises due to incomplete reduction of $Cu_xAl_yO_4$. In the successive cycles, the $Cu_xAl_yO_4$ content remained zero until the end of the reduction steps.

4.3.3 Post-mortem SEM characterisation

In terms of morphological evolution, five different zones are observed in *Figure 4.23*: zone 1: does not seem to have much porosity; zone 2 contains larger copper aluminate particles with lower copper concentration; zone 3 is composed of alpha alumina, zone 4 contains copper oxide, and zone 5 contains copper aluminate with higher copper concentration.

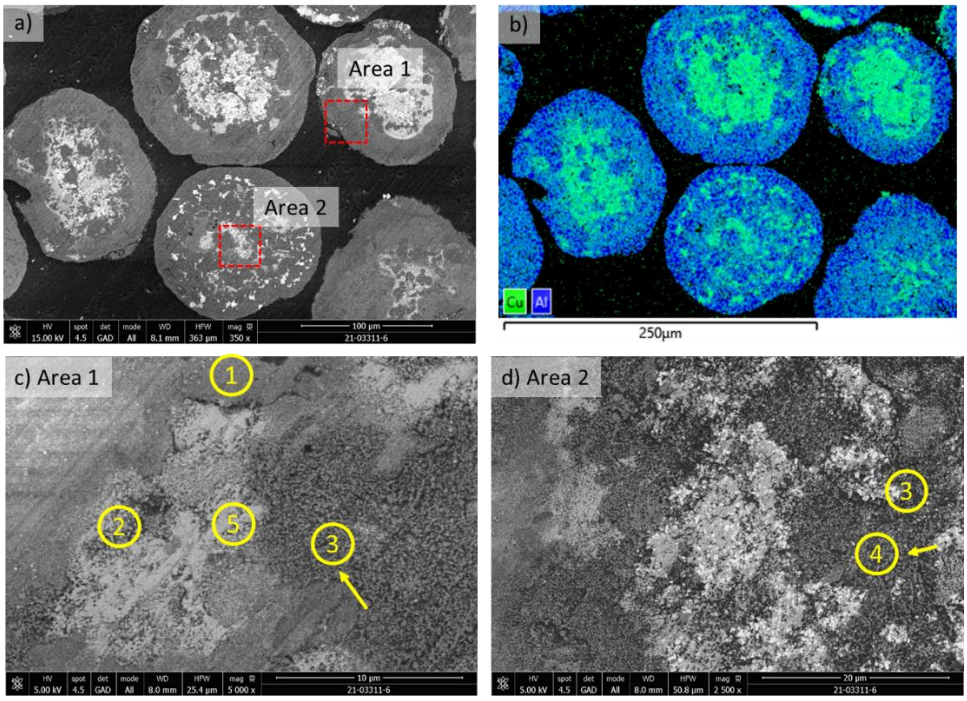

Figure 4.23: Post-mortem characterisation of the sample after the H_2 – Air experiment, a) SEM image of the sample, b) EDS elemental mapping of the SEM image and c-d) higher magnification image of area 1 and 2, respectively, marked with red square in (a).

Compared to the H_2-O_2 dataset the sample grains from the H_2-air dataset are very heterogeneous (Appendix D.2). The heterogeneity observed from one grain to another can explain the different reactions evolution observed in the two different areas of the reactor.

The concentration of O_2 seems to affect only the presence of copper oxide phase, which is either present as CuO in the H_2-air experiment or as Cu_2O under 2.5 vol% O_2 in the other

three datasets. Otherwise, the trend in the evolution of the H_2-O_2, CO-O_2 and H_2-air datasets are very similar, depicting an initial slow decrease in the copper aluminate phase content followed by a drastic decrease after about 20 cycles.

4.4 COMPARISON WITH *EX SITU* CYCLING

At the end of each *in situ* experiment, XAS spectra were acquired at room temperature. The phase percentage obtained from the *in situ* experiment with H_2-O_2 and H_2-air are compared to the *ex situ* sample. The *ex situ* sample was cycled 50 times in the TGA. The redox reaction was carried out under air and H_2, respectively. *Figure 4.24* displays the room temperature spectra of the *ex situ* sample, H_2-O_2 and H_2-air datasets from the experimental run. These spectra were fitted with Linear Combination Fitting algorithm using the reference spectra collected at room temperature. The fitting was performed in Athena software.

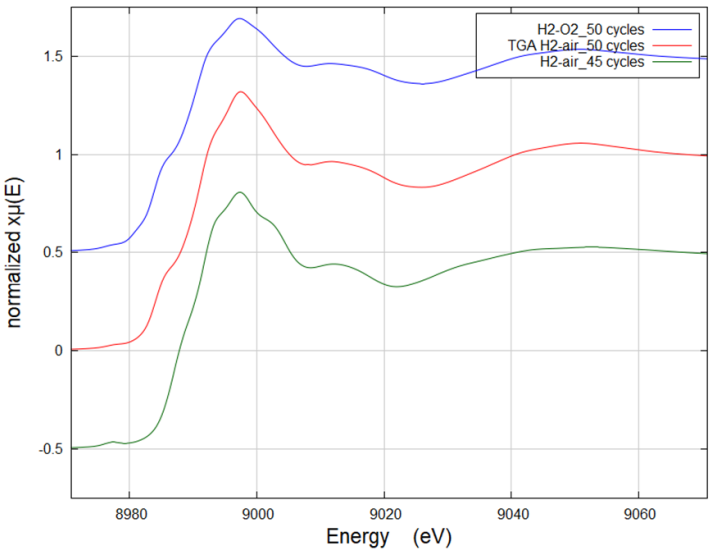

Figure 4.24: XAS spectra at room temperature for H_2-O_2 (blue), TGA-cycled sample (red), and H_2-air (green)

Only the CuO and $Cu_xAl_yO_4$ species were found from the data fitting. The relative spectral percentages are reported in Table 4.3. Although, the three samples vary in the number of cycles, they display a general trend of increasing CuO contribution with the number of cycles. The cycle-dependant increase in CuO is expected from the CuO/Al_2O_3 materials.

Table 4.3: Spectral contributions of the $CuAl_2O_4$ and CuO phases in the RT data of the in situ and ex situ samples.

Sample	#Cycles	$CuAl_2O_4$ (%)	CuO (%)
H_2 – Air_TGA – *ex situ*	**50**	**25**	**75**
H_2 – air *in situ*	**45**	**40**	**60**
H_2 – O_2 *in situ*	**55**	**10**	**90**

The morphology of these three samples complements the spectral percentage reported in Table 4.3. While the H_2 – air *in situ* sample exhibits Cu-rich areas comprising of CuO surrounded by dense areas of $Cu_xAl_yO_4$ phase, the H_2 – O_2 sample contains porous Al_2O_3 matrix with dispersed CuO crystallites. In comparison, the morphology of the *ex situ* sample contains dense $Cu_xAl_yO_4$ phase and porous Al_2O_3 phase with CuO (Cf Chapter 3). In other words, both spectrally and microstructurally the *ex situ* sample cycled 50 times displays a transitional step between the H_2-air *in situ* (45 cycles) and H_2-O_2 *in situ* (55 cycles).

It should be noted that during the *in situ* run some of the samples might not have reached full oxidation or reduction. Moreover, compared to the TGA, the sample in the *in situ* run sustained lower thermal stress as the total duration of the reactions is half the duration in the TGA. Notwithstanding the differences, the outcome of the *in situ* experimental run seem to be analogous to that of the TGA.

4.5 DISCUSSION

For all experiments, the $Cu_xAl_yO_4$ content decreased while the copper oxide (I or II) is increased as function of the number of cycles. As the oxidation step and the O_2 partial pressure for the H_2-O_2, CO-O_2 and the CH_4-O_2 datasets were low, it is reasonable to assume in some areas full oxidation was not reached, thereby, resulting in slow accumulation of the copper/copper oxide phases via sintering. However, from the phase transition phenomena observed during the redox cycling, a threshold point is noted after which the system evolved rapidly and irreversibly. This phenomenon cannot stem from the incomplete reaction alone.

Besides, the trend was observed in all the *in situ* experiments and as well as in the *ex situ* sample.

One plausible explanation for the accumulation of copper oxide is linked to the gradual conversion of the aluminate to form α-Al_2O_3 leading to phase segregation between the copper oxide (either Cu (I) or Cu (II)) and the α-Al_2O_3 phase.

Previously, we have established that the presence of copper promotes the formation of the α-Al_2O_3 phase, by decreasing the temperature of the phase transition. In Chapter 3 a phase transition mechanism was proposed based on the structural modification induced by the formation of the copper aluminate phase. It was assumed that the alpha alumina transformation is gradual which occurred during the reduction of the copper aluminate phase following the removal of the structural copper. Thanks to the detailed analysis of the dynamic process obtained by the QXAS study, in this chapter it was observed that the phase transition does not seem to occur before a certain number of cycles is reached, also supported by the SEM images.

In brief, is the segregation of copper phase at the origin or the consequence of alpha alumina formation?

Besides the role of copper, the alpha alumina phase transition is influenced by many factors including, the presence of other cations, alumina particle size, nucleation sites, etc. The alpha alumina phase transition is governed by nucleation and growth mechanisms [18,19]. Most of the literature reports coarsening of the transition alumina grains prior to the alpha alumina formation. The resulting alpha alumina particles are always larger than their preceding polymorph [20]. Hence, the idea of a "critical size" is proposed. Bagwell et al. proposed that the "critical size" or the coarsening of the transition alumina is rather a result of incubation time required to produce the alpha alumina nuclei. Whether it is the requirement of "critical size" or the "incubation period", indeed coarsening and increase of transition alumina particle size is observed prior to the alpha phase formation. From previous SEM characterisations (*Figure 4.2*), two types of copper-aluminate areas can be identified: one with large particles and porosity, similar to that of the α-Al_2O_3 (in red) and another area contains clusters of smaller aluminate particles. The α-Al_2O_3 nuclei may form spontaneously via local structural organisation on the $Cu_xAl_yO_4$ particles. Meanwhile,

persistent heating during the redox cycle may induce sintering of the small aluminate particles. Eventually, when $Cu_xAl_yO_4$ phase attains a certain particle size or once there are enough alpha alumina nuclei, the growth of the alpha phase propagates.

If we consider all the H_2-air dataset, the appearance and accumulation of the copper oxide phase occurs only after a certain number of cycles and before that there is full conversion metallic copper to $Cu_xAl_yO_4$. We can assume that during reduction of $Cu_xAl_yO_4$, metallic copper would randomly form on the alumina surface. This provides less chance for long-term sintering, unless in the subsequent oxidation, some Cu oxide phase is formed rather than $Cu_xAl_yO_4$. From the SEM images, the sintered CuO particles were not observed in the denser area containing the $Cu_xAl_yO_4$ phase but only within the α-Al_2O_3 matrix. Hence, the long-term sintering is only possible when the copper oxide starts to accumulate due to the formation of α-Al_2O_3 which would inhibit the re-formation of the $CuAl_2O_4$ phase. The accumulation of the copper oxide is prominent in the 2nd part of the redox cycling which is thus associated to the α-Al_2O_3 phase transition.

A schematic representation of the morphological evolution of CuO/Al_2O_3 materials is proposed in *Figure 4.25*. The fresh sample is composed of small copper aluminate particles, as discussed in Chapter 3. Upon high temperature redox cycling, the aluminate particles sustain sintering and increase in their particle size (*e.g.* cycle 5). Until a certain particle size is reached or alpha alumina growth is induced (*e.g.* cycle 20), the insertion and expulsion of copper phases continues to construct or deconstruct the copper aluminate (*e.g.* cycle 26).

Once a threshold size is reached, the alpha alumina phase transition takes place via a nucleation and growth process (thus the domino-like effect of $Cu_xAl_yO_4$ loss) (*e.g.* cycle 50).

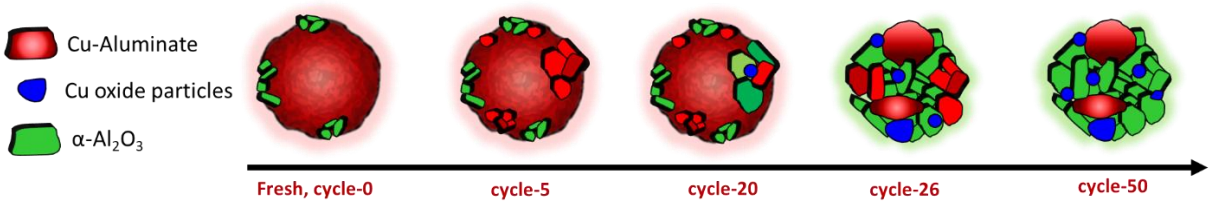

Figure 4.25: Schematic representation of redox cycle induced α-Al_2O_3 phase transition.

We can assume that during reduction of $CuAl_2O_4$, metallic copper particles randomly form on the alumina surface. This provides less chance for long-term sintering, unless in the subsequent oxidation, some Cu oxide phase is formed rather than $Cu_xAl_yO_4$.

5 CHALLENGES AND PERSPECTIVES

As specified many times in section 2 and 3, we believe in all the datasets the reactions are not complete except the oxidation reaction in the H_2-air sample. This is evident from the residual metallic copper at the end of the oxidation steps.

The main challenges of these experiments lie in the extraction of information, the necessity to favour for example spectral information over temporal information and chose the parameters accordingly to achieve the best trade off. For example if we want to know the extent of phase transition of the sample, it is crucial to carry out a large number of cycles (at least 50 cycles), which translates to more than 12 hours of experiment time considering 12 min/cycle. This is indeed a very long duration to carry out during a synchrotron run. Hence, one idea is to reduce the duration of the cycles to 6 min thus reducing the total duration to about 8 hours, including the temperature ramp steps. However, reducing the cycle duration could potentially lead to incomplete reaction. In addition, it is difficult to have a knowledge of whether the reaction was complete or not without conducting a thorough data analysis, during the experimental run. Moreover, higher gas concentration could be used to achieve a complete reaction, the reaction would be faster but the information on the intermediate phase transitions is likely to be lost.

Following improvements should be made for further experiments:

- Acquisition of the reference spectra at high temperature (at the temperature of the *in situ* experiments) to impose the spectra, rather than finding through the MCR-ALS, which might not be the exact representation of the phases.
- Carry out test cycles and a proper data analysis, by changing the reaction parameters such as duration of reaction steps, gas flow rate and concentration, to choose the suitable variable before carrying out the actual experiments.

- Having complementary information on the mass spectrometer data, hence it is crucial to calibrate the mass spectrometer with all the gases used during the experiment.
- For the oxygen carrier material, it might be beneficial to focus on the achieving complete reaction, with higher concentration of the reaction gases over 50 cycles. Information on the intermediate phase might not be as essential as establishing a trend. Moreover, temperature-dependant redox cycling could provide complementary information on the stability of the different phases.

6 CONCLUSION

In situ Quick XAS has enabled to monitor the dynamic structural evolution of the CuO/Al_2O_3 sample over a period of 50 oxidation-reduction cycles. The effect of three different reducing gases (H_2, CO and CH_4) as well as O_2 concentration (21 vol% and 2.5 vol%) were investigated. The samples from the *in situ* experimental run were compared to the *ex situ* sample cycled in a TGA. The final phase percentage and the morphology of the *in situ* and *ex situ* samples displayed the consistent outcome.

The thermodynamic phase stability is also dependent on the gas, especially for the copper oxide phases existing as Cu_2O under 0.025 atm and converting to CuO under 0.21 atm O_2 partial pressure. Similar trend in the relative percentage of the copper phases is noted in all the datasets. Globally, the percentage of the copper -aluminate phase decreased in favour of copper oxide phase. The trend in phase evolution directed to the idea of a threshold point for drastic conversion from the aluminate phase to copper oxide. At the end of the redox cycles the oxygen carrier was composed of α-Al_2O_3 and CuO. Based on the morphology of the oxygen carrier this transition point was linked to the growth and propagation of α-Al_2O_3. A mechanism concerning the role of particle size has been proposed for the alpha alumina phase transition.

7 REFERENCES

[1] W. Hu, F. Donat, S. A. Scott and J. S. Dennis. The interaction between CuO and Al2O3 and the reactivity of copper aluminates below 1000 C and their implication on the use of the Cu–Al–O system for oxygen storage and production, *RSC Advances*, 2016, **6**, 113016-113024.

[2] J. Jaumot, A. de Juan, and R. Tauler. MCR-ALS GUI 2.0: New features and applications, *Chemometrics and Intelligent Laboratory Systems*, 2015, **140**, 1-12.

[3] J. Jaumot, R. Gargallo, A. de Juan, and R. Tauler. A graphical user-friendly interface for MCR-ALS: a new tool formultivariate curve resolution in MATLAB, *Chemometrics and Intelligent Laboratory Systems*, 2005, **76**, 101-110.

[4] W. H. Cassinelli, L. Martins, A. R. Passos, S. H. Pulcinelli, C. V. Santilli, A. Rochet and V. Briois. Multivariate curve resolution analysis applied to time-resolvedsynchrotron X-ray Absorption Spectroscopy monitoring of theactivation of copper alumina catalyst, *Catalysis Today*, 2014, **229,** 114-122.

[5] K-I. Shimizu, H. Maeshima, H. Yoshida, A. Satsuma and T. Hattori. Spectroscopic characterisation of Cu–Al2O3 catalysts for selective catalytic reduction of NO with propene, *Phys. Chem. Chem. Phys*, 2000, **2**, 2435-2439.

[6] T. Tangcharoen, W. Klysubun and C. Kongmark. Synchrotron X-ray absorption spectroscopy and cation distribution studies of NiAl2O4, CuAl2O4, and ZnAl2O4 nanoparticles synthesized by sol-gel auto combustion method, *Journal of Molecular Structure*, 2019, **1182**, 219-229.

[7] N. Daichakomphu, A. Sakulkalavek and R. Sakdanuphab. Effects of iron doping on the oxidation/reduction properties of delafossite CuAlO2 synthesized via a solid-state reaction, *Journal of Materials Science: Materials in Electronics volume*, 2020, **31,** 9481-9485.

[8] M. L. Baker, M. W. Mara, J. J. Yan, K. O. Hodgson, B. Hedman, and E. I.Solomon. K- and L-edge X-ray absorption spectroscopy (XAS) and resonant inelastic X-ray scattering (RIXS) determination of differential orbital covalency (DOC) of transition metal sites, *Coordination Chemistry Reviews*, 2017, **345**, 182-208.

[9] W. Klysubun, Y. Thongkam, S. Pongkrapan, K. Won-in, J. T-Thienprasert and P. Dararutana. XAS study on copper red in ancient glass beads from Thailand, *Analytical and Bioanalytical Chemistry volume*, 2011, **399**, 3033-3040.

[10] Q. Imtiaz, D. Hosseini and C. R. Müller. Review of Oxygen Carriers for Chemical Looping with Oxygen Uncoupling (CLOU) : Thermodynamics, Material Development, and Synthesis, *Energy Technology*, 2013, **1,** 11, 633-647. DOI: 10.1002/ente.201300099.

[11] M. Arjmand, A-M. Azad, H. Leion, A. Lyngfelt, and T. Mattisson. Evaluation of CuAl2O4 as an Oxygen Carrier in Chemical-Looping Combustion, *Industrial & Engineering Chemistry Research*, 2012, **51,** 43, 13924-13934.

[12] T. Narushima, H. Tsukamoto and T. Yonezawa. High temperature oxidation event of gelatin nanoskin-coated copper fine particles observed by in situ TEM, *AIP Advances*, 2012, **2**.

[13] K. T. Jacob and C. B Alcook. Thermodynamics of CuA102 and CuA120, and Phase Equilibria in the System Cu20-Cu0-Al2O3, *Journal of American Ceramic Society*, 1975, **58**, 192-195.

[14] M.T. Izquierdo, F. García-Labiano, A. Abad, A. Cabello, P. Gayan, L.F. de Diego and J. Adanez. On the optimization of physical and chemical stability of a Cu/Al2O3 impregnated oxygen carrier for chemical looping combustion, *Fuel Processing Technology*, 2021, **215**.

[15] A. Lambert, A. Tilland, W. Pelletant, S. Bertholin, F. Moreau, I. Clemençon and M. Yazdanpanah. Performance and degradation mechanisms of CLC particles produced by industrial methods, *FUEL*, 2018, **216**, 71-82. DOI: 10.1016/j.fuel.2017.11.115.

[16] A. M. Volodina, A. F. Bediloab, V. O. Stoyanovskiia, V. I. Zaikovskiiac, R. M. Kenzhina, I. V. Mishakovad and A. A. Vedyagin. Nanocrystalline carbon coated alumina with enhanced phase stability at high temperatures, *RSC Advances*, 2017, **7**, 54852-84860.

[17] Sorina Cretu. *In-situ TEM Operando study of the copper mobility in Chemical Looping Combustion supported on alumina*, July 2018.

[18] R. B. Bagwell, G. L. Messing and P. R. Howell. The formation of ®-Al2O3 from μ-Al2O3: The relevance of a “critical size” and: Diffusional nucleation or “synchro-shear”?, *Journal of Material Science*, 2001, **36**, 1833-1841.

[19] T. C. Chou and T. G. Nieh. Nucleation and Concurrent Anomalous Grain Growth of a-AI203 During + (Y Phase Transformation, *Journal of American Ceramic Society*, 1991, **74,** 9, 2270-2279.

[20] I. Levin and D. Brandon. Metastable Alumina Polymorphs: Crystal Structures andTransition Sequences, *Journal of the American Ceramic Society*, 1998, **81**, 1995-2012.

Chapter 5:
Redox behaviour and mobility of copper nanoparticles

1. INTRODUCTION

The previous two chapters were dedicated to the study of the supported CuO/Al_2O_3 oxygen carriers, specifically focusing on the chemical and polymorphic phase transitions and macroscopic grain scale mobility of the copper phase. The role of temperature and copper has been identified in phase transformation of the copper-alumina system in the range of 700 – 900 °C.

In this chapter and the next one, we will particularly focus on Cu mobility and diffusion at nanoscale on different supports. Especially, considering the effect of temperature and of nature of the support on its diffusion and sintering behaviour.

Diffusion studies are often carried out using Rutherford backscattering (RBS) or Secondary ion mass spectroscopy (SIMS) characterisation techniques on the bulk substrate [1,2]. While RBS and SIMS provide essential understanding, these studies might not represent the material evolution at the nanoscale. Moreover, information on the nanoparticle growth and sintering might be difficult to obtain. *In situ* STEM is frequently used for real time observation of the atomic/ionic diffusion during chemical reactions or heating [3,4]. In addition to diffusion, *in situ* STEM often provides better understanding of the nanoparticle growth mechanism(s), especially in supported materials [5,6]. Hence, in the next two chapters the dynamic evolution in the copper-based material is investigated using STEM.

Supported materials based on small alumina/aluminate particles are often complicated to characterise due to overlapping grains and poor contrast. Moreover, the relative low electron density (related to atomic number Z) of the copper oxide makes it difficult to identify the copper containing particles within the alumina grains without having prior knowledge of the particle morphology. Initial studies are often undertaken using flat model

supports. This helps to achieve a simplified understanding of the morphology and phase transformations as well as the mobility and the growth mechanisms of the copper/copper oxide nanoparticles, as a function of temperature and the oxidation-reduction gas.

In Chapter 5, two model systems are studied based on copper nanoparticles supported on flat substrates. The substrates are SiN_x (membrane of the e-chip) and Al_2O_3 deposited on the SiN_x e-chip. The choice of the supports is based on the copper-support interactions which is supposedly different for the two substrates. Besides that, alumina support is used to comprehend the temperature induced reaction-diffusion of the copper-alumina system leading to $CuAl_2O_4$. The amorphous model support would also provide complementary understanding to the supported sample (Chapter 6).

The first part of this chapter is dedicated to the Cu/SiN_x system to comprehend the oxidation-reduction of the copper nanoparticles as well as to identify the growth mechanism (Ostwald ripening/Particle Migration and Coalescence). Even though CLC is performed at high temperature (typically 900°C), we also studied evolution at lower temperatures, starting at 150°C and progressively increasing the temperature to 900 °C.

The second part of this chapter is focused on Cu/Al_2O_3 system. The mobility of the copper is investigated under H_2 and O_2 atmosphere up to a temperature of 800 °C. The mechanism of copper migration is discussed in terms of Cu/SiN_x and Cu/Al_2O_3 interactions as a function of the two gaseous environments.

In the first part of section 3, the results of the Cu/SiN_X are presented in the original format of the article as published in Nanoscale. The second part dealing with the Cu/Al_2O_3 is presented in standard format.

1 EXPERIMENTAL AND DATA TREATMENT PROTOCOL

The *in situ* experimental setup has been described in chapter 2, section 3.7.5. The reduction and oxidation reactions were carried out with a mixture of 50% H_2 in Ar and 50% O_2 in Ar at 1 bar pressure, for all the experiments. Between every alternating gas environment, the gas manifold and the sample holder were purged with Ar, to avoid mixing of the gases. This protocol has been followed in Chapters 5 and 6.

Details of the sample preparation and experimental setup and parameters are provided in the respective sections.

The data treatment was carried out using DigitalMicrograph from Gatan , PlugIm software developed at IFPEN and ImageJ.

The particle size distribution (PSD) measurement of the nanoparticles was performed on PlugIm using the following workflow: Median filter → luminosity correction → segmentation (using greyscale threshold) → disk morphology (to calculate the individual particle dimension in pixel).

To track the nanoparticles (NPs) sintering behaviour, first the areas are aligned using "registration" plugin in ImageJ and then NPs size evolution was analysed using PlugIm.

2 BEAM EFFECT CONSIDERATION

Beam induced artefacts are a common problem faced in the TEM observation in both *ex situ* and *in situ* conditions. Although damages in the sample can be minimised by carefully controlling the beam dose, the effect of the beam is difficult to eliminate fully. The beam effect takes on three mains forms [7]:

- Radiolysis: Ionisation of certain species due to inelastic scattering.
- Knock-on damage or sputtering: Sputtering causes atomic displacement from the crystal lattice resulting in point defects.
- Heating: Energy transfer during inelastic collision between the electron and the sample can increase the local sample temperature.

Presence of gas may increase the extent of damage due to the ionisation of the gas. The ionised gas can either cause direct damage to the sample or influence the kinetics of the observed reaction.

For the current samples reported in Chapters 5 and 6, the beam effect is manifested in several forms. The nanoparticles of copper may undergo structural disintegration to form cluster of atoms in some areas. At high temperature (> 800 °C) and high beam dose the nanoparticles eject smaller nanoparticles. Beam effect can also cause enhanced atomic

mobility leading to slow depletion of the nanoparticles. Additionally, beam induced reduction of the oxide material is also observed in some cases.

Beam effect is material and reaction specific, so the acquisition parameters must be adjusted based on conditions of the experiment. Most of the dynamic evolutions were imaged in STEM mode and due to raster scanning mode, the beam dose is significantly lower than in TEM mode. Typically, in the STEM observation a beam dose of 10^4-10^6 e^- nm^{-2} s^{-1} was used in our study. In each experiment the extent of beam dose was checked in areas further way from the chosen observation areas to determine the magnification and acquisition suitable for the observation. Additionally, most of the observations were carried out periodically to avoid continuous exposure of the sample to the beam. Unexposed areas were regularly checked to make sure that the sample morphology was the same as the tracking areas.

3 RESULTS AND DISCUSSION

3.1 MODEL SYSTEM – COPPER NANOPARTICLES ON SINX SUBSTRATE

These results have been published in Nanoscale journal from RSC publication. The main article is provided as it has been published, together with the supplementary information provided in Appendix G. The paper is entitled:

"*In-situ* STEM study on the morphological evolution of copper-based nanoparticles during high-temperature redox reactions" - Nanoscale, 2021,**13**, 9747-9756. [8]

DOI: https://doi.org/10.1039/D1NR01648B

3.2 *IN-SITU* STEM STUDY ON THE MORPHOLOGICAL EVOLUTION OF COPPER-BASED NANOPARTICLES DURING HIGH-TEMPERATURE REDOX REACTIONS

Sharmin Sharna [a, b], Mounib Bahri [b], Corinne Bouillet [b], Virgile Rouchon [a], Arnold Lambert [a], Anne-Sophie Gay [a], David Chiche [a] and Ovidiu Ersen [*b]

[a]IFP Energies Nouvelles, Rond-Point de l'échangeur de Solaize, 69360 Solaize, France

[b]Institut de Physique et Chimie des Matériaux de Strasbourg (IPCMS), UMR 7504 CNRS – Université de Strasbourg, 23 rue du Loess, BP 43, Strasbourg Cedex 2, France

---

3.2.1 Abstract

Despite the broad relevance of copper nanoparticles in industrial applications, the fundamental understanding of oxidation and reduction of copper at the nanoscale is still a matter of debate and remains within the realm of bulk or thin film-based systems. Moreover, the reported studies on nanoparticles vary widely in terms of experimental parameters and are predominantly carried out using either *ex-situ* observation or environmental transmission electron microscopy in a gaseous atmosphere at low pressure. Hence, dedicated studies in regard to the morphological transformations and structural transitions of copper-based nanoparticles at a wider range of temperatures and under industrially relevant pressure would provide valuable insights to improve the application-specific material design. In this paper, copper nanoparticles are studied using *in-situ* Scanning Transmission Electron Microscopy to discern the transformation of the nanoparticles induced by oxidative and reductive environments at high temperatures. The nanoparticles were subjected to a temperature of 150 °C to 900 °C at 0.5 atm partial pressure of the reactive gas, which resulted in different modes of copper mobility both within the individual nanoparticles and on the surface of the support. Oxidation at an incremental temperature revealed the dependency of the nanoparticles' morphological

evolution on their initial size as well as reaction temperature. After the formation of an initial thin layer of oxide, the nanoparticles evolved to form hollow oxide shells. The kinetics of formation of hollow particles were simulated using a reaction-diffusion model to determine the activation energy of diffusion and temperature-dependent diffusion coefficient of copper in copper oxide. Upon further temperature increase, the hollow shell collapsed to form compact and facetted nanoparticles. Reduction of copper oxide was carried out at different temperatures starting from various oxide phase morphologies. A reduction mechanism is proposed based on the dynamic of the reduction-induced fragmentation of the oxide phase. In a broader perspective, this study offers insights into the mobility of the copper phase during its oxidation-reduction process in terms of microstructural evolution as a function of nanoparticle size, reaction gas, and temperature.

3.2.2 Introduction

Copper nanoparticles (NPs) in both metallic and oxide forms are widely utilized in industrial applications ranging from technological use as interconnects [9] to photovoltaics [10] and sensors [11], as well as in heterogeneous catalysis [12] such as Water-Gas-Shift reaction (WGS) [13], methanol synthesis[14], CO oxidation [15] and selective catalytic conversion of NO_x [16]. Recently, copper-based nanoparticles have received renewed interest as oxygen carrier (OC) in Chemical Looping Combustion (CLC), an alternative combustion process with low energy penalty carbon dioxide capture solution [17]. CLC can be performed using a supported copper-based OC that undergoes successive reduction (combustion of hydrocarbon) and oxidation (regeneration of the oxide phase) cycles to produce energy; this approach eliminates direct contact between the air and the fuel and allows the generation of a readily separable stream of CO_2 [18]. Depending on the application, copper-based NPs are subjected to different oxidizing/reducing environments at variable pressures and temperatures ranging from 200-300 °C in WGS to above 800-1000 °C in CLC application [13,17,18]. The exposure of Cu-based NPs to different reaction conditions leads to chemical, structural and morphological transformations in the material resulting in oxidation [19], reduction [18], and sintering [20] of the copper phases, causing degradation in their reactivity and selectivity. Although a wealth of literature is available depicting the oxidation-

reduction mechanisms of copper, variable experimental conditions give rise to discrepancies in the observations, making it difficult to unravel the contribution of different experimental parameters such as NP size, temperature, type, and pressure of gas and metal-support interactions [20,20–24]. Thus, understanding the oxidation mechanism of copper NPs and their subsequent reduction under reaction conditions is of special interest to not only optimize oxygen carrier design but also to stabilize specific copper phases for other applications.

A significant amount of research has been dedicated to the comprehension of copper oxidation, but much of it remains within the domain of thin films [25]. However, several works on the oxidation of copper nanoparticles were also carried out using either transmission electron microscopy (TEM) to understand the effect of temperature on the morphology of the oxide phase [23,26,27], thermogravimetric analysis (TGA) to study the kinetics of oxidation [24,28], environmental scanning TEM (e-STEM) to directly visualize the dynamic evolution of the nanoparticle morphology [29], or real-time surface plasmon spectroscopy [21,22]. The oxidation of copper nanoparticles is affected by the reaction conditions as well as the microstructure of the starting metallic phase leading to a final morphology of the oxide nanoparticles which is determined by the temperature of oxidation. Typically, at intermediate temperatures (50-300 °C), for a NP size distribution of 10-30 nm diameter, the oxidation can be considered as a two-steps process: the initial step involves the formation of a thin layer of Cu_2O oxide encapsulating the metallic copper core, followed by the genesis of hollow nanoparticles related to outward growth of oxide, due to differential diffusion of the reaction species via Nanoscale Kirkendall Effect (NKE), at 0.21 atm O_2 partial pressure [21,23,24,26,30–32]. In contrast, LaGrow et al. have reported layer-by-layer growth of compact oxide nanoparticles from a single nucleation point of the metallic copper at 300-500 °C under a very low O_2 partial pressure (2×10^{-5} - 10^{-4} atm) [29]. Regarding the phase changes throughout oxidation, Nakamura et al. reported a phase transition from Cu_2O to CuO above a temperature of 300 °C at 0.21 atm O_2 partial pressure, while LaGrow et al. reported the presence of Cu_2O phase only, up to a temperature of 500 °C [23,29]. The oxygen partial pressure is hence an important parameter affecting the oxidation mechanism that requires further investigation. Indeed, according to Haugsrud and Kofstad, depending on the O_2 partial pressure, the oxidation of Cu proceeds either via

singly charged copper vacancy at low pressure or via neutral copper vacancy at higher pressure, consequently affecting the mechanism of oxidation [33]. Upon further increase in temperature, the hollow NPs are subjected to collapse and formation of compact NPs, as demonstrated by Nakamura et al. [23] and Rice et al [22].

Not many studies can be found in the literature for the reduction of copper oxide NPs. Recently, the morphological transformation during Cu_2O reduction has been discerned by *in-situ* STEM at 300-500 °C under 2×10^{-5} - 10^{-4} atm H_2 partial pressure. The reduction of Cu_2O to Cu NPs occurred from a single nucleation site on the surface of the copper oxide where the reaction front moved unidirectionally with time [29]. In comparison, other transition metal-oxide NPs such as oxides of Ni or Co undergo NP re-dispersion via fragmentation during the reduction reactions [34,35]. The difference in the observations could stem from the shape and microstructure of the initial oxide NPs or the reaction conditions, such as H_2 partial pressure. Particle morphology and H_2 partial pressure also have an impact on the kinetics of reduction as demonstrated by Kim et al. [36] and Rodriguez et al. [37]. It was suggested that an increase in the particles' structural defect concentration and H_2 partial pressure induces faster nucleation, and a faster rate of metallic copper formation was observed.

Notwithstanding the number of studies conducted on copper, numerous open questions remain, including how the dynamic shape evolution proceeds during oxidation under high O_2 partial pressure, or the assessment of the reduction mechanism of copper oxide NPs. In this context, our general goal is to investigate, by directly monitoring the various phenomena involved in the oxidation and reduction processes of copper NPs, by systematically varying the temperature of the reaction and quantifying the structural changes induced in the NPs. Herein, we report the dynamic chemical, structural, and morphological transformation of copper phases using *in-situ* Scanning Transmission Electron Microscopy (STEM). Notably, the *in-situ* setup operates at atmospheric pressure to approach the industrial operating conditions.

3.2.3 Experimental

3.2.3.1 Materials and Methods

Nanoparticle synthesis: In the present study, two types of NPs preparation were used: Cu NPs produced via sputtering and by chemical synthesis route.

The sputtered samples were prepared by magnetron sputtering of copper from a copper target using DP650 sputtering equipment (from Alliance Concept) by directly sputtering 1-2 nm thickness of Cu thin-film at 150 mA onto the amorphous SiN_x MEMS chip (from Protochips). The assembled SiN_x e-chip was then inserted in the TEM for *in-situ* heat treatment at 300 °C under 0.5 atm H_2 partial pressure to produce oxide-free metallic copper NPs. Three experiments were conducted to achieve different particle size distributions (PSD) by varying either the thickness of the film or the rate of heating during the NPs formation step. The details of the preparation steps and the resulting PSD are presented in Supporting Information (SI - 1.1). The samples are called Sputt-1 (bimodal PSD of 4 ± 2 nm and 35 ± 7 nm), Sputt-2 (bimodal PSD of 4 ± 2 nm and 21 ± 6 nm) and Sputt-3 (monomodal PSD 9 ± 4 nm).

The second type of sample was produced via a chemical route adapted from Carenco et al. by thermally reducing copper acetate in the presence of oleylamine and octadecene [38]. Typically, 25.1 mL (10 parts) of oleylamine was added together with 10 mL of octadecene in a 100 mL round bottom flask, followed by 1.53 g (1 part) of copper acetate, then stirred at 50 °C. The mixture was then heated to 250 °C in a sand bath for 2 hours until the mixture turned reddish black. The resulting nanoparticles were isolated using centrifugation in a mixture of methanol/n-hexane/acetone in a 1:2:10 ratio and finally suspended in a solution of hexane. For the *in-situ* STEM observation, a few drops of the sample dispersed in hexane were deposited on the SiN_x membrane and dried. The colloidal nanoparticles were heated under Ar at 200 °C for 2.5 hours, followed by a reduction reaction under 0.5 atm H_2 at 500°C for 1 hour to ensure the removal of the organic surfactants and presence of metallic NPs (*Figure S2* in Appendix G) [39]. This sample is referred to as Syn-1 (with a bimodal PSD of 17 ± 5 nm and 42 ± 6 nm) after heat treatment (*Figure 5.1*). The NPs were imaged by HR-STEM under Argon after synthesis and under H_2 after heat treatment at 500 °C (*Figure S2* and *S3*).

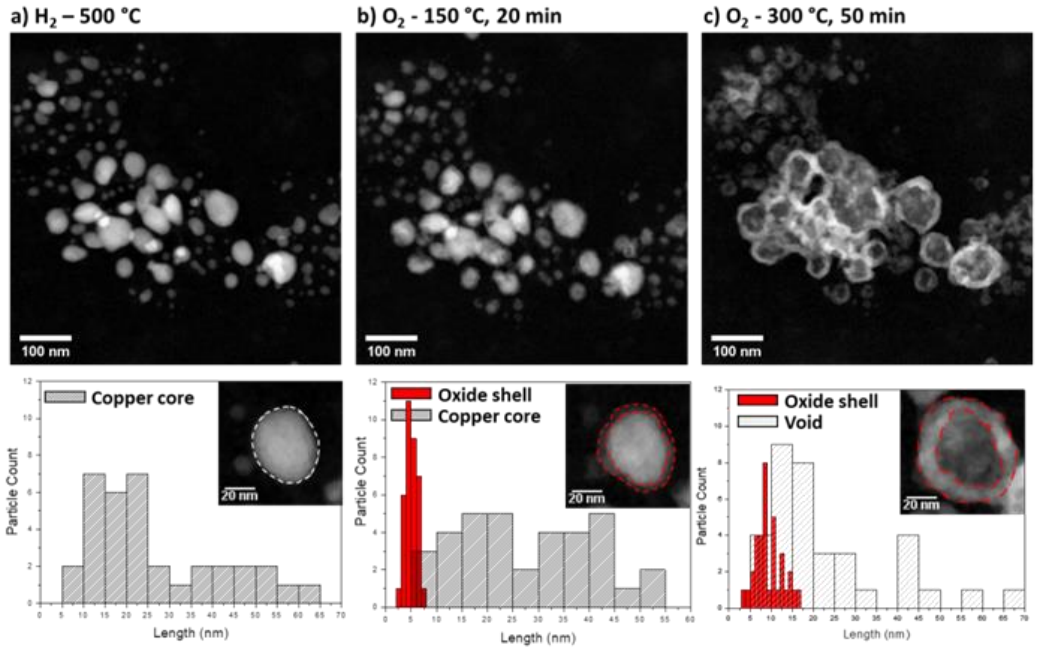

Figure 5.1: In-situ HAADF-STEM analyses with respective particle size distribution and oxide shell thickness from the same area of observation after 1 hour of reaction under, a) 0.5 atm H_2 partial pressure at 500 °C, b) 0.5 atm O_2 partial pressure at 150 °C and c) 0.5 atm O_2 partial pressure at 300 °C. Sample: Syn-1.

***In-situ* STEM**: The experiments were carried out using a JEOL JEM-2100F microscope operated at 200 kV equipped with a spherical aberration probe corrector (Cs from CEOS), high-resolution objective lens pole piece and an UltraScan 1000 CCD array detector (GATAN). For *in-situ* observations, a Protochips Atmosphere system was used [40]. The samples were suspended between two micro-electro-mechanical systems (MEMS) based closed cells made up of transparent SiN_x (for observation) and SiC (for heating) [41,42]. The *in-situ* observations were carried out at a pressure of 1 atm (10^5 Pa) and a temperature of up to 900 °C under oxidative-O_2/Ar (1:1) and reductive-H_2/Ar (1:1) environments, at a flow rate of 0.1 ml/min. The system was purged with argon between every alternating gas environment to ensure proper cleaning of the gas lines and the sample holder. To minimize the effects of electron beam such as contamination and sample damage, observations were made to determine the maximum electron beam dose the sample can withstand under each gaseous environment without damage. Hence, the electron dose rate was kept below 10^5 e nm^{-2} s^{-1}. Furthermore, the *in-situ* observation areas were not continuously exposed to the electron beam, in addition, areas outside the *in-situ* observation zones were systematically

observed for comparison, to check for any significant artefacts caused by electron irradiation.

3.2.4 Results and Discussion

Four experiments have been carried out on samples sputt1-3 and syn1 to assess the role of the nanoparticle size and reaction temperatures on the morphology and phase evolution of the NPs during the oxidation and reduction processes.

3.2.4.1 Oxidation as a function of temperature

3.2.4.1.1 NKE and Void Formation

Following the formation of copper nanoparticles (syn-1) at 500°C under H_2, the temperature was lowered down to 150 °C and oxygen at 0.5 atm partial pressure was introduced. At 150 °C, the initial stage of oxidation involves the formation of a thin layer of oxide on the surface of the Cu NPs (*Figure 5.1*). The oxide phase can be easily identified from the change in contrast on the STEM-HAADF images, resulting from the lower electron scattering intensity of the oxidized phase compared to the metallic phase due to the lowering of the local averaged atomic number as copper oxide is formed. At this temperature, only the presence of Cu_2O is reported in the literature [27,43]. With the augmentation of the temperature to 300 °C, three distinct morphologies can be distinguished with respect to the initial size of the metallic NPs (*Figure 5.2a* and *Figure 5.2d*).

The different NP morphologies are as follows:

(1) NPs with an initial size in the range of ~2 – 10 nm (*Figure 5.2a*, NP category-1) form compact oxide NPs after oxidation at 150 °C (*Figure 5.2b*).

(2) NP in the size range of ~10 – 25 nm (*Figure 5.2a*, NP category-2) form a central void Figure 5.2b) at the centre of an oxide rim. The hollow NPs eventually collapse upon increasing the temperature to 300 °C (*Figure 5.2c*).

(3) NPs with an initial diameter over 25 nm (*Figure 5.2d*, NP category-3) undergo the formation of a core@shell type morphology with a metallic copper core encapsulated by an oxide shell. Upon increasing the temperature from 150 °C to 300 °C at 5°C/min, these nanoparticles form hollow NPs (*Figure 5.2e*). After 30 min of oxidation at 300 °C, the

presence of both Cu_2O and CuO phases is deduced from the analysis by Fast Fourier Transforms (FFT) of the STEM bright-field (BF) images (*Figure S4a*). After a prolonged flow of O_2, only the presence of the CuO phase is evidenced in *Figure S4b*, in agreement with the literature [23][44].

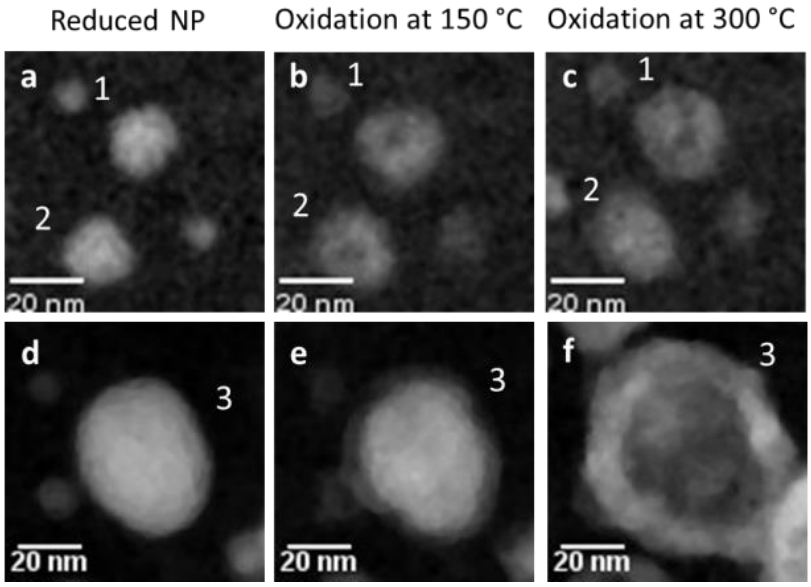

Figure 5.2: Illustration of size-dependent morphological transformation of cooper nanoparticles from the reduced state (a and d), after oxidation at 150 °C (b and e) and after oxidation at 300 °C (c and f). Numbers 1-3 represent the nanoparticle sets undergoing size-dependent shape evolution. Sample Syn-1.

The smaller NPs (category-1, 2-10 nm) are expected to form compact oxide NPs in a shorter period due to the smaller distance of diffusion for copper and oxygen species [45]. Also, as the size of the NPs is very small, the number of nucleation sites on the particles is likely to be reduced, possibly leading to unidirectional oxide-phase growth [29,46]. On the contrary, for larger NPs, the nucleation frequency is expected to be higher, consequently favouring multiple nucleation points of the oxide phase on the surface of the metallic copper. Morphological evolution as a function of NP size and temperature of oxidation is consistent with the nano Kirkendall effect, wherein the deferential diffusion of Cu and O atoms results in outward growth of the oxide phase [22,31,34]. Above 8-10 nm diameter, the diffusion distance and the difference in diffusion coefficients between Cu and O atoms through bulk metallic Cu allow for the generation and aggregation of vacancies, leading to voids creation.

In addition to the size of the nanoparticles, an increase in temperature results in increased kinetics of oxidation as well as hollowing of the NPs. The time to complete the formation of

hollow copper oxide for nanoparticles of an average initial diameter of ~40 nm and ~20 nm is plotted (*Figure 5.3a*) as a function of different constant temperature from 150 – 300 °C. The duration to form hollow oxide increases radically from ~2 hours at 150 °C to few seconds at 300 °C, for the same NPs size. The difference in the kinetics of hollowing stems from the temperature dependency of the diffusion coefficients of copper and oxygen atoms. Herein, we calculated the self-diffusion coefficient of copper as a function of temperature and size-dependent kinetics of hollowing at different temperatures using the reaction-diffusion model developed by Svoboda et al. [47]. The model estimates the duration to form hollow NPs by oxidation of metallic copper NPs in a gaseous environment where the diffusion coefficient of copper atoms in Cu_2O is much larger than that of the oxygen diffusion coefficient. The time to form hollow NPs from metallic Cu NPs according to Svoboda's equation is given by:

$$t = \frac{RT{R_0}^2 A}{D_{Cu\ in\ Cu_2O}\left|\Delta g_{Cu_2O}\right|}$$

Where *R* is the ideal gas constant, *T* is the temperature of oxidation, R_0 is the initial radius (nm) of the nanoparticle, $D_{Cu\ in\ Cu_2O}$ is the self-diffusion coefficient of Cu in Cu_2O and Δg_{Cu_2O} is the Gibbs energy of formation of the Cu_2O phase. The temperature-dependent Δg_{Cu_2O} is taken from the FactSage thermodynamic database [48]. Finally, *A* is a constant, taken from a range of values provided in the original paper. Here, a value of 0.07 is chosen based on the assumption that the diffusion coefficient of Cu in Cu ($D_{Cu\ in\ cu}$) is significantly higher than $D_{Cu\ in\ Cu_2O}$ and which in turn is larger than the value of the diffusion coefficient of O in Cu_2O ($D_{O\ in\ Cu_2O}$).

Using the experimental data for nanoparticles of an average diameter of ~40 nm and ~20 nm (*Figure 5.3a*), the diffusion coefficient of Cu in Cu_2O is estimated using the Svoboda model taking the experimental duration of complete oxidation into account, at a constant temperature. The temperature dependency of the diffusion coefficient of copper is modelled and plotted (*Figure 5.3b*) using the Arrhenius relation to determine the activation energy and pre-exponential coefficient of diffusion of copper:

$D_{Cu\ in\ Cu_2O} = D_{0,Cu\ in\ Cu_2O}\ exp\ (-\frac{E_{a,Cu\ in\ Cu_2O}}{RT})$, where $D_{0,Cu\ in\ Cu_2O}$ is the pre-exponential diffusion coefficient, $E_{a,Cu\ in\ Cu_2O}$ is the activation energy of diffusion (*R* and *T* carry the usual meaning). The activation energy and the pre-exponential coefficient are calculated to be 79 and 83 kJ/mol and 1.2× 10^{-8} and 3.6 × 10^{-9} cm²/s for 20 and 40 nm size particles, respectively. In comparison to the literature, the activation energy of copper self-diffusion reported here is in between that of Rice et al. (37.5 kJ/mol) for 5-10 nm size NPs and that in bulk copper (115 – 120 kJ/mol) (*Figure S5*) [22,49,50].

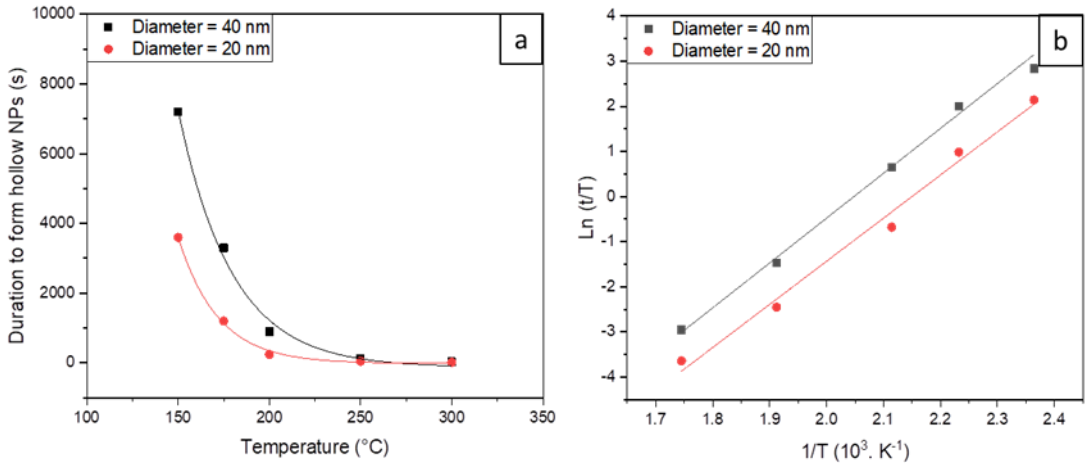

Figure 5.3: a) Experimental observation of hollow copper oxide nanoparticle formation during oxidation at constant temperature for 20 and 40 nm-sized Cu and b) linearized form of Arrhenius relation of self-diffusion coefficient of copper in Cu_2O, as a function of temperature.

The extrapolated diffusion coefficient of Rice et al. (2.3 ×10^{-17} cm²/s) is an order of magnitude higher than in this study (3.7 ×10^{-18} cm²/s), at 150 °C [22]. Additionally, the predicted kinetics of hollow particle formation is comparatively slower than that of Rice et al. as shown in *Figure S6*. The slower diffusion coefficient and the transformation kinetics reported here may stem from the differences in the initial state of the particles and the experimental conditions. While the calculation of Rice et al. is based on the kinetics of chemical phase transition from metallic

copper to copper oxide derived from *in-situ* UV-Vis analysis, we have considered the morphological transformation from an initial core@shell (Cu@Cu_2O) structure to a hollow NP (Cu_2O). UV-Vis spectroscopy tracks the bulk valence change of the NPs with the deduction of the precise time of oxidation completion. Instead, with STEM, the attainment

of oxide layer stabilization is deduced from the imaging of the shell thickness. There is a probable time difference between the two techniques because the stabilization of the shell thickness may be delayed compared to the full oxidization i.e. the shell may continue to morphologically stabilize even after full oxidation, to attain surface energy minimisation through restructuring.

Furthermore, the presence of different defects concentrations (point, planer and volume defects) in individual NPs affects the kinetics as well as the intermediate morphological transformation during the NKE [51,52]. Hence, different diffusion regimes (surface, grain-boundary and/or bulk diffusion) are facilitated as a function of the nanoparticle microstructure and reaction condition [53]. In the current experiment, different intermediate states of nano-voids formations are noted. In some NPs, a single void is formed at the metal/metal oxide interface which then undergoes hollowing in a radially unidirectional manner (*Figure 5.4a*), in agreement with the report of Nilsson et al. [32]. Some NPs undergo multiple voids formation at the metal/metal oxide interface (*Figure 5.4b*), similar transformation has been observed by Nakamura et al [31]. In other NPs, three layers made of void@Cu@Cu_2O are observed (*Figure 5.4c*).

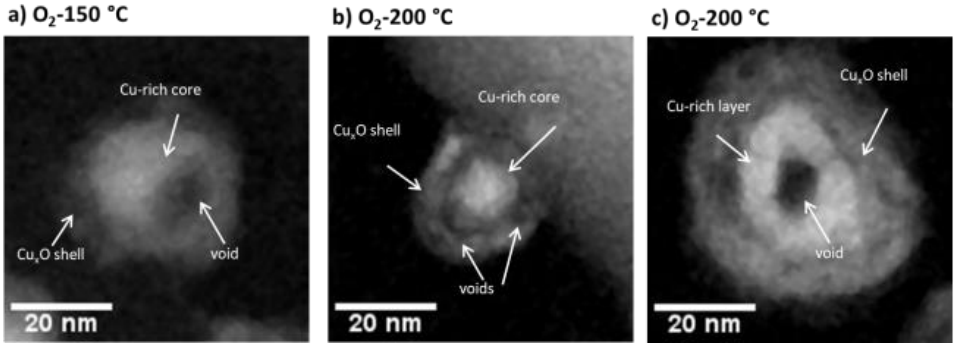

Figure 5.4: Intermediate stages of Kirkendall hollowing under 0.5 atm O_2 partial pressure, a) NP from Syn-1 at 150 °C, after 15 min – unidirectional hollowing, b) NP from Sputt-2 at 200 °C, after 20 min – multiple void formation and c) NP from Sputt-2 at 200 °C, after 20 min – evidence of void@Cu-rich@Cu_xO morphology.

The density of defects within the NPs plays a role in the kinetics of oxidation of Cu_2O which is highly dependent on neutral and singly charged copper vacancies [54]. In addition to the point defects, planar defects such as grain boundaries or twin boundaries are known to act as vacancy source and sink thus, affecting the void formation [52]. Similar to the present study, an *in-situ* liquid STEM study on the oxidation of bismuth NP revealed such

intermediate nanostructures [51]. The authors reported three different intermediate structures leading to the central void formation in bismuth oxide NPs, seemingly stating the difference in the rate of diffusion of the reaction species due to different diffusion pathways facilitated by the presence of defects [51]. The kinetics of hollowing is a complex phenomenon and not only does it depend on the experimental/reaction conditions, but also largely varies from one NP to another within the same experimental setup.

3.2.4.1.2 Collapsing of the hollow nanoparticles

Upon increasing the temperature from 300 to 400 °C under 0.5 atm oxygen and after 20 min at 400°C, most hollow NPs have collapsed to form compact particles within the size range of 5-35 nm (sputtered samples), as shown in *Figure 5.5*. Under the same conditions, hollow NPs with an average diameter larger than 40 nm are still in the process of shrinking from their hollow nanostructures after 20 min. Moreover, different size-dependent intermediate states of transformation are observed after 20 min at 400 °C (*Figure 5.5*). From the difference in the HAADF contrast, segregation of copper species is noted at the interface between the hole and the oxide shell, as indicated by red arrows in *Figure 5.5*.

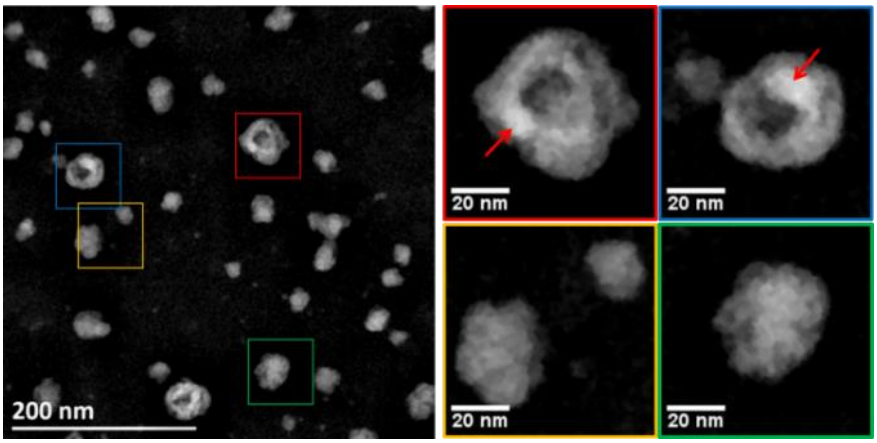

Figure 5.5: Evolution of the particles at 400 °C under 0.5 atm oxygen, after 20 min, showing the size-dependent intermediate state the hollow nanoparticles shrinkage. Sample: Sputt-2.

Collapsing of the NPs is a consequence of surface energy minimization since compact nanoparticles are energetically favoured due to their lower surface energy in comparison to hollow nanospheres which are thermodynamically unstable [55,56]. The kinetics of shrinkage is affected by a number of parameters including the temperature of the reaction as well as the size of the NPs [22,23,56,57].

The occurrence the shrinkage phenomena is evidenced by the *in situ* STEM data acquired at 400 °C (*Figure 5.5*). For larger NPs, below 400 °C, the duration to form compact NPs is significantly longer and above 500 °C the NPs tend to undergo sintering with the other NPs (*Figure 5.9*). Besides temperature, the initial size of the hollow NPs, the concentration of defects and the thermal history of the NPs impact the kinetics of shrinkage [57,58].

3.2.4.1.3 Faceting of nanoparticles

Faceting of the NPs becomes prominent when the NPs are either subjected to increasing temperature during oxidation or directly re-oxidized at 500 °C. In terms of phases, the presence of both Cu_2O and CuO is noticed at the beginning of the oxidation which eventually converts to CuO after prolonged exposure to oxygen.

The faceting of the copper oxide NPs is a contribution of surface atoms reorganisation since at 500 °C the NPs are above the Hüttig temperature of copper oxide (480 °C) which semi-empirically defines the temperature at which surface atoms start to exhibit significant mobility [59]. Thus atomic rearrangement on the surface of the NPs results in reconstruction and minimization of the surface energy of certain surface types. Additionally, adsorbed gas species can also induce surface reconstruction to stabilise certain facets [60].

To summarize, *Figure 5.6* displays a schematic representation of the evolution of copper-based NPs in the size range of 30-40 nm as a function of incremental temperature for 1 hour at each temperature step, under O_2. At low temperature (50 - 150 °C), oxidation proceeds via the formation of a thin Cu_xO layer. At 300°C, voids are formed due to the oxide phase growth mechanism governed by the outward diffusion of copper atoms, which leads to the formation of hollow nanoshells composed of a mixture of Cu_2O and CuO. Upon prolonged oxidation at 300°C, Cu_2O is fully converted to CuO. A further increase in the temperature to 400°C results in the collapse of the hollow shells. Finally, at 500 °C and above, the copper oxide phase starts to form facetted NPs.

It should be noted that both NKE and hollow NP shrinkage are influenced by the duration of oxidation and the size distribution of the NPs. Therefore, the NPs can undergo void formation at a temperature as low as 50°C if either the NPs are dimensionally smaller or subjected to a longer oxidation duration [22,27]. Similarly, shrinkage can occur at a lower temperature for smaller NPs or depending on the heating duration. Hence, the

representation *Figure 5.6* is a general overview and pathway of the shape changes occurring during the oxidation of copper NPs as a function of temperature.

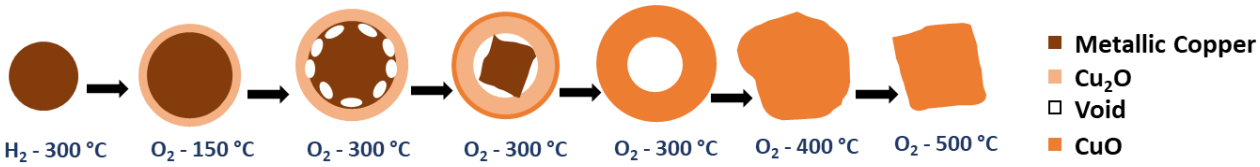

Figure 5.6: Schematic representation of the evolution of nanoparticle morphology as a function of the reaction temperature during oxidation of ~30-40 nm sized particles.

3.2.4.2 Reduction of Copper Oxide Nanoparticles

Hydrogen at 0.5 atm partial pressure was introduced to copper oxide nanoparticles at different temperatures from 200°C to 500 °C and for different oxide phase morphologies, exhibiting either hollow or compact shapes. The gas was introduced at a constant temperature as well as at an increasing temperature.

The formation of metallic copper is very slow below 250 °C. Between 250 and 300 °C, the reduction of copper oxide results in metallic copper, as deduced from the change in HAADF contrast and the analysis of the FFT patterns of the HR images. Substantial changes can be noticed in the morphology in *Figure 5.7*, where images were taken from the same area of observation under different gas environments. Reduction leads to fragmentation of the particles as can be seen in several areas of the images. For instance, in the area highlighted by the red dotted circle, one hollow nanoparticle ends up forming three smaller nanoparticles after reduction in H_2. Moreover, the nanoparticles circled in blue are in the process of sintering under oxygen, followed by fragmentation under H_2 into one large nanoparticle (comparable in size to the initial metallic phase diameter of ~40 ± 5 nm) and eight smaller nanoparticles of ~2-6 nm. The fragmentation process is also illustrated by the size distribution histograms shown in *Figure S7-S9*. It is found that the NPs in the size range 0-10 nm are more numerous after re-reduction compared to the initial reduced sample.

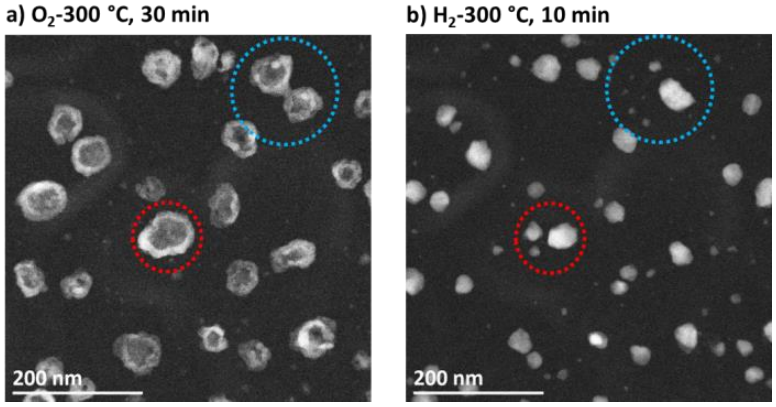

Figure 5.7: Fragmentation of hollow copper oxide nanoparticles at 300 °C upon reduction: a) copper oxide NPs under O_2 after 30 min and b) under H_2 after 10 min of gas flow. Sample: Sputt-1.

The underlying phenomenon of fragmentation is visualised in real-time during the reduction reaction. The H_2 induced breakage of the particles into multiple fragmented NPs as a function of increasing temperature (from 150 °C to 300 °C) is presented in *Figure 5.8*, along with a schematic representation. Initially, the hydrogen molecules diffuse inside the hollow porous shell where the presence of defects promotes the reduction, thereby forming multiple reduction sites. The reduction sites can be deduced from the contrast of *Figure 5.8*. Once the reduction sites have been formed at around 220 °C (visualised from the difference in phase contrast), the metallic particles start to grow via particle migration and coalescence (PMC) mechanism with the neighbouring clusters. The process is very dynamic and stabilizes once the surface energy of the resulting particles is minimized.

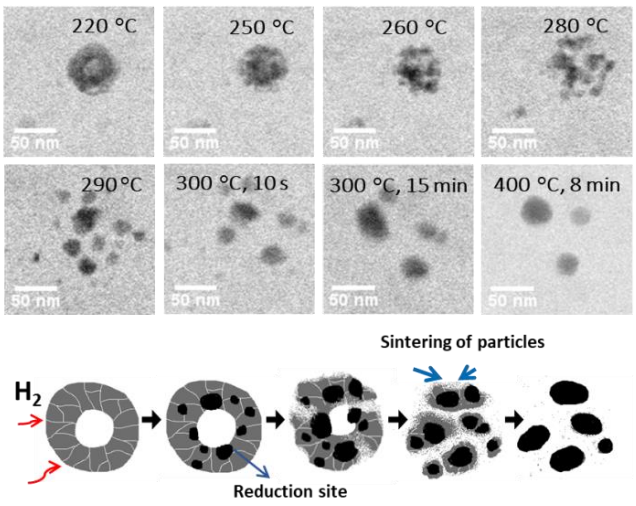

Figure 5.8: Reduction of hollow copper oxide nanoparticles under hydrogen heated from 150 °C to 300 °C at 5 °C/min rate, at 400 °C (top) and the schematic representation of fragmentation process with suggested mechanism (bottom). Sample: Synth-1.

The reduction of hollow CuO NPs has also been carried out at a constant temperature of 250 °C (*Figure S10 – S12*), which showed a similar fragmentation behaviour as discussed above.

At 400 °C, the reaction is too fast to observe any intermediate transformation step. Both collapsed (size below 40nm) and collapsing (above 40nm) CuO NPs are initially present, and form fragmented metallic copper particles within a few seconds of the introduction of the H_2 gas (*Figure S13*). With longer exposure to high temperature under H_2, the NPs tend to grow into larger particles (*Figure S14*) and the process of fragmentation is evidenced only in few areas. This could be explained by the high rate of PMC induced by the temperature. In other words, the reduction mechanism at 400 °C is likely similar to that at 300 °C, but due to increased temperature, the dynamics of the fragmentation and the subsequent growth process are faster.

The reduction of fully compact shaped NPs at 250°C (*Figure S15*) also produces fragmented nanoparticles. This observation contradicts the speculation of Weststrate et al. who have suggested the presence of Kirkendall void as a prerequisite for the fragmentation of cobalt-based NPs [61]. Based on our observations, it can be concluded that the oxide NPs (copper) undergo fragmentation regardless of the shape of the particles (hollow and compact morphologies).

The origin of reduction-fragmentation is visualised under different temperatures and nanoparticle morphologies could arise from a combination of unit cell volume shrinkage, nucleation and growth phenomena [34,35,61]. The unit cell accounts for 60 % shrinkage in volume during the transformation of CuO to metallic Cu. In terms of nucleation and growth, the genesis of numerous nucleation sites is more likely to produce multiple individual metallic particles as opposed to the growth of an already reduced domain, observed from the difference between the present study and the literature [29]. At higher H_2 pressure, the formation of multiple nucleation sites was observed, followed by growth, to form individual NPs. In contrast at lower H_2 partial pressure, growth of metallic copper phase occurred in a layer by layer fashion from an initial nucleation site formed on the Cu_2O surface [29].

3.2.4.3 Shape, sintering and evaporation of the copper nanoparticles

At 500 °C, the shapes of copper-based nanoparticles are drastically different depending on whether they are composed of metallic phase under hydrogen (*Figure 5.9b*) or copper oxide under O_2 (*Figure 5.9a, c*). The compact facetted oxide nanoparticles exhibit spherical morphology after reduction, with some of the NPs forming truncated octahedron-like shapes. From the HR-STEM image, the (111) and (200) facets of copper have been identified. After re-oxidation at the same temperature, the oxide NPs undergo faceting with major (111) and (-111) surfaces exposed. Similar gas-induced NP morphology evolution has been observed in other transition metal-based nanoparticles [62–65].

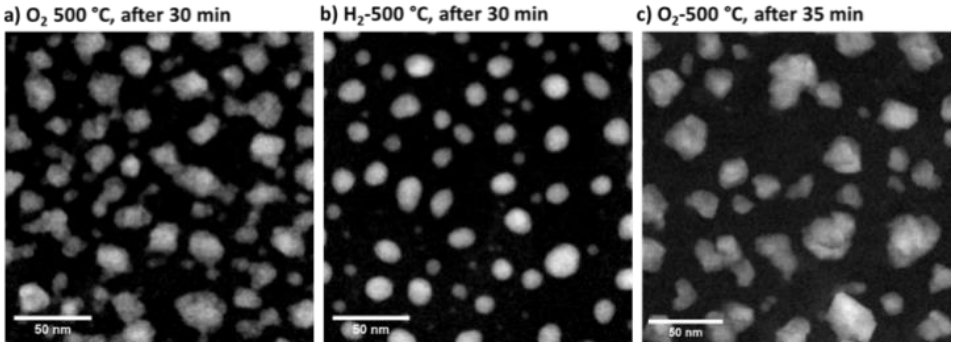

Figure 5.9: Reduction and re-oxidation of copper oxide nanoparticles at 500 °C: a) under O_2 after 30 min of gas flow b) under H_2 after 30 min of gas flow and c) NPs after re-oxidation after 35 min of oxidation. The images are not from the same area of observation. Sample: Sputt-3.

Upon increasing the temperature from 400 to 900 °C at 1°C/s, the NPs are subjected to different growth mechanisms, namely particle migration and coalescence (PMC), Ostwald ripening (OR) and coalescence via bridge formation, as a function of gas atmosphere (O_2 and H_2). Under O_2, OR is the dominant growth mechanism as visualised from the growth of the particles in the yellow squares in *Figure 5.10* at the expense of the smaller NPs in blue squares in *Figure 5.10*. The growth of the NPs is either visualised through an increase in the apparent size of the NPs or through the increase in the thickness-dependent contrast. In some areas, the NPs grow via surface reconstruction to form bridges between the NPs, indicated by the green squares in *Figure 5.10*. This type of growth is also observed at a lower temperature for NPs undergoing hollowing (blue dotted circle in *Figure 5.7a*). The process of bridging and eventual sintering of the nanoparticles have been termed as attractive migration and coalescence by Yang et al [66]. Attractive migration and coalescence differ from that of PMC since the particles do not experience Brownian-like motion and the

underlying mechanism is similar to that of OR, involving atomic migration [67]. For this growth mechanism, the distance between the NPs as well as the wetting behaviour of the NPs are deemed to be important. Compared to metallic copper, copper oxide exhibits increased wetting behaviour due to stronger adhesion between the NPs and the support [68]. The resulting spreading of the oxide NPs and proximity to the neighbouring NPs promotes atomic migration and eventual coalescence [69].

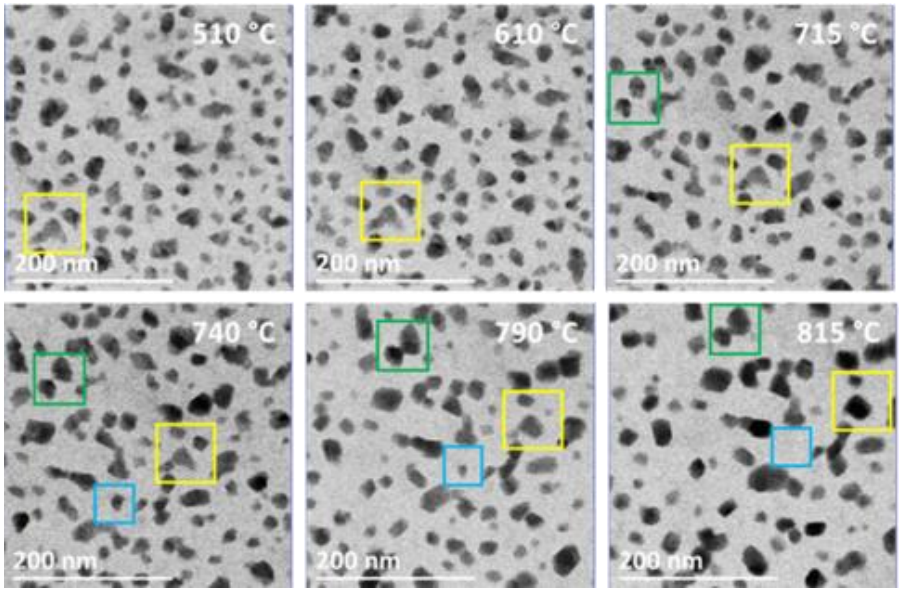

Figure 5.10: Sintering behaviour of copper oxide NPs, heat treatment from 500 °C to 815 °C at 1 °C/s. The coloured squares illustrate the different growth mechanisms of the NPs. Sample: Sputt-2.

Under H_2, the metallic copper NPs undergo temperature-dependent growth mechanism as identified by red and green squares in *Figure 5.11*. The red square shows the area where PMC is noticed between 400 and 500 °C. The snapshots of the video depict the dynamic movement of the nanoparticles captured in real-time until the temperature reached 500 °C. Particles 3 and 4 remain fixed in their position while particles 1 and 2 undergo hopping movement. The distance moved by particle 1 is negligible but Brownian-like motion is particularly discernible for particle 2. Besides, the very small particles marked by black arrows are merged to particle 2 via coalescence. Interestingly, particle number 2 does not experience any more hopping motion once the temperature reaches 500 °C.

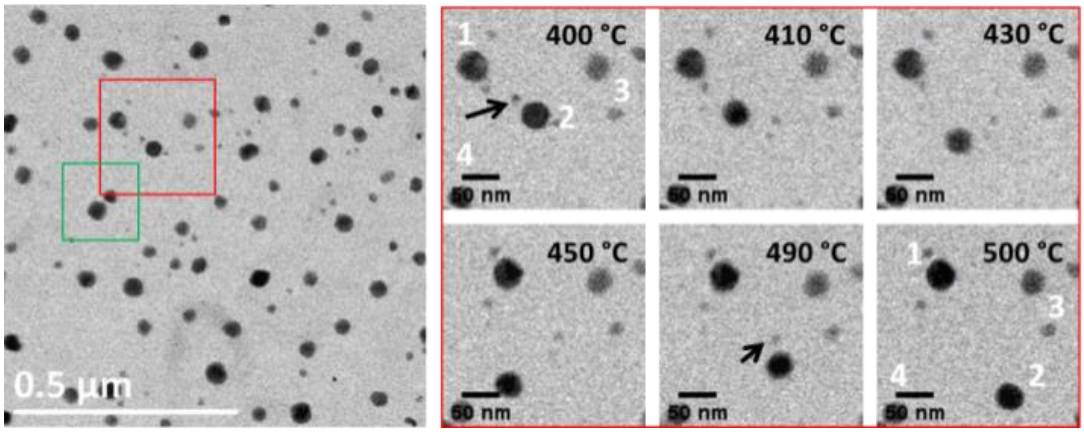

Figure 5.11: BF image extracted from a video with red and green squares depicting PMC and coalescence via bridging, respectively (left) and series of images presenting PMC during in-situ heating from 400 to 900 °C, 1 °C/s under H_2. The snapshots are taken at 400 °C (0 s), 410 °C (10 s), 430 °C (30 s), 450 °C (50 s), 490 °C (90s) and 500 °C (100 s).

The green square in *Figure 5.11* depicts the coalescence of the NPs via bridging at a temperature of 500 °C and above. The emergence of the bridge and the progressive sintering are presented in a series of images from 420 to 900 °C in *Figure 5.12*. Martin et al. have studied the sintering of metallic copper at low H_2 partial pressure (9 x 10^{-5} atm) and under vacuum [20]. They state that at 500 °C under H_2, the NPs undergo growth via atomic migration (OR) while under vacuum, the size of the NPs stays constant for the same annealing duration. No other sintering mechanism such as PMC or coalescence via bridging has been reported in their study, hence highlighting the importance of partial pressure on nanoparticles behaviour.

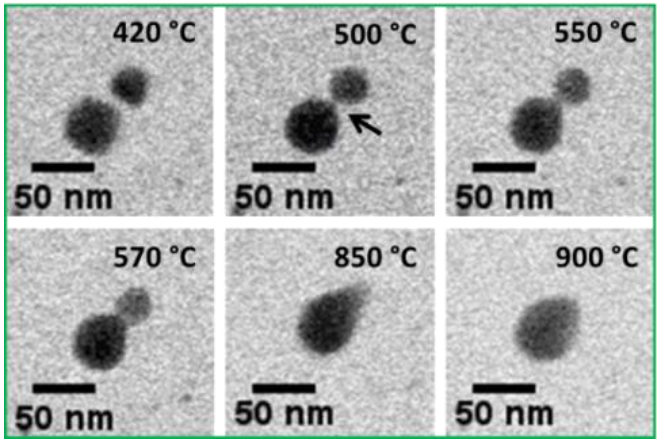

Figure 5.12: Particles undergoing attractive migration and coalescence as observed during in-situ heating from 400 to 900 °C, 1 °C/s under H_2. The snapshots are taken at 420 °C (20s), 500 °C, (100 s), 550 °C (150 s), 570 °C (170 s), 850 °C (350 s) and 900 °C (400 s).

As a consequence, several factors including metal-support interactions, NPs size and distribution across the substrate and gas partial pressure determine the mechanisms of sintering.

The last aim of this study was to understand the oxidation-reduction behaviour of copper NPs at operating conditions close to those of CLC, i.e .between 800 and 1000 °C. However, it is difficult to stabilise the NPs in the *in-situ* STEM setup above 700 °C. Depending on the duration of thermal treatment and the initial size of the NPs, starting at 700 °C, the NPs undergo slow depletion in size until all the NPs are evaporated from the substrate. The rate of evaporation is even faster at 900 °C - taking only a few minutes for 10 – 30 nm-sized NPs to evaporate (*Figure S17*). The effect of different gas atmospheres on the evaporation kinetics could not be discerned from the current experiments since the rate of evaporation is very fast and the kinetics is influenced by other factors such as NPs size, shape and the physical properties of the substrate. Size-dependent melting temperature depression and eventual evaporation either via liquid phase or direct sublimation have been reported previously for similar NP systems during *in-situ* STEM observation [70–72].

3.2.5 Conclusions

In-situ analyses by transmission electron microscopy of the oxidation/reduction reactions at different temperatures were carried out on chemically synthesized and sputtered copper nanoparticles to understand the changes in the morphology of the NPs. At a low temperature, with the introduction of an oxidative environment, a thin layer of oxide is formed surrounding the metallic core that eventually turns into a hollow particle upon increasing the temperature. Further augmentation of the temperature leads to collapsing of the hollow nanoparticles with subsequent faceting of the NPs. The reduction of the hollow nanoparticles results in fragmentation into smaller particles. The process of fragmentation is very dynamic and stabilizes once the surface energy of the resulting particles is minimized.

The shape evolution of the NPs during oxidation and reduction are subjected to various parameters including NP initial size and density of structural defects, temperature, pressure, and duration of the gas exposure. Furthermore, depending on the temperature and the gas atmosphere, different sintering mechanisms are activated. The underlying

phenomena concerning the different morphological changes and the growth mechanisms illustrated throughout this study originate from the migration of the copper phase and are connected by the minimization of the energy of the global system.

In this work, the significance of *in-situ* STEM under relevant industrial reaction condition (particularly, higher gas pressure) is demonstrated in comparison to previous studies conducted at lower partial pressure. Nevertheless, we have also highlighted some challenges faced during the experiments, for instance, the difficulties to monitor some of the intermediate changes during the reaction when the reaction kinetics is very fast, and more importantly, the evaporation of the copper phase during high-temperature reaction. The confinement of the nanoparticles remains a challenge to characterise such systems at very high operating temperature, using *in-situ* STEM.

3.3 MODEL SYSTEM – CU/AL_2O_3 SUBSTRATE

This section focuses on the mobility of copper on the alumina substrate in the presence of H_2/Ar and O_2/Ar. As stated in the introduction, owing to the copper-support interaction the migration mechanism as well as the kinetics of mobility may be influenced depending on the type of support. Furthermore, it is crucial to determine the temperature range at which the lattice diffusion of copper atoms leads to the $CuAl_2O_4$ formation. Based on the experience on Cu/SiN_x material, gradual depletion of copper particles is expected under both H_2 and O_2 environments. Hence, the question would be if the copper-alumina interaction is enough to prevent such migration or at what temperature would the migration occur?

Moreover, a comparative study of the Cu/SiN_x and Cu/Al_2O_3 model systems would provide qualitative information on the strength of the copper-support interaction, copper nanoparticles stability and preferential mobility crucial to explain porous supported systems behaviour (later studied in chapter 6).

3.3.1 Experimental

To prepare the Cu/Al_2O_3 sample, first a 10 nm layer of alumina is deposited directly on the SiN_X membrane of the commercial e-chips. The alumina deposition was carried out via pulsed laser deposition method (PLD) using an alumina target at room temperature. The thickness of the sample is carefully controlled by fixing the deposition parameters over few trial and error runs on Si substrate and measuring the resulting thickness by X-ray reflectometry. To remove any oxygen vacancy and to stabilise the surface of the alumina, the e-chip was heated in the microscope under 0.5 bar oxygen partial pressure at 600 °C for 2 hours. At the end of the heating the alumina support was amorphous in nature, based on selected area electron diffraction.

The copper thin film of 1.5 nm was deposited using e-beam evaporator directly on the alumina substrate. The PLD and the evaporation were conducted at IPCMS, using R2D2 device from MECA2000 and Plassys MEB550S, respectively.

For the ease of explanation in the later part of the text, the e-chip nomenclature is shown in *Figure 5.13* where the SiN_x transparent windows or “holes” are numbered from 1-6. It

should also be noted that the “lower side” and the “upper side” on the image is named because of the position in the sample holder where the “lower side” is near the gold contact and the gas inlet/outlet side.

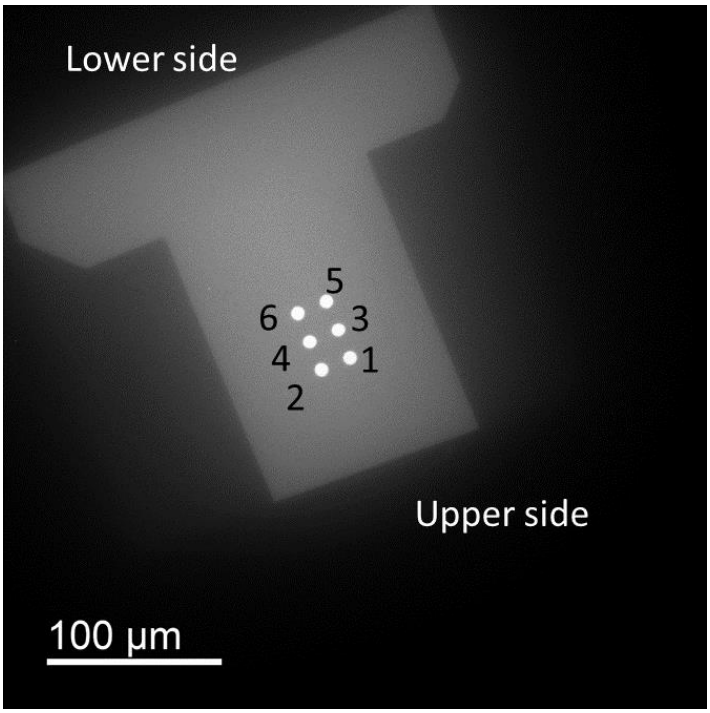

Figure 5.13: Presentation of the e-chip with SiN_X windows “holes” numbered from 1 – 6 and the position of the e-chip relative to the sample holder.

3.3.2 Mobility under H_2

The sample was heated from 25 °C to 200 °C under H_2/Ar at 5 °C/min. At this temperature no NP was formed so the temperature was increased to 300 °C at a rate of 3 °C/min. From 300 °C to 750 °C the heating ramp was kept 3 °C/min. The temperature program and steps are presented in *Figure 5.14.*

Figure 5.14: Experimental steps and heating scheme for Experiment- $Cu/Al_2O_3 – H_2$.

It should be noted that, considering the amorphous nature of the alumina film and the thickness of 10 nm, it is likely that the actual temperature on the alumina and copper might

be lower than the set temperature of the e-chip. Since no attempt has been done to determine the actual temperature, the analysis of these data is limited to a qualitative approach.

3.3.2.1 Nanoparticle formation

The NP formation took place during the 2h30 step under H_2/Ar. During the acquisition of the *in-situ* images the sample was sensitive to beam effect.

In some areas the change/loss of Cu nanoparticles was more drastic than other areas. In comparison, the nanoparticles on SiN_x membrane were stable at this temperature and similar beam dose. Hence, to minimise the beam induced effect the right imaging condition was set by adjusting to lower magnification and acquisition time. This reduced the resolution of the images, in addition to the presence of thick alumina layer and of the gas atmosphere. The particle size distribution is presented in *Figure 5.15*. The average NP size is 8 ± 5 nm with a NP density of about 750 NP/µm². The NP density and the average size is lower than the Cu/SiN_x system, perhaps due to the amount of copper deposited is lower.

3.3.2.2 Mobility under H_2 from 500 to 700 °C

Followed by the formation of the nanoparticles, the particles are heated under H_2 from 300 °C to 700 °C with a plateau at 500 °C for 2.5 hours, at 600 °C for 45 minutes and at 700 °C for 1 hour. The imaging was carried out every 15 minutes. The heating duration was chosen either based on the size evolution of the nanoparticles (for 500 °C) or depending on the loss of the particles at 600 and 700 °C for the given area of observation.

During the heating, some discrepancies were observed concerning the different areas of observations. For example, at the end of the 500 °C and 600 °C the NP density of the viewing areas was relatively lower than on other areas in the e-chip. Hence, every time a different area had to be observed to consider only the effect of heating duration on the PSD of a given area. The disparity in the NP density leads to the assumption that the temperature profile was not the same throughout the e-chip.

Table 5.1 provides a summary of the temperature, heating duration, area where the observation was carried out and the overall changes in the NP density and size at the

beginning and the end of the heating. *Figure 5.15* reports the STEM images at different temperatures of heating and the effect of heating duration on a set of particles.

At 500 °C, there was an overall decrease in the number of the NP from 700 NP/µm² (average size is 8 nm) at the beginning to 620 NP/µm² (average size of 9 nm) at the end of the 2.5 hours (*Figure 5.15 a-c*). The loss of the NPs occurred mostly for the particles smaller than 5 nm in diameter at a rate of ~0.05 nm/min. Particles larger than 5 nm remained relatively constant since the beginning of attaining 500 °C.

At 600 °C, by the end of the 45 minutes of heating duration, the density of the nanoparticles declined, while the average size increased from 10 nm to 20 nm. *Figure 5.15 d-f* displays the tracking of some the nanoparticles, NP#1 increased in mean size from 36 ± 8 nm to 59 ± 11 nm after 30 minutes of heating, followed by a reduction in the size after 45 minutes. Meanwhile, nanoparticles less than 15 nm size were no longer visible after 30 minutes of heating. The depletion rate of the nanoparticle size was approximately 0.3 nm/min.

Similarly, at 700 °C there is an overall loss in the NPs density over a period of 1 hour roughly at a rate of 1.5 nm/min. Finally, at the end of the 1 hour heating no particle was found on the viewing area, as displayed in *Figure 5.15 g-i*. Surprisingly, very few or no nanoparticles were found in holes 1 to 4. Comparatively there were many nanoparticles in holes 5 and 6. The remaining nanoparticles found in holes 5 and 6 displayed a broad size range of 20 – 100 nm. These larger nanoparticles were much more stable and displayed a slower rate of overall size loss after 30 minutes of heating at 750 °C. As the temperature was increased further to 900 °C, all the nanoparticles disappeared within few minutes. The nanoparticles were eventually found on the non-heated e-chip. This phenomenon will be discussed later in the chapter.

Table 5.1: Particle density and average size as a function of temperature and heating duration.

Temperature (°C) Heating duration	**Hole**	**At the beginning**	**At the end of heating**
500 °C, 2.5 hours	1	700 NP/µm², 8 ±2 nm	620 NP/µm², 9 ± 2nm
600 °C, 45 minutes	1, different area	700 NP/µm², 10 ± 3 nm	30 NP/µm², 20 ± 5 nm
700 °C, 1 hour	2	- 150 NP/µm², 40 ± 10 nm	Total loss in the viewing area
750 °C, 30 minutes	6	180 NP/µm², 60 ± 20 nm	150 NP/µm², 60 ± 20 nm

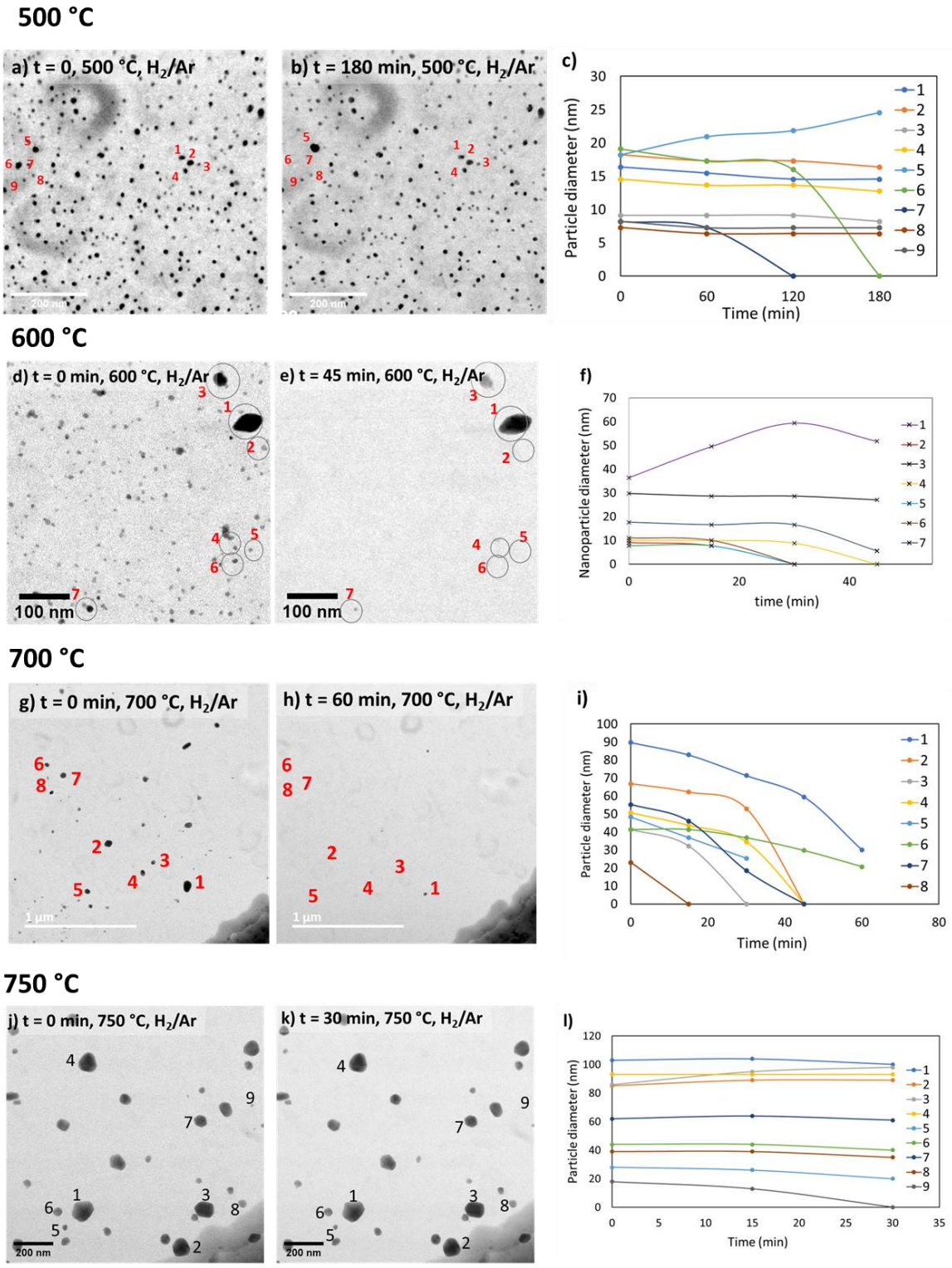

Figure 5.15 : STEM-BF images of the nanoparticles at the beginning and end of heating period and size evolution profile of selected NPs under H_2, at 500 °C (a-c), 600 °C (d-f) and 700 °C (f-g). For a given temperature the images were taken from the same area.

To conclude, the nanoparticles were relatively stable up to 500 °C, afterwards there was an overall decrease in size until they depleted completely as the calcination temperature was periodically increased to 900 °C. From the overall change in size distribution and the position of the nanoparticles, the sintering mechanism is assigned to Ostwald ripening. The presence of very large nanoparticles at the end of the 750 °C plateau in different holes also confronts the idea of Ostwald ripening. However, it could not be discerned whether the atomic migration of the copper occurs via substrate surface or vapour phase. Few nanoparticles also displayed Brownian-like motion at different temperatures for a brief time, but they stabilised after some time. No attractive or particle migration and coalescence was observed unlike the Cu/SiN_x system. Compared to the SiN_x substrate, atomic migration of copper encompassed a larger distance in the Cu/Al_2O_3 system (based on the copper PSD in holes 1-4 compared to holes 5-6). The nanoparticles appeared to be more mobile in the Cu/Al_2O_3 sample than in the Cu/SiN_X sample.

In general, the rate of NP loss followed an exponential trend as a function of increasing temperature. Nevertheless, a firm conclusion cannot be drawn due to poor statistical significance and possible experimental discrepancies. There is disparity between the different areas of the e-chip. While at 700 °C in hole 1 there is complete depletion of nanoparticles less than 50 nm within 30 minutes of exposure, in hole 6 nanoparticles of similar size were stable up to 30 minutes at 750 °C. Presumably, the temperature profile throughout the e-chip was not homogeneous. In our previous experiments with SiN_X substrate such discrepancies were not observed. The distribution of the particles was homogeneous throughout the e-chip. Therefore, any difference in the area-dependant behaviour of the nanoparticles may arise due to the alumina layer.

3.3.3 Reaction under O_2

The sample was heated under H_2, in a similar way as the previous setup up to 300 °C, until there was formation of the nanoparticles. To keep equivalent heat treatment time, the sample was kept under H_2 for 1 hour before the introduction of the O_2. The idea was to observe the sintering during temperature ramp up as well as at constant temperature, under O_2. After 1 hour at 300 °C, the temperature was increased to 500 °C at a rate of 3 °C/min. However, due to some difficulties with the observation (discussed later in section

4.2.3.2), H_2 had to be re-introduced, afterwards the steps of oxidation were repeated and heated up to 600 °C (*Figure 5.16*).

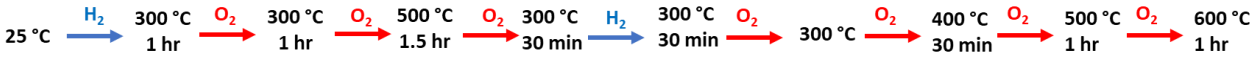

Figure 5.16: Experimental steps and heating scheme for Experiment- Cu/Al_2O_3 – O_2.

3.3.3.1 Nanoparticle formation

The nanoparticles of copper are formed on the alumina substrate by heating under H_2 at 300 °C. The average size of the NPs was about 11 ± 7 nm and a density of 500 NP/µm². Considering the uncertainties, these values are in good agreement with the previous experiment under H_2.

3.3.3.2 Mobility under O2 from 300 to 600 °C

Following the formation of the NPs under H_2, O_2 was introduced in the chamber at 300 °C and heated for 1 hour. Some of the NPs underwent hollow particle formation within the first 15 minutes as displayed in *Figure 5.17b*. The overall size of the NPs increases from 11 ± 7 nm to about 18 ± 10 nm under oxidation. The phenomenon of hollow particle formation is similar to behaviour of Cu/SiN_x sample, in section 3.2.4.1.1. In terms of sintering, there was overlapping of some of the NPs due to increase in the volume in the hollow nanoparticles. Some small nanoparticles either disappeared or exhibited Brownian-like motion on the substrate before sintering via PMC.

When the temperature was increased to 500 °C, the same area of observation displayed drastic change as displayed in *Figure 5.17c*. The hollow nanoparticles were no longer found, instead, there were some large structures. As the imaging was only carried out once the temperature was reached, the exact nature and dynamics of this growth could not be monitored which must have occurred during the temperature ramp.

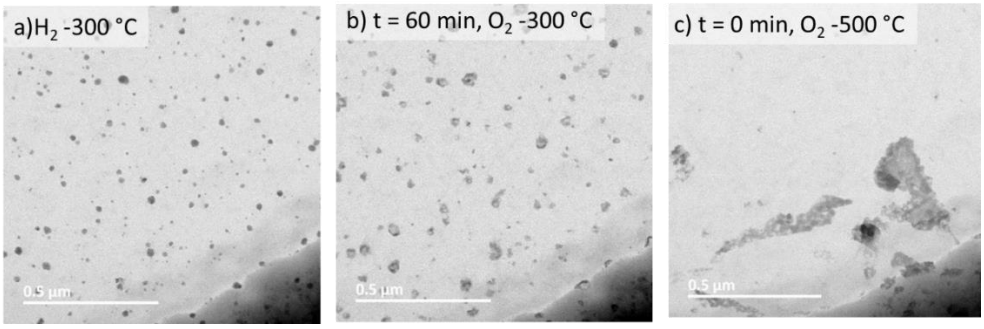

Figure 5.17: STEM-BF images of the nanoparticles from the same area under a) H_2 at 300 °C, b) O_2 at 300 °C after 1 hour and c) at 500 °C

Other holes of the SiN_x viewing areas were checked and copper was only found on the lower part of holes 2, 4 and 6. In holes 1, 3 or 5 there was no particle at all. Like in the H_2 experiment, the differences among the holes may arise due to inhomogeneous alumina deposition resulting in temperature profile disparities. The fact that the particles are found on the same chip points out surface atomic migration and growth of the copper nanoparticles.

The sample was kept at 500 °C for 1 hour. After 1 hour, no particle was observed in any of the holes, except hole 6. As seen in *Figure 5.18*, in a span of 1.5 hours there was gradual growth of large structures. A closer look at the structures reveals very unusual morphology, the area circled in blue displays amorphous-like feature and a large crystalline looking particle exhibiting darker contrast. The dark contrasted particles resembled the faceted structure of CuO as observed in the Cu/SiN_x system under O_2 at high temperature.

In the area circled in red the structure appeared to be a single entity, like a network, with features containing steps and edges. In some areas stacking of lamellae with porosity are also observed.

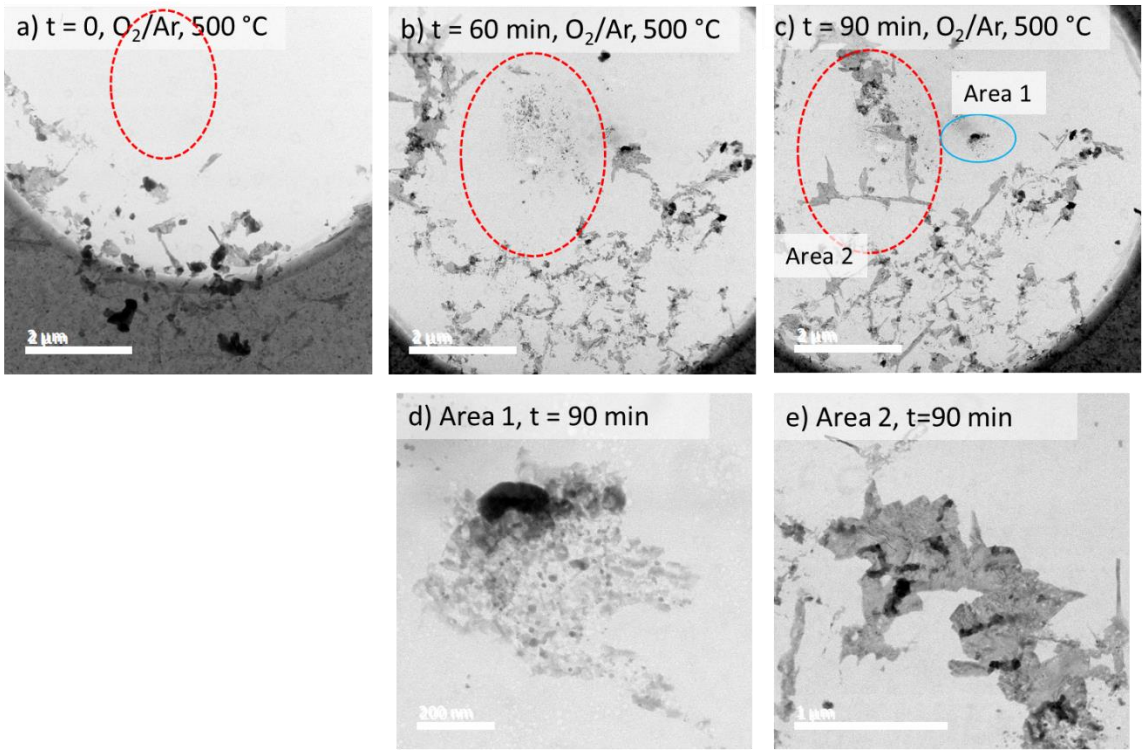

Figure 5.18: STEM-DF image of the same area in hole #6 a) at t=0 when the temperature reached 500 °C, b) after 1 hour and c) after 1.5 hours. The higher magnification areas of the red and blue circled regions are displayed in the bottom row.

The formation of such large entities with unusual morphology was not observed in our previous studies with Cu/SiN_x. As discussed in section 3.1, on SiN_x, the hollow particles undergo collapse followed by faceting, upon increase in the temperature, under O_2.

Hence, we can ask if these structures are copper aluminate or copper oxide. Indeed, the diffusion of copper atoms into the bulk amorphous substrate has been reported using in-situ TEM and chemical profile analysis, at 200 °C under O_2 [73]. In addition, amorphous aluminium hydroxides are reported to react with copper at relatively lower temperature than γ or α Al_2O_3 [74].

Due to issues with the focus it was difficult to obtain a reliable diffraction pattern using selected area electron diffraction. Consequently, it was decided to introduce H_2 to observe their evolution. Within few minutes the structure underwent fragmentation alike the copper oxide nanoparticles in the Cu/SiN_x system. The presence of metallic copper was verified by EDS. The reduction of the copper aluminate phase usually results in the formation of small spherical nanoparticles on the alumina surface (will be discussed in chapter 6). Therefore, it could be concluded that the unusual structure was made of copper

oxide, seemingly formed via atomic migration and layer-by-layer attachment. Atomic migration is assumed rather than PMC as no Brownian-like movement of particles were observed.

O_2 was re-introduced at 300 °C, and the temperature was increased to 500 °C. With the increase in the temperature some areas (*Figure 5.19*, circled in red) underwent slow disintegration and loss of the copper phase, while some continuous structures started to emerge in other areas (*Figure 5.19*, circled in green). The newly formed structures have similar texture and morphology as the first ramp-up structures and likely to be formed via similar mechanism.

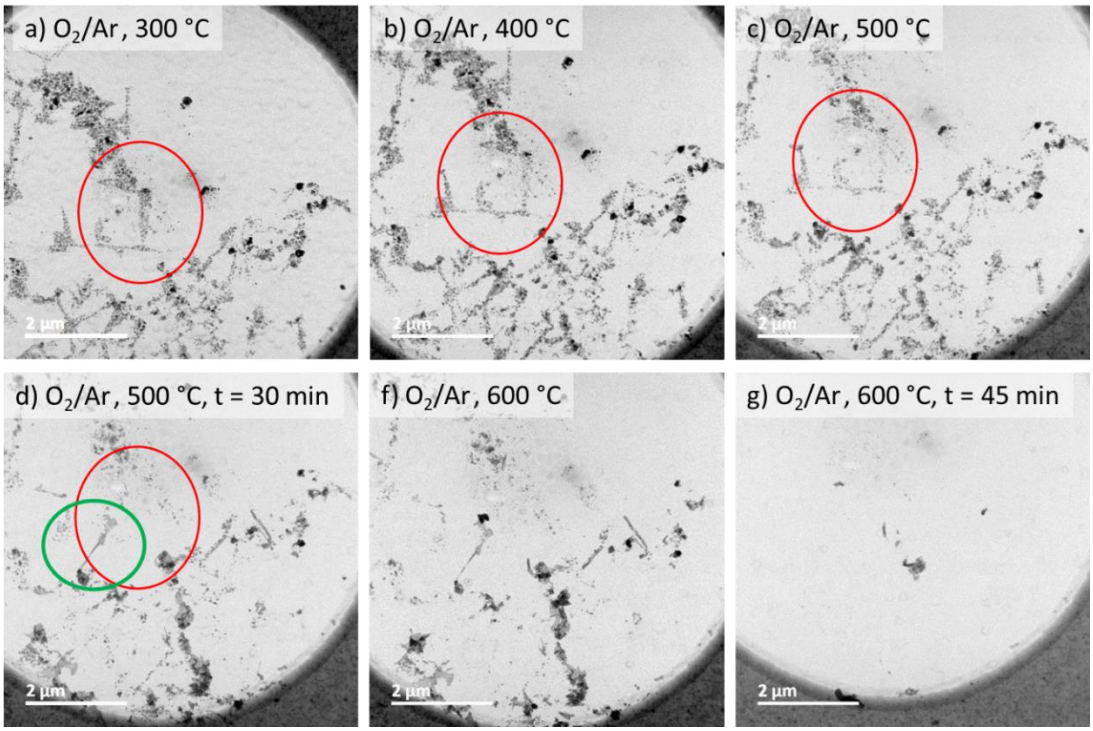

Figure 5.19: BF images of the same area in hole #6 undergoing copper-phase depletion (marked with red circle) and formation of new areas (green circle) at an increasing temperature from 300 °C to 600 °C.

Eventually when the temperature was increased to 600 °C, after about 1 hour there was complete loss of the copper phase from the last available area (hole 6). A large number of faceted structures were found on the SiC membrane, at the lower portion of the e-chip. These structures ranged from few 100 nm to few µm in size. Finally, a large block of particles was visible on the lower side of the chip, away from the heating area (*Figure 5.20*). The

presence of particles in the colder part of the e-chip suggests that the migration might be driven by the temperature difference between the hole and the substrate.

Unlike the experiment with H_2 on the Cu/SiN_x sample where the nanoparticles are found on the non-heated e-chip, in this experiment the particles are found on the heating e-chip.

These two different observations might stem from different copper migration mechanisms involving vapour phase transport in case of the Cu/SiN_x system and Cu/Al_2O_3 with H_2, and surface migration in Cu/Al_2O_3 under O_2.

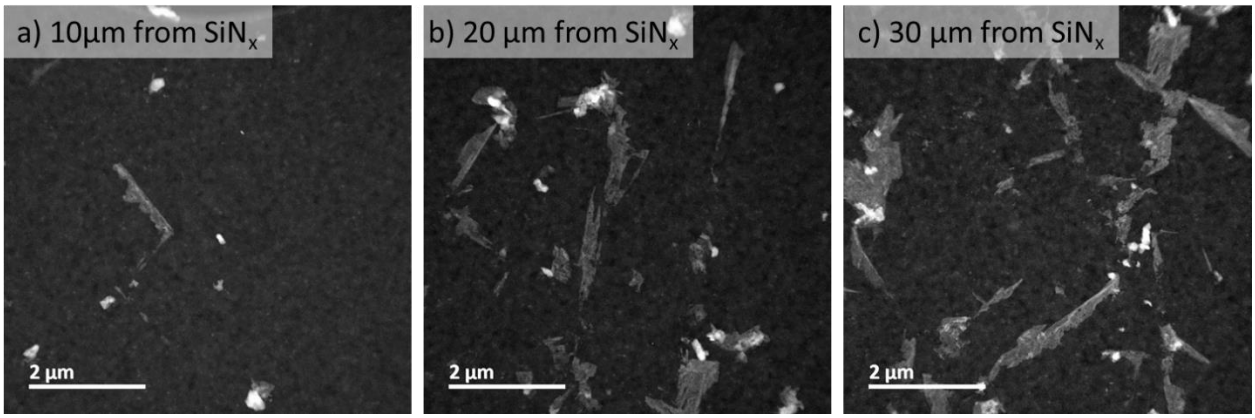

Figure 5.20: DF images of areas outside the SiN_x membrane a) 10 µm b) 20 µm and c) 30 µm from hole 6.

4 CONCLUSION

The mobility of the copper-based nanoparticles on the SiN_x and alumina substrate was monitored under H_2 and O_2. Under H_2, copper nanoparticles exhibited spherical morphologies in both Cu/SiN_x and Cu/Al_2O_3 samples. In contrast, under O_2, the morphology of the two systems were significantly different. Moreover, at high temperature copper undergo evaporation regardless of the difference in the support or the gas atmosphere. However, in general, based on the thermal stability and the migration behaviour of the nanoparticles, copper-SiN_x appeared to exhibit stronger metal-support interaction compared to Cu-Al_2O_3.

Similarly, under O_2 the Cu-SiN_x sample displayed superior metal-support interaction and the CuO nanoparticles were stable up to a very high temperature on SiN_x membrane. In contrast, the CuO-Al_2O_3 sample showed unusual atomic migration and structural growth.

The differences in the observations copper particles behaviour upon the two substrates were likely to be contribution of multiple factors, including the metal/metal oxide support interaction, presence of gas influencing the surface energy and the experimental discrepancies. Indeed, experimental discrepancy was a major issue. The different areas of the e-chip in both Cu/Al_2O_3 samples showed drastic disparities in terms of copper phase evolution, indicating possible inhomogeneity in the alumina layer. Inhomogeneous substrate may either have different temperature-profile or surface physical properties thus affecting the stability of the copper phase. Besides that, the gas atmosphere has significant influence on the nanoparticle stability. Despite the expected stabilising effect of O_2 reported in many literatures on a variety of metal-support systems, the contrary was observed in the $Cu\text{-}Cu/Al_2O_3 – O_2$ sample. This highlights the synergetic effect of the metal-support-gas system.

The model systems reported in this chapter provided information on the expected nanoparticle morphology which would be beneficial to identify in the more complicated supported materials reported in the next chapter. Although, the different diffusion regimes and $CuAl_2O_4$ phase formation could not be observed in the Cu/Al_2O_3 system, but the study provided insights on the influence of support and the gas atmosphere on the stability of the copper particles.

5 REFERENCES

[1] F. Moya, E.G. Moya, D.Juve, D. Tr6heux, C. Grattepain and M. Aucouturier. SIMS study of copper diffusion into bulk alumina, *Scripta Metallurgica et Materialia*, 1993, **28**, 343-348.

[2] Bolt, P. H., et al. Formation of Nickel, Cobalt, Copper, and Iron Aluminates from a- and c-Alumina-Supported Oxides: A Comparative Study.

[3] M. Luong, Eric Robin, N. Pauc, P. Gentile, M. Sistani, A. Lugstein, M. Spies, B. Fernandez and M. den Hertog. In-situ high resolution Transmission Electron Microscopy

observation of Aluminum diffusion in Germanium nanowires: fabricating sub-10 nm Ge quantum dots, *ACS Applied Nano Materials*, 2020, **3**, 1891-1899.

[4] L. Han, Q. Meng, D. Wang, Y. Zhu, J. Wang, X. Du, E. A. Stach and H. L. Xin. Interrogation of bimetallic particle oxidation in three dimensions at the nanoscale, *Nature Communications*, 2016, **7**.

[5] Simonsen S.B., Chorkendorff I., Dahl S., Skoglundh M., Sehested J., Helveg S. Direct observations of oxygen-induced platinum nanoparticle ripening studied by in situ TEM, *Journal of the American Chemical Society*, 2010, **132,** 23, 7968-7975. DOI: 10.1021/ja910094r.

[6] Hansen T.W., Delariva A.T., Challa S.R., Datye A.K. Sintering of catalytic nanoparticles : Particle migration or Ostwald ripening?, *Accounts of Chemical Research*, 2013, **46,** 8, 1720-1730. DOI: 10.1021/ar3002427.

[7] R. F. Egerton and P. Li, M Malac. Radiation damage in the TEM and SEM, *Micron*, 2004, **35,** 6, 399-409.

[8] S. Sharna, M. Bahri, C. Bouillet, V. Rouchon, A. Lambert, A.-S. Gay, D. Chiche and O. Ersen. In situ STEM study on the morphological evolution of copper-based nanoparticles during high-temperature redox reactions, *Nanoscale*, 2021, **13,** 9747-9756.

[9] W-H. Xu, L. Wang, Z. Guo, X. Chen, J. Liu and X-J. Huang. Copper Nanowires as Nanoscale Interconnects: Their Stability, Electrical Transport, and Mechanical Properties, *ACS nano*, 2015, **9,** 1, 241-250.

[10] P. Shen, Y. Liu, Y. Long, L. Shen and B. King. High-Performance Polymer Solar Cells Enabled by Copper Nanoparticles-Induced Plasmon Resonance Enhancement, *The journal of physical chemistry. C, Nanomaterials and interfaces*, 2016, **120,** 16, 8900-8906.

[11] Y. Gao, F. P. Cao, X. Lei, L. Mang, S. Cheng and J. SOng. Fluorescent copper nanoparticles: Recent advances in synthesis and applications for sensing metal ions, *Nanoscale*, 2016, 8, 4852-4863.

[12] M. B. Gawande, A. Goswami, F-X. Felpin, T. Asefa, X. Huang, R. Silva, X. Zou, R. Zboril and R. S. Verma. Cu and Cu-Based Nanoparticle : Synthesis and Applications in Catalysis, *Chemical reviews*, 2016, **116,** 6, 3722-3811. DOI: 10.1021/acs.chemrev.5b00482.

[13] C. Ratnasamy and J. P. Wagner. Water gas shift catalysis, *Catalysis Reviews*, 2009, **51,** 3, 325-440.

[14] K. C. Waugh. Methanol synthesis, *Catalysis Today*, 1992, **15,** 1, 51-75.

[15] T-J. Huang and D-H.Tsai. CO oxidation behaviour of copper and copper oxides, *Catalysis Letters*, 2003, **87**, 173-178.

[16] M. Ozawa, H. Toda, O. Kato and S. Suzuki. Solid-state thermal behavior of copper-modified alumina toward lean-burn exhaust NO removal catalyst, *Applied Catalysis B: Environmental*, 1996, **8**, 123-140.

[17] J. Adanez, A. Abad, F. Garcia-Labiano, P. Gayan and L. F. De Diego. Progress in Chemical-Looping Combustion and Reforming technologies, *Progress in Energy and Combustion Science*, 2012, **38,** 2, 215-282. DOI: 10.1016/j.pecs.2011.09.001.

[18] A. Lambert, A. Tilland, W. Pelletant, S. Bertholin, F. Moreau, I. Clemençon and M. Yazdanpanah. Performance and degradation mechanisms of CLC particles produced by industrial methods, *FUEL*, 2018, **216**, 71-82. DOI: 10.1016/j.fuel.2017.11.115.

[19] X. He, Y. Wang, W. Zhang, M. Dong, G. Wang, B. Zhang, Y. Niu, S Yao, X. He and H. Liu. Controllable in-situ surface reconstruction of Cu catalysts and remarkable enhancement of their catalytic activity, *ACS Catalysis*, 2019, **9,** 3, 2213-2221.

[20] T. E. Martin, P. L. Gai, and E. D. Boyes. Dynamic Imaging of Ostwald Ripening by Environmental Scanning Transmission Electron Microscopy, *ChemCatChem*, 2015, **7,** 22, 3705-3711. DOI: 10.1002/cctc.201500830.

[21] M. D. Susman, Y. Feldman, T. A. Bendikov, A. Vaskevich and I. Rubinstein. Real-time plasmon spectroscopy study of the solid-state oxidation and Kirkendall void formation in copper nanoparticles, *Nanoscale*, 2017, **9,** 34, 12573-12589. DOI: 10.1039/c7nr04256f.

[22] K. P. Rice, A. S. Paterson and M.P Stoykovich. Nanoscale Kirkendall Effect and Oxidation Kinetics in Copper Nanocrystals Characterized by Real-Time, In Situ Optical

Spectroscopy, *Particle & Particle Systems Characterization*, 2015, **32,** 3, 373-380. DOI: 10.1002/ppsc.201400155.

[23] R. Nakamura, D. Tokozakura, J. G. Lee, Mori and H. Nakajima. Shrinking of hollow Cu2O and NiO nanoparticles at high temperatures, *Acta Materialia*, 2008, **56,** 18, 5276-5284. DOI: 10.1016/j.actamat.2008.07.004.

[24] M. Mansoor, L. Favergeon and M. Pijolat. Kinetic modeling of low temperature oxidation of coppernanoparticles by O2, *Thermochimica Acta*, 2013, **570**, 41-50.

[25] Q. Zhu, L. Zou, G. Zhou, W. A. Saidi and Y. C. Judith. Early and transient stages of Cu oxidation : Atomistic insights from theoretical simulations and in situ experiments, *Surface Science*, 2016, **652**, 98-113. DOI: 10.1016/j.susc.2016.03.003.

[26] R. Nakamura, D. Tokozakura, J. G. Lee, H. Mori, H. Nakajima. Oxidation Behavior of Cu Nanoparticles and Formation of Hollow Cu_2O Spheres, *Materials Science Forum*, 2007, **561-565**, 1703-1706. DOI: 10.4028/www.scientific.net/MSF.561-565.1703.

[27] D. Tokozakura, R. Nakamura, H. Nakajima, J. G. Lee and H. Mori. Transmission electron microscopy observation of oxide layer growth on Cu nanoparticles and formation process of hollow oxide particles, *Journal of Material Research*, 2007, **22**, 2930-2935.

[28] A. Yabuki and S. Tanaka. Oxidation behavior of copper nanoparticles at low temperature, *Materials Research Bulletin*, 2011, **46**, 2323-2327.

[29] A. P. LaGrow, M. R. Ward, D. C. Lloyd, P. L Gai, E. D. Boyes. Visualizing the Cu/Cu2(O) Interface Transition in Nanoparticles with Environmental Scanning Transmission Electron Microscopy, *Journal of the American Chemical Society*, 2017, **139,** 1, 179-185. DOI: 10.1021/jacs.6b08842.

[30] R. Nakamura, G. Matsubayashi, H. Tsuchiya, S. Fujimoto, H. Nakajima. Transition in the nanoporous structure of iron oxides during the oxidation of iron nanoparticles and nanowires, *Acta Materialia*, 2009, **57,** 14, 4261-4266. DOI: 10.1016/j.actamat.2009.05.023.

[31] R. Nakamura, D. Tokozakura, H. Nakajima, J-G Lee, H. Mori. Hollow oxide formation by oxidation of Al and Cu nanoparticles, *Journal of Applied Physics*, 2007, **101,** 7, 74303. DOI: 10.1063/1.2711383.

[32] S. Nilsson, D. Albinsson, T. J. Antosiewicz, J. Fritzsche and C. Langhammer. Resolving single Cu nanoparticle oxidation and Kirkendall void formation with in situ plasmonic nanospectroscopy and electrodynamic simulations, *Nanoscale*, 2019, **11,** 43, 20725-20733. DOI: 10.1039/c9nr07681f.

[33] P. Haugsrud and P Kofstad. On the oxygen pressure dependence of high temperature oxidation of copper, *Material Science Forum*, 1997, **251-254**, 65-72.

[34] A. P. LaGrow, D. C. Lloyd, P. L. Gai and E. D. Boyes. In Situ Scanning Transmission Electron Microscopy of Ni Nanoparticle Redispersion via the Reduction of Hollow NiO, *Chemistry of Materials*, 2017, **30,** 1, 197-203. DOI: 10.1021/acs.chemmater.7b04184.

[35] S. Sadasivan, R. M. Bellabarba and R. P. Tooze. Size dependent reduction-oxidation-reduction behaviour of cobalt oxide nanocrystals, *Nanoscale*, 2013, **5,** 22, 11139-11146. DOI: 10.1039/c3nr02877a.

[36] J. Y. Kim, J. A. Rodriguez, J. C. Hanson, A. I. Frenkel and P. L. Lee. Reduction of CuO and Cu2O with H2: H Embedding and Kinetic Effects in the Formation of Suboxides, *Journal of the American Chemical Society*, 2003, **125**, 10684-10692.

[37] J. A. Rodriguez, J. Y. Kim, J.C. Hanson, M. Perez and A. I. Frenkel. Reduction of CuO in H2: in situ time-resolved XRD studies, *Catalysis Letters*, 2003, **85**, 247-254.

[38] S. Carenco, C. Boissière, L. Nicole, C. Sancez, P. Le Floch and N. Mézailles. Controlled Design of Size-Tunable Monodisperse Nickel Nanoparticles, *Chemistry of Materials*, 2010, **22**, 1340-1349.

[39] K. Dembélé. *Étude des catalyseurs hétérogènes à base de Co en conditions réactives « réalistes » par microscopie électronique in-situ et operando.* PhD. Strasbourg, France: University of Strasbourg, 20 December 2017.

[40] Protochips. Protochip Atmosphere.https://www.protochips.com/products/atmosphere/.

[41] L. F. Allard, W. C. Bigelow, M. Jose-Yacaman, D. P. Nackashi, J. Damiano, S. E. Mick. A new MEMS-based system for ultra-high-resolution imaging at elevated temperatures, *Microscopy research and technique*, 2009, **72,** 3, 208-215. DOI: 10.1002/jemt.20673.

[42] L. Allard, S. Overbury, W.C. Bigelow, M. Katz, D. Nackashi and J. Damiano. Novel MEMS-Based Gas-Cell/Heating Specimen Holder Provides Advanced Imaging Capabilities for In Situ Reaction Studies, *Microscopy and Microanalysis*, 2012, **18,** 4, 208-215.

[43] R. Nakamura, J. G. Lee, D. Tokozakura, H. Mori and H. Nakajima. Formation of hollow ZnO through low-temperature oxidation of Zn nanoparticles, *Materials Letters*, 2007, **61**, 1060-1063.

[44] Li J, Vizkelethy G, Revesz P, Mayer JW, Tu KN. Oxidation and reduction of copper oxide thin films, *Journal of Applied Physics*, 1991, **69**.

[45] G. J. Cheng and A. R. H. Walker. Transmission electron microscopy characterization of colloidal copper nanoparticles and their chemical reactivity, *Anal Bioanal Chem*, 2010, **397**, 1057-1069.

[46] L. Favergeon, M. Pijolat and M. Soustelle. Surface nucleation and anisotropic growth models for solid-state reactions, *Thermochimica Acta*, 2017, **654**, 18-27.

[47] J. Svoboda, F.D. Fischer and D. Vollath. Modeling of formation of binary-phase hollow nanospheres from metallic solid nanospheres, *Acta Materialia*, 2009, **57**, 1912-1919.

[48] C.W. Bale, P. Chartrand, S.A. Decterov, G. Eriksson, K. Hack, R. Ben Mahfoud, J. Melançon, A.D. Pelton and S. Petersen. FactSage thermochemical software and databases, *CALPHAD Journal*, 2002, **62**, 189-228.

[49] N. L. Peterson and C. L. Wiley. Diffusion and point deffects in Cu2O, *Journal of Physical Chemistry Solids*, 1984, **45**, 281-294.

[50] R. Haugsrudz and T. Norby. Determination of Thermodynamics and Kinetics of Point Defects in Cu2O Using the Rosenburg Method, *Journal of Electrochemical Society*, 1999, **146**, 999-1004.

[51] K-Y. Niu, J. Park, H. Zheng and A. P. Alivisatos. Revealing bismuth oxide hollow nanoparticle formation by the Kirkendall effect, *Nano letters*, 2013, **13,** 11, 5715-5719. DOI: 10.1021/nl4035362.

[52] C-L. Huang, W-L Weng, C-N. Liao and K. N. Tu. Suppression of interdiffusion-induced voiding in oxidation of copper nanowires with twin-modified surface, *Nature Communications*, 2018, 9, 340.

[53] H. J. Fan, M. Knez, R. Scholz, D. Hesse, K. Nielsch, M. Zacharias, and U. Gösele. Influence of Surface Diffusion on the Formation of Hollow Nanostructures Induced by the Kirkendall Effect: The Basic Concept, *Nano letters*, 2007, **7,** 4, 993-997.

[54] E. A. Goldsteina, T. M. Gür, R. E. Mitchell. Modeling defecttransportduringCuoxidation, *Corrosion Science*, 2015, **99**, 53-65.

[55] A.V. Evteev, E.V. Levchenko, I.V. Belova & G.E. Murch. Shrinking kinetics by vacancy diffusion of hollow binary alloy nanospheres driven by the Gibbs–Thomson effect, *Philosophical Magazine*, 2008, 1525-1541.

[56] A. M. Gusak, T. V. Zaporozhets, K. N. Tu & U. G. Kinetic analysis of the instability of hollow nanoparticles, *Philosophical Magazine*, 2007, 4445-4464.

[57] A. M. Gusak and K. N. Tu. Interaction between the Kirkendall effect and the inverse Kirkendall effect in nanoscale particles, *Acta Materialia*, 2009, **57**, 3367-3373.

[58] K. N. Tu and U. Gösele. Hollow nanostructures based on the Kirkendall effect: Design and stability considerations, *Applied Physics Letters*, 2005, **86**, #093111.

[59] Y. Dai, P. Lu, Z. Cao, C. T. Campbell and Y. Xia. The physical chemistry and materials science behind sinter-resistant catalysts, *Chem Soc Rev*, 2018, **47,** 12, 4314_4331.

[60] F. Tao and P. A. Crozier. Atomic-Scale Observations of Catalyst Structures under Reaction Conditions and during Catalysis, *Chemical reviews*, 2016, **116**, 3487-3539.

[61] C. J. Weststrate, M. M. Hauman, D. J. Moodley, A. M. Saib, E. van Steen and J. W. Niemantsverdriet. Cobalt Fischer–Tropsch catalyst regeneration: The crucial role of the Kirkendall effect for cobalt Redispersion, *Top Catalysis*, 2011, **54**, 811-816.

[62] T. Uchiyama, H. Yoshida, Y. Kuwauchi, S. Ichikawa, S. Shimada, M. Haruta, and S. Takeda. Systematic Morphology Changes of Gold Nanoparticles Supported onCeO2during CO Oxidation, *Angewandte Chemie (International ed. in English)*, 2011, **50**, 10157-10160.

[63] H. Mistry, F. Behafarid, S. R. Bare, and B. R. Cuenya. Pressure-Dependent Effect of Hydrogen Adsorption onStructural and Electronic Properties of Pt/ g-Al2O3Nanoparticles, *ChemCatChem*, 2014, **6**, 348-352.

[64] P. L. Hansen, J. B. Wagner, S. Helveg, J. R. Rostrup-Nielsen, B. S. Clausen, H. Topsoe. Atom-Resolved Imaging of Dynamic Shape Changes in Supported Copper Nanocrystals, *Science*, 2002, **295**, 2053-2055.

[65] C. Dessal, A. Sangnier, C. Chizallet, C. Dujardin, F. Morfin, J-L. Rousset, M. Aouine, M. Bugnet, P. Afanasiev and L. Piccolo. Atmosphere-dependent stability and mobility of catalytic Pt single atoms and clusters on γ-Al2O3, *Nanoscale*, 2019, **11,** 14, 6897-6904. DOI: 10.1039/c9nr01641d.

[66] W.C. Yang, M. Zeman, H. Ade, R.J. Nemanich. Attractive Migration and Coalescence: A Significant Process in the Coarsening of TiSi2 Islands on the Si(111) Surface, *Physical review letters*, 2003, **90**.

[67] A. T. Delariva, T. W. Hansen, S. R. Challa and A. K. Datye. In situ Transmission Electron Microscopy of catalyst sintering, *Journal of Catalysis*, 2013, **308**, 291-305. DOI: 10.1016/j.jcat.2013.08.018.

[68] P. L. Gai, B. C. Smith and G. Owen. Bulk diffusion of metal particles on ceramic substrates, *Nature*, 1990, **348**, 430-432.

[69] Li R. Ouyang J.-X.L. a. W.-X. Atomistic Theory of Ostwald Ripening and Disintegration of Supported Metal Particles under Reaction Conditions, *Journal of the American Chemical Society*, 2013, **135,** 5, 1760-1771.

[70] M. A. Asoro, D. Kovar and P. J. Ferreira. In situ transmission electron microscopy observations of sublimation in silver nanoparticles, *ACS nano*, 2013, **7,** 9, 7844-7852. DOI: 10.1021/nn402771j.

[71] J. Li, Z. Wang, Y. Li and F. L. Deepak. In Situ Atomic-Scale Observation of Kinetic Pathways of Sublimation in Silver Nanoparticles, *Advanced science (Weinheim, Baden-Wurttemberg, Germany)*, 2019, **6,** 8, 1802131. DOI: 10.1002/advs.201802131.

[72] A. Chmielewski, J. Nelayah, H. Amara, J. Creuze, D. Alloyeau, G. Wang and C. Ricolleau. Direct Measurement of the Surface Energy of Bimetallic Nanoparticles : Evidence of Vegard's Rulelike Dependence, *Physical review letters*, 2018, **120,** 2, 25901. DOI: 10.1103/PhysRevLett.120.025901.

[73] Gai P.L., Boyes E.D., Yoshida K., Hansen T.W. *Development of the Atomic-Resolution Environmental Transmission Electron Microscope.* Springer, Cham, 2016.

[74] W. Hu, F. Donat, S. A. Scott and J. S. Dennis. The interaction between CuO and Al2O3 and the reactivity of copper aluminates below 1000 C and their implication on the use of the Cu–Al–O system for oxygen storage and production, *RSC Advances*, 2016, **6**, 113016-113024.

Chapter 6:
Nanoscale interaction in Cu – Al_2O_3 systems under redox conditions

1 INTRODUCTION

In chapter 5, the Cu/Al_2O_3 model system was investigated under O_2 to determine the temperature range associated to the different diffusion regimes as well as the formation of the $CuAl_2O_4$ phase. Unfortunately, only the surface atomic migration was observed and eventual loss of the copper phase up to a temperature of 600 °C. No bulk diffusion and/or formation of $CuAl_2O_4$ could be discerned. Stabilising the copper phase proved to be difficult on the amorphous Al_2O_3 substrate. Even though the real alumina support is difficult to characterise during *in situ* STEM conditions, it may provide better anchoring effect to the copper nanoparticles owing to the presence of surface groups or morphological inhomogeneity. Therefore, similar tests were carried out on the supported sample analysed in chapters 3 and 4.

In terms of morphological evolution of CuO/alumina oxygen carriers under redox cycling at high temperature, we have observed two important aspects: one is the accumulation and sintering of the copper phase and another is the increase in porosity due to the formation of the alpha alumina phase. The phase transformation to α-Al_2O_3 is driven by the presence of the copper containing phases, and the growth of α-Al_2O_3 is linked to the segregation and sintering of CuO. The question arises regarding the role of the copper containing phases (whether in metallic form or aluminate form): how does it aid to the α-Al_2O_3 formation? Furthermore, what is the role of redox reactions on this phase transition? We have already discussed briefly (in chapter 3, section 4) and proposed a hypothesis in relation to the copper-induced structural changes in the alumina framework. In chapter 4, the role of the number of redox cycles is linked to the nucleation and growth of the α-Al_2O_3 particles. It remains to be seen how the initial structural changes can be linked to the α-Al_2O_3

nucleation, whether other factors such as epitaxial relation between the copper-aluminate and the α-Al_2O_3 plays a role in the phase transition.

To answer these questions, *in situ* STEM has been employed to observe the dynamic evolution of the supported material. The aim of these experiments was to have a detailed comprehension of the copper migration in and out of the alumina as well as the surface migration at the nanoscale during the high temperature redox reactions. To carry out the studies, three different CuO/Al_2O_3 oxygen carriers were used: CuO/Al_2O_3 with either 13wt% or 28 wt% copper oxide, and 13wt% CuO supported on alumina nanospheres. The 13wt% CuO/Al_2O_3 is used to replicate and compare the conditions of ageing in TGA (mentioned in Chapter 2). The 28wt% CuO/Al_2O_3 sample composition has been chosen to identify any effect of higher Cu concentration. As identified in chapter 5, the persistent disappearance of copper oxide at high temperature in the STEM cell leads to the proposal of several hypotheses, including the effect of confinement on the stability of the copper containing phases. The idea of confinement has been discussed by DeLaRiva in the light of Pd based nanoparticles, where the disappearance of Pd has been observed when the nanoparticles were subjected to heating on a flat Si substrate as opposed to a supported sample [1]. Hence, in an attempt to confine the copper phase, alumina nanospheres were used as support.

Another purpose was to carry out oxidation/reduction at lower temperatures for qualitative comparison with the unsupported copper-based nanoparticles. *In situ* STEM experiments were performed at different temperatures between 300 and 900 °C, under oxidative and reduction environments.

2 EXPERIMENTAL SECTION

2.1 SAMPLES DESCRIPTION AND EXPERIMENTAL STEPS

2.1.1 13wt% CuO /Al_2O_3 – 900 °C sample

The 13wt% CuO impregnated on alumina support and calcined at 900 °C is the same sample as the one reported in Chapters 2 to 4. The fresh sample is described in detail in chapter 3, section 3.1 in terms of the phases present, the crystallinity, the distribution of the copper phases and the bulk and nanoscale morphology.

Reaction steps

The reaction and heating steps for this *in situ* STEM experiment are presented in *Figure 6.1*. After the introduction of the sample in the microscope chamber, a few purging cycles were carried out using Ar at 1 bar pressure and room temperature. The sample was kept under Ar for about 30 min to carry out an initial imaging and to choose the areas to follow during the reaction. Afterwards, the temperature was increased under H_2 from 25 °C to 300 °C at a rate of 3 °C/min. Redox reactions were conducted by alternating H_2/Ar, O_2/Ar and re-introducing H_2/Ar, at 300 °C. The temperature was increased from 300 °C to 400 °C and eventually to 900 °C, under H_2. At 900 °C, 1 redox cycle was carried out with O_2/Ar and then re-introducing H_2/Ar.

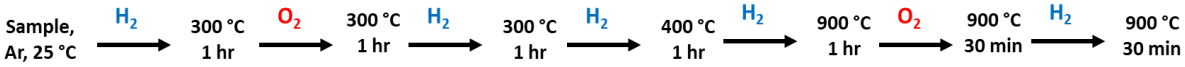

Figure 6.1: Schematic representation of the experimental steps with the heating duration and gas change.

2.1.2 28wt% CuO supported on alumina

This sample contains half the stoichiometric amount of copper compared to the copper aluminate phase. The theoretical formula of such a sub-stoichiometric copper aluminate spinel phase would be $Cu_{0.57}Al_{2.29}O_4$. The reason for using a higher copper content was to check whether increasing the amount of copper in the sample has any impact on the

stabilisation of the copper phase (either in copper aluminate or copper oxide) during the *in situ* observation.

The final sample contained different phases including various transition aluminas, copper aluminate, CuO and α-Al_2O_3 (according to XRD data in Appendix E2). The complete incorporation of the large quantity of copper was not achieved resulting in a heterogeneous morphology in the 28wt% CuO/Al_2O_3 sample.

According to TEM-SAED reported in *Figure 6.2*, four types of morphologies are observed: large crystals made of α-Al_2O_3 phase pointed by the white arrow in *Figure 6.2*a, large crystallites of copper-aluminate phase as circled in red in *Figure 6.2*a, a mixture of small copper aluminate grains and alumina particles without copper circled in yellow in *Figure 6.2*b, and big crystals of CuO (not shown here). According to the SAED, the d-spacing 2.1 Å and 1.6 Å correspond to (113) and (116) planes of α-Al_2O_3 structure. The d-spacing of the copper aluminate varied from 2.7 to 2.8 Å and 2.3 to 2.4 Å for the (220) and (311) planes respectively. In the inset in *Figure* 6.2a, areas corresponding to the (113) and (116) planes of α-Al_2O_3 phase, and the (311) plane of $Cu_xAl_yO_4$ phase are displayed in green, blue and red, respectively.

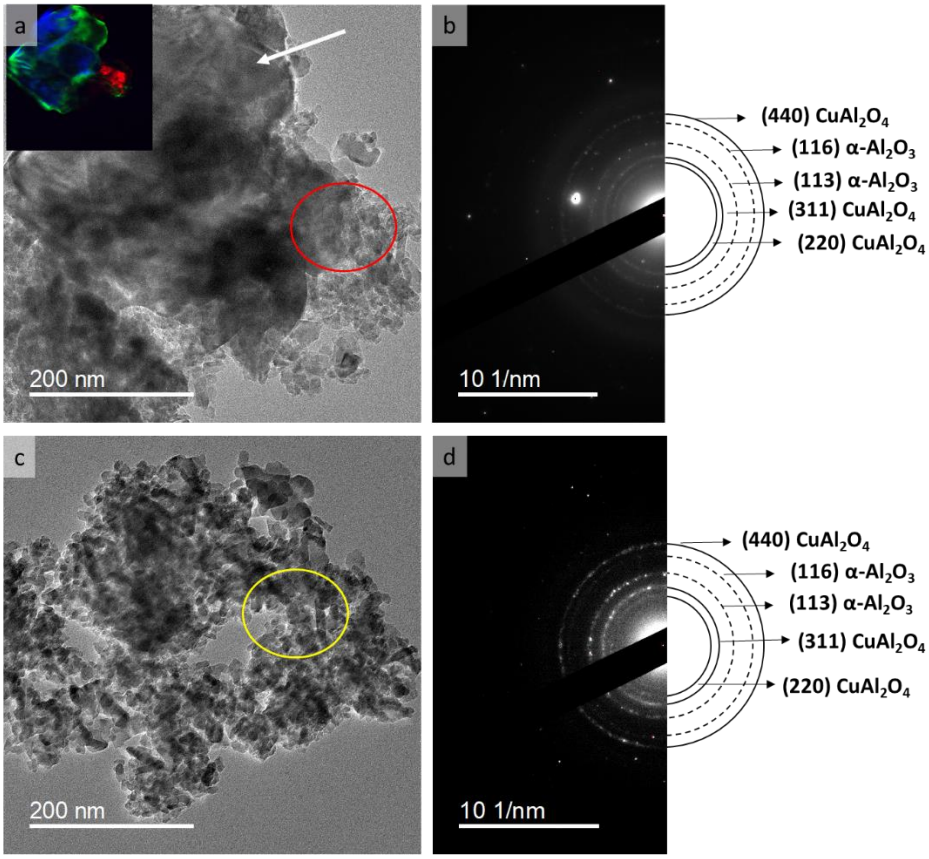

Figure 6.2: Ex situ TEM (a and c) and the corresponding SAED (b and d) of the 28wt% CuO/Al_2O_3 sample.

Reaction steps

The steps of the *in situ* experiment are given in *Figure 6.3*. The sample was heated under Ar at a rate of 3 °C/min, then reduction was performed starting from 200 °C to 400 °C. O_2 was re-introduced. Afterwards the sample was oxidised from 400 °C to 900 °C under O_2.

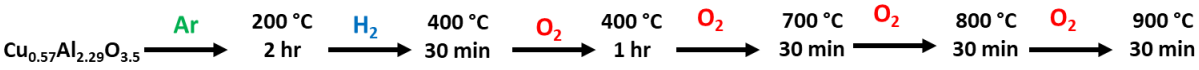

Figure 6.3: Schematic representation of the experimental steps with the heating duration and gas change.

2.1.3 Cu-Al nanospheres

In an attempt to confine the copper phase, alumina nanospheres were used as support. The alumina nanospheres were synthesised chemically and impregnated with copper to achieve a 13wt% copper oxide, similar to the first sample.

2.1.3.1 Alumina synthesis

The synthesis of the alumina nanospheres was adapted from the protocol of Roh et al. [4]. The synthesis follows a forced hydrolysis method using aluminum sulphate and aluminum nitrate as precursors. The size of the alumina spheres depends on the ratio of the nitrate and sulphate precursors. Therefore, in order to get a size distribution of 200 ± 50 nm, the ratio was fixed to 1:6 for sulphate : nitrate proportions. In a typical reaction, 500 mL solution was prepared by dissolving $Al(NO)_3 \bullet 9\ H_2O$, $Al_2(SO_4)_3 \bullet 18\ H_2O$ and urea in deionised water. The concentration of the aluminium precursors and urea was 0.01 $mol.L^{-1}$ and 0.1 $mol.L^{-1}$, respectively. The mixture was heated at 95 °C under constant stirring for 8 hours, until a white precipitate was observed. The white precipitate was separated and washed repeatedly with water, to remove any sulphate or nitrate ions. The synthesised powder was dried in the oven at 120 °C for 12 hours and calcined at 900 °C for 15 hours.

The synthesised material before calcination and after calcination is presented in *Figure 6.4*a. The material before calcination is amorphous (from HRTEM image) consisting of nanospheres of 250 – 400 nm composed of aluminium hydroxide [4]. After calcination, the aluminium hydroxide is transformed to form γ-Al_2O_3 nanoplatelets of 2-6 nm length organised to form porous spheres of 250 – 350 nm diameter (*Figure 6.4*b). The inset in *Figure 6.4* confirms the presence of γ-Al_2O_3 with (311), (400) and (440) planes corresponding to, 2.3 Å, 1.9 Å and 1.3 Å d-spacing values, respectively.

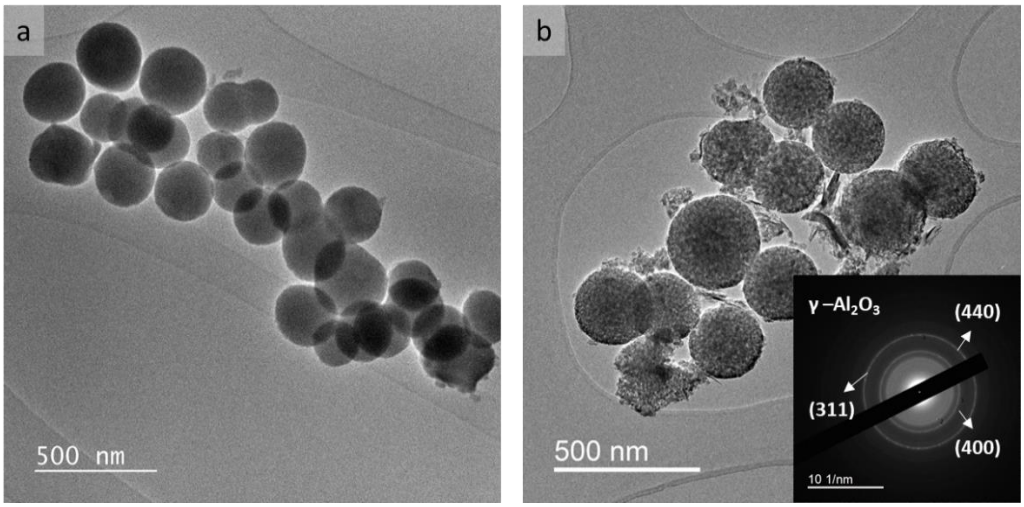

Figure 6.4: TEM images of a) alumina precursor before calcination and b) after calcination at 900 °C / 15 hours with inset containing the SAED pattern from the same area.

Following the formation of γ-Al_2O_3, the nanospheres were impregnated with a copper nitrate solution, using the same procedure as for the commercial alumina sample. The impregnated nanospheres were then dried at 120 °C for 12 hours and calcined at 800 °C and 900 °C for 12 hours. The different calcination temperatures lead to the formation of different morphologies and crystallinities in the samples. The samples are referred as Cu-Al NP.

2.1.3.2 Cu-Al NP – calcined at 800 °C

The sample calcined at 800 °C shows a morphology similar to that of calcined alumina nanospheres before impregnation. No indication of CuO phase was detected from the SAED analysis of a few areas. No CuO nanoparticle was visible in either TEM or STEM mode. Therefore, it is assumed either copper phases exist in the form of very small nanoparticles (not detectable in the imaging / diffraction mode) or it undergoes formation of aluminate as reported for the case of the commercial support sample (chapter 3, section 3.1).

According to EDS elemental speciation, the copper phase is distributed in different proportions in the different alumina nanospheres. For example, in *Figure* 6.5 three areas are marked with different copper to aluminum ratio. In circled area 1, the copper concentration is about 24wt% (Cu:Al = 20:80), which is much higher than in areas 2 and 3 where the concentration is ~5wt%, (Cu:Al = 4:96) and ~12wt% (Cu:Al = 10:90), respectively. The majority of particles contains a copper concentration between 4 and 12wt% compared to the theoretically expected value of 10wt% based on the impregnated copper nitrate content. Although the percentage of copper varies from one alumina nanoparticle to another, the copper content within the particles is homogeneous.

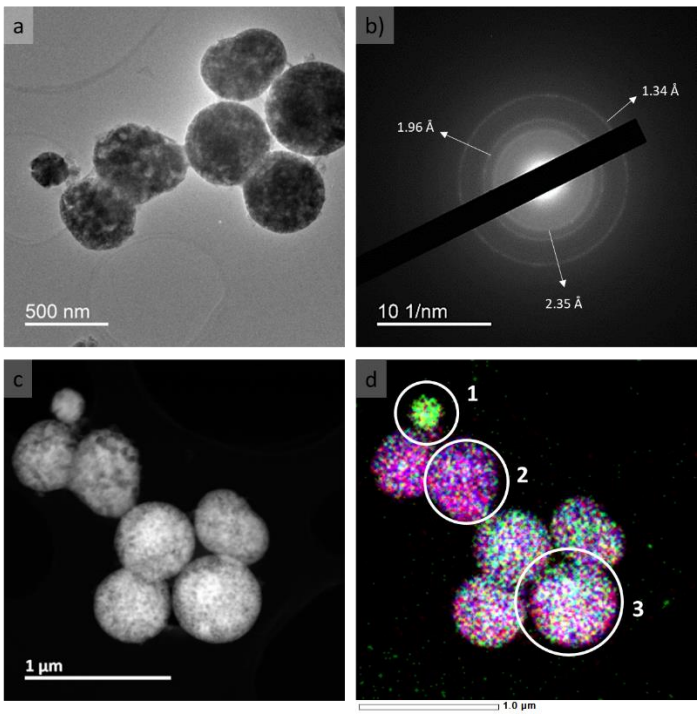

Figure 6.5: Images of Cu-Al NP calcined at 800 °C, a) TEM b) SAED c) HAADF-STEM d) STEM-EDS (The three elements Cu, Al and O are represented by green, blue and red respectively).

Reaction steps:

The sample was heated from 25 °C to 200 °C, under Ar flow at a rate of 6 °C/min. The sample was kept under argon atmosphere for 2 hours to remove any residual organic and to be imaged. A mixture of O_2/Ar was introduced after the 2 hours period and kept for 1 hour. Afterwards the sample was subjected to gradual heating from 200 °C to 1000 °C at a rate of 6 °C/min. Every 50 °C, the heating was halted for about 5 min to carry out the analysis of the chosen areas (*Figure 6.6*).

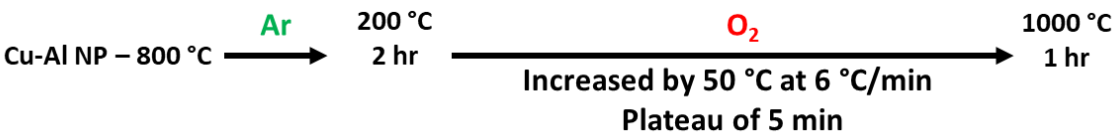

Figure 6.6: *Schematic representation of the experimental steps of in situ annealing of Cu-Al NP-800 °C under constant O_2 flow.*

2.1.3.3 Cu-Al NP – calcined at 900 °C

The sample calcined at 900 °C displays a well-crystallised morphology compared to the sample calcined at 800 °C. The morphology does not seem to be composed of organised platelets but is rather composed of continuous spherical particles with a smooth surface. Some cracks and porosity are also observed in some of the particles. The nanospheres size distribution remains the same within a broad range of 250 to 350 nm. According to SAED reported in *Figure 6.7b*, the major contributions point to the presence of a copper aluminate phase. The main planes are (220), (311) and (440) with respective 2.76 Å, 2.35 Å and 1.37 Å d-spacing values, attributed to copper aluminate phase.

In STEM-HAADF, two types of particles were observed with different mass densities, which arise due to the presence of copper according to EDS analysis. For example, Figure *6.7*d, the particle in the dotted circle has a copper concentration of 30-35wt% whereas the other particles showed a negligible copper concentration of about ~2-5wt%.

Some d-spacing values related to α-Al_2O_3 planes were also identified in the SAED. The copper-deficient nanoparticles in pink in *Figure 6.7*d could be made of α-Al_2O_3.

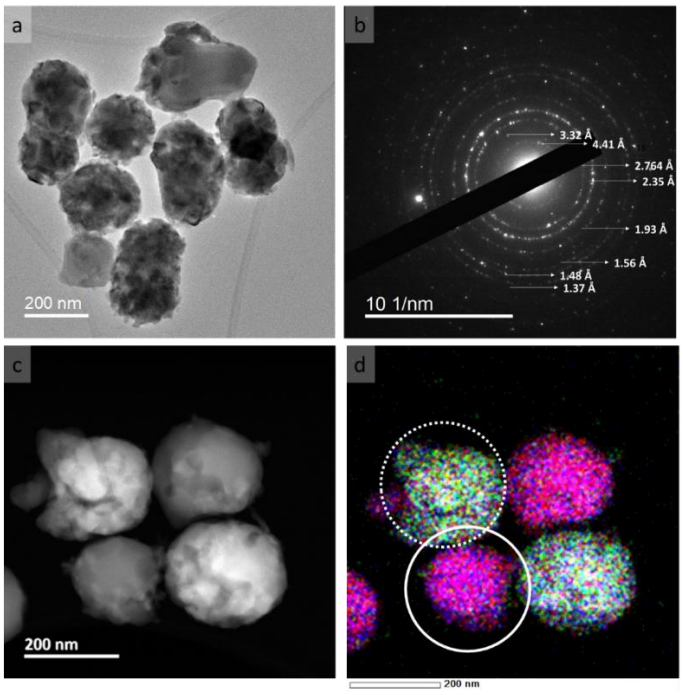

Figure 6.7: Images of Cu-Al NP calcined at 900 °C, a) TEM b) SAED c) HAADF-STEM d) STEM-EDS (The three elements Cu, Al and O are represented by green, blue and red colour respectively).

Reaction steps:

Three experiments were carried out with this sample. Two experiments were dedicated to the thermal annealing of the sample in an oxidative environment under continuous oxygen flow (same protocol as the Cu-Al NP-800 °C sample outlined in *Figure 6.6*), and the second one was a thermal annealing at very low rate of heating at static condition under low oxygen pressure.

The third experiment was focused on redox reaction at every 100 °C from 200 °C to 500 °C. Under every reaction gas, the sample was kept for approximately 30 mins.

3 RESULTS AND DISCUSSION

The results are presented as follows: first, redox reactions and thermal treatment at low temperature (up to 500°C); high temperature redox cycling at 500 °C, and evolution of the oxygen carrier during calcination under O_2 atmosphere. Finally, a specific focus is made on alumina phase transformation at high temperature.

Since no significant difference in the behaviour of the 13wt% CuO/Al_2O_3-900 and 28wt% CuO/Al_2O_3-900 were noted either at lower or higher temperature, the result of these two samples are presented together in the sub-sections named CuO/Al_2O_3 – 900.

3.1 REACTIONS AT LOW TEMPERATURE (< 500 °C)

At low temperature, two aspects are reported: 1) the reduction of the copper aluminate as a function of the temperature from 200 °C to 400 °C and 2) The redox behaviour of the particles at specific temperatures (300 °C and 400 °C).

Then the low temperature data is compared to the Cu/SiN_x system.

3.1.1 CuO/Al_2O_3 – calcined at 900 °C

3.1.1.1 Reduction reaction under H_2 from 200 to 400 °C

So far, in chapter 5 reduction reactions were only carried out on the copper oxides phase. The copper oxide is reduced by H_2 at relatively lower temperature (200 – 300 °C) than copper-aluminate which is reported to reduce between 300 and 400 °C [2,3]. As reported

in Chapters 3 and 4, the reduction of copper-aluminate phase results in metallic copper via reaction 6.1.

$CuAl_2O_4 + H_2 \rightarrow Cu^0 + Al_2O_3 + H_2O$ Reaction 6.1

However, in the initial stage of the reduction process, the metallic copper formation has not been directly visualised. Hence, to determine the initial step of the metallic particle formation and its morphology, reduction was performed from 200 to 400 °C.

The presented experiment concerns 28%wt CuO/Al_2O_3. H_2 gas was introduced at 200 °C and kept for 2 hours, then the temperature was increased to 400 °C (for 30 minutes) at a rate of 60 °C/min. *Figure 6.8* displays two areas of the sample undergoing transformations under argon at 200 °C, under H_2 at 200 °C and under H_2 at 400 °C. The white circles in Area 1 display irregular shaped nanoparticles of CuO under Ar. Upon the introduction of H_2 at 200 °C these areas exhibit slow disintegration of the structure (fragmentation) leading to the formation of small nanoparticles and clusters near the particles, on the SiN membrane. Increasing the temperature to 400 °C leads to sintering of the small nanoparticles.

The yellow-circled zones also display the emergence of copper clusters or small copper nanoparticles on the SiN_x membrane. Upon further increase in temperature bigger nanoparticles were formed. In area 2 (*Figure 6.8*e) the zone circled in red shows a large particle which does not undergo significant changes at 200 °C. However, after 30 minutes at 400 °C large nanoparticles of copper could be seen. The support that displayed a dense structure at the beginning of the experiment becomes porous after the formation of the large copper particles. The large particle in the red circle in *Figure 12*e is therefore likely to be copper aluminate.

Two phenomena are occurring simultaneously: gradual expulsion of copper atoms from the structure of copper aluminate during the reduction process and sintering of copper atoms to form metallic particles from the initial clusters. The substantial difference in the number and size of the nanoparticles at the end of 2 hours at 200 °C compared to 400 °C suggests that the reduction of the $Cu_xAl_yO_4$ phase may occur in steps. Plyasova et al. proposed two reaction steps for the reduction of $CuAl_2O_4$ [5]. Indeed, as stated in Chapter 3, section 2.1.5, $Cu_xAl_yO_4$ displays CuO_4 and CuO_6 environments. The energy required to break the two bond

environments would be different. Presumably, copper atoms from CuO_4 sites are reduced at a lower temperature than in CuO_6 environment.

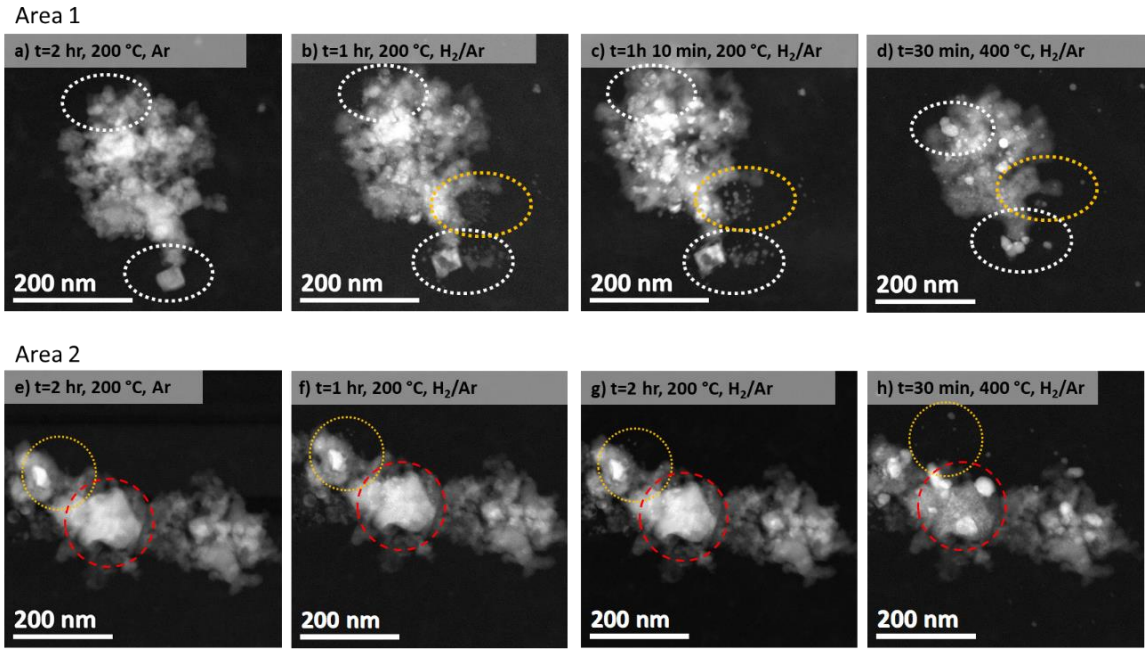

Figure 6.8: STEM-HAADF images of the same area at 200 °C under a,e) pure Ar after 2 hours, b,f) a mix of H_2 and Ar after 1 hour, c,g) H_2 after 1 hour 10 min, and d,h) after 30min at 400°C.

Among the different zones, some differences can be observed in terms of the texture of the support and the mobility of the copper. For example, in the area depicted in *Figure 6.8*h (red circle), the expulsion of copper gives rise to a porous alumina framework. In other areas, such a change is either not observed due to the smaller size of the grains, or the grains do not undergo any morphological changes.

Additionally, the mobility of the metallic copper is evident even starting at 200 °C. Nanoparticles are present both on the support and the SiN_x membrane (pointed in yellow circle in *Figure 6.8*e-h). On the alumina support, the particle size distribution is around 11 ± 6 nm, whereas on the SiN_x membrane the size is 5 ± 1 nm. At 400 °C, the mobility is even higher, and a very high number of nanoparticles is found on the membrane surface. There is also a relative increase in their size. On the support, the average nanoparticle size at 400 °C is 33 ± 11 nm. On the membrane the size range is very broad with most of the nanoparticles ranging from 5 to 15 nm, and few very large particles within 30-60 nm size range are also observed.

3.1.1.2 Redox reaction

For the CuO/Al_2O_3-900 °C, redox reaction was carried out at 300 °C and 400 °C.

Reduction -Oxidation – Reduction at 300 °C

In the following, the sequence of reduction – oxidation – reduction was carried out at 300 °C on 13wt% CuO/Al_2O_3. The areas highlighted on *Figure 6.9* with dotted red circles show some of the nanoparticles undergoing evolution under respective reaction atmospheres.

The particle on the left side of the image undergoes morphological changes from spherical shape (under H_2/Ar – *Figure* 6.9a) to cubic-shaped (under O_2/Ar – *Figure 6.9*b) to spherical particles again (under H_2/Ar – *Figure 6.9*c). In terms of the change in nanoparticle dimensions, in a), the NP size is 50 nm, in b), slightly larger than the NPs under H_2 and the smaller NPs in c) are in the range of 15-25 nm. During oxidation, there is evidence of hollow nanoparticles formation in some areas such as the NPs marked on the right. However, it is difficult to conclude since the contrast with the alumina support is not high for the oxide phases. During the subsequent reduction, fragmentation of the NPs can be seen in the different areas in *Figure 6.9*c.

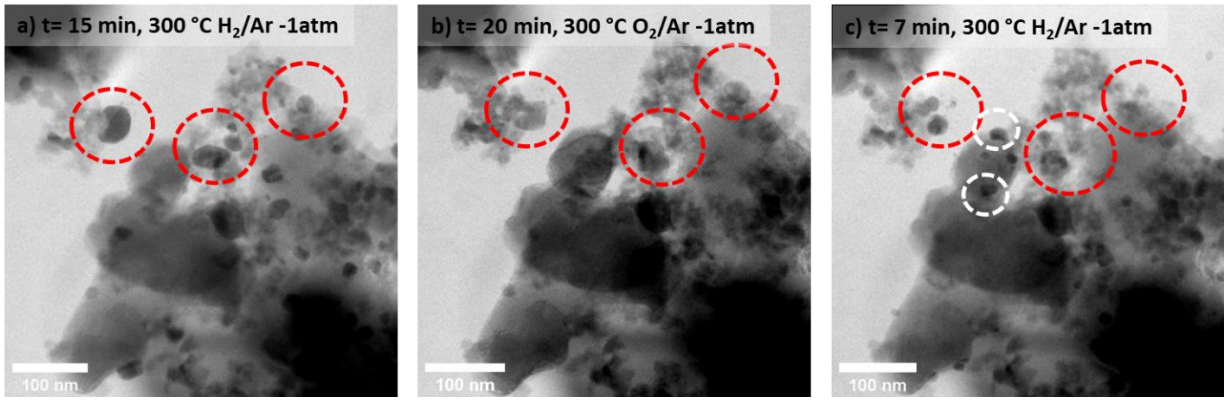

Figure 6.9: STEM -BF images of the same area during the redox cycle at 300 °C under a) reduction with H_2, b) oxidation under O_2 and c) re-reduction under H_2. The red and white circles depict the areas undergoing changes in the copper phase.

Evidence of nanoparticles fragmentation and hollow nanoparticles formation is more distinguishable for larger particles as shown in Appendix E.

Reduction -Oxidation at 400 °C

Similarly, after heating the 28%wt CuO/Al_2O_3 sample to 400°C in a reducing atmosphere, oxygen was introduced to carry out oxidation at 400 °C, which leads to the changes depicted in *Figure* 6.10.

It is easy to visualise the size evolution of the nanoparticles that diffused onto the SiN_x membrane – there is an overall increase in the volume with distinct faceting observed in some nanoparticles as stated in the previous sub-section. In contrast, it is difficult to "see" the supported particles especially during the oxidation step because of the lower diffraction contrast of oxidised copper phases and of the aggregation of the small support particles. Due to these difficulties the particle size distribution is not stated. Moreover, measuring the individual size of NPs on the membrane would not provide an accurate picture of the oxidation volume as some of the oxidised copper forms larger particles via coalescence and sintering. Besides that, from the displacement of the particles on the support as well as on the SiN_x membrane it can be concluded that the overall mobility of the particles is quite significant.

Although in some areas it may look like copper reacted back with the support, based on the imaging alone such conclusion would not be realistic. Besides that, based on the literature and the previous experience, the reaction between CuO and alumina occurs above 600 °C, and even at 600-700 °C the formation of the copper aluminate would require very long heating duration.

From the SAED, changes in the oxidation state of copper are observed: the 1.8 Å (200) and the 1.3 Å (220) distances assigned to metallic copper disappear (*Figure* 6.10c), while the 2.5 Å (-111) distance assigned to CuO appears (*Figure* 6.10f). The 1.6 Å (116) and 2.1 Å (113) distances are assigned to the alpha alumina phase. The diffraction spots related to 2.4 Å (311) and 1.4 Å (440) d-spacing values were assigned to the copper-deficient aluminate frame.

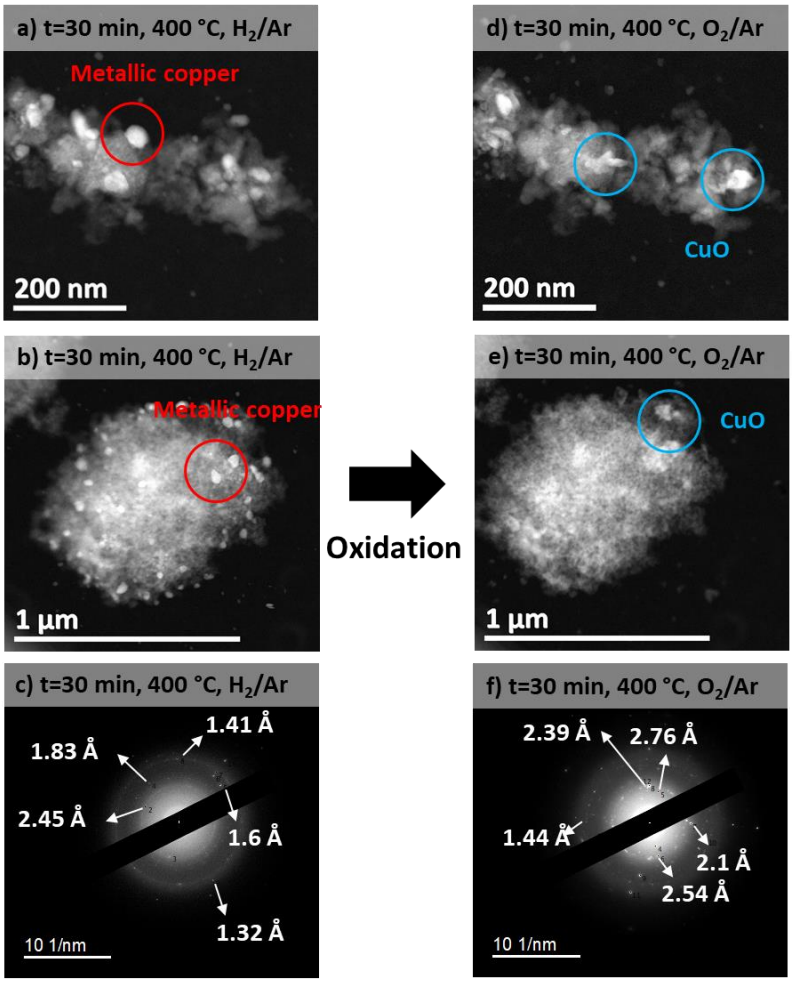

Figure 6.10: STEM-HAADF images of two different areas under H_2 (a and b) and O_2 (d and e) and their corresponding SAED (c and f), at 400 °C.

3.1.2 Cu-Al NP – 900 °C redox reaction

For the Cu-Al NP-900 °C, the evolution during the redox reaction at different temperatures is presented separately since the overall morphology of this material is considerably different from the other two samples. However, alike the other samples the Cu-Al NP-900 °C sample displays similar behaviour in terms of morphology, extent of reaction and copper mobility.

Redox reactions were carried out at 200, 300, 400 and 500 °C on the fresh sample. The sequence of the reaction followed oxidation-reduction-oxidation; the temperature was increased of 100 °C at a rate of 3 °C/min under O_2 gas. At every gas environment the sample was kept for 30 minutes. The imaging was performed approximately after 10-15 minutes after the set temperature-reaction gas was reached. *Figure* 6.11 displays the redox reaction sequence from 200 to 500 °C.

At 200°C, no major change was observed when the gas was switched from O_2/Ar to H_2/Ar and back.

Similarly, at 300°C reduction in H_2/Ar triggered the formation of only a few copper nanoparticles after 1 hour of reaction (*Figure* 6.11). Under O_2/Ar, only few particles with poor contrast could be seen.

As expected, at 400 °C under H_2/Ar significantly more metallic copper was observed on the surface of the spherical support. The metallic copper emerged from further reduction of the $Cu_xAl_yO_4$ phase. At the time of the imaging the newly formed metallic copper was undergoing particle formation and exhibited very high mobility. By the end of the 30 minutes reaction period, in some areas few copper nanoparticles were observed on the SiN_x membrane. Upon switching back to O_2/Ar, a mixture of hollow and cubic-shaped nanoparticles of CuO were observed. In some areas, the nanoparticles sustained coalescence to form large surface CuO NPs, perhaps due to proximity to each other.

Under H_2/Ar at 500 °C, the nanoparticles transformed to metallic phase and formed fragmented particles with faceted spherical shape. With the re-introduction of O_2/Ar, faceted cubic-shaped particles were formed.

Under both oxidation and reduction gases, the sintering and the mobility of the particles were quite high. In some areas, a large proportion of the initial copper-based particles migrated to the SiN_x membrane.

Compared to the fresh sample, the Cu-deficient nanospheres displayed loss of contrast due to loss of the structural copper. Additionally, some porosity formation was also noticed.

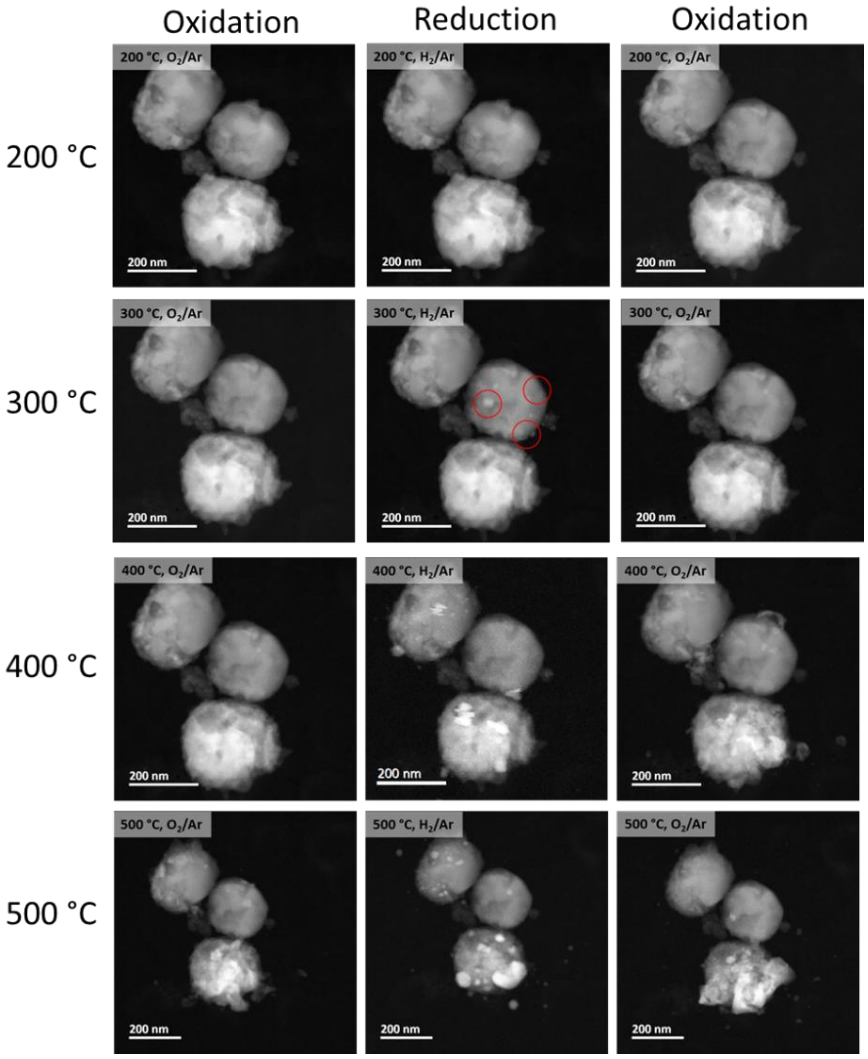

Figure 6.11: STEM-HAADF images of the same area undergoing redox reactions at 400 °C (top row) and 500 °C (bottom row), the gas atmosphere and the temperature are displayed on the images.

3.1.3 Conclusion

Globally, the three oxygen carriers with either different copper contents or support morphology tend to demonstrate similar behaviour. Hence, the overall result was presented considering the copper phase-support morphology change and copper mobility during the reduction as well as redox reaction at specific temperatures.

The reduction of the copper-aluminate phase produces metallic copper on the support's surface. Following the nucleation and growth theory, presumably, the copper would initially form atomic cluster which would grow into nanoparticles. With the progression of the reduction, the nanoparticles might grow further either by the integration of the evicted copper atoms or by other growth mechanism (PMC or OR).

Once the metallic copper is formed the temperature dependant shape evolution of the nanoparticles under H_2 and O_2 is also analogous to the Cu/SiN_x model system presented in chapter 5, section 4.1. The Cu^0 nanoparticles displayed increased faceting of the spherical nanoparticles under H_2 and the oxide nanoparticles under O_2 displayed hollow and faceted particle shape as a function of increasing temperature. In contrary, the Cu-deficient support showed increased porosity and low contrast due to the removal of copper. No change in the structural change is noted according to SAED as the Cu-deficient copper aluminate displayed similar diffraction pattern as the fresh sample.

As illustrated multiple times in these experiments, the mobility of copper is noticeable even at temperatures as low as 200 °C. Moreover, at higher temperature, the mobility of copper became an issue as a large percentage of the nanoparticles migrated to the SiN_x membrane instead of remaining on the alumina support.

3.2 REACTIONS AT HIGH TEMPERATURE (> 500 °C)

As demonstrated, the copper nanoparticles displayed preferential mobility to SiN_x membrane, especially at high temperature. As a result, it was difficult to carry out similar redox reaction above 500 °C. Therefore, it was decided to directly rise the temperature to 900°C (temperature of CLC reaction) before the copper phase could migrate to the SiN_x membrane at lower temperature.

Two high temperature experiments are presented in this sub-section. In the first experiment, the sample containing CuO and Cu-deficient aluminate phase was calcined under O_2 from 400 °C to 900 °C to reform the $Cu_xAl_yO_4$ phase. In the second experiment, the sample containing metallic copper and Cu-deficient aluminate phase was heated under H_2 from 400 °C to 900 °C to carry out oxidation and re-reduction at 900 °C.

3.2.1 Heating under O_2 atmosphere

The sample 28%wt CuO/Al_2O_3 was heated under O_2 from 400 °C to 900 °C with temperature plateau at 700 °C and 800 °C for 30 minutes, at a rate of 3 °C/min. As noticed from *Figure 6.12a* (area in the green circle), at 400 °C some of the CuO particles have already migrated to the SiN_x membrane. With the rise in temperature, the CuO particles started to sinter to form very large particles of CuO within 100-500 nm size range as displayed in *Figure 6.12b*

(red circle). The growth process observed is attributed to Ostwald ripening as no Brownian-like particle motion has been observed during the observation. Evidently, Ostwald ripening is the dominant form of sintering in the Cu/SiN_x model system as shown in chapter 5, section 4.2.3.3.

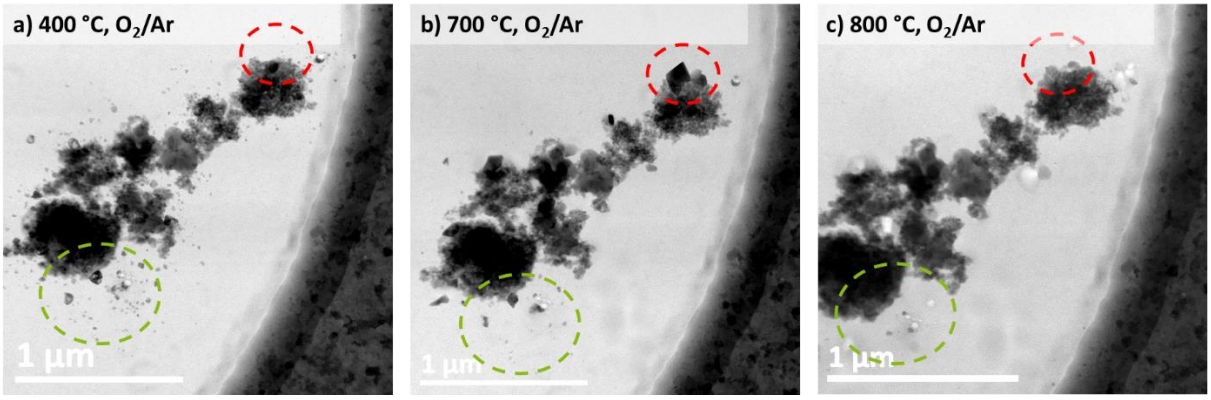

Figure 6.12: STEM-BF images depicting the evolution of a large area at lower magnification in oxidative environment at a) 400 °C, b) 700 °C and c) 800°C.

Hence, under oxygen at the temperature range of 400 – 700 °C, the copper oxide particles are either found on the SiN_x membrane or as large particles anchored to the alumina particles. Formation of copper aluminate was not observed.

With further increase in temperature to 800 °C, the CuO nanoparticles disappeared. They were eventually detected on the non-heated side of the e-chip as shown in *Figure 6.13*. The distance between the heated and non-heated chip was found to be about 20 µm. The presence of these copper nanoparticles was confirmed with TEM-SAED under oxygen at 800 °C, depicted by the CuO phase with the 2.5 Å d-spacing relating to (-111) plane, as well as EDS after the temperature of the cell was brought down to 200 °C (EDS cannot be performed above 300 °C). The presence of copper was not detected either by EDS on the different areas of the heated e-chips.

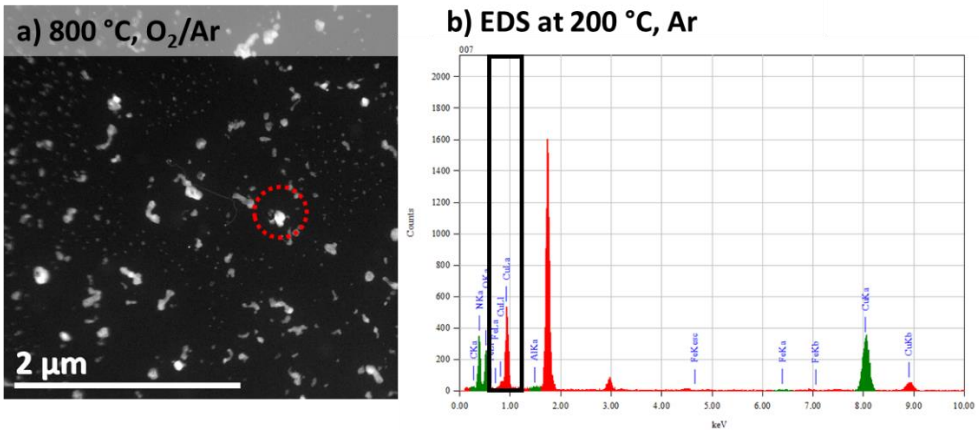

Figure 6.13: a) STEM-HAADF images of non-heated e-chip at a set temperaure of 800 °C and EDS of the zone marked with red dotted circle (b).

Here, the preferential migration of copper particles to the SiN_x membrane reinforces the hypothesis that the Cu-SiN_x system may be characterised by stronger metal-support interaction compared to that of the Cu-Al_2O_3 system, as previously discussed in chapter 5, section 4.2.

3.2.2 Heating under H_2 atmosphere

Reduced 13%wt CuO/Al_2O_3 sample containing copper on the support was heated under H_2 from 400 °C to 900 °C. A very high rate of heating (300 °C/min) was chosen this time. *Figure 6.14* displays an area which was imaged only at the beginning of the experiment under Ar and after increasing the temperature.

Right after attaining 900 °C, the nanoparticles displayed a size range of 30 ± 15 nm which is comparable to the particle size distribution at 400 °C. Nevertheless, the average nanoparticle size increased to 42 ± 12 nm after about 1 hour of heating at 900 °C in H_2 (*Figure 6.14b*). It was surprising to still find copper nanoparticles even after such a long thermal exposure, since during the calcination under O_2 loss of the particles was observed, and as earlier results on copper nanoparticles on SiN_x membrane also showed the disappearance of copper closer to 900 °C (chapter 5, section 4.1). Additionally, no copper particle was found on the membrane, all the copper was on or with contact with the support.

When the atmosphere was switched to O_2/Ar gas, no copper containing particle was observed in any areas of the sample after only 5 minutes of exposure (*Figure 6.14c*). The

morphology of the support at 900 °C under O_2 resembles that of the sample under Ar at 25 °C. Also, considering the typical reaction temperature of 900 °C for the formation of copper aluminate, it was presumed that the zone represented in *Figure 6.14c* is made of copper aluminate. Hence, to re-check the presence of copper the reaction atmosphere was switched back to H_2. No appearance of copper nanoparticles took place. No difference in the contrast was observed either between *Figure 6.14c* and *Figure 6.14d*.

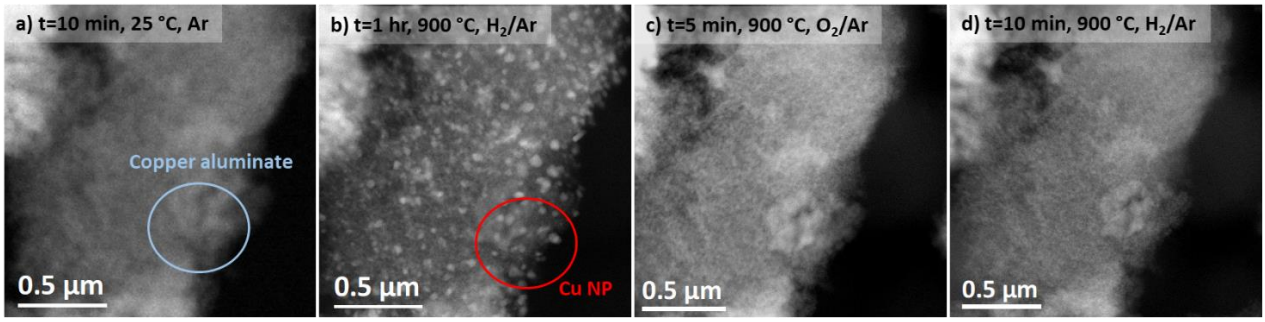

Figure 6.14: In situ HAADF-STEM characterisation of fresh CuO/Al_2O_3 OC a) in Ar atmosphere at 25 °C and b) reduction by H_2 at 900 °C after 1 hour, c) under O_2, d) under H_2.

To investigate the disappearance of Cu from the sample, post- mortem characterisation of the e-chip using SEM was performed. *Figure 6.15* shows a difference in contrast between the heated area marked by the white circle and the rest of the sample, suggesting a similar loss of the copper phase as the earlier samples and observations.

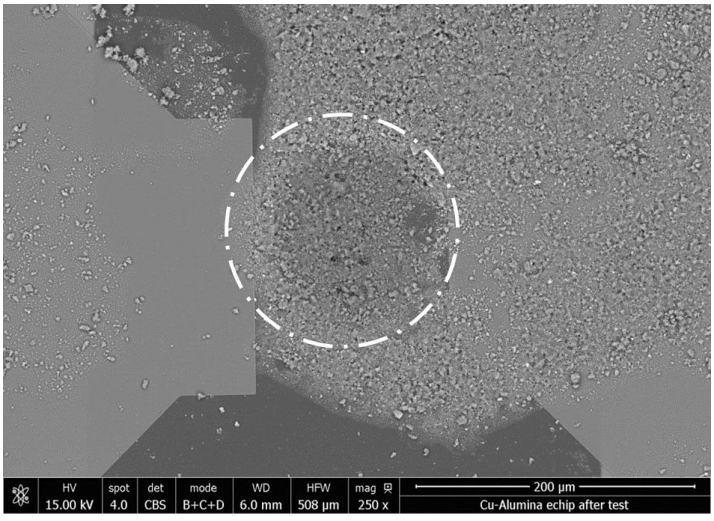

Figure 6.15: Post-mortem SEM image of the e-chip after in situ STEM test.

3.2.3 Conclusion

To sum up, the stabilisation of the copper phase has proven to be difficult in the model systems as well as the different supported samples presented in this chapter. Preferential migration of the copper or copper oxide nanoparticles from the alumina support to the SiN_x membrane is inevitable at low temperatures (below 700 °C). Whereas, above 700 °C the vapour phase migration seems to be dominant with most of the copper phase ending up condensing and re-forming nanoparticles on the non-heated side of the e-chip.

It seems that the disappearance of copper phases might be linked to the presence of O_2, despite CuO having a higher melting temperature than Cu. However, it is not clear what other factors affect the stability of the nanoparticles and why under H_2 the nanoparticles were stable in the CuO/Al_2O_3 sample but not in the model systems in chapter 5.

To understand and confirm the negative effect of O_2 atmosphere in the stability of the copper oxide nanoparticles, another set of calcination experiment was performed on stable copper-aluminate phase, as presented in the next part.

3.3 CALCINATION OF CU-AL-NP UNDER O_2

3.3.1 Cu-Al NP – 800 °C sample

The calcination of the Cu-Al NP – 800 °C is outlined in section 2.1.3.3. First, the nanoparticles were heated from room temperature to 200 °C under Ar for 2 hours. The sample was then heated under O_2/Ar in steps of 100 °C, up to 1000 °C. The imaging was performed on selected areas by halting the temperature ramp for 3-5 minutes.

After 2 hours of exposure to argon at 200 °C, some changes were noticed as depicted in *Figure 6.16*. In some zones nanoparticles have emerged on the surface of the support (*Figure 6.16c*). The exact oxidation state of these nanoparticles was not identified by SAED to avoid possible beam damage. However, they are believed to be metallic Cu, from the brighter contrast of the nanoparticles and since the sample was heated in the absence of oxygen. Most of the sample looked like the area 2 shown in *Figure 6.16c*, where no visible nanoparticle was noted. Even though according to EDS, copper was present in all the support particles.

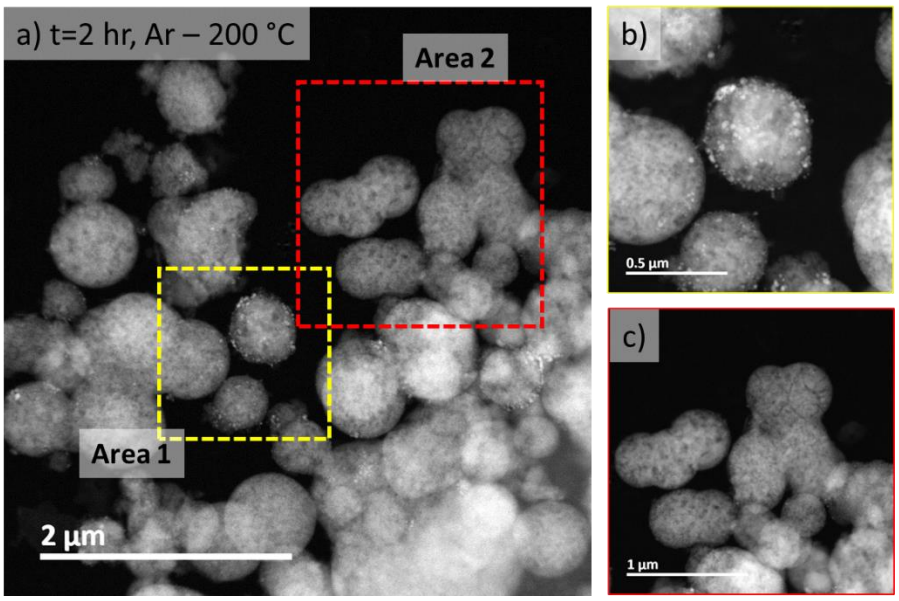

Figure 6.16: STEM-HAADF images of one of the selected areas (a) and b) and c) are the areas marked in red and yellow square in image (a).

Looking at the evolution of the two areas in *Figure 6.17* and *Figure 6.18*, respectively, different behaviours were observed over the course of heating under oxygen. The nanoparticles in area 1 displayed a wide particle size distribution of 5 to 30 nm and presumably coarsened as a function of heating duration and temperature increase. However, it is difficult to identify the nature of the particle growth, whether it is PMC, Ostwald ripening or growth due to the emergence of atomic copper from the aluminate phase. The particles marked in blue circles on *Figure 6.17* display an overall increase in their volume and shape change. The smaller nanoparticles nearby slowly disappeared during the heating from 200 to 300 °C, possibly via Ostwald ripening. Heating to 400 °C and 500 °C leads to loss of the surface particles that were formed. No new copper-based particle was visible at 400 or 500 °C, probably due to diffusion inside the support. In contrast, no copper particle was visible in area 2, from 200 to 500 °C.

However, above 550 °C the copper-based particles were visible in area 2 and some nanoparticles also re-emerged in area 1. Between 600 °C and 700 °C, very large nanoparticles are formed on the alumina surface. These nanoparticles were bigger in size (about 20 to 80 nm) and exhibited a different shape and contrast compared to the particles formed at lower temperature. The shape of the particles was faceted, corresponding to CuO phase (as determined in chapter 5, section 4.2.3.1.3). These particles remained similar in

shape and size until 750 °C. Gradual decrease in the size of the nanoparticles is observed starting at 750 °C. Finally, at 800 °C no more copper-based particles could be observed. The evaporation of the copper particles occurred in between. Since the imaging and observations were only carried out at every 50 °C, the exact temperature of evaporation cannot be pointed out and the range at which it occurs is between 750 and 800 °C.

The difference in the two areas, especially at lower temperature could arise from the presence of copper oxide species of very small sizes (perhaps as clusters) within the support. The presence of atomic copper species has been reported in several studies on CuO/Al_2O_3 [2,3]. If that was the case it would be almost impossible to visualise these clusters due to poor contrast with the support, low atomic number of copper (copper oxide), and the presence of gas. Besides that, the Cu-Al nanoparticles displayed variable copper content from one support particle to another. Perhaps, the areas with higher copper content manifested as nanoparticles during the heating.

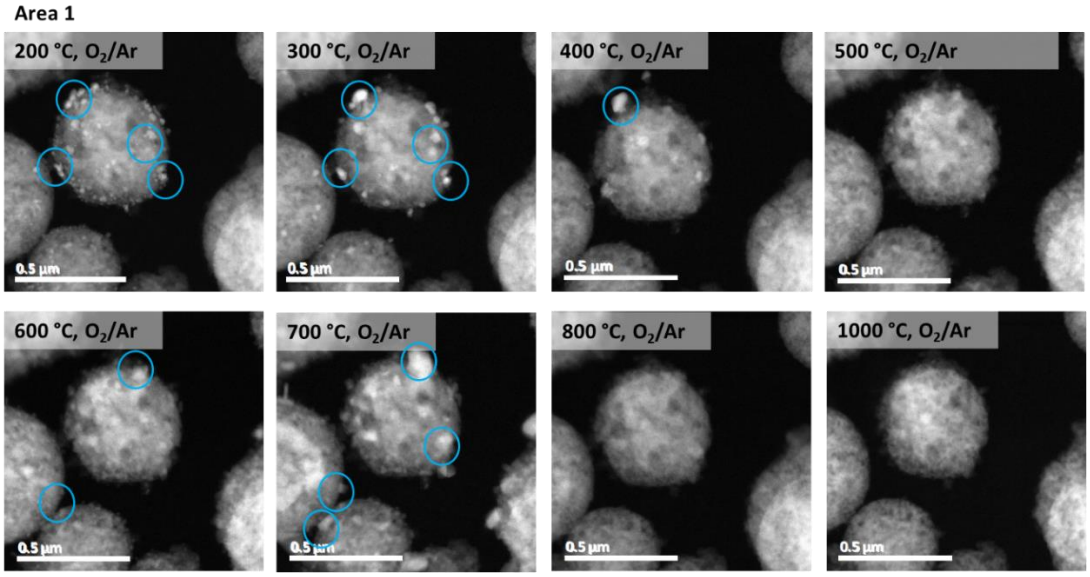

Figure 6.17: STEM-DF images displaying the evolution of the area presented in Figure 6.16b, during thermal treatment from 200 °C to 1000 °C, under O_2.

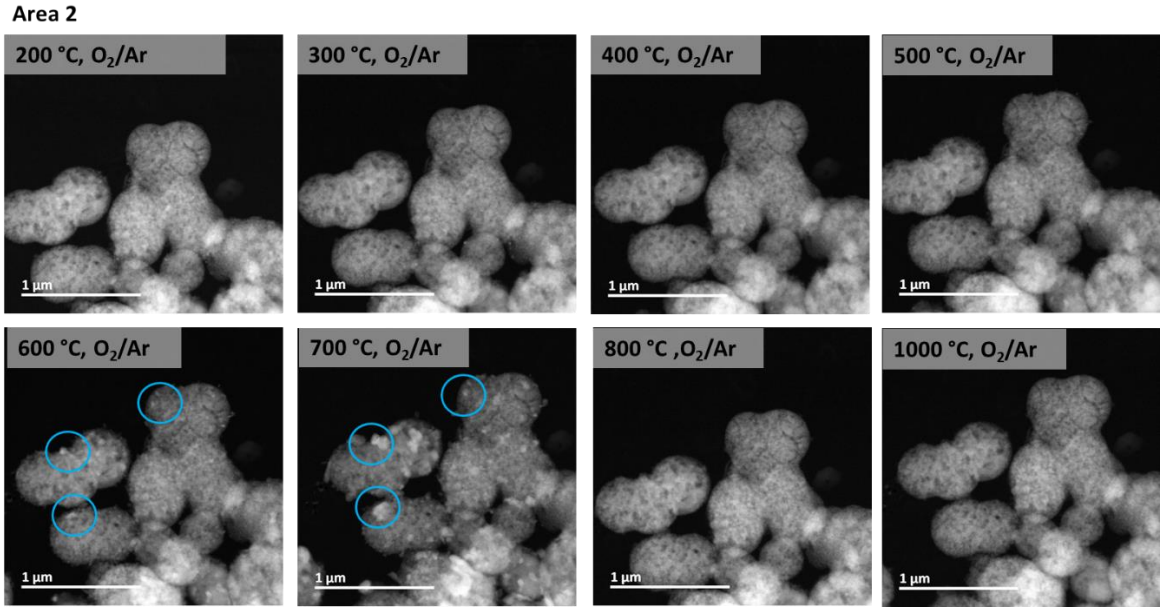

Figure 6.18: STEM-DF images displaying the evolution of the area presented in Figure 6.16c, during thermal treatment from 200 °C to 1000 °C, under O_2.

Areas that were not exposed to the beam during the observations were analysed after the sample was brought down to 200 °C for EDS. Comparison of the area at the beginning and at the end of the experiment confirmed the absence of the copper phase.

In terms of the support morphology, no noticeable change was observed except in some areas sintering of the support particles were noted. The relation between the alumina morphology and the phase transition is discussed in section 3.4.

3.3.2 Cu-Al NP – 900 °C sample

Similarly, the Cu-Al NP-900 °C sample was calcined up to 1000 °C. To remind, compared to the Cu-Al NP-800 °C sample, the Cu-Al NP-900 °C sample is more crystalline with planes corresponding to the copper aluminate phase and heterogeneous copper distribution, where some of the support particles contain similar copper content as the stoichiometric $CuAl_2O_4$ and other particles display very small or no copper at all.

Figure 6.19 depicts the behaviour of the Cu-Al-900 nanoparticles as they are gradually heated from 200 to 1000 °C, in O_2. No evolution of the particle's morphology is observed up to 300°C. After 400 °C, very small spherical nanoparticles of about 2-10 nm appear on the surface of the support. They became numerous as the temperature reached 550 °C. The number and size of these particles increased with temperature augmentation. In the area

marked in red at 700 °C, there are numerous particles with a broad particle size distribution within 5 to 50 nm range displaying a variety of shapes – from spheres to faceted cubes. Compared to the lower temperature calcination, where the particle size distribution was narrower, and the shape of the particles were mostly spherical. Few facetted particles of few hundred nm are also noted (pointed with yellow circle), attributed to CuO phase. Some of these copper-based particles migrate to the SiN_x membrane, but to a rather low extent compared to the 28wt% CuO/Al_2O_3 sample.

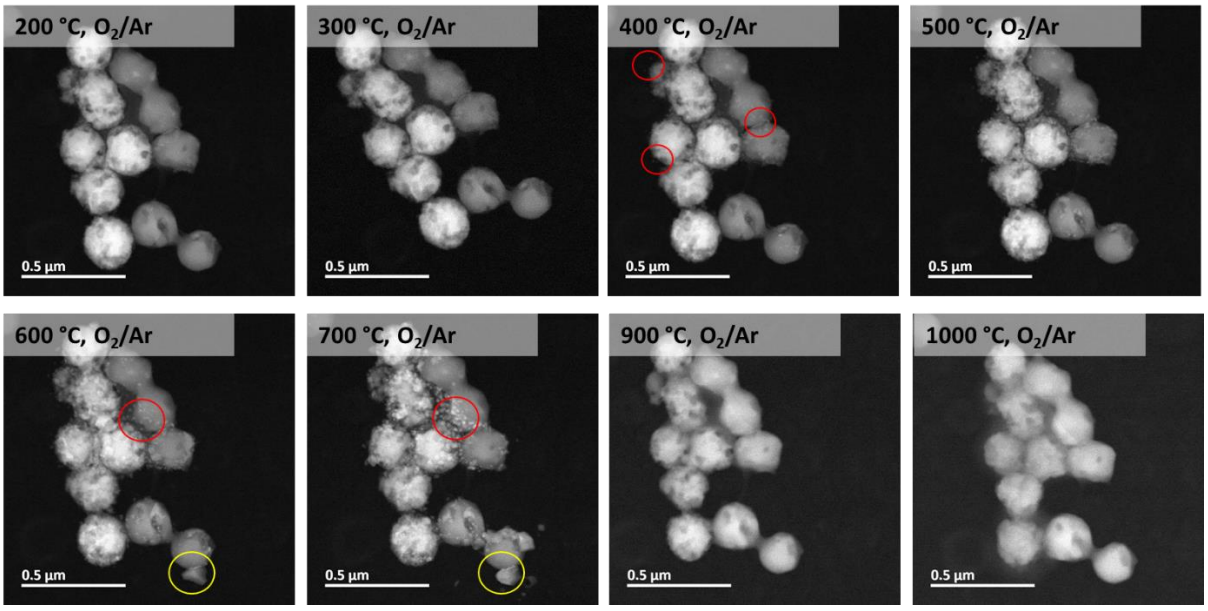

Figure 6.19: Evolution of the Cu-Al NPs – 900 °C as a function of temperature under oxygen.

Both Cu-Al NP-800 °C and Cu-Al NP-900 °C samples displayed the eviction of the copper phase. For the Cu-Al-800 sample, it started earlier (already at 200 °C under Ar) than the Cu-Al-900 sample (above 300 °C, under O_2). In both cases, the nanoparticle formation was higher above 550 °C. It seems the eviction of the copper phase occurs in three steps – 200 °C, 400 °C and above 550 °C. The temperature range is closer to the reduction temperature of the copper aluminate phase as described in section 3.1.1.1. Here, under the presence of 0.5 atm O_2 partial pressure it is puzzling to observe spontaneous reduction or Cu/CuO nanoparticle expulsion from an otherwise very stable copper aluminate phase.

Alike the Cu-Al NP-800 °C sample, between 750 and 800 °C, the copper particles are no longer visualised. No trace of copper was detected either from the EDS analysis after the experiment (*Figure 6.20*)

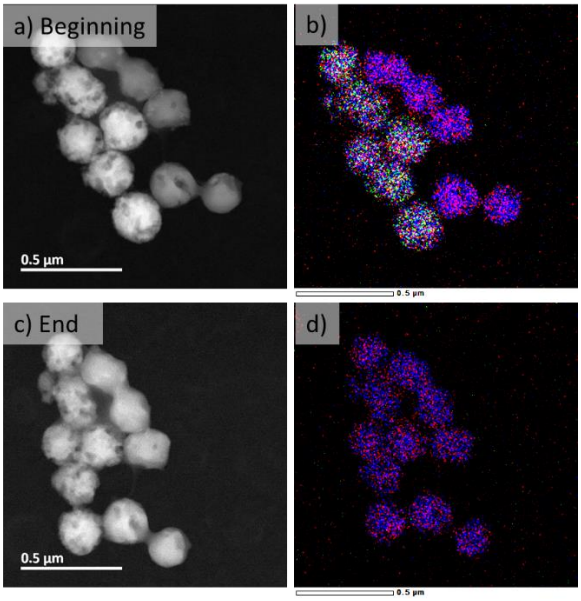

Figure 6.20: STEM-EDS analysis of Cu-Al-NP-900 at beginning (a,b) and at the end of the experiment(c-d).

Following the complete loss of the copper phase, the temperature was augmented to 1000 °C to understand the effect of the initial sample on the possible phase transition of the alumina. The morphological and structural evolution in light of alumina phase transition is discussed in section 3.3.4.

3.3.3 Calcination in static O_2

In a last attempt to stabilise the copper phase, the Cu-Al NP-900 °C sample was heated at a very slow heating rate (1 °C/min) and static condition under O_2 gas, to achieve more homogeneous heating throughout the volume of the e-chip. This time, the evaporated nanoparticles were found on the non-heated side of the e-chip but not directly on top of the e-chip (outside the ~130 µm heating diameter) as seen from the SEM observation reported in *Figure 6.21*. According to Protochip product specifications, the main heating zone of the heating e-chip is about 90 µm, afterwards the temperature profile follows a gradient. Similar type of gradient was observed on the non-heated chip.

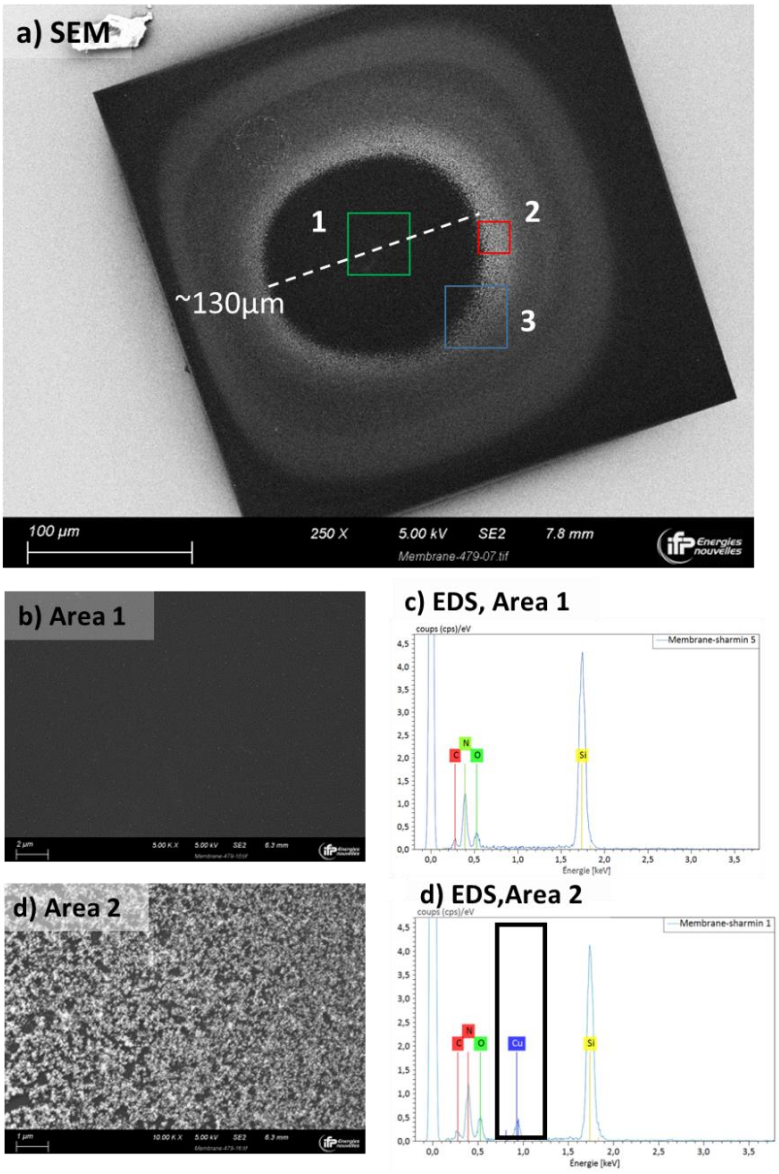

Figure 6.21: Post-mortem SEM characterisation of the non-heated SiNx e-chip: a) image of the whole e-chip. The areas marked with green and red square are presented along with the EDS analysis in b-d. The dotted line measuring the dark circular area of the e-chip in a is about 130 µm. In d), the copper signal is highlighted with black square.

3.3.4 "Quasi" *in situ* experiment

The post-mortem characterisations of the e-chip after the end of two different experiments lead to different observations. At the end of the redox-calcination experiment on the CuO/Al_2O_3 sample (section 3.2.1), the nanoparticles were found on the non-heated side of the e-chip. However, as presented in the last section, when the Cu-Al NP-900 °C sample was subjected to a slow heating rate (1 °C/min) under static O_2 environment, the evaporated nanoparticles were still found on the edge of the non-heated e-chip.

This led to the assumption that the e-chip configuration might play a role on the phenomenon of the evaporation and the instability of the copper phase. Hence, two control experiments were carried out – whereby the materials were drop-casted on a SiN_x membrane chip (supported on Molybdenum) and put inside the TGA to carry out heating under air followed by 2 redox cycles at 800 °C and 900 °C. In total the materials were subjected to 1 hour of heating at 800 °C and 900 °C, respectively. At the end of the experiment the chips were directly analysed in TEM. In both cases, copper was still present on the particles, as shown in *Figure 6.22*. Thus, implying the possible role of the *in situ* STEM setup on the disappearance of the copper.

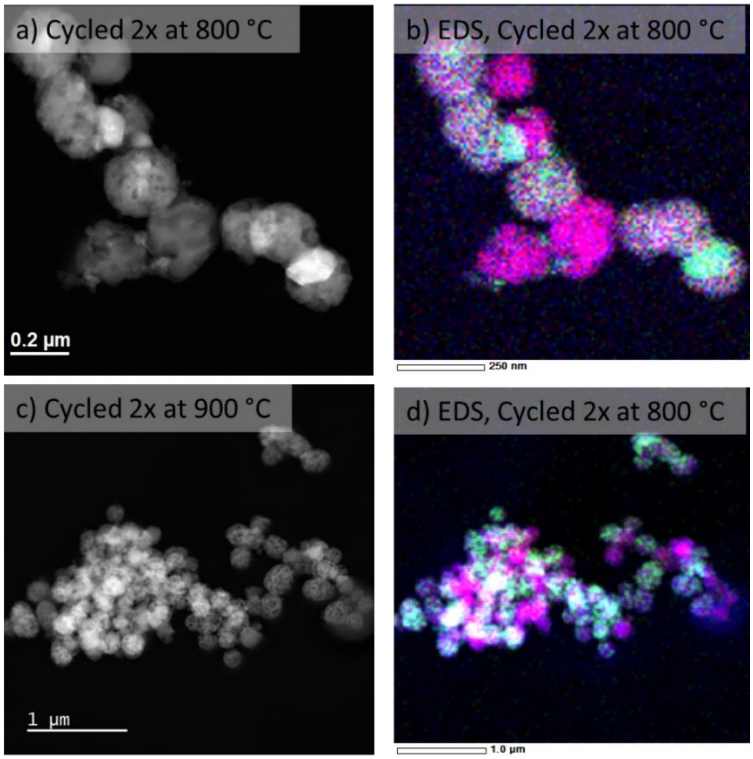

Figure 6.22: STEM-HAADF and EDS mapping of Cu-Al NP-800 °C sample (a and) b) and Cu-Al NP – 900 °C sample (c and d) deposited on SiN_x chip and underwent 2 redox cycles in a TGA.

It is speculated that the heating is not homogeneous throughout the experimental volume, which could cause a temperature gradient effect and drive the nanoparticles migration via thermo-migration process. Since the gas is under flow, it is likely that the gas near the heating surface is heated while the gas in contact with the non-heated chip might be at the temperature of the vacuum chamber of the microscope. Furthermore, there is a chance of heat loss due to convective heat transfer from the membrane surface to the gas atmosphere, aiding in the inhomogeneity of the surface temperature.

It should be noted that in the high temperature redox experiment detailed in section 3.2.2, nanoparticles of copper were still found after up to 1 hour of heating at 900 °C under H_2. The stable particle observed in that particular experiment could either be due to the thermal conductivity of H_2 or due to the anchoring effect of the support under H_2. H_2 is known to have a high thermal conductivity (~0.182 W/mK), a value about 7 times higher than that of oxygen/air (~0.026 W/mK), and 10 times higher than Ar, at 300 K. Therefore, the presence of H_2 is likely to have mitigated the issue of the temperature inhomogeneity in the e-chip reaction volume. Furthermore, the surface tension minimisation mechanism is perhaps linked to the rate of heating; the growth of the nanoparticles is preferred rather than the migration to the SiN_x. Or, possibly the Cu-Al_2O_3 and Cu-SiN_x samples have temperature dependant adhesion properties which may favour the interaction between Cu and Al_2O_3 rather than Cu-SiN_x, as observed throughout the experiments.

3.3.5 Conclusion

The stability of the copper phase could be influenced by a multitude of factors. For instance, the physical properties of the nanoparticles, the interactions between copper-support-gas atmosphere as well as the reactor configuration. The reactor configuration is especially important for the e-chip as the evolution occurs at a very local scale.

The inherent physical properties of copper containing particles may have a role in the evaporation of the copper phase. More precisely, the low melting temperature of the copper phases could be even lower for nanoparticles. Other low melting temperature metals such as silver and gold also displayed such evaporation behaviour when the nanoparticles were subjected to thermal treatment [6,7]. On the contrary, metals with high melting points such as Pd or MoS_2 particles displayed no evaporation/disappearance up to 800 °C [8,9].

During the calcination under O_2, the emergence of copper oxide particles on the alumina surface is related to copper atoms expulsion from the copper aluminate. This observation was not expected, especially in presence of 0.5 atm O_2 partial pressure. The copper-aluminate is a thermodynamically stable phase at least up to 1000 °C, under air [10,11]. Therefore, it is speculated that the instability of the copper phase or the evaporation of the

copper phase is perhaps promoted by the experimental setup (as the control experiment showed).

It is quite difficult to point out the exact role of either of the above-mentioned parameters. Dedicated experiments are required to have a comprehensive understanding which was outside the scope of the current work. However, qualitatively it could be concluded that the nanoparticles are more stable under H_2 than under O_2.

3.4 ALUMINA PHASE TRANSITION

The second objective of this study was to investigate the alumina phase transition phenomena. As stated in section 3.3.2, after the total loss of the copper species during the calcination of the Cu-Al NP – 800 °C and Cu-Al NP – 900 °C, the temperature was increased to 1000 °C to induce the α-Al_2O_3 phase transition. These two samples are considerably different in terms of initial morphology and crystallinity. Since the samples were exactly treated the same way, any disparity at the end of the calcination would originate from their initial structures.

3.4.1 Cu-Al 800 °C sample

At the end of the thermal treatment to 1000 °C, the sample was brought down to room temperature again to conduct SAED to identify possible phase transitions.

The SAED of two different areas displayed an overall increase in the crystallinity of the alumina phase (*Figure 6.23b* and d). The diffraction spots are brighter and more distinct compared to the fresh sample. Besides, the 2.8 Å d-spacing value corresponding to the (220) plane related to the *FCC* spinel structure could be identified which was not visible before. According to *Figure 6.23c* (marked in red circle) coarsening of the alumina platelets and a large particle with round edge is observed. However, there was no evidence of alpha alumina formation at this point.

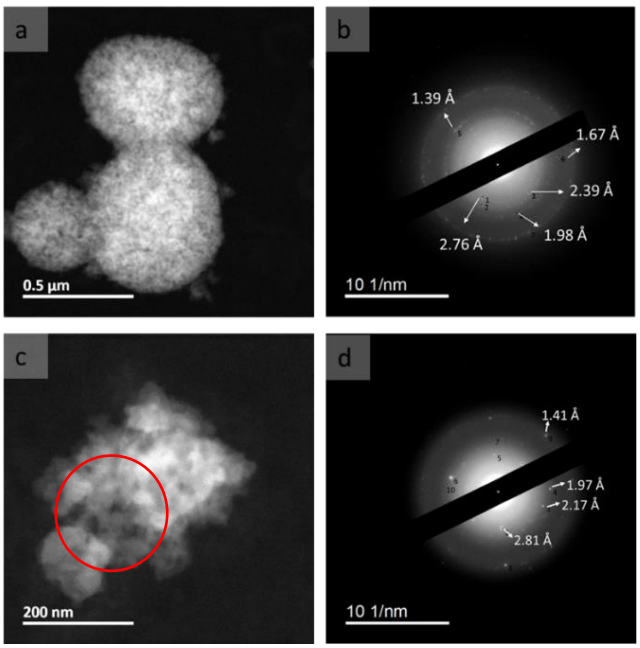

Figure 6.23: STEM-HAADF (a and c) and the respective TEM-SAED (b and d) of the Cu-Al NP-800 °C sample at the end of the experiment.

3.4.2 Cu-Al 900 °C sample

For the Cu-Al NP-900 °C sample, if we compare to the beginning of the experiment, after the total loss of copper (900 °C) and at the end of the experiment (1000 °C), the morphological changes are quite drastic. At 900 °C, the support particles exhibit a porous structure; after attaining 1000 °C, there is a little shrinkage of the overall grains of the support particles. In most of the particles which initially contained copper, new domains/growth are observed (marked in red circles in *Figure 6.24d*). Neck formation is also observed between the Cu-containing and non-Cu-containing alumina.

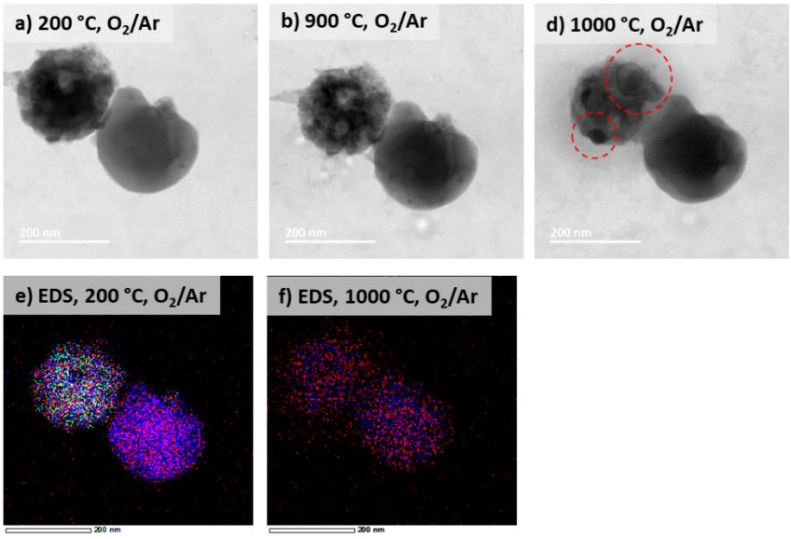

Figure 6.24: STEM-BF images and Elemental mapping of two different Cu-Al nanospheres at the beginning of the experiment (a and e), at 900 °C, and at 1000 °C.

The same goes in terms of crystallinity: in some of the particles, prominent reflections from specific planes are observed. The post-mortem characterisation of the sample after the end of the experiment reveals 3.45 Å, 2.57 Å, 2.01 Å and 1.61 Å d-spacing values corresponding to (012), (104), (113) and (116) planes related to α-Al_2O_3 phase, respectively (*Figure 6.25*). At the beginning of the experiment, a very fade signal for (116) plane was noted. Particles 1 and 3 contained copper (from EDS) at the beginning of the experiment. While #1 transformed into crystalline alumina with (104) prominent plane, #3 displays a mixture of diffraction spots of both α and transition alumina phase. Similarly, the initial Cu-deficient #2 and #4 displayed alpha and mixed alumina phases, respectively.

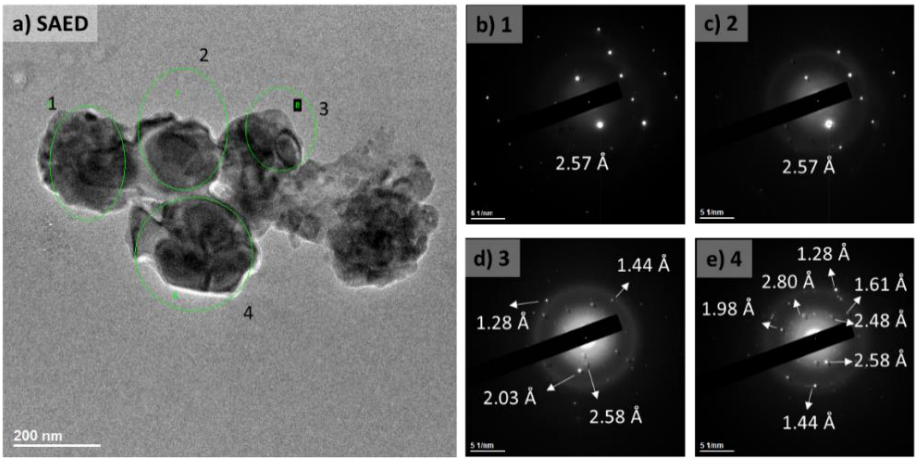

Figure 6.25: Post-mortem TEM image of the Cu-Al NP- 900 °C redox experiment (a) and SAED images of the areas circled 1-4 in (a) presented in b-e, respectively.

Experimentally, it is difficult to deduce the epitaxial relationship between the *FCC* Cu-deficient spinel and the hexagonal α-Al_2O_3 phase.

3.5 DISCUSSION

The structure of γ-Al_2O_3 phase is believed to be defective spinel with a 32-36% of the Al^{3+} ions occupying tetrahedral sites and the rest occupying octahedral sites. Without the presence of copper, the phase transition of γ-Al_2O_3 involves the transition from δ to θ-Al_2O_3. With every transition step, the percentage of the Al^{3+} ions in the tetrahedral configuration increases, to finally reach a AlO_4:AlO_6 ratio of 1:1 in the θ-Al_2O_3 phase. During the α-Al_2O_3 formation, the overall oxygen position must be reconfigured from an *FCC* structure to *HCP* structure whereabout the Al^{3+} ions only exist in AlO_6 sites. The phase transition of the θ-Al_2O_3 to α-Al_2O_3 phase would require reconstruction of the bonding environments and the lattice structure. In chapter 3, section 4, it was deduced that the presence of copper changes some of the Al^{3+} ion occupancy from tetrahedral to octahedral configuration, compared to the other transition alumina polymorphs. The change in the AlO_4:AlO_6 ratio is the first step as it greatly reduces the activation energy in the later stage of the α-Al_2O_3 phase transition [12,13]. The FCC to *HCP* transformation in metallic phases can occur via reconstruction of the different planes. For example, often the (111) $_{FCC}$ // (0001) $_{HCP}$ relationship is reported where the sliding of the (111) plane leads to the reconstruction of the (0001) plane of the *HCP* lattice [14]. However, the reconstruction relation between the Cu-deficient spinel to α-Al_2O_3 phase might not be that straightforward, as the exact occupancy/vacancy related to Al^{3+} ions position is unknown. The identification of such epitaxial relation would require good experimental data which is resolvable by electron diffraction.

Based on the current knowledge gained through the various characterisation techniques, a global phase transition mechanism is proposed in Figure 6.26. Initially, majority of the fresh sample is composed of small platelets of $Cu_xAl_yO_4$. At every reduction steps, with the removal of copper, the copper-aluminate undergoes local structural reconstruction, which can be considered as the starting of the α-Al_2O_3 phase nucleation. As the system is continuously undergoing oxidation-reduction reactions, the reformation of $Cu_xAl_yO_4$ phase slows down the growth of the α-Al_2O_3 phase. Over the course of the redox cycling, the thermal stress in the reactor leads to the sintering of the aluminate platelets as well as the

α-Al_2O_3. After ~20 cycles, once the particles are big enough or the number of the nucleation sites in a single particle are numerous, the growth of the α-Al_2O_3 phase proceeds dramatically.

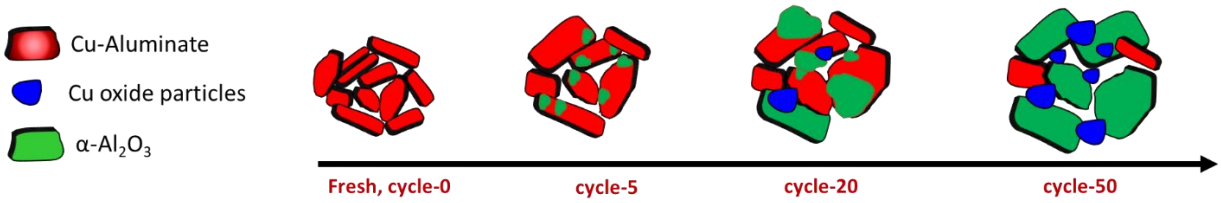

Figure 6.26: Global mechanism of the α-Al_2O_3 phase transition.

4 CONCLUSION

It is important to note that the initial goal of these *in situ* STEM experiments were to understand the temperature and alumina phase-dependant migration mechanism of copper active phases. Specifically, an objective was to distinguish the different regimes of diffusion (surface, grain boundary and bulk diffusion) and the parameters affecting the boundaries of these regimes. In addition to that, it is equally pertinent to identify the role and influence of the copper phase concerning the α-Al_2O_3 formation. Nevertheless, the objective to understand the diffusion behaviour at high temperature could not be achieved because of difficulties in terms of copper stability mentioned throughout chapter 5 and chapter 6. Many experimental runs have been dedicated to stabilising the copper phases. Different strategies have been adapted as well by either changing the morphology or copper concentration of the materials or by changing the rate or heating or reaction gas without any apparent success.

Finally, it was decided to focus on the 2nd objective of the work, that is, the alumina phase transition to understand the driving force leading to formation of the alpha alumina phase. The thermal treatment of the Cu-Al NP – 800 °C and Cu-Al NP – 900 °C samples brought an interesting insight in the phase transition phenomena. The initial Cu-Al NP-800 °C sample was composed of organised nanoplatelets containing copper phase (from EDS) but displayed a diffraction pattern like that of γ-Al_2O_3. After the heat treatment, Cu-Al NP – 800

°C sample displayed little change in its morphology but tended to be more crystalline than the starting material. In comparison, the Cu-Al NP – 900 °C sample was made of dense particles with varying percentage of structural copper and diffraction signal corresponding to $CuAl_2O_4$ phase (with slightly lower d-spacing values). After an hour of heat treatment, the Cu-Al NP – 900 °C sample exhibited d-spacing values corresponding to α-Al_2O_3 planes. It was initially suggested that the insertion of the copper in the aluminate structure leads to displacement of Al^{3+} ions to fill in the octahedral sites which is a necessary step towards the α-Al_2O_3 formation.

5 REFERENCES

[1] A. DeLaRiva. *The sintering and stability of catalytic nanoparticles.* Ph.D. Albuquerque, New Mexico: The University of New Mexico, 2009.

[2] Gayán P., Forero C.R., Abad A., Diego L.F. de, García-Labiano F., Adánez J. Effect of Support on the Behavior of Cu-Based Oxygen Carriers during Long-Term CLC Operation at Temperatures above 1073 K, *Energy & Fuels*, 2011, **25,** 3, 1316-1326. DOI: 10.1021/ef101583w.

[3] Y. Liu, S. Qing, X. Hou, G. Feng, R. Zhang and X. Wang. Synthesis and structural characterization of CuAl2O4 spinel with an unusual cation distribution, *Journal of Materials and Applications*, 2018, **7,** 2, 82-89.

[4] H-S. Roh, G. K. Choi, J-S. An, C. M. Cho, D. H. Kim, I. J.Park, T. H. Noh, D-W. Kim and K. S. Hong. Size-controlled synthesis of monodispersed mesoporous a-Alumina spheres by a template-free forced hydrolysis method, *Dalton Transactions*, 2011, 40, 6901-6905.

[5] L. M. Plyasova, T. M. Yur'eva, I. Yu. Molina, T. A. Kriger, A. M. Balagurov, L. P. Davydova, V. I. Zaikovskii, G. N. Kustova, V. V. Malakhov, and L. S. Dovlitova. Dynamics of structural transformations in the reduction of copper aluminate, *Kinetics and Catalysis*, 2000, **41**, 429-436.

[6] A. Chmielewski, J. Nelayah, H. Amara, J. Creuze, D. Alloyeau, G. Wang and C. Ricolleau. Direct Measurement of the Surface Energy of Bimetallic Nanoparticles : Evidence of Vegard's Rulelike Dependence, *Physical review letters*, 2018, **120,** 2, 25901. DOI: 10.1103/PhysRevLett.120.025901.

[7] M. A. Asoro, D. Kovar and P. J. Ferreira. In situ transmission electron microscopy observations of sublimation in silver nanoparticles, *ACS nano*, 2013, **7,** 9, 7844-7852. DOI: 10.1021/nn402771j.

[8] Baaziz W., Bahri M., Gay A.S., Chaumonnot A., Uzio D., Valette S., Hirlimann C., Ersen O. Thermal behavior of Pd@SiO2 nanostructures in various gas environments : A combined 3D and in situ TEM approach, *Nanoscale*, 2018, **10,** 43, 20178-20188. DOI: 10.1039/c8nr06951d.

[9] J. Chen, S. Zhou, Y. Wen, G. H. Ryu, C. Allen, Y. Lu, A. I. Kirkland and J. H. Warner. Dynamique in situ au niveau atomique à haute température de grandes formations à domaine d'inversion en monocouche MoS 2, *Nanoscale*, 2019, **9**, 1901-1913.

[10] K. T. Jacob and C. B Alcook. Thermodynamics of CuA102 and CuA120, and Phase Equilibria in the System Cu20-Cu0-Al2O3, *Journal of American Ceramic Society*, 1975, **58**, 192-195.

[11] M. Ozawa, H. Toda, O. Kato and S. Suzuki. Solid-state thermal behavior of copper-modified alumina toward lean-burn exhaust NO removal catalyst, *Applied Catalysis B: Environmental*, 1996, **8**, 123-140.

[12] R. Prins. On the structure of γ-Al2O3, *Journal of Catalysis*, 2020, **392**, 336-346.

[13] K. Okada, A. Hattori, T. Taniguchi, A. Nukui and R. N. Das. Effect of Divalent Cation Additives on the γ-Al2O3-to-α-Al2O3 Phase Transition, *Journal of American Ceramic Society*, 2000, **83,** 4, 928-932.

[14] T. Wu, M. Sun, H. H. Wong and B. Huang. Decoding of crystal synthesis of fcc-hcp reversible transition for metals: theoretical mechanistic study from facet control to phase transition engineering, *Nano Energy*, 2021, **85**.

CONCLUSIONS

The Chemical Looping Combustion process relies on oxygen carriers for the indirect combustion of fossil fuel. The stability of the oxygen carriers remains one of the most challenging aspects for the industrial scaling of the process. Although Cu-based oxygen carriers have been the subject of many studies, the degradation of the materials associated with the migration of copper phases and formation of alpha alumina requires further studies. Therefore, in this PhD thesis, CuO/Al_2O_3 materials were studied to understand their ageing process in terms of the migration behaviour of the copper phases.

Oxygen carriers with 13 wt% CuO were prepared via impregnation of a commercial γ-Al_2O_3 support. The materials were calcined at either 700 °C, 800 °C or 900 °C. The oxygen carriers were subjected to multiple oxidation-reduction cycles at different temperatures to highlight the different migration patterns of the copper phases associated to the Cu/CuO-Al_2O_3 phases interactions. Two model systems based on copper nanoparticles deposited on flat SiN_x and amorphous Al_2O_3 substrates were also studied. The objective was to achieve a simplified understanding of the Cu/CuO redox behaviour and to define the temperature-dependent oxidation state, shape evolution and migration of the copper nanoparticles. Copper impregnated spherical Al_2O_3 nanoparticles were also synthesised in an attempt to mimic the 3D architecture of the commercial support at the nanoscale and to focus on alumina phase transitions.

In order to achieve a comprehensive overview of the materials' evolution, several characterisation techniques were employed: STXM-XANES, XAS, XRD, SEM, and STEM, aimed at characterising the samples at different scales. Moreover, *in situ* XAS and STEM allowed monitoring of the real-time evolution of the materials.

A thorough characterisation of the fresh 13 wt% CuO/Al_2O_3 samples calcined at 700°C, 800 °C and 900 °C revealed differences in their phases and morphology. All samples contained copper aluminate with different proportions of copper revealed by SEM-EDS. Additionally, CuO/Al_2O_3-calcined at 700 °C and at 800 °C displayed the presence of unreacted copper oxide, while CuO/Al_2O_3-900 °C contained α-Al_2O_3 phase. The oxygen

carriers were subjected to up to 200 redox cycles at their respective calcination temperatures. At 700 °C, the cycled oxygen carrier is composed of Cu-rich $Cu_xAl_yO_4$ patches in a matrix of transition aluminas and low Cu-concentration $Cu_xAl_yO_4$. After cycling at 800 °C, the material displayed sintered CuO on a support matrix composed of a mixture of transition aluminas and $Cu_xAl_yO_4$ with varying concentration. In contrast, at 900 °C the formation of porous α-Al_2O_3 support with dispersed CuO was noted.

Initially, the formation of α-Al_2O_3 was assumed to occur as a gradual process as a function of the number of cycles. Later it was uncovered that the conversion was not gradual from the beginning. From SEM imaging, the α-Al_2O_3 phase is not visible before a certain number of cycles are reached. Additionally, the evolution of $Cu_xAl_yO_4$:CuO phases proportion from the *in situ* XAS experiments also indicates a threshold number of cycles beyond which the percentage of $Cu_xAl_yO_4$ phase decreased drastically. This drastic change, associated to the nucleation and growth of the α-Al_2O_3, is very probably induced by the diffusion of copper in/out of the alumina.

Thereupon, *in situ* STEM was employed to investigate, at first, the nanoscale migration and the redox behaviour of copper nanoparticles supported on flat SiN_x or Al_2O_3 substrates. Qualitatively, the stability of the nanoparticles with respect to the support and the gas could be compared. The shape and phase changes of copper particles observed during oxidation and reduction was useful later during the characterisation of the real oxygen carriers

Finally, the mobility and the phase transitions of the oxygen carrier based on the commercial support and the synthesised alumina nanoparticles were observed in real-time by STEM. The materials were characterised starting from 200 °C to 1000 °C. At higher temperatures (> 500 °C), stabilising the Cu nanoparticles on the alumina support was difficult either due to the preferential migration of copper to the SiN_x membrane or to the evaporation of the particles. As a result, no conclusion could be drawn concerning the migration behaviour of copper in/on the support at high temperatures. Nevertheless, α-Al_2O_3 phase transition could be observed in the supported alumina nanospheres. Among possible assumptions to be investigated, the α-Al_2O_3 phase nucleation could occur via reconstructive transition of FCC to HCP lattice structure, following an epitaxial relationship.

Due to the presence of copper, the energy barrier for this structural reconstruction is lowered, hence decreasing the phase transition temperature.

Based on the observation carried out at different scales of the material, an overview of the copper migration mechanism is proposed. During oxidation, migration of the copper phases can either lead to sintering and formation of large CuO particles via surface or grain-boundary diffusion, or to the formation of non-stoichiometric $Cu_xAl_yO_4$ spinel via solid-state reaction between copper oxide and alumina. At lower temperatures (≤ 800 °C), the surface or grain-boundary diffusion is dominant, and cumulated redox cycling of the oxygen carrier results in the dispersion of large CuO particles within the Cu-containing alumina grains. At higher temperatures (≥ 900 °C), the non-stoichiometric $Cu_xAl_yO_4$ spinel formation is dominant, and CuO reacts with alumina to form Cu-aluminate phase. While the oxidative formation of spinel is favourable in the CuO + transition alumina system, it is kinetically limited in the case of CuO + α-Al_2O_3. Hence, with an increasing number of cycles, α-alumina and CuO phases segregate and eventually large CuO crystals are formed within a porous α-alumina support. At 900 °C, the α-Al_2O_3 phase transition is responsible for the dramatic morphology change in the oxygen carrier. As it turns out, the presence of copper tends to promote the α-Al_2O_3 formation, likely from Cu-deficient aluminate during reduction. It is speculated that copper contributes to the local structural organisation leading to a higher proportion of octahedral Al-O environments compared to transition aluminas. Since, the α-Al_2O_3 phase is composed of octahedrally coordinated Al^{3+} ions, a slight change in the local bonding environment in the aluminate may reduce the overall phase transition energy barrier. Consequently, instead of following the conventional γ → δ → θ→ α-Al_2O_3 transition sequence (which generally occurs above 1000 °C), the copper-induced structural change leads to the direct transition to α-Al_2O_3 at a lower temperature.

In this study two mechanisms are proposed, one is concerning the temperature-dependant diffusion in the CuO-Al_2O_3 system and the other one is highlighting the role of copper in the α-Al_2O_3 formation. These new insights would help to identify ways to prevent the α-Al_2O_3 transition or to stabilise the $Cu_xAl_yO_4$ phase.

PERSPECTIVES

This study may provide prospects in several directions in terms of better understanding of the proposed mechanisms, improvements in the experimental techniques and methodologies as well as suggestions for the development of copper-based oxygen carriers.

The current understanding of the material can be improved. For instance, the role of copper in the mechanism of $\gamma/\delta/\theta$-aluminas transition to α-Al_2O_3 should be further studied. ^{27}Al MAS NMR characterisations might provide more precise quantification and distinction between the AlO_4 and AlO_6 environments in the various alumina polymorphs as well as in $CuAl_2O_4$ phase. This can be accompanied by molecular dynamic modelling of the $CuAl_2O_4$ phase reduction. Additionally, the molecular dynamic simulation may help to provide favourable pathway(s) for the reconstructive phase transition proposed in this work. Furthermore, *in situ* STXM on samples cycled at 700 °C and 800 °C would possibly provide an accurate insight into the materials evolution and substantiate the temperature-dependent migration mechanism suggested in this study.

Concerning the characterisation techniques used, some improvements can be made in the methodology. Already in Chapter 4 some specific suggestions have been made for the *in situ* XAS experiments. It is crucial to estimate the reaction duration, gas residence time considering the exact reaction parameters used in the specific reactions such as flowrate, gas concentration and sample mass. Besides, proper calibration of the complementary techniques such as mass spectrometer (at the ROCK beamline) is essential. Quantitative information on the relative phase percentage and lattice parameters might be gained through XRD characterisations. Finally, there is a lot of room for improvements in the *in situ* STEM experiments. First, the reaction parameters like duration, heating rate, temperature steps should be defined and kept constant throughout all the experiments. Secondly, since the copper nanoparticles were only stable on Al_2O_3 under H_2, investigating the Cu-Al_2O_3-H_2 (metal-support-gas) interactions could provide insights into the disappearance of copper phases, especially from the stable $CuAl_2O_4$ phase under high O_2 partial pressure. This could include changing the H_2 partial pressure or the rate of heating. Thirdly, to achieve better temperature homogeneity, O_2 could be diluted with higher thermal conductivity gas such

as He. Finally, a core-shell type material without any porosity could be used to confine the copper phases.

Concerning materials improvement, the mobility of the copper phase supported on other supports such as TiO_2 or SiO_2 can also be investigated to achieve a comparative understanding of the effect of support.

In terms of development of CuO/Al_2O_3 oxygen carriers, the alumina phase transition temperature can probably be modified by doping with aliovalent cations. For example, Na^+ or Ca^{2+} have been reported to increase the phase transition temperature of alumina by suppressing the diffusion of Al^{3+} ions. Also, Cu-based bimetallic oxygen carriers could be developed. For example, $Cu\text{-}Ni/Al_2O_3$ material has been shown to display better morphological stability compared to Cu/Al_2O_3.

Finally, the scope of the present work concerns the behaviour of the material, deeper analysis of the conversion and reactivity is therefore missing from the current understanding. The next step could be to correlate the reactivity with microstructural evolution.

Appendixes

A. STANDARD CHARACTERISATION OF 13WT%/CUO/AL$_2$O$_3$

The specific surface area and the porosity of the alumina support and of 13wt% CuO/Al_2O_3 samples calcined at 800 °C and 900 °C were estimated by N_2 adsorption isotherm and Hg porosimetry. As observed from the N_2 adsorption isotherm and the Hg intrusion profile in Figure 1 and the values provided in Table 1, a significant loss of BET surface area is observed with the impregnation of the support followed by 800 °C calcination. A further decrease in the surface area is noted with the increase in the calcination temperature. Similarly, there is a gradual increase in the size of the mean pore size from an initial 8.5 nm in the Al_2O_3 support to 14 nm in the supported sample calcined at 900 °C. Some macroporosity is also oberved in the CuO/Al_2O_3 – 900 °C sample. The loss in surface area and the increased pore diameter is consistent with the temperature induced sintering.

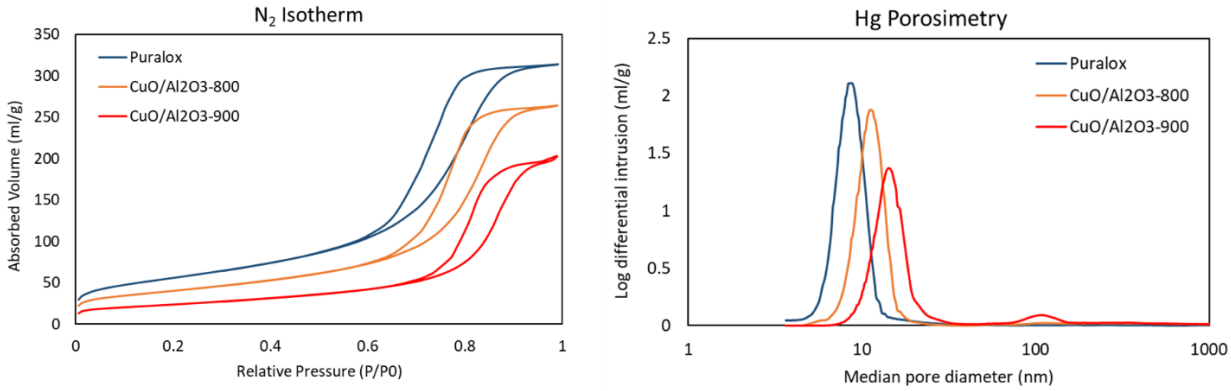

Figure 1 : N_2 isotherm and Hg porosimetry profile of the puralox support, CuO/Al_2O_3 – 800 °C and CuO/Al_2O_3 – 900 °C.

Table 1: The specific surface area and the mean pore diameter values of the Puralox support (Al_2O_3), CuO/Al_2O_3-800 °C and CuO/Al_2O_3 – 900 °C.

	Al_2O_3	CuO/Al_2O_3 – 800 °C	CuO/Al_2O_3 – 900°C
S_{spe}[1] (m^2/g)	202 ± 10	143 ± 7	84 ± 4
Mean pore diameter (nm)	8.5 ± 0.2	11.0 ± 0.2	14.1 ± 0.3

B. WORKING PRINCIPLE OF THE ANALYSIS TECHNIQUES USED

B.1 APPENDIX 1: X-RAY ABSORPTION SPECTROSCOPY (XAS)

XAS is a characterization technique that provides information on the electronic state and the local environment of a given atom. The sample is scanned using a monochromated X-ray beam over an energy range suited to the absorption of the material, to measure the variation of the absorption coefficient as a function of incident X-ray energies. The absorption coefficient is determined by Beer-Lambert's law [12].

$$\boldsymbol{I_t = I_0 e^{-\mu(E)\rho t}} \qquad \textit{Eq. A.1}$$

Where I_t is the measured transmitted intensity related to the incident intensity (I_0), sample thickness (t), density (ρ) of the sample and energy (E) dependent mass absorption coefficient (μ).

The absorption of the X-ray beam concerns the electrons in the core level. When the core electrons are excited, they undergo transition to partially occupied or unoccupied orbitals. The energy of excitation corresponds to the binding energy of the removal of the core electrons. The edges are named by which core electrons are excited and determined by their principle quantum numbers n = 1, 2 and 3 corresponding to K, L and M edges, respectively. For example, the binding energies of electrons from the 1st and 2nd shells of Cu-based compounds lie in the range of 8980 – 8990 and 930 – 960 eV, respectively.

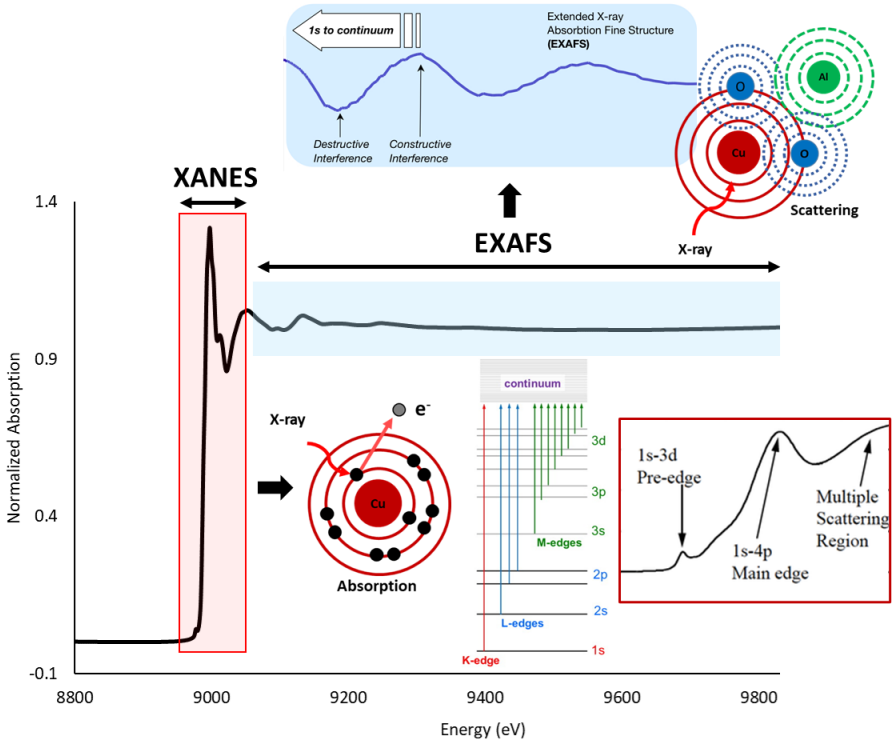

Figure 2: Schematic representation of different zones of XAS spectrum with example of Cu K-edge, depicting the XANES and EXAFS region.

Figure 2 represents different zones of the a XAS spectrum. During the analysis the sample is generally illuminated starting at a lower energy than the edge. At lower energy, there is some absorption which could either arise due to other atomic species present in the sample or due to other electronic transition of the element of interest. This absorption at lower energy gives rise to flat background signal as presented in the inset in red. This zone is called the pre-edge. Presence of pre-edge peak is sometimes noted due to transitions to partially occupied valence levels, such as in the case of pre-edge peak of Cu^{2+} species due to $3d^9$ orbital.

When the energy of the beam reaches closer to the binding energy of the electron from the respective level, a jump in absorption energy is observed which is referred to the edge. Sometimes the edge appears as a sharp feature termed as “white line”. Depending on the atomic environment and coordination state, there is slight variation in the absorption energies. The probability of the transition determines the intensity of the edge. The analysis

of the electronic density of the final state is used to measure the probability of the transition.

Above the edge, several peaks or shoulder peaks can appear due to interaction of the ejected core electrons with neighboring species in the continuum. The ejected electrons have low kinetic energy and a large mean free path. Hence, due to their large mean free path they can interact with the neighboring atoms via multiple scattering and can probe roughly 10 to 20 Å. Thus, providing information on the geometry and structure around the absorbing atoms.

At even higher incident beam energy, the photoelectrons have higher kinetic energy thus shorter mean free path. The probing distance of the neighboring atoms is up to 5 Å. The electron-wave can be scattered by the electronic potential of the neighboring atoms. The backscattering and the forwards scattering result in an interference pattern, as modulation of the measured absorption coefficient. The phase and amplitude of the backscattered wave are determined by the backscattering atomic species and the distance between the backscattering atom and the central atom.

B.1.1 X-ray absorption Near Edge Spectroscopy (XANES)

XANES or NEXAFS signature is dominated by core transition to quasi bound states (multiple scattering resonance). The XANES part of the spectrum provides information on the electronic structure, local geometry, and symmetry of the absorbing atom [12]. The interpretation of the XANES data is generally carried out by correlating the absorption features to known reference compounds.

B.1.2 Extended X-ray Absorption Fine Structure (EXAFS)

The EXAFS region of the spectrum provides information on the closest neighbors, quantification of their numbers and the distance from the absorbing atoms, by fitting the data with a structural model. As mentioned above, as the ejected photoelectron wave interacts with the neighboring atoms, the interaction generates scattering waves. This interference between the scattered and the emitted waves depends on the incident beam which determines the kinetic energy of the photoelectron. The EXAFS region is termed at $\chi(k)$, where k is the wavenumber of the photoelectron. The wavenumber k is expressed by

equation 1, where *m* is the mass of an electron, $\hbar$ is the reduced Planck's constant, *E* is the energy of the incided X-ray beam, and E_0 is the ionisation energy.

$$k = \frac{2\pi}{\lambda} = \sqrt{\frac{2\,m\,(E-E_0)}{\hbar^2}} \qquad \text{Eq. A.2}$$

The χ(*k*) can be expressed as the difference between the measured absorption coefficient and the atomic absorption, given by equation 2.

$$\chi\,(k) = \frac{\mu\,(E) - \mu_0(E)}{\mu_0(E)} \qquad \text{Eq. A.3}$$

This function can be expressed by a sum of damped sinusoid functions representing possible scattering events for each neighboring atom *j*, given in equation 3. Few approximations are assumed in this equation: 1) only one electron is considered, 2) the incident beam is assumed to be a plane close to the neighboring atoms, 3) only single scattering events are taken into account, 4) harmonic approximation where the disorder is assumed to be small and the bond-length distribution can be assumed to be a Gaussian function, and 5) a spherical symmetry is assumed for the eletronic potential of the absorbing atom.

$$\chi\,(k) = S_0^2 \sum_j N_j \frac{f_i(k)}{k\,R_j^2}\, e^{\frac{-2R_j}{\lambda\,(k)}}\, e^{-2\,k^2\sigma_j^2} \sin(2kR_j + \delta_j(k)) \qquad \text{Eq. A.4}$$

Where,

- S_0^2 is the amplitude reduction term, which expresses the relaxation of all the other electrons in the absorbing atom to the hole of the core level.

N_j is the number of atoms in the *j* sphere of the coordination.

- $F_j(k)$ is the scattering amplitude of the photoelectron, and $\delta_j(k)$ is the corresponding scattering phase shift.
- $e^{-2\,k^2\sigma_j^2}$ introduces the Debye-Waller factor (σ_j^2), which expresses the thermal and the structural disorder in the sample.
- $e^{\frac{-2R_j}{\lambda\,(k)}}$ is the damping factor accounting for the elastic loses associated to the mean free path of the photoelectron.
- R_j is the average distance between the absorbing atom and the jth coordination sphere.

In our data treatment, the EXAFS region of the spectrum was not treated due to presence of a multiple phases as well as lack of reference samples at high temperature which would significantly affect the $e^{-2\,k^2\sigma_j^2}$ term of the equation. Therefore, only the XANES part of the spectrum was considered.

B.2 OPERATION OF TEM

As illustrated in Figure 3, the column of a transmission electron microscope consists of three main stages, namely the illumination stage, the optical system, and the specimen imaging stage. In the illumination stage, the electrons are produced in the electron gun either by thermionic effect either by heating a tungsten filament (high melting point material) or LaB_6 (lower electron extraction energy compared to tungsten), or by field effect (FEG, field emission source) by applying an intense electric field (~ 1010 V/m) to an ultrafine tip of tungsten. The emitted electrons are accelerated by applying a voltage (usually 200 keV) and guided by the condenser lenses (electromagnetic lenses) to the sample. Condenser lenses also control the spatial distribution and the intensity of the beam. As the electron beam reaches the sample, it interacts with the specimen generating a wide variety of signals. Furthermore, at the specimen level there is the objective lens responsible for enlarged image of the sample. In addition to that, at the lower level of the microscope column, intermediate lenses allow to enlarge the image even further and the projector lenses project the image of the sample on the fluorescent observation screen or on the detector of a CCD camera.

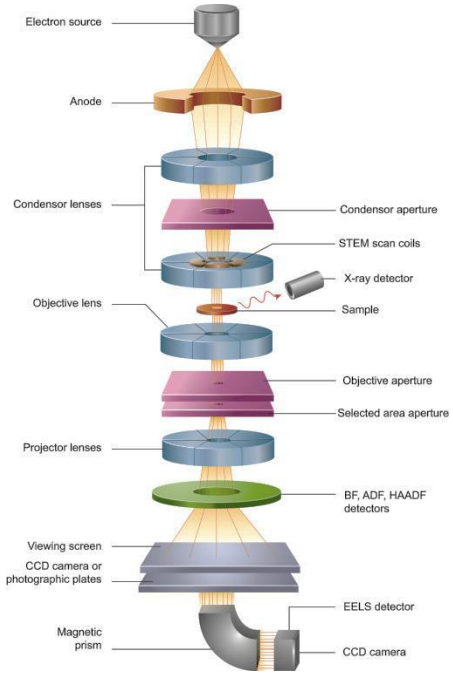

Figure 3: Schematic representation of a Transmission Electron Microscopy (TEM) with the main components.

B.3 ABERRATION CORRECTORS

The optical quality of the objective lens and the energy distribution of the electron beam are the main determining factors for high resolution atomic scale imaging. Indeed, lenses imperfections of an electron microscope result from spherical and chromatic aberrations, as detailed *Figure 4*. Spherical aberrations result in multiple focal points and blurred image. On the other hand, the chromatic aberrations occur due to the energy spread of the electrons from the source resulting in focusing electrons with different energies at different points. Notably, the most important features in current generation microscopes are the use of correctors for spherical and chromatic aberrations.

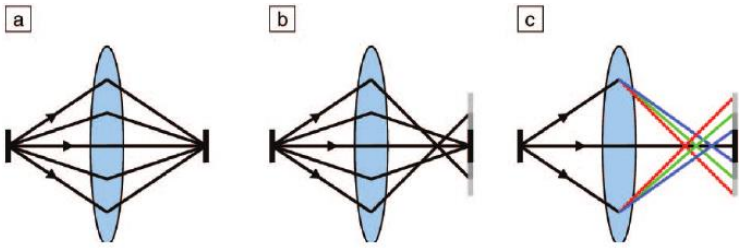

Figure 4: Representation of a perfect lens (a) that focuses a point source to a single image point, (b) lens with spherical aberrations caused by overfocus of rays a higher angles, and (c) lens with chromatic aberrations caused by different energies being focused differently [13].

B.4 IN SITU ELECTRON MICROSCOPY

Two different technologies are currently available for in-situ TEM observation, 1) open-cell configuration with differential pumping, and 2) sealed gas/liquid configuration.

The open-cell configuration uses differential pumping in different stages of the microscope column to allow large pressure difference within the specimen area and the electron source (Figure 5). The specimen area can reach a pressure within 10^{-3} – 2000 Pa range, while maintaining ultra-high vacuum at the level of electron gun and camera chambers. Thus, the introduction of gaseous environment for dynamic observation could be achieved without hindering the vacuum sensitive part of the microscope and imaging conditions.

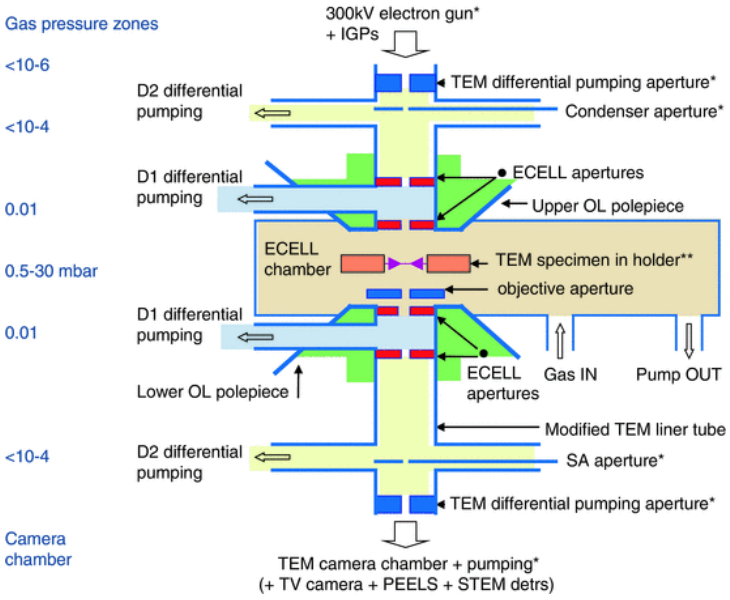

Figure 5: Schematic representation of differential pumping environmental TEM (ETEM) [14].

For the second type of configuration, no modifications in the microscope column is required. The specimen is enclosed by two membrane windows that are transparent to the electron beams. These membranes are made up of amorphous silicon nitride (SiN_x) and they are typically termed as e-chip or e-cell. These MEMS or (MicroElectroMechanical Systems) based technology comes with electrical contacts that heat a ceramic membrane, which is in direct contact with the SiN_X membrane thus allowing the heating of the sample. A dedicated sample holder is used where a range of gas/liquid can be introduced and the sample can be

heated under atmospheric pressure. A range of commercial e-cells are available from companies such as Protochips or DENS Solution (Figure 6).

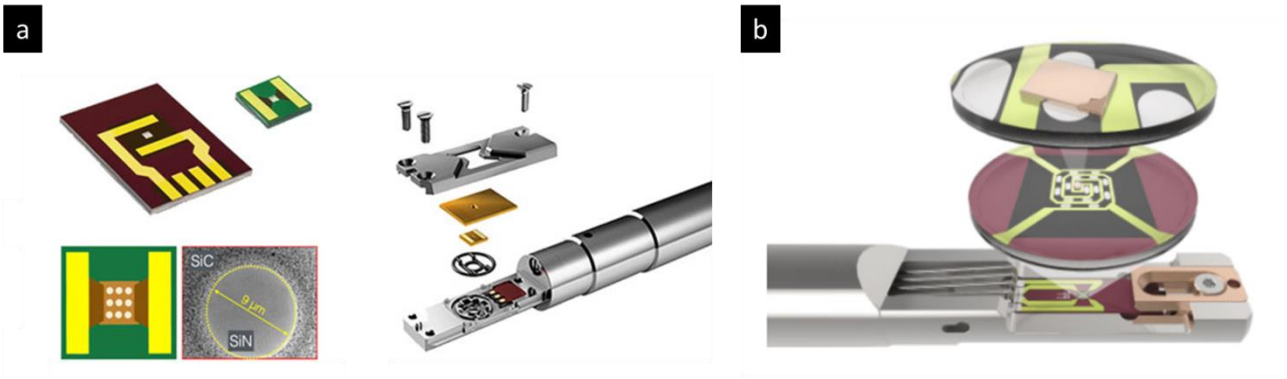

Figure 6: Commercial MEMS based e-cell and the corresponding heating holders for in-situ STEM gas experiments a. from Protochips [9] b. from DENS solution [15].

C. XRD

C.1 DIFFRACTOGRAM OF $CuAl_2O_4$

Figure 7 displays the diffractogram of stoichiometric copper-aluminate used as a reference sample for the STXM-XANES (chapter 3) and XAS (chapter 4) characterisations. XRD displays a major $CuAl_2O_4$ with a very small impurity of CuO and $CuAlO_2$ phases.

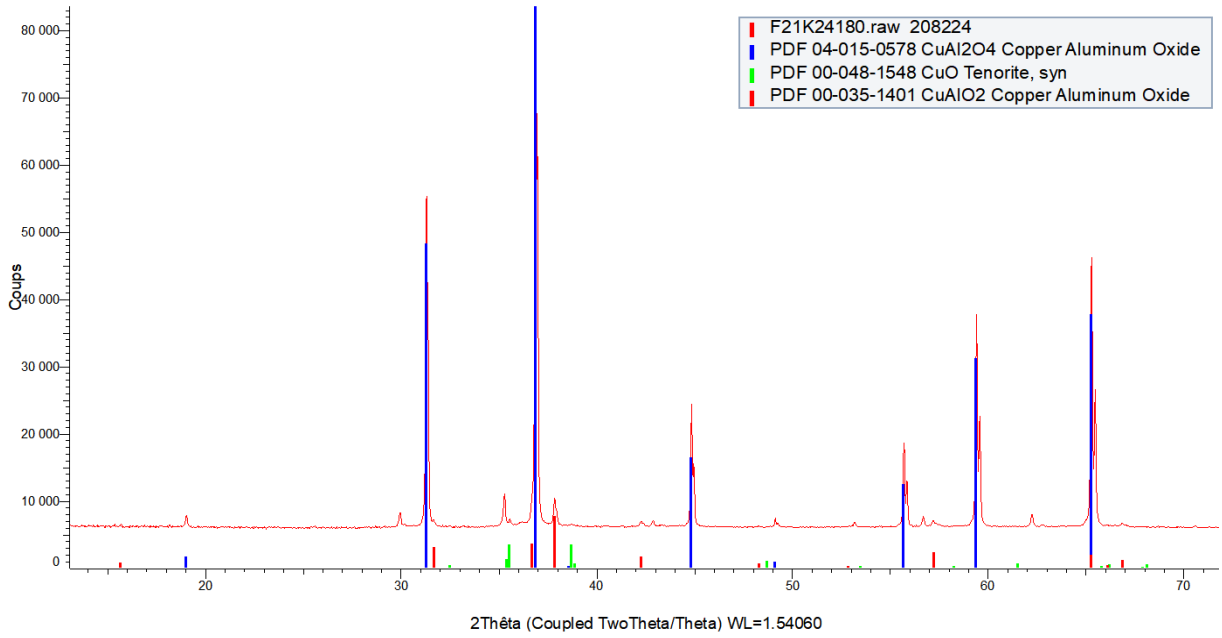

Figure 7: XRD of reference Copper-aluminate, containing copper aluminate (blue), $CuAlO_2$, (red), and CuO (green).

C.2 DIFFRACTOGRAM OF 28WT% CUO/AL_2O_3

Figure 8, displays the XRD data containing copper-aluminate, transition alumina, α-Al_2O_3 and CuO. The synthesis protocol of the material is provided in chapter 2. This material was used to carry out redox cycling reactions in STEM provided in chapter 5.

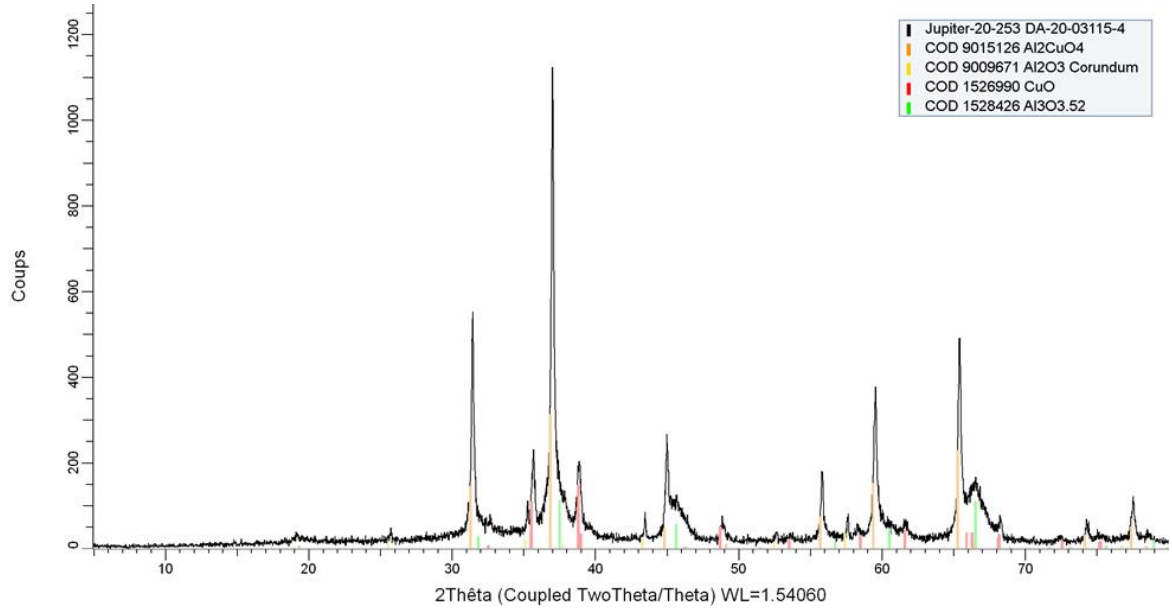

Figure 8: XRD of sample 28wt%CuO/Al_2O_3 , containing copper aluminate (orange line), α-Al_2O_3 (yellow), CuO (red), transition Al_2O_3 (green).

D. SEM

D.1 POST-MORTEM SEM IMAGE OF THE SAMPLES AFTER CYCLED IN TGA

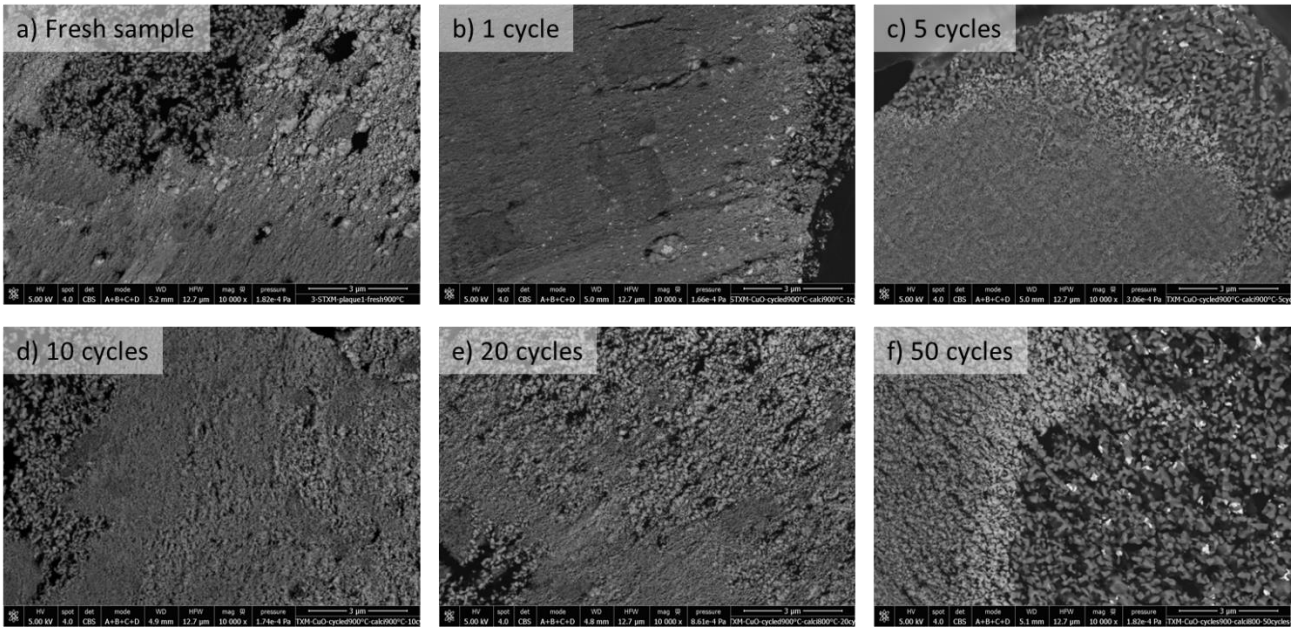

Figure 9: SEM image of samples in fresh condition (a) and after redox reactions at 900 °C, carried out in TGA after b) 1 cycle, c) 5, c) 10, d) 20 and e) 50 cycles.

D.2 POST-MORTEM SEM IMAGES OF THE 13WT%CUO/AL_2O_3 AFTER THE *IN SITU* XAS EXPERIMENT

Figure 10 to Figure 13 presents the SEM images of the four samples collected from the reactor, after the *in situ* XAS experiments (chapter 4). These samples were imaged at lower magnification to achieve a statistical overview of the morphological/copper phase distribution changes in the sample grains.

$H_2 - O_2$

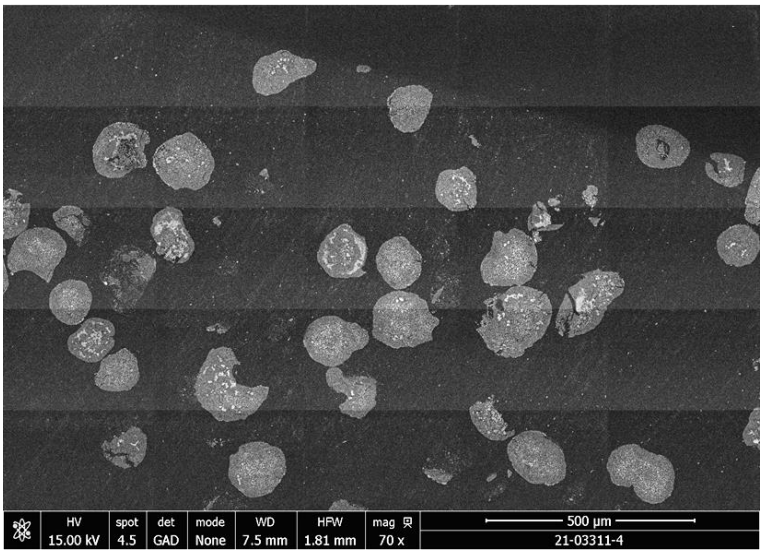

Figure 10: SEM image of H_2-O_2 sample.

$CO - O_2$

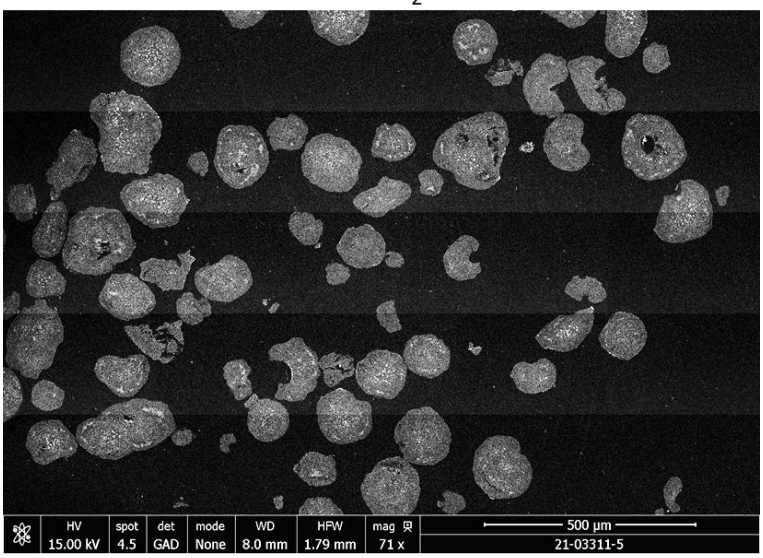

Figure 11: SEM image of CO-O_2 sample.

$CH_4 - O_2$

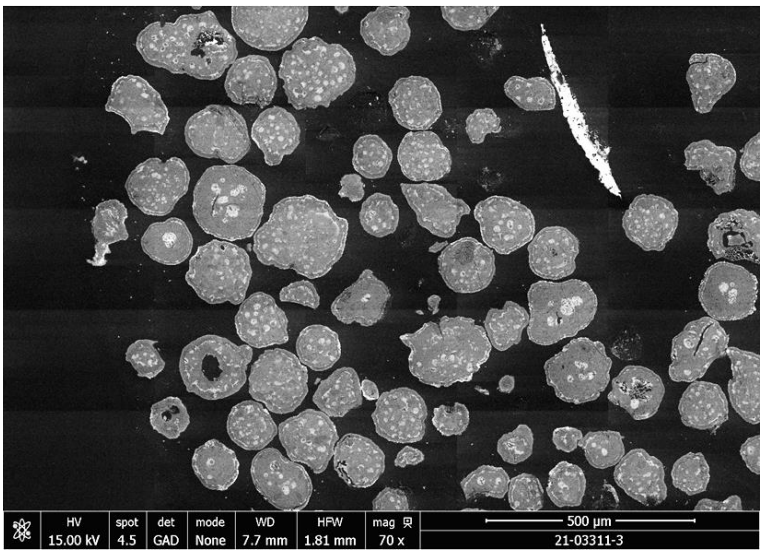

Figure 12:SEM image of CH_4-O_2 sample.

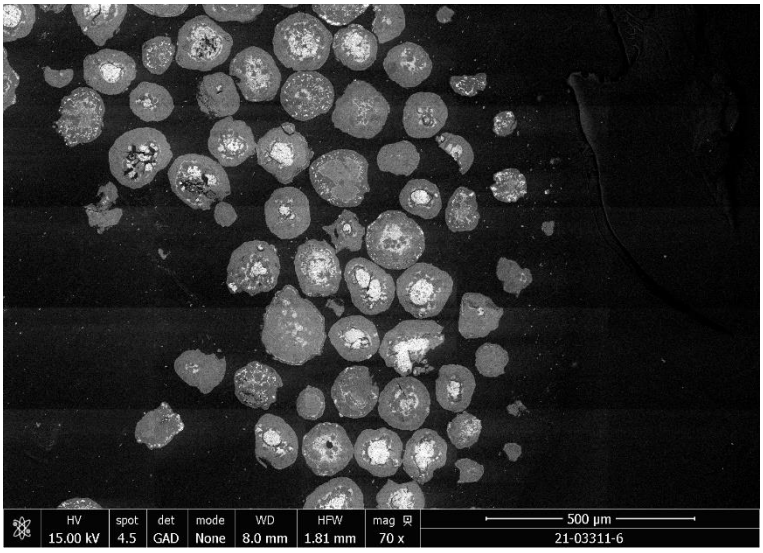

Figure 13: SEM image of H_2-air sample.

E. STEM IMAGE

Figure 14: displays the dynamic shape and phase change of copper-based particles during *in situ* STEM redox reaction at 300 °C. At the start of the experiment, the particle pointed out by yellow square is composed of CuO (from the HAADF contrast). After the introduction of the H_2 at 300 °C the particle undergoes fragmentation. In the re-oxidation step, the fragmented particles tend to oxidise to form hollow nanoparticles.

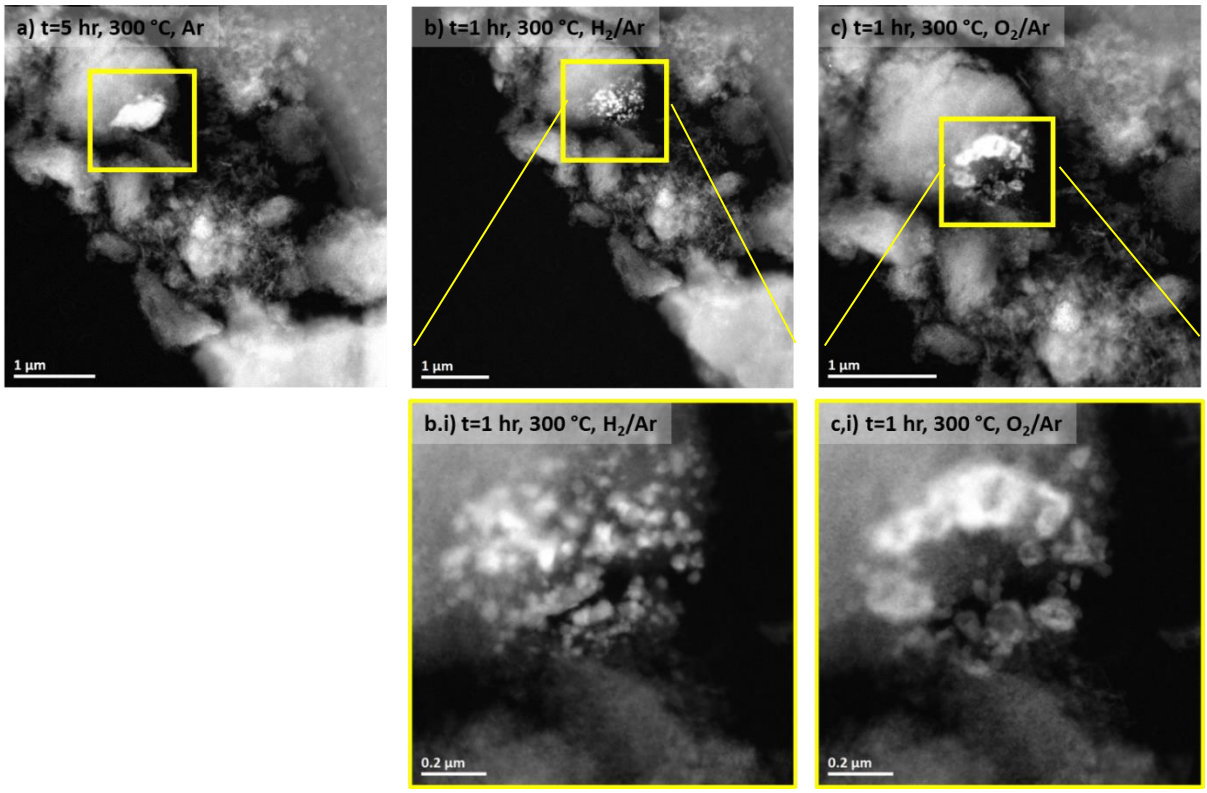

Figure 14:STEM-HAADF images of the same area of observation during redox reaction at 300 °C under a) Ar, b) H_2 and c) O_2.

F. *IN SITU* XAS

F.1 EVOLUTION OF THE METALLIC COPPER SPECIES

Figure 15 and Figure 16 presents the relative spectral percentage of the two metallic copper species identified during the *in situ* XAS run (chapter 4). Figure 15, displays the information for the samples cycled under 2.5 vol% O_2 and 3 different reduction atmospheres: H_2, CO and CH_4.

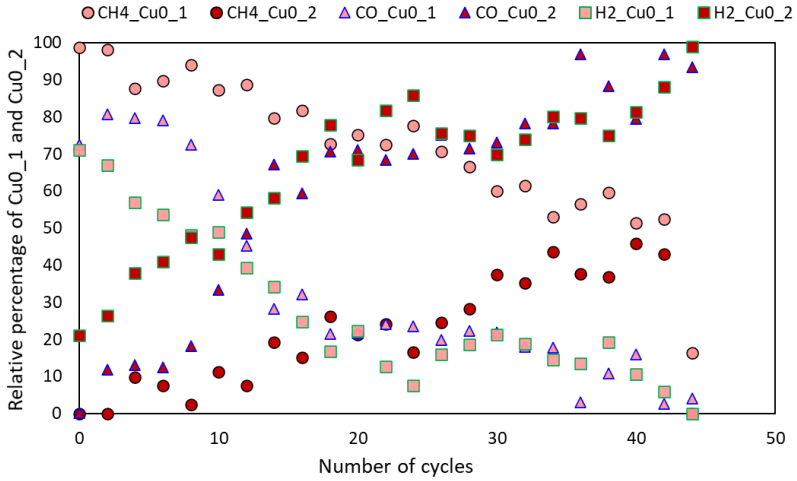

Figure 15: Relative percentage of Cu^0_1 and Cu^0_2 species from the H_2-O_2, CO-O_2 and CH_4-O_2 datasets.

Figure 16, displays the changes in the metallic copper components in the samples cycled under 2.5 vol% and 21 vol% O_2 and H_2.

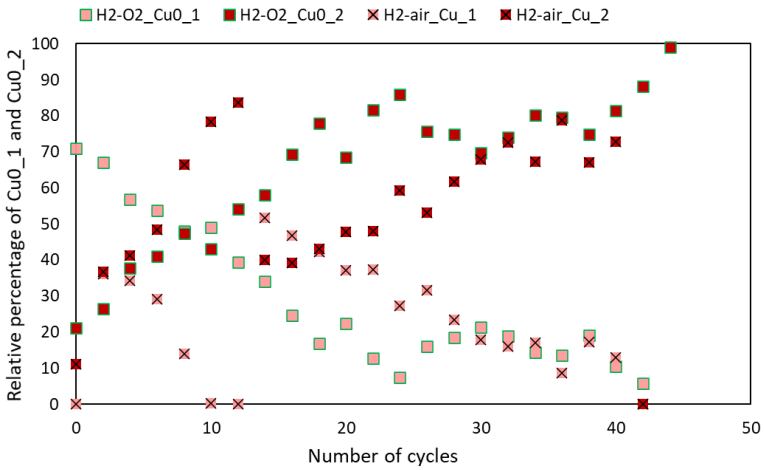

Figure 16: Relative percentages of Cu^0_1 and Cu^0_2 species from the H_2-O_2 and H_2-air datasets.

F.2 OVERALL CONCENTRATION PROFILE DURING THE *IN SITU* CYCLING

Figure 17- Figure 20 presents the overall evolution of the relative percentage of the copper species during reduction and oxidation reactions, at every 5 cycles. These four samples were cycled during *in situ* XAS experiments. The results are provided in chapter 4, separately for the reduction and oxidation.

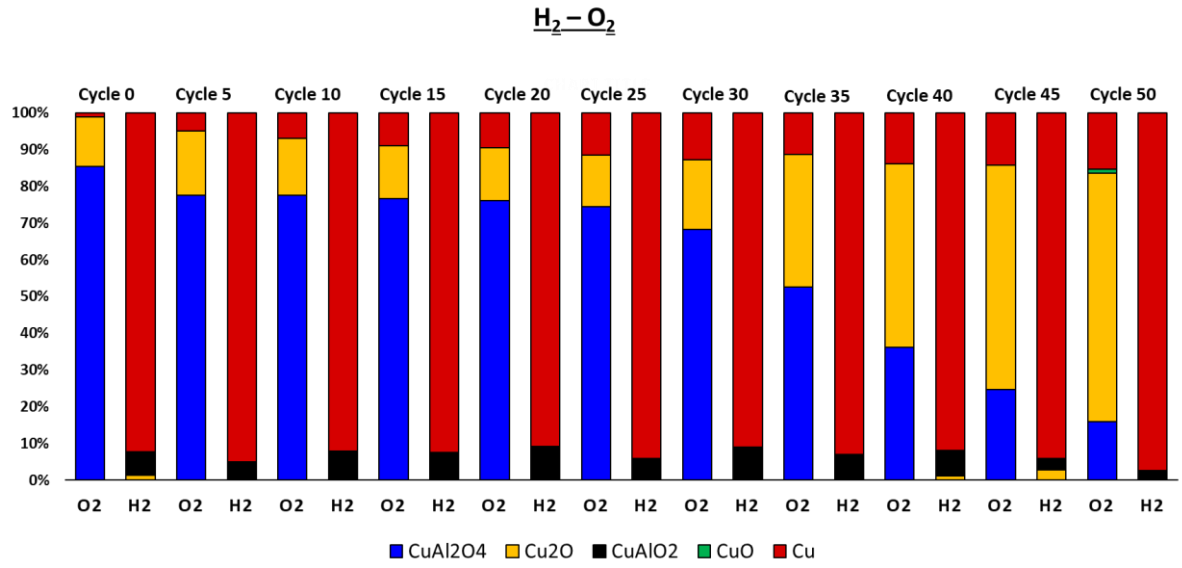

Figure 17: The relative contributions of the copper phases at the of the oxidation and reduction at every 5 cycles, of the H_2-O_2 dataset.

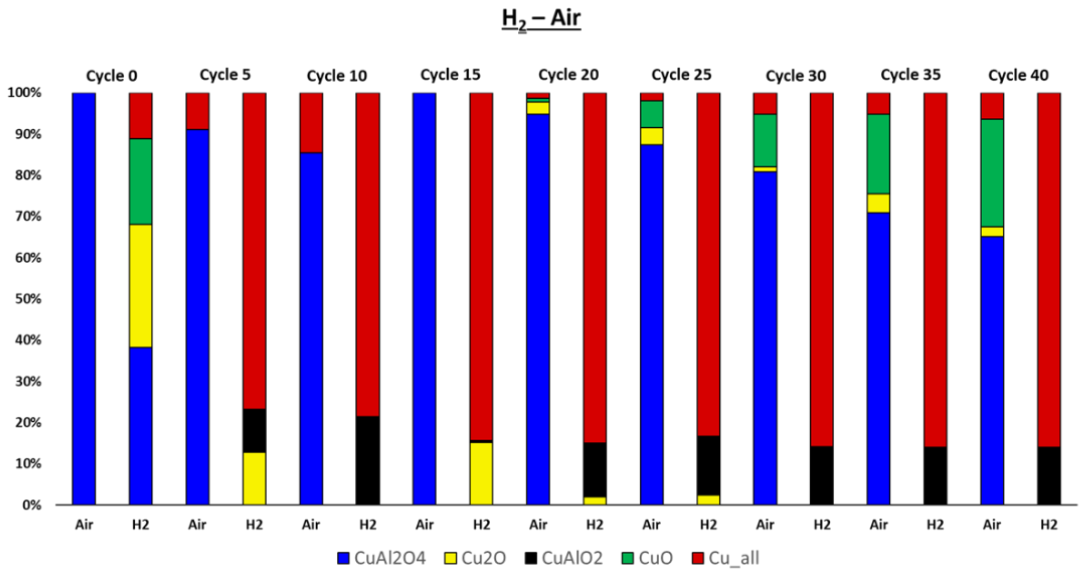

Figure 18: The relative contributions of the copper phases at the of the oxidation and reduction at every 5 cycles, of the H_2-air dataset

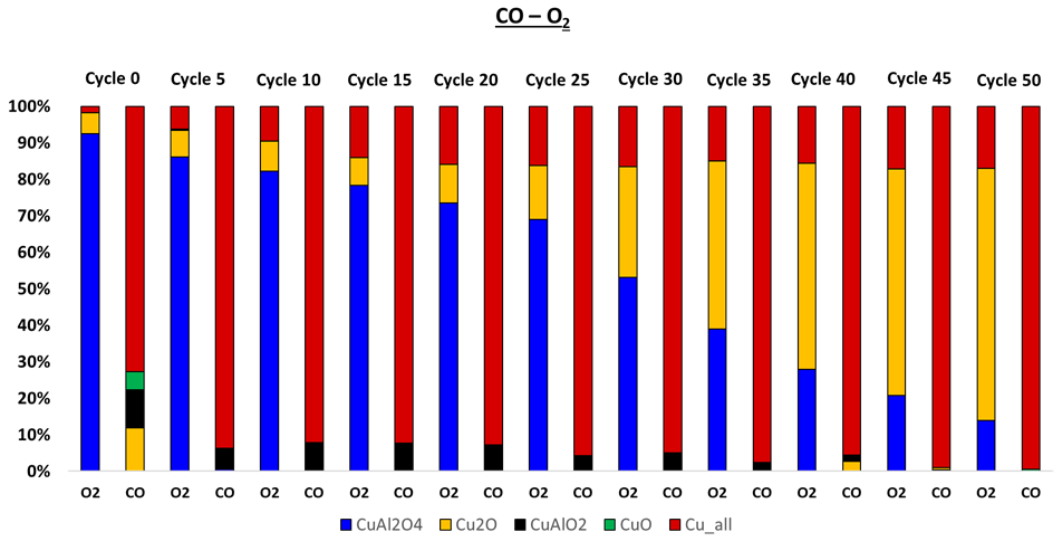

Figure 19: The relative contributions of the copper phases at the of the oxidation and reduction at every 5 cycles, of the CO-O_2 (top) and CH_4-O_2 (bottom) datasets.

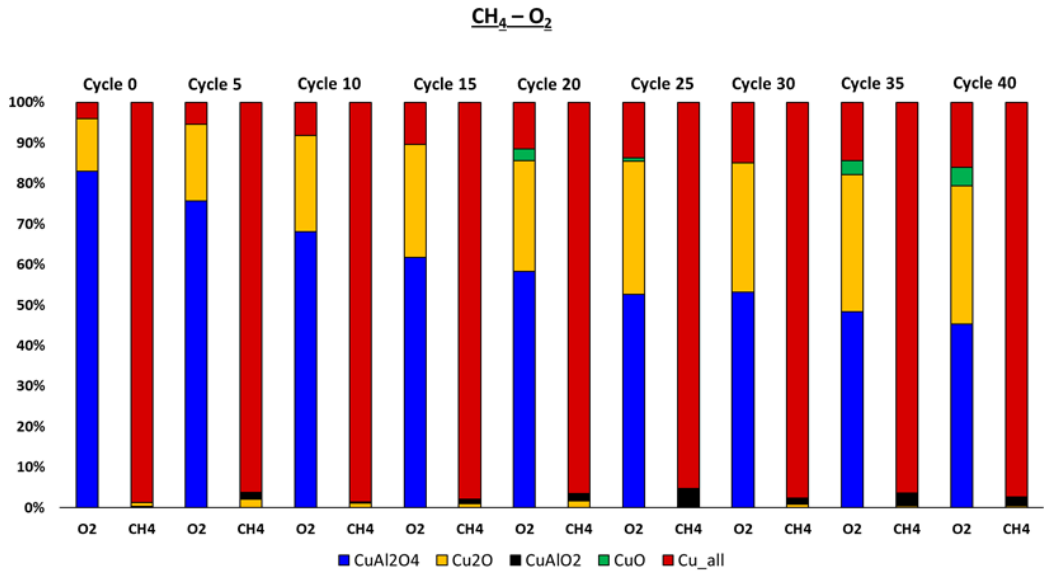

Figure 20: The relative contributions of the copper phases at the of the oxidation and reduction at every 5 cycles, of the CO-O_2 (top) and CH_4-O_2 (bottom) datasets.

G. SUPPLEMENTARY INFORMATION

This section provides the supplementary information of the published article presented in chapter 5, section 4.1.

G.1 NANOPARTICLE SYNTHESIS

G.1.1 Sputtered nanoparticles:

Three sputtering experiments were conducted varying the initial NP formation steps (presented in Table S). The thickness of the film in the 1st experiment was 2 nm while in the 2nd and 3rd experiment 1 nm films were used. For all three experiments, the samples were heated from room temperature to 150 °C at 5 °C/min and kept for 2 hours. However, no particles were formed at this temperature, and the system had to be heated to 300 °C. For experiments 1 and 2, a slower heating rate of 5 °C/min was used in contrast to 5 °C/sec for the 3rd experiment.

Table S1: Experimental parameters used for the formation of sputtered nanoparticles.

Samples	Film thickness	Gas atmosphere	Heating rate	Final Temperature	Duration	NP average size and density
Sputt-1	2 nm	0.5 bar H_2	5 °C/min	300 °C	2 hours	4 ± 2 (<10 nm) 35 ± 7 (>10 nm) 675 NP/µm²
Sputt-2	1 nm	0.5 bar H_2	5 °C/min	300 °C	2 hours	4 ± 1 (<10 nm) 21 ± 6 (>10 nm) 1015 NP/µm²
Sputt-3	1 nm	0.5 bar H_2	5 °C/s	300 °C	2 hours	9 ± 4 nm 3730 NP/µm²

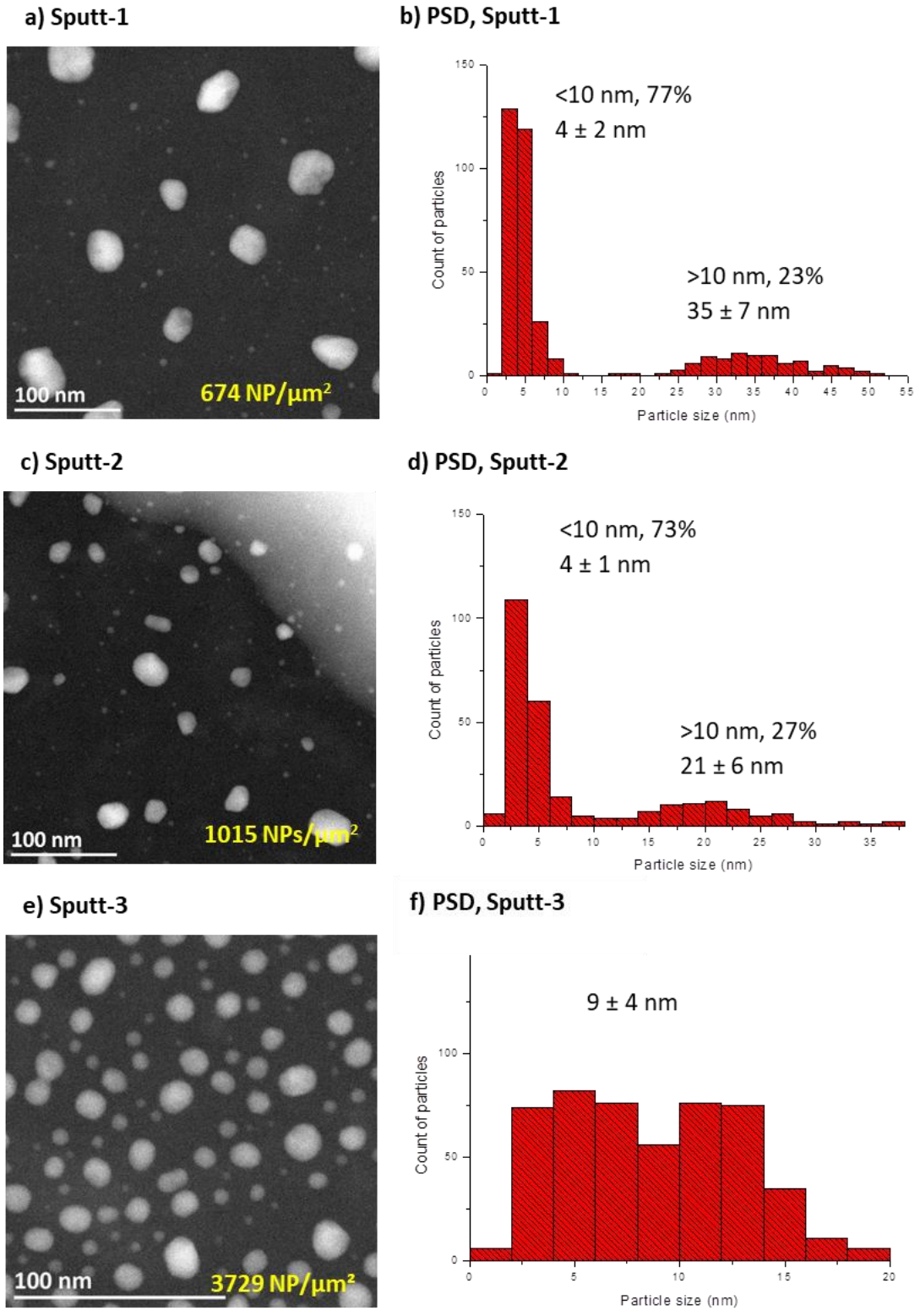

Figure S1: (a-c) Formation of Cu nanoparticles at different experimental conditions. (a) Sputt-1 (c) Sputt-2 (d) Sputt- 3 and their corresponding particle size distribution in (d, e and f).

G.2 CHEMICALLY SYNTHESIZED NANOPARTICLES:

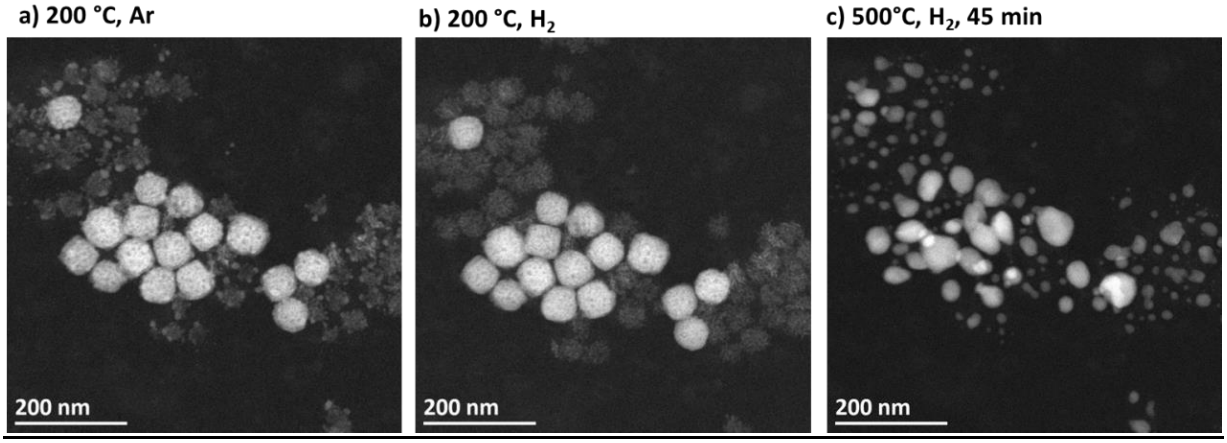

Figure S2: Heat treatment of sample: Syn-1: a) at 200 °C under Argon, b) at 200 °C under H_2 and c) at 500 °C after 42 min of gas flow.

Initially, the surface of the nanoparticles was passivated by organic ligands and large particles were rather composed of smaller nanoparticles, aggregated together. Upon heating at 500 °C, under H_2 for an hour the organic layer is removed and the initial porous structure is lost, forming compact nanoparticles of metallic copper.

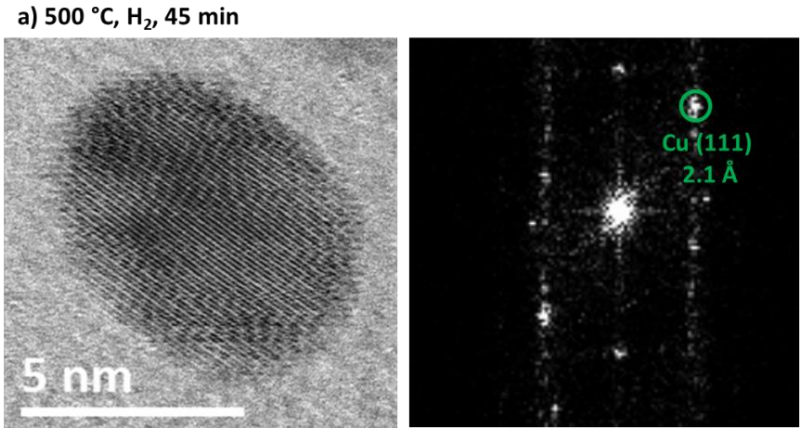

Figure S3: a) high resolution image (HR) of metallic copper after 45 min of heat treatment under H_2 at 500 °C and Fast Fourier Transform (FFT) of the HR image.

:

G.3 IN-SITU STEM ANALYSIS

G.3.1 Oxidation of metallic Copper

G.3.1.1 Phases present

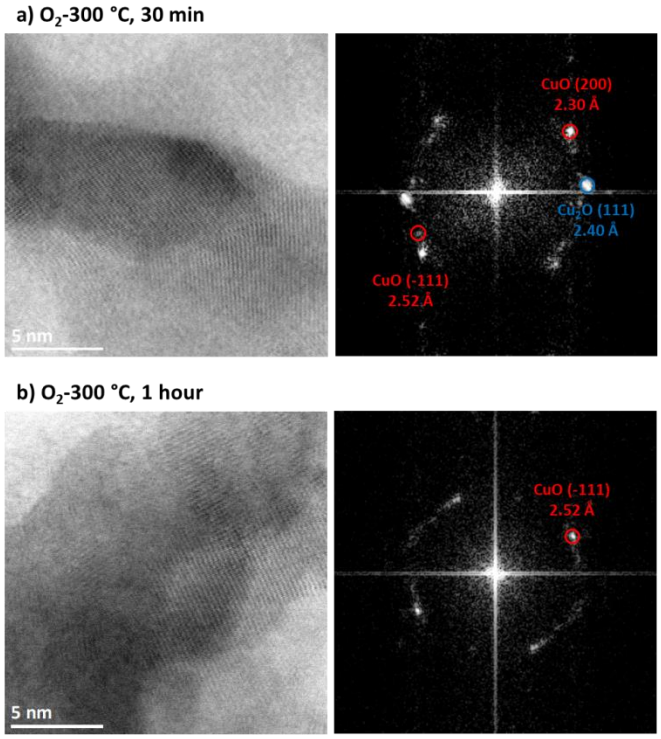

Figure S4: HR-STEM images of copper oxide during oxidation at 300 °C, a) after 30 min of oxygen flow and b) after 1 hour of gas flow (inset contains Fast Fourier Transformation (FFT) pattern of the HRSTEM image).

G.3.2 Kirkendall Void Formation

4Cu (s) + O_2 (g) → 2Cu_2O (s)

Calculations - Δg_{Cu_2O}

Δg_{Cu_2O} = – 339758 + 149.14T [48]

Diffusion Coefficient (cm²/s):

Using the reaction-diffusion model developed by Svoboda et al. the self-diffusion coefficients of Cu in Cu_2O is calculated to eventually determine the activation energy of diffusion and pre-exponential parameter to fit Arrhenius model for a temperature range of 323 – 773 K [47].

$$t = \frac{ARTR^2{}_0}{D_{Cu\ in\ Cu_2O}\left|\Delta g_{Cu_2O}\right|}$$

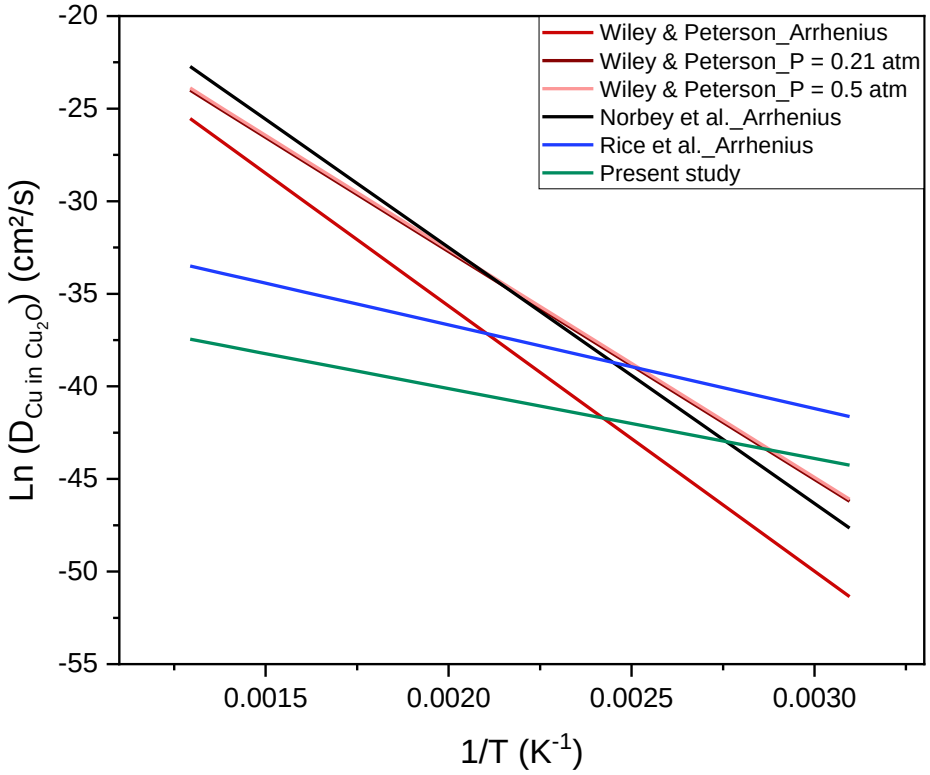

Figure S5: Comparison of self -diffusion coefficient of copper in Cu_2O in bulk sample by Wiley and Peterson [49] and Norby et al. [50] and in nanoparticles by Rice et al. [22] and the current study.

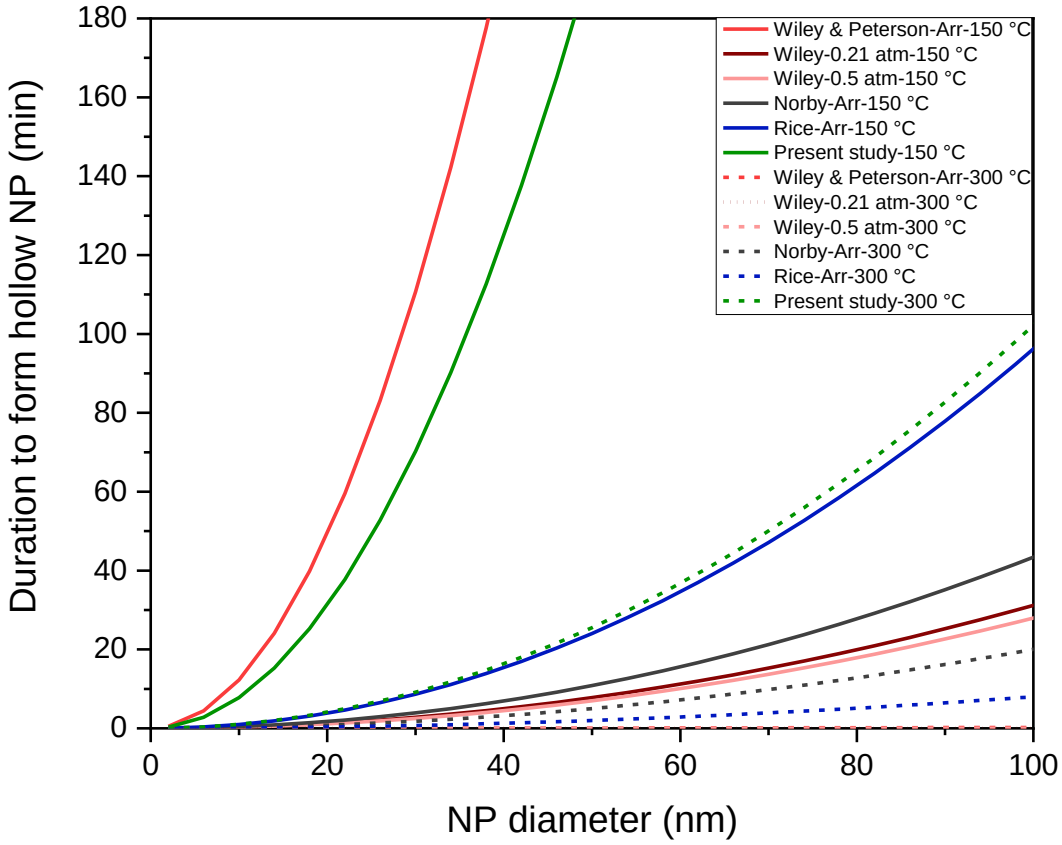

Figure S6: The duration of completion to form Kirkendall void as a function of nanoparticle diameter using the diffusion coefficients at a temperature of 150 °C and 300 °C.

G.3.3 Nanoparticle Size Distribution:

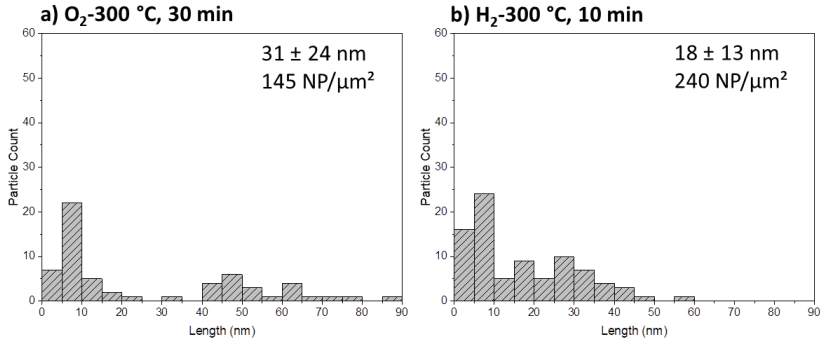

Figure S7: PSD for the NPs at 300 °C under a) O_2 after 30 min of oxidation and b) H_2 after 10 min. Sample: Sputt-1.

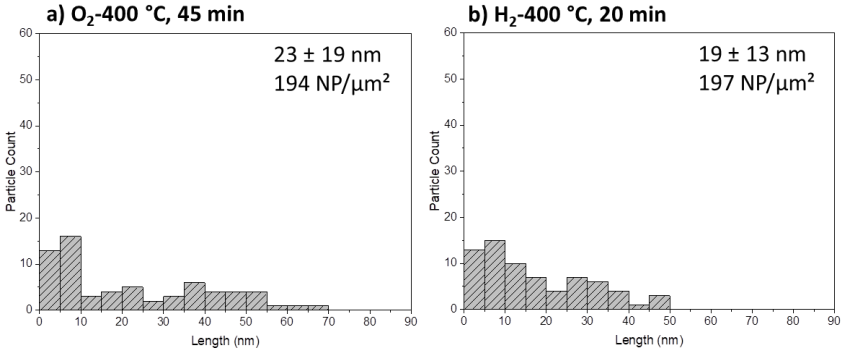

Figure S8: PSD of the nanoparticles at 400 °C, a) copper oxide NPs under oxygen after 45 min and b) under hydrogen after 20 min of gas flow. Sample: Sputt-1.

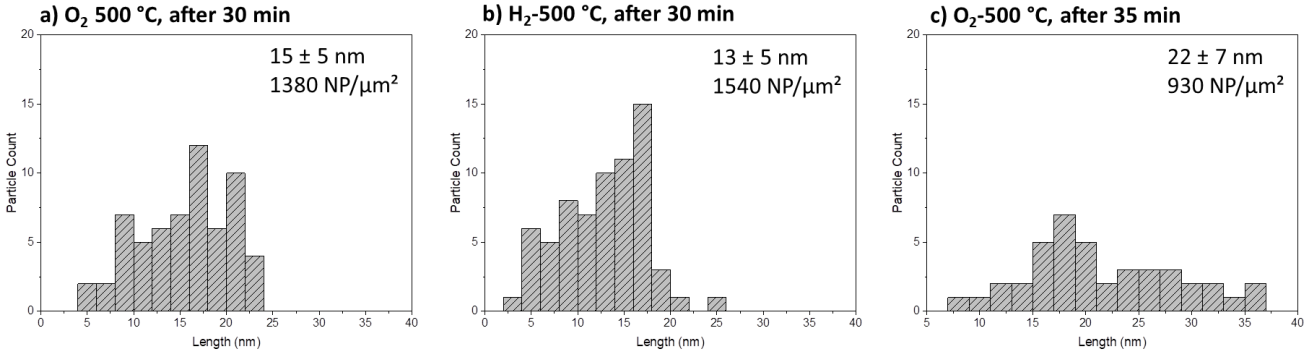

Figure S9: PSD of the NPs at 500 °C: a) under O_2 after 30 min of gas flow b) under H_2 after 30 min of gas flow and c) NPs after re-oxidation after 35 min of oxidation. The images are not from the same area of observation. Sample: Sputt-3.

G.3.4 Reduction of Copper Oxide Nanoparticles

G.3.4.1 Reduction of hollow NPs at 250 °C

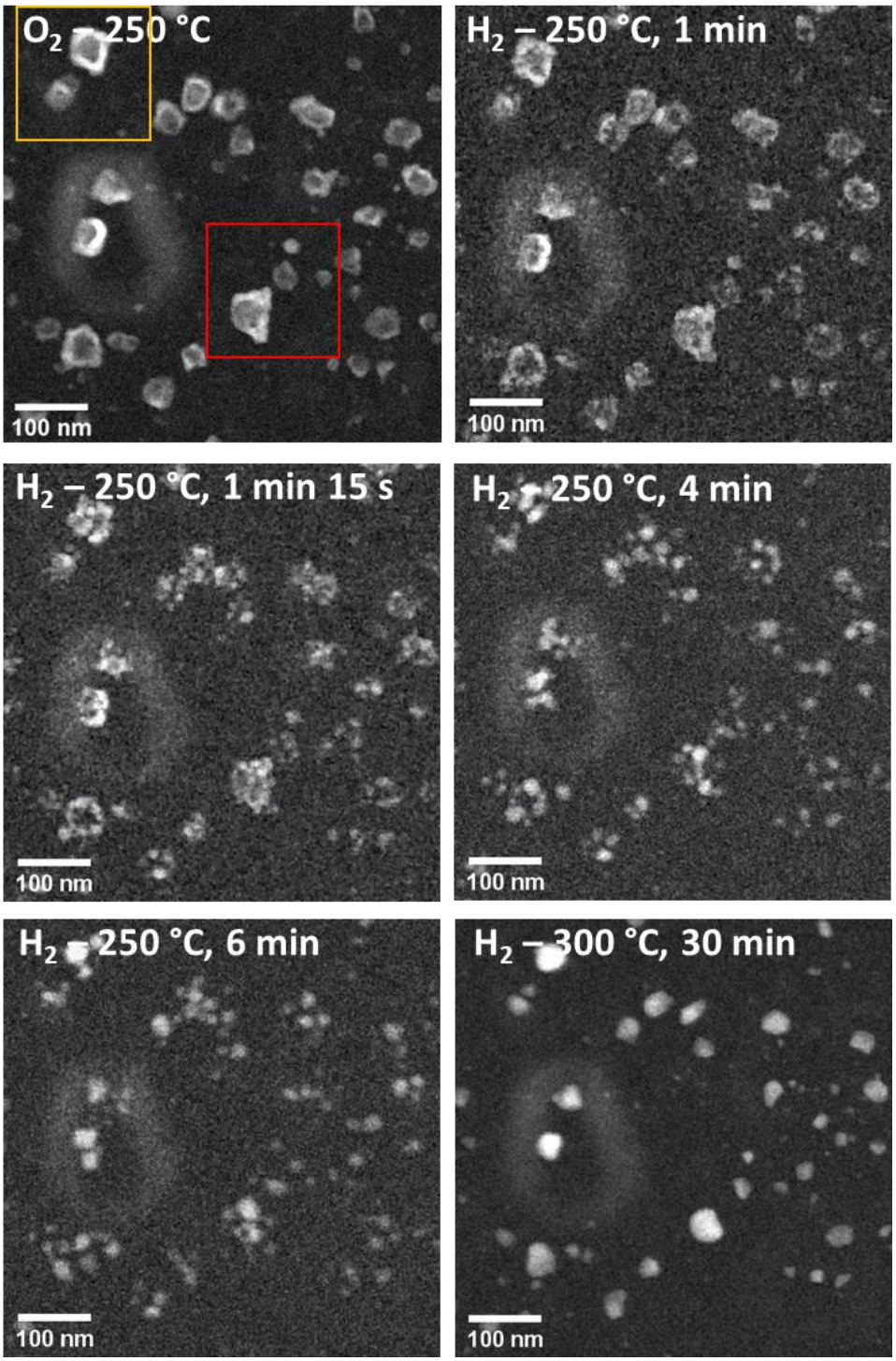

Figure S10: Reduction of hollow copper oxide nanoparticles under hydrogen at 250 °C up to 6 min and heated to 300 °C, after 30 min. Sample: Sputt-2.

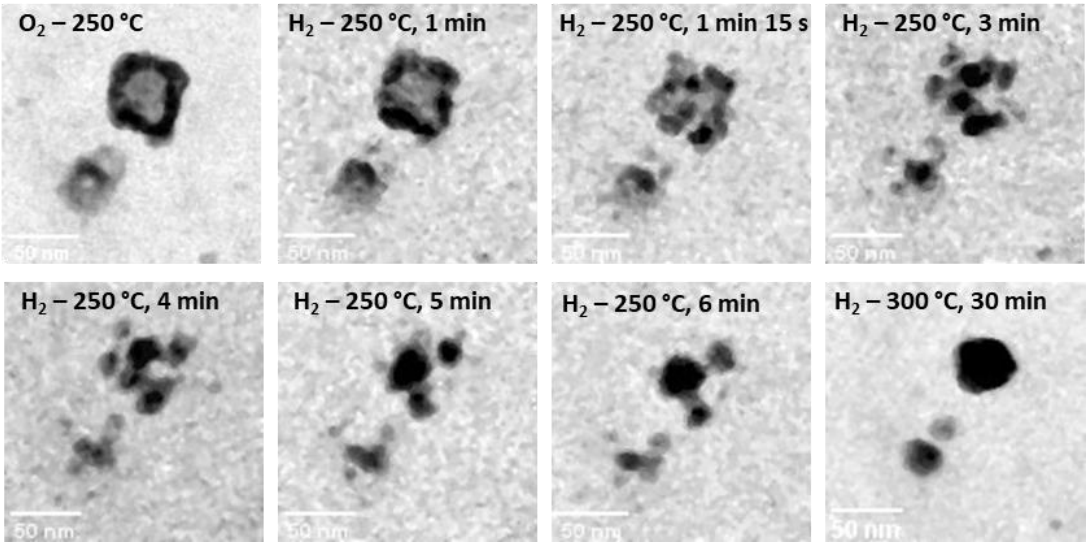

Figure S11: Reduction of hollow copper oxide nanoparticles under hydrogen at 250 °C up to 6 min and heated to 300 °C, after 30 min. Area marked by yellow square on Figure S9. Sample: Sputt-2.

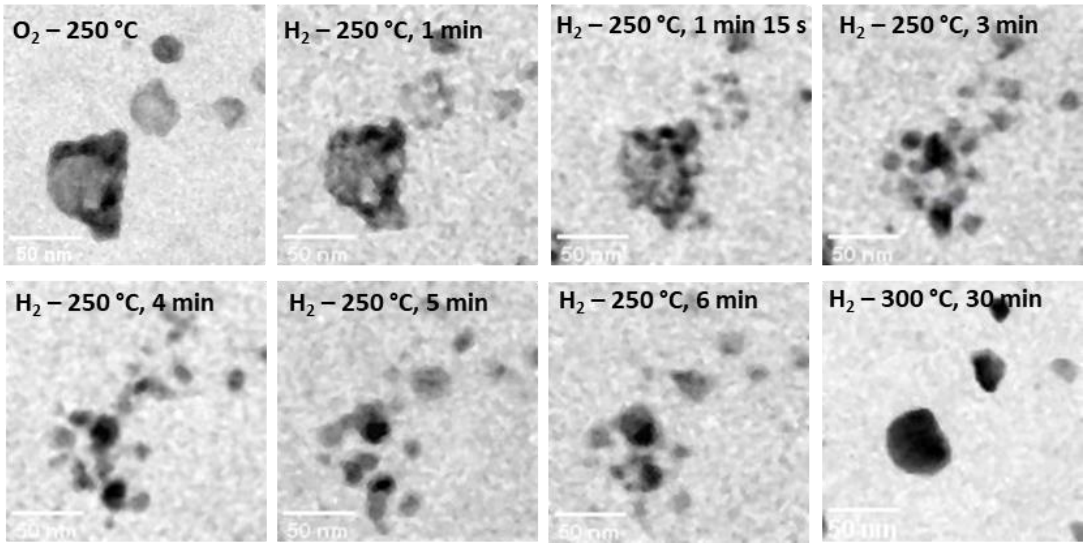

Figure S12: Reduction of hollow copper oxide nanoparticles under hydrogen at 250 °C up to 6 min and heated to 300 °C, after 30 min. Area marked by red square on Figure S9. Sample: Sputt-2.

G.3.4.2 Reduction of hollow and compact NPs at 400 °C

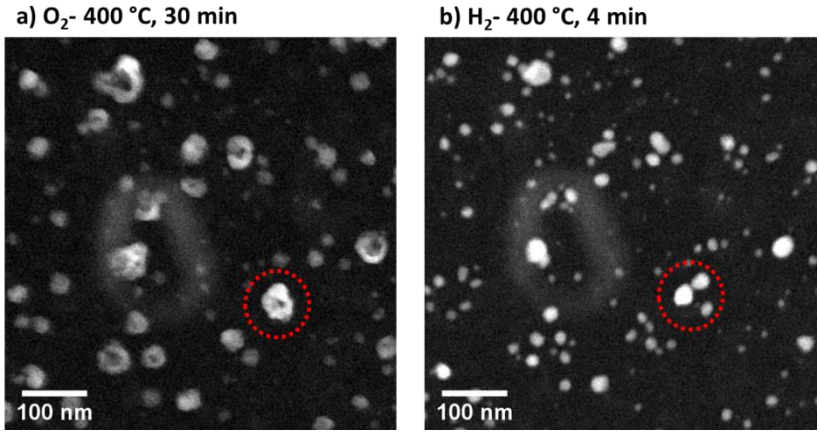

Figure S13: Reduction of Copper oxide nanoparticles at 400 °C, a) copper oxide NPs under oxygen after 30 min and b) under hydrogen after 4 min of gas flow. Sample: Sputt-2.

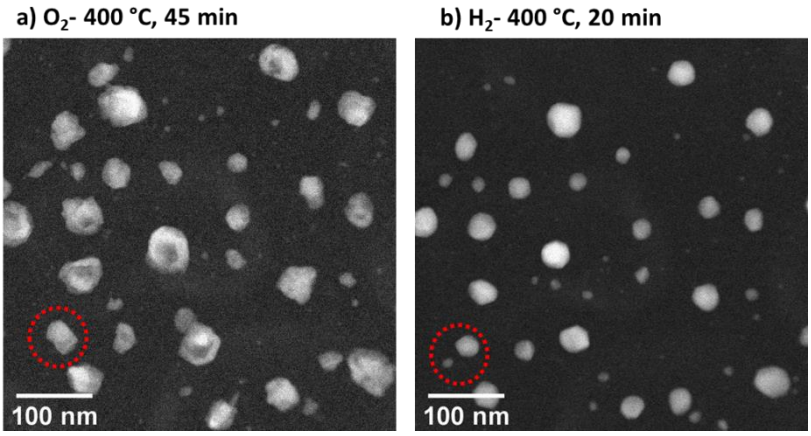

Figure S14: Reduction of Copper oxide nanoparticles at 400 °C, a) copper oxide NPs under oxygen after 45 min and b) under hydrogen after 20 min of gas flow. Sample: Sputt-1.

G.3.4.3 Reduction of compact NPs at 250 °C

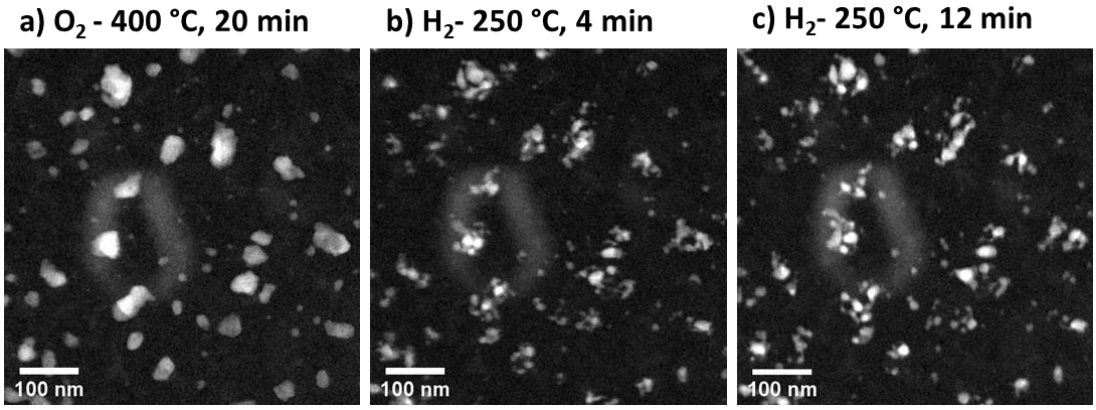

Figure S15: Reduction of Copper oxide nanoparticles at 250 °C, a) copper oxide NPs under oxygen after 20 min and under H_2 after 4 and 12 min of flow, respectively in b) and c). Sample: Sputt-2.

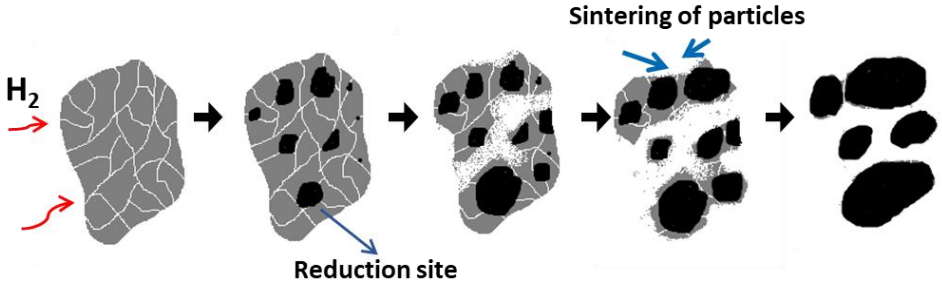

Figure S16: Schematic representation of Figure S15 illustrating the reduction of compact copper oxide nanoparticle which leads to the fragmentation into multiple nanoparticles of metallic copper.

G.3.5 Evaporation of the copper phase

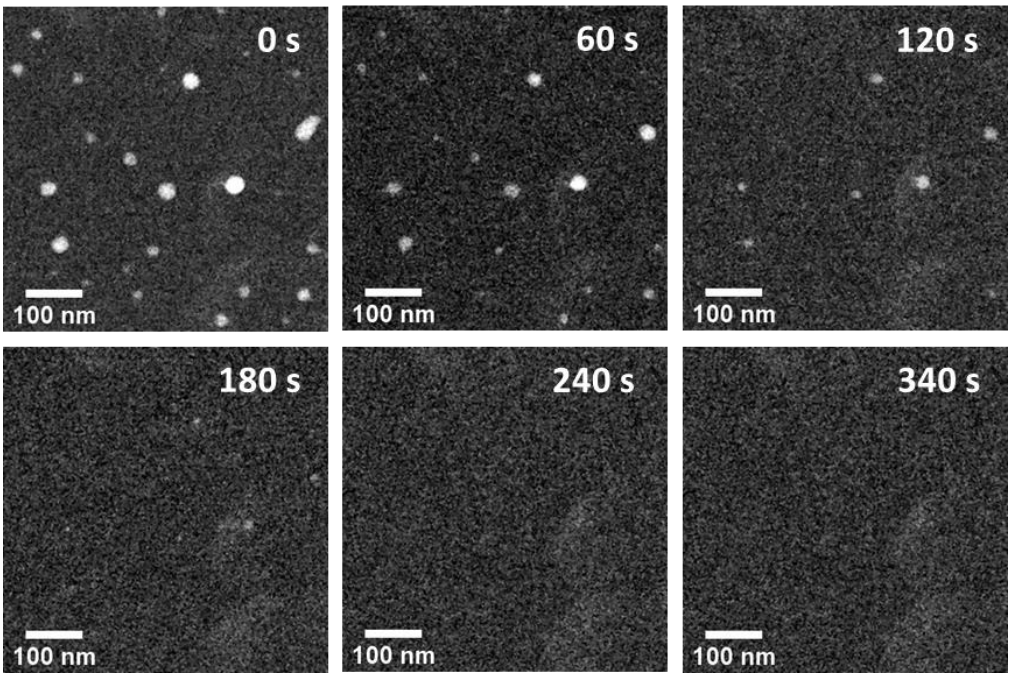

Figure S17: Evaporation of metallic copper NPs at 900 °C under H_2.

Résumé étendu en Français

L'augmentation du niveau de CO_2 dans l'atmosphère et le changement climatique qui en résulte sont une préoccupation mondiale. Malgré cela, l'utilisation de combustibles fossiles reste pour l'instant inévitable afin de maintenir la demande énergétique actuelle. Par conséquent, en association avec les solutions de stockage de CO_2, les procédés de combustion en boucle chimique (CLC) sont considérés comme une alternative à moyen terme pour la production d'énergie à partir de combustibles fossiles. Le principe de base de la réaction CLC est l'utilisation de matériaux transporteurs d'oxygène en substitution de l'air pour la combustion. Ces matériaux sont généralement composés d'oxydes métalliques tels que CuO, NiO and Fe_2O_3 supportés par des supports céramiques comme Al_2O_3 ou SiO_2. Le procédé démarre dans un « Réacteur à Combustible » dans lequel les matériaux sont réduits pour fournir de l'oxygène au combustible et assurer ainsi une combustion indirecte. Une large variété de combustibles peuvent-être utilisés à ce titre (gaz naturel, pétrole, charbon, biomasse etc.). Le produit de la combustion indirecte est constitué d'un mélange de CO_2 et d'eau facilement séparables par condensation. Après la combustion, les oxydes métalliques réduits sont envoyés dans un « Réacteur à Air » où ils sont regénérés par réaction d'oxydation avec l'air. Le matériau est soumis à plusieurs cycles d'oxydation-réduction à pression atmosphérique et à une température d'au moins 800°C. La durée de vie des matériaux est un critère important pour minimiser les coûts d'opération. Cependant, à cause des contraintes thermiques et chimiques qui apparaissent pendant les cycles redox, les matériaux ont tendance à subir des modifications morphologiques importantes amenant à une dégradation des propriétés mécaniques des matériaux ainsi que de leur réactivité. Le lien entre les paramètres de réaction comme la température, le nombre de cycles et l'évolution des paramètres microstructuraux et chimiques des matériaux n'est pas encore complètement compris dans la littérature. La plupart des études réalisés sur les transporteurs d'oxygène avec comme objectif l'amélioration de leurs performances et durée de vie souffrent d'un manque de compréhension phénoménologique de l'évolution des matériaux, particulièrement au niveau atomique ou nanométrique. Peu d'études réalisées à cette échelle sont disponibles dans la littérature, malgré leur intérêt, ce qui justifie encore plus la nécessité de développer des approches permettant d'analyser les propriétés

structurales et morphologiques des matériaux en fonction des conditions de réaction. Ceci est particulièrement vrai pour les matériaux à base de cuivre qui sont au cœur de cette thèse. Dans une étude récente, il a été proposé un mécanisme de transformation de ces systèmes basé sur les réactions entre le cuivre et l'alumine lors des phases d'oxydation et de réduction. L'échantillon initial est composé d'aluminate de cuivre ($CuAl_2O_4$) qui se transforme en particules de cuivre métallique et en alumine pendant la réaction de réduction. Les particules de cuivre ont tendance à grossir par frittage. Durant la réoxydation la reformation de $CuAl_2O_4$ est cinétiquement limitée à cause de la taille plus importante des particules métalliques. Par conséquent, en augmentant le nombre de cycles, une séparation de plus en plus prononcée entre l'oxyde de cuivre et l'alumine se produit, le cuivre migrant au sein des grains du support. Le matériau subit donc des transformations à la fois chimiques et physiques pendant les réactions. Néanmoins, les mécanismes aboutissant à ces changements restent à découvrir, ce qui justifie amplement l'objectif principal de cette thèse qui se propose de comprendre le comportement des oxydes de cuivre et de l'alumine des matériaux lors des cycles redox successifs en relation avec le(s) mécanisme(s) de migration de la phase cuivre.

Pour obtenir une vue d'ensemble, de l'échelle nanométrique jusqu'à l'échelle du grain, des phénomènes de migration des phases à base de cuivre lors des cycles redox, une approche multi- échelle et multi-technique a été utilisée via la mise en œuvre de méthodes suivantes : la microscopie électronique en transmission environnementale (MET *in situ*) utilisant une cellule fermée par des membranes de SiN_x, la microscopie électronique à balayage couplée à la spectroscopie de rayons X à dispersion d'énergie (MEB-EDS), la microscopie à rayons X en transmission couplée à la spectroscopie d'absorption des rayons X (STXM-XAS), la diffractométrie de rayons X (DRX) *in situ*, et la spectroscopie d'absorption des rayons X (XAS) *operando*. Les caractérisations à l'échelle micrométrique ont été utilisées pour comprendre la migration du cuivre dans un grain du support aluminique, sa mobilité et ses interactions, sans compromettre la distribution spatiale des phases chimiques. L'étude par XAS a fourni le pourcentage relatif des phases de chaque espèce. Pour mener à bien cette thèse et comprendre les caractérisations à différentes échelles, plusieurs types de systèmes ont été utilisés, en particulier des nanoparticules de cuivre supportées et non supportées.

Une première partie de l'étude a été consacrée à la compréhension des mécanismes d'oxydo-réduction de nanoparticules à base de cuivre non supportées. Les particules non supportées sont préparées par la pulvérisation magnétron (Cu-sputt) et par synthèse thermochimique (Cu-syn). Différentes évolutions morphologiques et les mécanismes associés ont été identifiées selon la température de réaction et la taille des nanoparticules. À basse température, sous atmosphère oxydante, une fine couche d'oxyde se forme autour des particules métalliques qui mène ensuite à la formation de particules d'oxyde creuses lors de l'augmentation de la température. Une augmentation supplémentaire de la température conduit à l'effondrement des nanoparticules creuses, puis à l'apparition d'un facettage. La réduction des nanoparticules aboutit à des processus successifs de fragmentation et de frittage. Nous avons montré que ces processus sont fortement dépendants de la température de réaction. A faible température (<350°C), la fragmentation, et par conséquent, l'apparition de nanoparticules fragmentées (plus petites) est observée. A température plus élevée (supérieure à 350-400 °C), la fragmentation est suivie immédiatement par le frittage, formant par conséquent des particules plus grosses. Par ailleurs, selon la température et la nature de l'atmosphère, différents mécanismes de frittage sont activés. Les phénomènes sous-jacents concernant ces différents changements morphologiques et les mécanismes de croissance mis en évidence sont gouvernés par la minimisation de l'énergie du système global.

Les matériaux supportés sont préparés par imprégnation de poudres commerciales de γ-Al_2O_3 (50 – 150 µm) avec une solution de nitrate de cuivre pour atteindre une concentration de 10 %mass Cu dans le matériau final, nommé CuO/Al_2O_3. Les matériaux sont calcinés à 900°C. La caractérisation initiale des échantillons supportés a montré la présence de cuivre sous la forme de d'alumine de cuivre non-stoechiométrique.

Le CuO supporté a été étudié par microscopie électronique environnementale dans des conditions expérimentales identiques au cas des nanoparticules non supportées. En partant d'une température de 300°C, l'alumine de cuivre non stoechiométrique est réduite pour former des nanoparticules de cuivre métallique à la surface du support d'alumine. En continuant l'oxydo-réduction jusqu'à 700°C, le matériau suit un comportement similaire aux nanoparticules non supportées. Cependant, au-dessus de 700°C la migration de la phase contenant le cuivre devient significative et après quelques minutes de flux de gaz, aucune particule de cuivre n'est observée sur le support d'alumine. La migration des nanoparticules sur la membrane de SiN_x et la formation

de nanoparticules de taille plus grande par frittage ont été observées. A plus haute température (750 – 800 °C) la phase cuivre commence à s'évaporer et est retrouvée sous la forme de nanoparticules sur la membrane de SiN_x non chauffée. A cause de la disparition de la phase cuivre la reformation de l'alumine de cuivre n'a pas pu être observée durant l'oxydation qui requiert une température élevée (>850°C). L'alumine subit des changements structuraux et texturaux progressifs à une échelle locale à des températures supérieures à 850°C. La capacité du cuivre à diffuser lorsqu'il est exposé à des hautes températures de réaction a clairement montré le rôle important du confinement dans ces expériences.

Pour comprendre et suivre la migration du cuivre confiné dans le support d'alumine, il est nécessaire de préserver la structure sphérique du grain du support. A partir des différentes analyses multi-échelles et multi sélectives réalisées, nous avons pu proposer un mécanisme réactionnel complet qui est résumé dans la représentation schématique présentée dans la figure 1. Il prend en considération les différentes interactions entre les phases CuO et alumine, selon la température et le nombre de cycles redox. Au cours de l'oxydation, la migration de la phase contenant le cuivre peut conduire soit au frittage et à la formation de particules de CuO de taille plus grande par diffusion de surface ou aux joints de grains, soit à la formation d'une phase spinelle d'aluminate de cuivre non stoechiométrique par diffusion à l'état solide du cuivre dans l'alumine. À plus basse température (< 800 °C), le premier mécanisme est dominant et les multiples cycles redox entraînent la dispersion des particules de CuO de grande taille dans le grain d'alumine. A plus haute température (> 800°C), le deuxième mécanisme est prépondérant et les particules de CuO réagissent avec l'alumine pour former un aluminate de cuivre. Par ailleurs, la présence de cuivre favorise également la transformation du support en alumine α en modifiant la structure locale de l'alumine de transition initiale. Alors que la formation du spinelle est favorable sous conditions oxydantes à partir du système CuO + γ-Al_2O_3, elle est thermiquement limitée dans le cas du système constitué du CuO et α-Al_2O_3. Par conséquent, lors de l'augmentation du nombre de cycles, la phase α et le CuO se séparent et finissent par former de larges cristaux de CuO dispersés dans un support poreux d'alumine α.

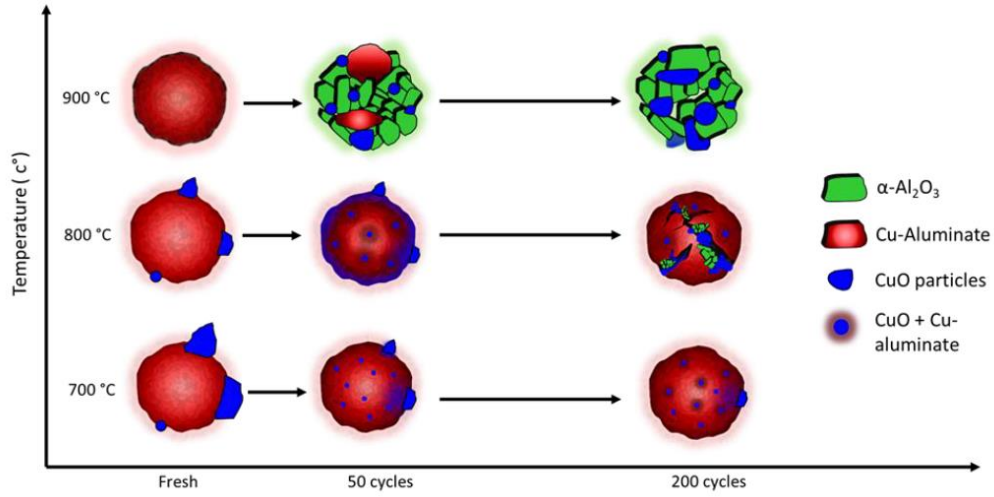

Figure 1 : Représentation schématique de l'évolution texturale et du comportement de migration du cuivre supporté sur de l'alumine fonction de la température et de nombre de cycles redox.

Pour résumer, l'étude in-situ TEM qui s'est proposé de suivre en temps réel les processus d'oxydation-réduction des nanoparticules de cuivre non supportées dans une large plage de température s'est avérée essentielle non seulement pour la compréhension des propriétés des CLC matériaux transporteurs d'oxygène mais grâce à l'ensemble des informations obtenues sur les transformations structurales et la réactivité des systèmes nanométriques à base de cuivre. De plus, il a permis de mettre en évidence deux aspects importants : 1. les limitations techniques pour caractériser des systèmes nanométriques à base de cuivre à haute température et 2. les multiples possibilités expérimentales que nous avons aujourd'hui pour visualiser en temps réel et dans l'espace direct des transformations de phase et de texture.

Du point de vue des matériaux transporteurs d'oxygène, la compréhension de la migration des phases de cuivre et de l'influence du support et les connaissances acquises durant ce travail de thèse permettent d'imaginer des nouvelles solutions pour inhiber le frittage du CuO, comme par exemple la diminution de la température de fonctionnement ou la minimisation de la transformation en α-Al_2O_3 par la préservation de la structure spinelle de l'aluminate de cuivre.

Mot-Clé: Chemical-Looping-Combustion, Redox, Oxygène-Carrier, Nanoparticule, Copper, Copper-Oxide, CuO-Alumine, in-situ MET, STXM, in-situ XAS

Université de Strasbourg

Sharmin SHARNA

Etude des mécanismes de migration du cuivre utilisé comme porteur d'oxygène dans le procédé de combustion en boucle chimique

École doctorale
Physique, chimie-physique
ED 182
Université de Strasbourg

Résumé en français suivi des mots-clés en français

La combustion en boucle chimique (CLC) est considérée comme une solution à moyen terme pour atténuer les émissions de dioxyde de carbone avec une utilisation continue des combustibles fossiles. Dans le procédé CLC, des matériaux porteurs d'oxygène sont utilisés pour réaliser une combustion indirecte, ce qui permet une séparation inhérente du CO2 avec une faible pénalité énergétique. Le transporteur d'oxygène est soumis à des réactions successives d'oxydoréduction à pression atmosphérique et typiquement à 800°C ou plus. Les conditions de réaction induisent des contraintes thermiques et chimiques conduisant à une dégradation importante de la durée de vie du transporteur d'oxygène. Peu d'études sont disponibles dans la littérature concernant la relation entre les paramètres de réaction tels que la température ou le nombre de cycles et l'évolution microstructurale et chimique du matériau, soulignant ainsi la nécessité de mener une analyse approfondie de la phase microstructurale. Ceci est particulièrement valable pour les transporteurs d'oxygène à base de cuivre qui forment le cœur de cette thèse.

L'étude actuelle se penche sur la compréhension du comportement redox des transporteurs d'oxygène oxyde de cuivre-alumine en relation avec les mécanismes de migration des phases de cuivre dans le matériau de support. Ici, pour obtenir une vue d'ensemble à l'échelle nanométrique et à l'échelle du grain (µm) de l'évolution du matériau, une approche multitechnique a été utilisée en utilisant la microscopie électronique à balayage couplée à la spectroscopie à dispersion d'énergie (SEM-EDS), la microscopie à rayons X à transmission à balayage. couplé à la spectroscopie d'absorption des rayons X (STXM-XAS), la diffraction des rayons X in situ (XRD), la spectroscopie d'absorption des rayons X operando (XAS) et la microscopie électronique à transmission environnementale (eTEM)

Les caractérisations microscopiques à l'échelle µm ont aidé à comprendre la migration des phases contenant du cuivre dans le grain de support d'alumine, leur mobilité et leur interaction, sans compromettre la distribution spatiale des espèces chimiques. Un aperçu global des espèces chimiques du matériau a été obtenu grâce à la caractérisation XAS qui a également fourni des données sur l'évolution de la composition du matériau en fonction des cycles redox. De plus, l'étude MET in situ a mis en évidence deux aspects importants : 1er en termes de compréhension des matériaux par observation directe des phases et des transformations texturales, et 2ème en termes de défis expérimentaux pour caractériser de tels systèmes à base de cuivre à haute température.

Deux mécanismes sont proposés concernant l'évolution du système CuO-Al_2O_3, liés à la diffusion dépendante de la température des espèces de cuivre, et au rôle du cuivre dans la transition de phase α-Al_2O_3. La compréhension de la migration du cuivre et de l'influence du support ouvre la voie à la recherche de solutions pour inhiber le frittage de la phase active CuO soit en abaissant la température de fonctionnement soit en limitant la transformation en α-Al_2O_3

Mots clés : *Chemical Looping Combustion, CLC, transporteur d'oxygène, cuivre, alumine, migration, transition de phase, XAS in situ, STXM, STEM in situ, eTEM*

Résumé en anglais suivi des mots-clés en anglais

Chemical Looping Combustion (CLC) is viewed as a midterm solution to mitigate carbon dioxide emissions with continued utilisation of fossil fuels. In the CLC process, oxygen carrier materials are used to carry out indirect combustion, which allows inherent separation of CO2 with low energy penalty. The oxygen carrier is subjected to successive oxidation-reduction reactions at atmospheric pressure and typically at 800 °C or above. The reaction conditions induce thermal and chemical stress leading to significant degradation of the oxygen carrier's lifetime. Few studies are available in the literature concerning the relation between reaction parameters such as temperature or number of cycles and the microstructural and chemical evolution of the material, thus highlighting the necessity to conduct in-depth microstructural-phase analysis. This is especially valid for copper-based oxygen carriers which form the core of this thesis.

The current study delves in the understanding of the redox behaviour of copper oxide-alumina oxygen carriers in relation to the migration mechanisms of the copper phases within the support material. Herein, to achieve a nanoscale as well as grain-scale (µm) overview of the material evolution, a multi-technique based approach was employed utilizing scanning electron microscopy coupled with energy dispersive spectroscopy (SEM-EDS), scanning transmission X-ray microscopy coupled with X-ray absorption spectroscopy (STXM-XAS), *in situ* X-ray diffraction (XRD), *operando* X-ray absorption spectroscopy (XAS) and environmental transmission electron microscopy (eTEM).

The µm-scale microscopic characterisations have aided in the understanding of copper containing phases migration within the alumina support grain, their mobility and interaction, without compromising the spatial distribution of the chemical species. Bulk overview of the material's chemical species has been gained through XAS characterisation which also provided data on the material's composition evolution as a function of the redox cycles. Furthermore, the *in situ* TEM study has highlighted two important aspects: 1st, in terms of material understanding by direct observation of the phases and textural transformations, and 2nd in terms of experimental challenges to characterize such copper-based systems at high temperature.

Two mechanisms are proposed concerning the evolution of CuO-Al2O3 system, related to the temperature-dependent diffusion of the copper species, and to the role of copper in the α-Al2O3 phase transition. The comprehension of copper migration and the influence of the support paves a way into finding solutions to inhibit the sintering of the CuO active phase either by lowering the operating temperature or by restricting the transformation to α-Al2O3.

Keywords : *Chemical Looping Combustion, CLC, oxygen carrier, copper, alumina, migration, phase transition, in situ XAS, STXM, in situ STEM, eTEM*